https://ntrs.nasa.gov/search.jsp?R=19720021626 2020-03-11T19:40:45+00:00Z

15621

UNIVERSITY OF ILLINOIS
URBANA

on C/L

AERONOMY REPORT
NO. 41

Get DRA

AN INVESTIGATION OF THE IONOSPHERIC D REGION AT SUNRISE

by
R. P. Turco
C. F. Sechrist, Jr.

14-005-013

December 1, 1970

N

(NASA-CR-127785) AN INVESTIGATION OF THE IONOSPHERIC D REGION AT SUNRISE R.P. Turco, et al (Illinois Univ.) 1 Dec. 1970 194 p
CSCL 03B
N72-29276
Unclas
G3/13 15621

Supported by
National Aeronautics and Space Administration
Grant NGL 14-005-013
National Science Foundation
Grant G[illegible]232

Aeronomy Laboratory
Department of Electrical Engineering
University of Illinois
Urbana, Illinois

Reproduced by
NATIONAL TECHNICAL INFORMATION SERVICE
US Department of Commerce
Springfield, VA. 22151

2[illegible] pp

CITATION POLICY

The material contained in this report is preliminary information circulated rapidly in the interest of prompt interchange of scientific information and may be later revised on publication in accepted aeronomic journals. It would therefore be appreciated if persons wishing to cite work contained herein would first contact the authors to ascertain if the relevant material is part of a paper published or in process.

AERONOMY REPORT

NO. 41

AN INVESTIGATION OF THE IONOSPHERIC D REGION AT SUNRISE

by

R. P. Turco
C. F. Sechrist, Jr.

December 1, 1970

Supported by
National Aeronautics and Space Administration
Grant NGR-013
National Science Foundation
Grant GA-14232

Aeronomy Laboratory
Department of Electrical Engineering
Urbana, Illinois
UILU-Eng-70-264

PRECEDING PAGE BLANK NOT FILMED

AN INVESTIGATION OF THE IONOSPHERIC D REGION AT SUNRISE

ABSTRACT

In this work the growth over sunrise of the C and D layers of the ionosphere are investigated. The model which is analyzed includes the negative ion species O^-, O_2^-, O_3^-, O_4^-, NO_2^-, NO_3^-, CO_3^-, and CO_4^-; ionization sources due to galactic cosmic rays, precipitated electrons, ionization of NO by scattered Lyman α radiation, and the direct solar radiation ionization of NO and $O_2(^1\Delta_g)$; the photodetachment of most of the negative ions; as well as the time variation of all of these parameters. Also calculated in this work are the detailed sunrise behaviors of the neutral atmospheric species O, O_3, and $O_2(^1\Delta_g)$.

The time variations of the electron, negative ion, and positive ion densities are calculated over sunrise. From these data the mesospheric C- and D-layer development is plotted. Several model parameters are varied until the best agreement with experimentally determined electron densities is obtained. The results are discussed in light of several atmospheric parameters including the O and NO concentrations and the electron-ion recombination coefficient.

TABLE OF CONTENTS

Page

ABSTRACT iii

LIST OF FIGURES vii

LIST OF TABLES xi

LIST OF SYMBOLS xii

1. INTRODUCTION 1

2. FORMULATION OF THE ABSORPTION PROBLEM AND ITS APPLICATION TO THE D REGION AT SUNRISE 4

   2.1 The Absorption of Radiation 4

      2.1.1 Absorption of a general atmosphere ignoring refraction and scattering 6
      2.1.2 Geometrical and orbital approximations for the earth 7
      2.1.3 Formulation of the absorption problem 9

   2.2 Ideal Radial Density Functions 13

   2.3 Solutions for the Optical Depth Problem 21

      2.3.1 The solutions of Swider for a uniform atmosphere 21
      2.3.2 An expansion solution for a more general atmosphere 25
      2.3.3 A perturbation solution for the sunrise region 30

3. APPLICATION OF THE ABSORPTION ANALYSIS TO THE OZONE AND ATOMIC OXYGEN PROBLEM AT SUNRISE 46

   3.1 Definition of the Sunrise Region 46

      3.1.1 A discussion of some special problems associated with the D region 49

   3.2 The All-Oxygen Atmosphere Model 51

      3.2.1 Data and data acquistion for the all-oxygen model 55
      3.2.2 Method of solution of the model 63
      3.2.3 Discussion of the results for the oxygen atmosphere model 69

4. MINOR CONSTITUENTS IN THE D REGION 83

   4.1 Oxygen Species 83

Page
4.2 Oxygen-Hydrogen Reactions. 92
4.3 Oxygen-Nitrogen Reactions. 100
4.4 Other Minor Neutral Constituents in the D Region 108
4.5 Photodissociation and Density Data for the Minor Constituents 110
5. IONIZATION SOURCES IN THE D REGION. 123
5.1 Cosmic Ray Ionization. 123
5.2 Nitric Oxide Ionization by Lyman α 125
5.3 Ionization of $O_2(^1\Delta)$ 129
5.4 X-Ray and Ultraviolet Ionization of the D Region 130
5.5 Ion-Pair Production in the D Region by Precipitated Electrons. 131
6. POSITIVE ION CHEMISTRY. 134
6.1 Positive Ions in the D Region. 135
6.2 Positive Ion Reactions 142
6.3 Positive Ions at Sunrise 147
7. NEGATIVE ION CHEMISTRY. 151
7.1 Electrons in the D Region. 151
7.2 Negative Ions in the D Region. 158
7.3 Negative Ion Reactions 161
7.4 Photodetachment at Sunrise 167
8. SOLUTION OF THE SUNRISE PROBLEM 175
8.1 The Continuity Equations 175
8.2 A Discussion of some Solutions and the Behavior of the Continuity Equations 181
8.2.1 Equilibrium solutions 181
8.2.2 The time dependent continuity equations 184
8.2.3 Some equilibrium properties of the continuity equations 191

Page

8.3 Models of the Sunrise Variables. 194

8.4 Specification of the Variable Parameters in the Computations 199

8.5 Computational Method 203

8.6 The Negatively Charged Species at Sunrise in the D Region 204

8.6.1 Sunrise from 50-60 kilometers 205
8.6.2 Sunrise from 65-75 kilometers 211
8.6.3 Sunrise from 80-90 kilometers 219
8.6.4 The charged specie distributions in the mesosphere. 225

8.7 The Development of the C and D Layers at Sunrise. 231

9. SUMMARY AND CONCLUSIONS 247

APPENDIX I. RAYLEIGH SCATTERING CROSS SECTIONS 252

APPENDIX II. A TWO-EXPONENTIAL ATOMIC OXYGEN MODEL 256

APPENDIX III. A MODEL OF THE ABSORPTION OF THE LOW ALTITUDE OZONE PEAK 257

APPENDIX IV. COMPUTER PROGRAM USED TO OBTAIN THE SUNRISE SOLUTIONS 260

APPENDIX V. EMPIRICAL MODELS FOR OZONE AT SUNRISE. 265

APPENDIX VI. OPTICAL DEPTH CORRECTION FOR THE FINITE SIZE OF THE SUN 267

APPENDIX VII. AN ILLUSTRATION OF TIME CONSTANT EFFECTS ON ATOMIC OXYGEN AT SUNRISE. 271

APPENDIX VIII. IONIC REACTIONS 274

REFERENCES. 275

LIST OF FIGURES

Figure Page

2.1 Earth-sun geometry for optical depth analysis. 10

2.2 Ramp sunrise model 31

2.3 Qualitative behavior of the sunrise angular distribution 35

3.1 Sunrise lines defined by the atmospheric extinction of solar radiation. 47

3.2 Daytime and nighttime ozone distributions in the D region 58

3.3 Solution scheme for the oxygen atmosphere. 65

3.4 Molecular oxygen photodissociation rates over sunrise. 70

3.5 Ozone photodissociation rates over sunrise for the uniform absorption case. 71

3.6 Ozone photodissociation rates over sunrise for the nonuniform absorption case 72

3.7 Ozone distributions during sunrise for both the uniform and nonuniform absorption cases. 73

3.8 Atomic oxygen distributions during sunrise for the uniform absorption case. 74

3.9 Atomic oxygen distributions during sunrise for the nonuniform absorption case 75

3.10 The O/O_3 density ratios over sunrise for both the uniform and nonuniform absorption cases. 76

4.1 Daytime distributions of excited species in the D region 87

4.2 Distribution of hydrogen compounds in the D region 96

4.3 Distribution of nitric oxide in the D region 102

4.4 Distribution of nitrogen compounds in the D region 106

4.5 $O_2(^1\Delta)$ densities during sunrise. 116

4.6 $O_2(^1\Delta)$ densities during sunrise calculated using an ozone model. 117

Figure Page

4.7 Absorption cross sections of the minor constituents in the near ultraviolet. 120

5.1 Ion-pair production rates in the D region. 126

6.1 Daytime positive ion densities in the D region 139

6.2 Nighttime positive ion densities in the D region 140

6.3 Positive ion reaction scheme 148

6.4 The average electron-ion recombination coefficient in the D region 149

7.1a Experimental diurnal electron density variations in the D region 152

7.1b Experimental diurnal electron density variations in the D region 153

7.1c Experimental diurnal electron density variations in the D region 154

7.1d Experimental diurnal electron density variations in the D region 155

7.2 Negative ion ladder. 166

7.3 Photodetachment cross sections of negative ions and infrared absorption cross sections of H_2O and CO_2. 168

7.4 O_2^- photodetachment rates over sunrise. 172

7.5 O^- photodetachment rates over sunrise. 173

7.6 NO_2^- photodetachment rates over sunrise 174

8.1 Ionization interaction scheme. 176

8.2 Nitric oxide ionization rates by direct solar radiation over sunrise 196

8.3 Nitric oxide ionization rates by scattered Lyman alpha radiation over sunrise 197

8.4 The charged species at 50 kilometers during sunrise. 206

8.5 The charged species at 55 kilometers during sunrise. 207

8.6 The charged species at 60 kilometers during sunrise. 208

Figure Page

8.7 The charged species at 65 kilometers during sunrise. 213

8.8 The charged species at 70 kilometers during sunrise. 214

8.9 The charged species at 75 kilometers during sunrise. 215

8.10 The charged species at 80 kilometers during sunrise. 221

8.11 The charged species at 85 kilometers during sunrise. 222

8.12 The charged species at 90 kilometers during sunrise. 223

8.13 Negative ion-to-electron density ratios in the presunrise D region 226

8.14 Negative ion-to-electron density ratios in the post-sunrise D region 227

8.15 Presunrise and post-sunrise electron and positive ion densities. 228

8.16a Experimental diurnal electron density variations in the D region. 232

8.16b Experimental diurnal electron density variations in the D region. 233

8.16c Experimental diurnal electron density variations in the D region. 234

8.16d Experimental diurnal electron density variations in the D region. 235

8.17 Calculated diurnal electron density variations in the D region: Case I. High-O-Low-NO model, fast electron-ion recombination, NO_3^- reaction rate with O, $k(NO_3^-) = 0$. 236

8.18 Calculated diurnal electron density variations in the D region: Case II. High-O-Low-NO model, fast recombination, $k(NO_3^-) = 10^{-14}$ cm^3 sec^{-1} 237

8.19 Calculated diurnal electron density variations in the D region: Case III. High-O-Low-NO model, fast recombination, $k(NO_3^-) = 5x10^{-14}$ cm^3 sec^{-1} 238

8.20 Calculated diurnal electron density variations in the D region: Case IV. High-O-Low-NO model, fast recombination, $k(NO_3^-) = 10^{-13}$ cm^3 sec^{-1} 239

Figure | | Page
8.21 Calculated diurnal electron density variations in the D region: Case V. High-O-High-NO model, fast recombination, $k(NO_3^-) = 5x10^{-14}$ cm^3 sec^{-1}. 240

8.22 Calculated diurnal electron density variations in the D region: Case VI. High-O-Low-NO model, slow recombination, $k(NO_3^-) = 5x10^{-14}$ cm^3 sec^{-1}. 241

LIST OF TABLES

Table Page

3.1 The neutral atmosphere. 56

3.2 Ozone and atomic oxygen data. 59

3.3 Solar radiation and absorption cross sections 60

3.4 Solar radiation and absorption cross sections 61

3.5 The low altitude ozone and neutral atmosphere densities and scale heights 62

3.6 Reaction rate constants for the oxygen atmosphere model 64

4.1 Reaction rates for neutral oxygen reactions 91

4.2 Oxygen-hydrogen reactions 93

4.3 Oxygen-nitrogen reactions 105

4.4 Nighttime minor constituent distributions in the D region. 111

4.5 Daytime minor constituent distributions in the D region. 112

4.6 Photodissociation rates for minor constituents. 119

6.1 D-Region positive ions. 138

6.2 Positive ion reactions. 143

6.3 Positive ion reactions. 144

7.1 Electron affinities 159

7.2 Negative ion reactions. 162

7.3 Negative ion reactions. 163

7.4 Ion-ion reactions 165

7.5 Infrared absorption data. 170

8.1 Continuity equation parameters. .180

8.2 Sunrise parameter models. . . . . .19[illegible]

8.3 Atomic oxygen and nitric oxide daytime distributions. 200

LIST OF SYMBOLS

λ - wavelength ; Å

$\tau(\lambda;\bar{r})$ - optical depth

$\mathcal{L}(\lambda)$ - solar energy flux per unit wavelength interval; ergs cm^2 sec Å

$I(\lambda)$ - solar photon flux per unit wavelength: photons cm^2 sec Å

χ - solar zenith angle

ϕ - spherical and polar angular coordinate - also earth hour angle

s - ray path coordinate (arc length parameter)

$n_j(\bar{r})$ - number density of the jth gas specie ; cm^{-3}

$k(\lambda)$ - absorption coefficient; cm^{-1}

$\sigma_j^a(\lambda)$ - absorption cross section; cm^2

$\sigma_j^d(\lambda)$ - dissociative cross section at wavelength λ of jth specie; cm^2

h - minimum ray height; km

H - scale height; km

$N(\bar{r})$ - number of particles in a unit column; cm^{-2}

$F'(\bar{r})$ - optical depth factor for a non-uniform atmosphere

$F(\bar{r})$ - optical depth factor for a uniform atmosphere

a - earth's radius; km

w - altitude coordinate; km of point where optical depth is measured

δ - earth's declination - or an angular width ; degrees

T - kinetic temperature; °K

p_j - pressure of the jth constituent; dynes cm^{-2}

z - variable altitude coordinate measured from earth; km

m - unit of atomic mass; gms

M_j - number of amu for the jth species (isotope effect included)

$\overline{M}$ - average atomic weight in atomic mass units

β - scale height gradient

X - reduced radial length = $\frac{\text{radial distance}}{\text{scale height}}$

Δ - sunrise angular width

ω_e - angular velocity of the earth; rad $\sec^{-1}$

$J(r,\phi)$ - dissociation rate due to solar radiation; $\sec^{-1}$

U - zenith angle (or hour angle) measured from 90°: $\chi = \pi/2 + U$

σ_R - Rayleigh scattering total cross section, cm^2

f_B - nighttime to daytime density ratio

$\hat{\tau}$ - τ/σ; cm^{-2}

k_j - reaction rate for a neutral specie in a reaction numbered j; cm sec units

I_j - ionization rate for the jth specie; $\sec^{-1}$

q - electron or ion-pair production rate; $\sec^{-1}$ cm^{-3}

α - electron-ion recombination coefficient; cm^3 $\sec^{-1}$

ε - ion-ion recombination coefficient; cm^3 $\sec^{-1}$

β - electron attachment rate; cm sec units

γ - ion-neutral reaction rate; cm sec units

δ - electron detachment rate; cm sec units

1. INTRODUCTION

The important processes in the D region of the atmosphere have yet to be completely determined. One important parameter which can be used as a diagnostic tool in this region is the electron density. The connection between ionization rates, ion chemistry, and electron densities has been greatly clarified in recent years by extensive laboratory measurements of reaction rates and cross sections. Yet these data are still incomplete, and uncertain in some cases. Simultaneously, the measurement of other atmospheric parameters such as minor constituent distributions and solar photon fluxes is helping to solidify the theoretical descriptions of the mesosphere. Still the theoretical problems are manifold because of the extensive number of species and processes present in the atmosphere.

Electron densities can be measured with rocket-borne electrostatic probes or radio wave propagation techniques. In the daytime D-region electron densities are of the order of 100 cm^{-3}. At night these electrons are converted into negative ions by attachment processes. The principle source of electrons at night in the lower D region is galactic cosmic ray ionization, the loss of charge is by ion-ion recombination.

The appearance of free electrons at sunrise has been detected by many researchers (Deeks, 1966; Smith et al., 1967; Mechtly and Smith, 1968a). A layer at about 65 km, the C layer, appears before ground sunrise. A more dense layer, the D-layer ledge, also develops over sunrise. The electrons in the lower region are produced by detachment processes from negative ions. Photodetachment can occur very early in sunrise for ions with a low electron affinity. The associative detachment of negative ions by atomic oxygen which is produced by ozone photodissociation also occurs. In addition there can be collisional detachment which is enhanced at sunrise by the presence of excited metastables. At the upper altitudes direct photoionization becomes important as sunrise progresses.

By studying the growth of the electron density at sunrise as well as its equilibrium values another dimension is added in helping to decipher the D-region processes. But in order to explain the electron density behavior with time the radiation densities in the atmosphere must be known accurately for the region around sunrise. This can be done by using an analytical model for the absorption of radiation based on Lambert's law. The alternative, a complete numerical solution of the problem, would be burdensome.

The analysis of the photochemistry of the D region can be divided into a distinct hierarchy of problems. The major neutral constituents, molecular oxygen and nitrogen, are distributed hydrodynamically, and show no significant diurnal variation. They act as a background for the distribution and reactions of the lesser constituents. The minor neutral constituents have densities many orders of magnitude smaller than the major constituents and comprise a highly variable system of chemically interacting species. In certain cases, subsystems of the minor constituents can be isolated (such as the oxygen-hydrogen system), simplying the overall analysis. The charged constituent densities (positive and negative ions and electrons) are several orders of magnitude smaller than those of the minor neutral constituents. So the minor neutral constituents act as a background for charged specie reactions.

The solution of the sunrise problem proposed here is approached as an initial value problem. Presunrise values of the constituents, which are consistent with the nighttime chemical models and various experimental measurements, are adopted. Solutions are then carried out over sunrise, and the post-sunrise results are compared to establish daytime values. By varying certain processes and observing the outcomes it is possible to remove some ambiguity from the photochemistry of the D region.

2. FORMULATION OF THE ABSORPTION PROBLEM AND ITS APPLICATION TO THE D REGION AT SUNRISE

In order to study in detail the behavior of the D region over the sunrise period, one must have an accurate knowledge of the solar radiations present in this region. Radiant energy input is logically the major driving force for the night-to-day transition, producing photodetachment, photodissociation and photoionization in the atmosphere.

One can obtain the radiation fluxes in a region of the atmosphere by either measuring them directly, or by deduction from known solar intensities and the absorptive properties of the atmospheric gases. The latter method is usually adopted since complete and accurate measurements of radiation fluxes are generally not available.

Some researchers have attempted to solve the optical depth problem in detail. Chapman (1931) first formulated the problem for a simple exponential atmosphere, arriving at his well-known Chapman functions. Later, Swider (1964) extended this work to include atmospheres with constant scale height gradients, and accounted for gravitational variations. Swider's results apply, however, to uniform atmospheres (i.e. those with only a radial variation). This is also true of the work of Nicolet (1945) and others.

In this study the optical depth problem will be solved for a non-uniform atmosphere, such as one would encounter in the sunrise region.

2.1 The Absorption of Radiation

If one considers an infinite absorbing medium, uniform in the x-y plane with a plane electromagnetic wave incident along the z-axis, the intensity of the incident wave will be attenuated according to Lambert's law

$$\frac{dI(\lambda;z)}{I(\lambda;z)} = -k(\lambda;z)dz \quad ; \quad \text{or:} \quad I(\lambda;z) = I_0(\lambda)e^{-\int_0^z k(\lambda;z)dz} \quad . \tag{2.1}$$

The field energy is absorbed by individual atoms and molecules by the excitation of their electronic degrees of freedom by the incident field. In some simple cases matrix elements can be calculated for the interaction Hamiltonian, and theoretical cross sections can thus be obtained. More practically, the absorptive cross section, $\sigma^a(\lambda)$, is measured in the laboratory. One uses, in this case, the relation

$$k(\lambda;z) = \sigma^a(\lambda)n(z) \quad . \tag{2.2}$$

This very simple equation assumes ideal experimental conditions.

The absorbed energy may result in dissociation, detachment, or ionization processes; in the excitation of the internal degrees of freedom of the atom or molecule; or in the emission of radiation over a wide spectrum. The incident radiation might also be simply scattered out of the beam.

Combining Equations (2.1) and (2.2) into a different form one can define the optical depth

$$\tau(\lambda;0,z) = \int_0^z k(\lambda;z')dz' = \sigma^a(\lambda)\int_0^z n(z')dz' \tag{2.3}$$

and so

$$I(\lambda;z) = I_0(\lambda)\exp\{-\tau(\lambda;0,z)\} \quad . \tag{2.4}$$

Here the photon flux, I, was used in Equations (2.1) through (2.4). It is directly related to the energy flux $\mathcal{Q}$, and so, to the incident intensity, by the equation

$$I(\lambda) = \frac{\lambda}{hc}\mathcal{Q}(\lambda) \quad . \tag{2.5}$$

2.1.1 Absorption of a general atmosphere ignoring refraction and scattering

The absorption problem for the atmosphere is more complex. The sun, the source of radiant energy, is an extended source which subtends about one-half degree of arc at the earth. The radiation incident on the atmosphere is in the form of spherical waves. Because of the small size of the source, and its large distance from earth, it is an excellent approximation to use a plane wave incidence, rather than integrating over the radiation source. The incident intensity is assumed measurable, as by satellites.

One consequence of this approximation is that the ideal geometrical earth shadow consists of only a cylindrical umbra, but this fact will have little importance here.

Refraction, due to the density variation of the atmosphere near the earth's surface, must also be considered in general. However, if one is interested primarily in wavelengths shorter than optical wavelengths, the refraction will be very small. Furthermore, since it is expected that for minimum ray heights less than 40 km very little ultra-violet will penetrate the atmosphere because of dense absorption, and since refraction at minimum ray heights greater than this is still smaller, then refraction may be ignored in calculating the ultraviolet sunrise. Also consider that the effects of refraction on the optical depth tend to be self-compensating. On the one hand refraction increases the length of the ray path, thereby increasing τ. Contrary to this, the ray path will tend to be higher in the atmosphere where absorption is reduced, thus decreasing τ. These effects by no means cancel exactly, however.

Archer (1964) has worked on the problem of albedo radiation in his study of the photodetachment of O_2^-. His results illustrate that at sunrise zenith angles >90° the albedo radiation is negligible. This is plausible since one would expect very little scattered and reflected radiation near the geometrical sunrise.

With these arguments one could conclude that an approximate description of sunrise will result from the use of an ideal earth shadow as the sunrise line at the altitude where ultraviolet extinction occurs (for a particular band of wavelengths). Lloyd (1968) has done absorption calculations accounting for both refraction and the sun's finite size. These results would apply in the long wave limit. Lloyd (1968) defines a screening ray height below which refraction and absorption compensate each other to yield less than 1% transmission. In this sense, one could define the ideal earth shadow by a minimum ray height equal to the screening height. The discussion of sunrise is taken up again in Chapter 3.

2.1.2 Geometrical and orbital approximations for the earth

Now consider the absorption of solar radiation by a general atmosphere. The particle density of the atmosphere is $n(\bar{r}) = n(r,\theta,\phi)$, where n is composed of the constituents, $n_j(\bar{r})$. One can generalize this to the case of time dependent densities, $n(\bar{r},t)$, so that

$$n(\bar{r},t) = \sum_j n_j(\bar{r},t) \quad .$$

Assuming that each species absorbs independently of the others, which is certainly true for low density gas mixtures, one defines the optical depth for some arbitrary, illuminated point in the atmosphere, $\bar{r}$, by

$$\tau_j(\lambda;\bar{r},\bar{r}_s) = \sigma_j{}^a(\lambda) \int_{\bar{r}}^{\bar{r}_s} n_j(\bar{r}')\,ds' \qquad (2.6$$

and

$$\tau(\lambda;\bar{r},\bar{r}_s) = \sum \tau_j(\lambda;\bar{r},\bar{r}_s) \qquad (2.7)$$

where $\bar{r}_s$ is the source (sun) coordinate, ds' is the element along the ray path to the source (assumed a point source), and time is suppressed in the equation.

The particle densities decrease exponentially at higher altitudes. Since the source is a great distance from the exponential "top" of the atmosphere, one lets $r_s \to \infty$. Also, one uses as input data the incident fluxes measured at the top of the atmosphere, ignoring the small discrepancy due to absorption at very high altitudes. Equivalently, one could consider the absorption integral from $\bar{r}$ to $\bar{r}_{top}$, where $\bar{r}_{top}$ is the altitude at which incident fluxes are measured. In either case, negligible error results by extending the integral to infinity. One then defines

$$\tau(\lambda;\bar{r}) \equiv \sum_j \sigma_j^a(\lambda) \int_{\bar{r}} n_j(\bar{r}')ds' = \tau(\lambda;\bar{r},\infty) \quad . \qquad (2.8)$$

If the total number of particles of a species (with subscript suppress) in a column of unit area extending from the point $\bar{r}$ along the ray path is given by

$$N(\bar{r}) \equiv \int_{\bar{r}}^{\infty} n(\bar{r}')ds' = \frac{\tau(\lambda;\bar{r})}{\sigma^a(\lambda)} \qquad (2.9)$$

it would then follow that

$$\tau(\lambda;\bar{r}) = \sum_j \sigma_j{}^a(\lambda)\, N_j(\bar{r}) \quad . \qquad (2.10)$$

2.1.3 Formulation of the absorption problem

In order to evaluate $N(\bar{r})$ one requires two fundamental sets of data. First, the earth's geometry must be accountable. Then the structure of the atmosphere above this surface must be known in detail. Swider (1964) has studied the earth geometry problem. If $\tilde{\theta}$ is the latitude variable, $\tilde{\phi}$ the longitudinal angle measured from east to west, and δ the earth's declination measured positive forward in the northern hemisphere (refer to Figure 2.1), then the zenith angle, χ, obeys the relationship

$$\cos\chi = \cos\delta \cos\tilde{\theta} \cos\tilde{\phi} + \sin\delta \sin\tilde{\theta} \quad . \tag{2.11}$$

The earth's declination introduces two complications. First, because the earth's radius has a latitude variation (and negligible longitudinal variation) the general ray passes over terrain that lacks circular symmetry when $\delta \neq 0$. Second, if one is considering an atmosphere with latitudinal density variations the problem becomes more nonuniform . Swider (1964) showed that for the limited range of zenith angles that are important in calculating $N(\bar{r})$ the latitudinal deviation in the earth's radius is very small. Consequently, the variation of both the earth's radius and the particle densities over latitude will be ignored in evaluating $N(\bar{r})$.

In essence, the problem is then reduced to considering the two-dimensional function, $f_\theta(r,\phi)$, where θ, either the polar or latitude angle, is a parameter specified by the end point of the ray path (see Figure 2.1). Because of the axial symmetry of the spherical earth-sun system only the declination angle, δ, need be specified to define the earth's position at any time--or short time duration. Also, the longitudinal angle, $\tilde{\phi}$, is related to the spherical coordinate, ϕ, for this configuration by, $\tilde{\phi} = 2\pi - \phi$.

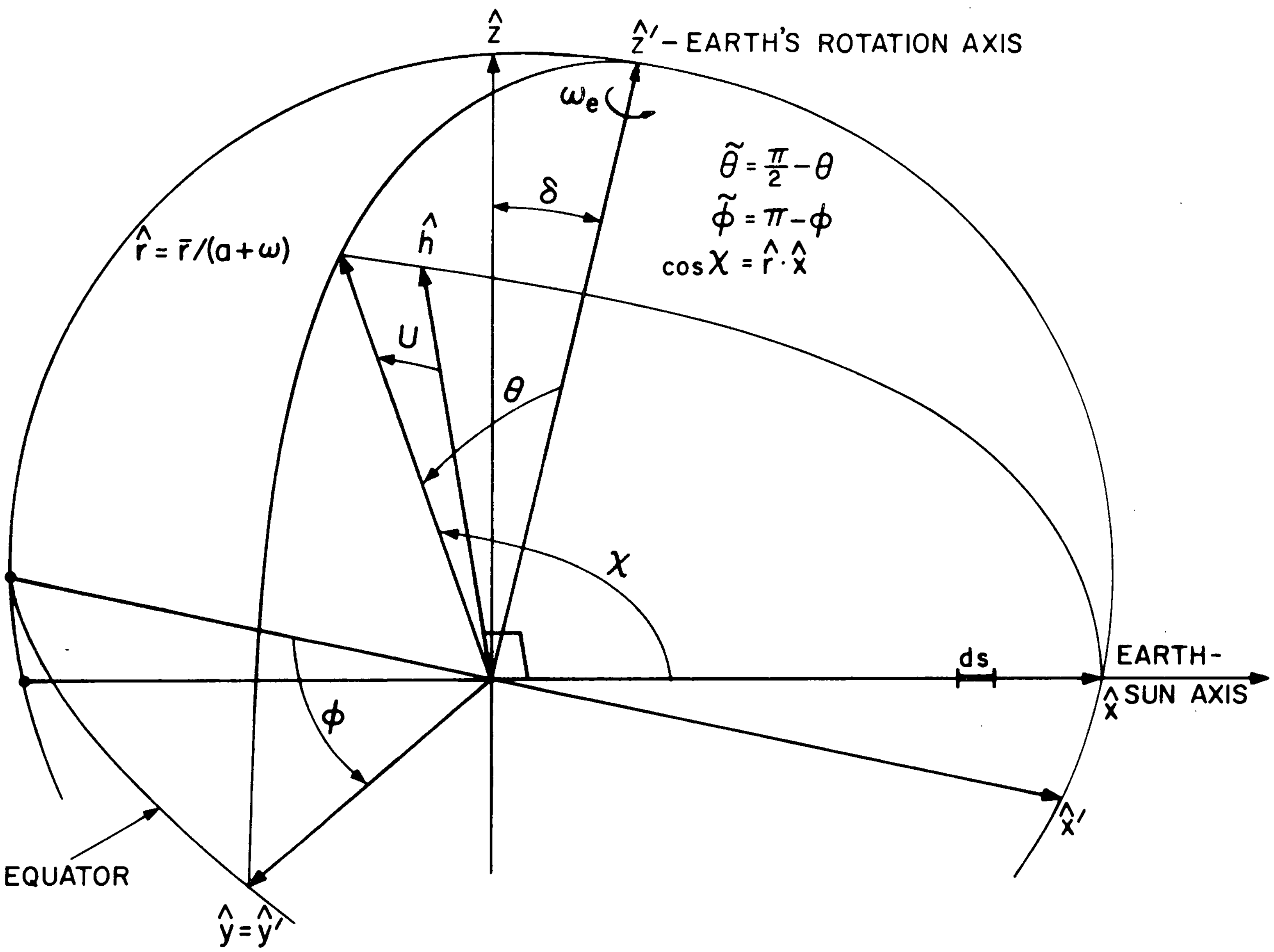

Figure 2.1 Earth-sun geometry for optical depth analysis.

One can proceed to reduce the integral

$$\int_C f_\theta \, (r',\phi')ds'$$

where C is the ray contour, by substitution. Thus

$$\int_s^\infty ds' \; f_\theta \left\{ \sqrt{s'^2+(a+h)^2} \; , \; \cos^{-1} \frac{s' + \varepsilon}{\sqrt{(s'+\varepsilon)^2 + \tau^2}} \right\} \tag{2.12}$$

where,

a = earth's radius

h = minimum ray height = $(a+w)\sin\chi - a$

$r = a+w = \sqrt{s^2 + (a+h)^2}$

$\varepsilon = \tan\delta \cos\tilde{\theta} \, (a+h)(1+\tan^2\delta \sin^2\tilde{\theta})^{-\frac{1}{2}}$

$\tau = \sec^2\delta \sin\tilde{\theta} \, (a+h)(1+\tan^2\delta \sin^2\tilde{\theta})^{-\frac{1}{2}}$

$(r,\tilde{\theta})$ specify the end point of the ray

Following Swider's development (1964), $N(\bar{r})$ can be written in terms of a dimensionless quantity $F(\bar{r})$, the optical depth factor, by defining

$$N(\bar{r}) = n(w)H(w)F(\bar{r}) \tag{2.13}$$

where subscripts are suppressed, w is the altitude from the earth's surface of $\bar{r}$, and H(w) is the scale height at the altitude w. It is assumed that the value n(w) is the largest value that $n(\bar{r})$ attains over the ray.

The following set of definitions are useful.

$$\begin{aligned} &\xi = s'/H(w) \quad , \quad \xi_0 = s/H(w) \\ &X_0 = (a+h)/H(w) = \eta \\ &X = (a+w)/H(w) \end{aligned} \tag{2.14}$$

ε,τ are defined with $(a+h) \to X_0$

$$F(\bar{r}) = \frac{1}{n(w)} \int_{\xi_0}^{\infty} d\xi \; n \left\{ \sqrt{\xi^2+\eta^2} \;,\; \cos^{-1} \frac{\xi+\varepsilon}{\sqrt{(\xi+\varepsilon)^2+\tau^2}} \right\} \tag{2.15}$$

where Equation (2.15) is defined with $f = n(\frac{r}{H},\phi)$, since $\cos\tilde{\phi} = \cos\phi$. Some important transformations for (14) are derived using

$$\begin{aligned} \xi_0 &= X \cos\chi \\ \eta &= X \sin\chi = X' \cdot \sin\chi' = X_0 \\ \xi &= X' \cos\chi' \end{aligned} \tag{2.16}$$

The next analytical step is to define the density function, $n(\frac{r}{H},\tilde{\phi})$, in terms of a realistic physical model of the atmosphere, and to calculate the optical depth factor, $F(\bar{r})$. This work is done in Section 2.2, where solution schemes are put forward.

Equation (2.15) is only one of several possible forms for the solution of the problem. Many useful transformations, such as those used by Swider (1964), are possible for particular cases of interest.

Take, for example Equation (2.15), and replace $\eta = X\sin\chi = X'\sin\chi'$ and $\xi = X'\cos\chi'$. Then Equation (2.15) reduces to

$$F(\bar{r}) = \frac{1}{n(w)} \int_{X}^{\infty} dX' \frac{1}{\sqrt{1 - \frac{X^2}{X'^2}\sin^2\chi}} \, n\{X';\phi(X')\} \tag{2.17}$$

a form commonly used when angular variations are absent.

Before proceeding to calculate $F(\bar{r})$ it is important to note the connection between the various representations used here, expressed by Equations (2.15) through (2.16). There is the equivalence of the representations

$$F(\bar{r}) = F(r,\theta,\phi) = F(w,\tilde{\theta},\tilde{\phi}) = F(\chi,X) = F(\xi_0,\eta) = F(\chi,w) = F(\chi,h) \text{ , etc.}$$

Swider uses the form, $F(\chi,X)$, for convenience in his analysis. Here we will use other forms freely.

The definition of F is intimately dependent on w, the altitude of the point of evaluation. For $\chi < \frac{\pi}{2}$, $\xi_0(\chi,w) > 0$ Equation (2.14) is valid as it stands. However, for $\chi \geq \frac{\pi}{2}$, $\xi_0(\chi,w) \leq 0$ one evaluates F for the lowest altitude of the ray, that is, using $n(h)H(h)$. This will force a renormalization of ξ, η, X, etc. in the resulting integrals. The effect is treated later. In any case, the definition of F is chosen to be consistent with Swider's work so that his results can be incorporated wherever possible.

2.2 Ideal Radial Density Functions

One first considers the ideal radial density distributions suggested by physical law. Assume that the atmosphere is in hydrodynamic and thermal equilibrium. The equation of state for an ideal gas in equilibrium (the first virial coefficient) is invoked for the rarefied atmosphere. Thus

$$\frac{pv}{kT} = 1 \quad ; \quad \text{or} \quad p = nkT \quad . \tag{2.18}$$

where k is Boltzmann's constant, p is pressure and T is temperature, local values of p, n, T are taken, all species are assumed to be at the same temperature, and the law of partial pressures is utilized, although subscripts are suppressed.

For the steady-state atmosphere, one applies the hydrostatic equation

$$\frac{dp}{dz} = - nmMg \tag{2.19}$$

where z is an altitude variable, g is the acceleration of gravity, m is a unit of atomic mass, and M is the average number of amu's for the species.

Combining Equations (2.18) and (2.19) one readily obtains

$$\frac{dp}{p} = -\frac{mMg}{kT}\,dz = -\frac{dz}{H}$$

or

$$p(z) = p(z_0)\,\exp\left\{-\int_{z_0}^{z}\frac{dz}{H}\right\} \quad ; \qquad (2.20)$$

$$\frac{1}{H} = M\,\frac{mg}{kT} \quad .$$

Usually the atmosphere at some altitude is considered to be either perfectly mixed, or in simple diffusive equilibrium (ignoring thermal effects), depending on which process dominates at that altitude. Somewhere between 90-100 kilometers the atmosphere changes from one of mixing at lower heights to one of diffusion. Since Equation (2.19) at lower altitudes represents the behavior of the mixed atmosphere it is written

$$\frac{dp}{dz} = -mg\sum_i n_iM_i \quad ; \quad p = \sum p_i \text{ here.} \qquad (2.21)$$

This leads one to define the average atomic weight in atomic mass units, $\overline{M}$ by

$$\overline{M} = \frac{\sum n_iM_i}{\sum n_i} = \frac{1}{n}\sum n_iM_i \quad . \qquad (2.22)$$

Then, for each component of the atmosphere, n_j, one defines

$$M_j = \begin{cases} M_j & \text{- diffusion} \\ \overline{M} & \text{- mixing} \end{cases} \quad . \qquad (2.23)$$

This definition preserves the validity of Equation (2.20) for each component of the atmosphere under either condition of equilibrium.

Using Equation (2.18), Equation (2.20) can then be cast in the general form

$$n(z) = n(z_0) \frac{T(z_0)}{T(z)} \exp\left\{ - \int_{z_0}^{z} \frac{dz}{H(z)} \right\} \quad . \tag{2.24}$$

Since this form is not convenient to use, consider an altitude coordinate, $\tilde{z}$, defined above a spherical level of altitude, w. Then

$$z = r-a = \tilde{z}+w, \quad \text{with } z_0 = w \quad .$$

One obtains from this transformation

$$n(r-a) = n(w) \frac{T(w)}{T(r-a)} \exp\left\{ - \int_{0}^{r-a-w} \frac{d\tilde{z}'}{H(\tilde{z}'+w)} \right\} \quad . \tag{2.25}$$

Equation (2.25) is reducible using certain approximations. First note that H can be expanded in a Taylor series about $\tilde{z}' = 0$

$$H(\tilde{z}'+w) = H(w) + \tilde{z}' \frac{\partial H(w)}{\partial w} + \frac{1}{2} \tilde{z}'^2 \frac{\partial^2 H(w)}{\partial w^2} + \ldots$$

or

$$H(\tilde{z}+w) = H(w) + \beta(w)\tilde{z}' + \ldots$$

where, $\beta(w) = \frac{\partial H(w)}{\partial w}$ is the scale height gradient at the altitude, w. Assuming that "w" is understood, the first order approximation for the scale height is

$$H(\tilde{z}'+w) = H + \beta\tilde{z}' \quad . \tag{2.26}$$

Insertion of Equation (2.26) into Equation (2.25) yields

$$n(r-a) = n(w)\,\frac{T(w)}{T(r-a)}\left[\frac{H(w)}{H(w) + \beta(r-a-w)}\right]^{\frac{1}{\beta}} \quad . \tag{2.27}$$

(Note, r → r' before insertion in the integrals of Section 2.1.3)

If one uses the notation of Section 2.1.3, where

$$X' = X'(w) = \frac{r'}{H(w)} = \sqrt{\xi^2 + \eta^2} \tag{2.28}$$

$$X = \frac{a+w}{H(w)} = \eta/\sin\chi$$

$$X_0 = \frac{a+h}{H(w)} = \eta \quad .$$

Then

$$n(X') = n(w)\,\frac{T(X)}{T(X')}\left[\frac{1}{1+\beta(X'-X)}\right]^{\frac{1}{\beta}} \quad . \tag{2.29}$$

Of course, the case where the scale height is constant is very simply derived from Equation (2.25), and is

$$n(X') = n(w)\ e^{-(X'-X)} \tag{2.30}$$

where the atmosphere is considered to be isothermal in this case.

Note that by inserting Equation (2.30) into Equation (2.17), setting $\chi = \lambda$, and transforming into an integral in $d\lambda$ by using $X'\sin\chi = X\sin\chi$, one obtains Swider's Equation (2.13) (1964).

Now, if in Equation (2.29) one assumes that the scale height gradient comes entirely from the temperature variation, it follows that since $H \propto T$

$$n(X') = n(w)\left[\frac{1}{1 + \beta(X'-X)}\right]^{1 + \frac{1}{\beta}} \qquad (2.31)$$

by using $\frac{T(X)}{T(X')} = \frac{T(w)}{T(\tilde{z}'+w)} = \frac{H(w)}{H(\tilde{z}'+w)}$.

For a uniform atmosphere, Chapman (1931) has utilized the form in Equation (2.30). Similarly, Swider (1964) has analyzed the problem with Equation (2.31). Other density functions are yet possible. Taking into account the effects of gravity, using

$$g(\tilde{z}+w) = g(w)\,\frac{(a+w)^2}{(a+w+\tilde{z})^2} = g(w)\,\frac{X^2}{(X + \frac{\tilde{z}}{H})^2} \qquad (2.32)$$

one can determine Equation (2.25) from both the case where a temperature gradient is present, and where the atmosphere is isothermal. For the isothermal case one defines

$$H(w) = \frac{kT}{mMg(w)} \qquad (2.33)$$

and finds that

$$n(X') = n(w)\,\exp\left\{-\frac{X}{X'}(X'-X)\right\} \quad . \qquad (2.34)$$

Now introduce a thermal gradient such that

$$T(\tilde{z}+w) = T(w) + \alpha\tilde{z} \quad . \qquad (2.35)$$

It is obvious that α and β are related, in the absence of gravity variations, by

$$\beta = \frac{k\alpha}{mMg}$$

and so one defines

$$H(w) = \frac{kT(w)}{mMg(w)} \quad .$$

Then, by substitution

$$H(\tilde{z}+w) = \left[\frac{kT(w)}{mMg(w)} + \frac{k\alpha\tilde{z}}{mMg(w)}\right]\left(\frac{X + \frac{\tilde{z}}{H}}{X}\right)^{2}$$

or

$$H(\tilde{z}+w) = H(1 + \beta\,\frac{\tilde{z}}{H})\left(\frac{X + \frac{\tilde{z}}{H}}{X}\right)^{2} \qquad (2.36)$$

and Equation (2.25) becomes

$$n(X') = n(w)\left[\frac{1}{1 + \beta(X'-X)}\right] \exp\left\{-\int_{0}^{(X'-X)} \frac{X^{2}dy}{(1+\beta y)(X+y)^{2}}\right\} .$$

This expression becomes

$$n(X') = n(w)\left[\frac{1}{1 + \beta(X'-X)}\right]^{1+\frac{1}{\beta}}\left(\frac{X'}{X}\, e^{\frac{X'-X}{X'}}\right)^{\frac{1}{\beta}} \qquad (2.37)$$

where it was assumed that $\beta X >> 1$. This expression is very similar to both Equations (2.31) and (2.34).

Here, variations in the mean atomic number, $\overline{M}$, are not specifically considered since it will be assumed that when $\overline{M}$ is determined by mixing, the atmospheric mixing is ideal, and $\overline{M}$ is a constant. Any variation in $\overline{M}$ could easily be incorporated by using $M(\tilde{z}+w) = M(w) + \gamma\tilde{z}$ (rather than a general Maclaurin expansion for $H(\tilde{z}+w)$. This work is not done here.

The results of this section can be summarized by the equations

$$n(X') = n(w)e^{-(X'-X)} \quad ; \quad H = \frac{kT}{mMg} = \text{constant} \tag{2.38a}$$

$$n(X') = n(w)\left[\frac{1}{1 + \beta(X'-X)}\right]^{1 + \frac{1}{\beta}} \quad ;$$

$$H(w) = \frac{kT(w)}{mMg} \quad ; \quad \beta = \frac{\partial H(w)}{\partial w} \tag{2.38b}$$

$$n(X') = n(w)\exp\left\{-\frac{X}{X'}\,(X'-X)\right\} \quad ; \quad H(w) = \frac{kT}{mMg(w)} \tag{2.38c}$$

$$n(X') = n(w)\left[\frac{1}{1 + \beta(X'-X)}\right]^{1 + \frac{1}{\beta}}\left(\frac{X'}{X}\,e^{\frac{X'-X}{X'}}\right)^{\frac{1}{\beta}} \quad ;$$

$$H(w) = \frac{kT(w)}{mMg(w)} \quad . \tag{2.38d}$$

As in the work of Swider (1964), the scale height gradient of a particular distribution will be indicated by the subscript β; thus, F_β and n_β. In Equation (2.38a) $\beta = 0$, and for the other distributions $\beta > 0$.

It can also be shown that Equation (2.38b) is valid for negative scale height gradients as long as the altitude where $n \rightarrow 0$ is not exceeded. If β indicates the magnitude of the scale height gradient for this case, the equivalent of Equation (2.38b) is

$$n(X') = \begin{cases} n(w)\,[1 - \beta(X'-X)]^{\frac{1}{\beta} - 1} & ; \quad X' \leq X + \frac{1}{\beta} \\ 0 & ; \quad X' > X + \frac{1}{\beta} \end{cases} \tag{2.38e}$$

$$\beta = -\frac{\partial H(w)}{\partial w} \quad .$$

For the most part Equations (2.38a) and (2.38b) will be used. It is useful to note the connection between the distribution referred to a spherical level, w, and to a spherical level corresponding to the minimum ray height, h. The following definitions are useful for purposes of clarity in what follows

$$X = \frac{a+w}{H(w)} \quad ; \quad X_h = \frac{a+w}{H(h)} \quad ; \quad X_0 = \frac{a+h}{H(w)} \quad ; \quad X_{0h} = \frac{a+h}{H(h)} \text{ etc.} \tag{2.39}$$

It is easy to show that

$$n(X'_h) = n(w)e^{X_h(1-\sin\chi)} \, e^{-(X'_h - X_{0h})} \tag{2.40a}$$

where h subscripts are used even though H = constant, for consistency. Then Equation (2.38b) becomes

$$n(X'_h) = n(w)\left(\frac{H(w)}{H(h)}\right)^{1+\frac{1}{\beta}} \left[\frac{1}{1+\beta(X'_h - X_{0h})}\right]^{1+\frac{1}{\beta}} \quad ; \quad \beta > 0 \quad . \tag{2.40b}$$

Rewriting Equation (2.40b) for more useful purposes

$$n(X'_h) = n(w)\,\frac{H(w)}{H(h)}\left[\frac{1}{1+\beta(X'_h - X_{0h})}\right]^{1+\frac{1}{\beta}} [1+\beta X_h(1-\sin\chi)]^{\frac{1}{\beta}} \quad . \tag{2.40c}$$

In evaluating Equations (2.15) and (2.17), (2.40a) and (2.40c) are useful transformations for $\chi > \frac{\pi}{2}$. Also, for $\chi \geq \frac{\pi}{2}$ the equivalent expressions for the distributions are

$$n(X'_h) = n(h)e^{-(X'_h - X_{0h})} \quad ; \quad \beta = 0 \tag{2.41}$$

$$n(X'_h) = n(h)\left[\frac{1}{1 + \beta(X'_h - X_{0h})}\right]^{1+\frac{1}{\beta}} \quad ; \quad \beta = \text{const} > 0 \quad .$$

Equations (2.40c) and (2.41) can be used with negative scale height gradients by inserting $-\beta$ for β and observing the appropriate limit on X'.

2.3 Solutions for the Optical Depth Problem

2.3.1 The solutions of Swider for a uniform atmosphere

Several simple approximations exist which give accurate descriptions of the atmospheric absorption under special conditions. For the cases of the distributions (2.38a), (2.38b) and (2.38e), it is an easy matter to show that the radial integrals are

$$\int_{r(w)}^{\infty} dr'\, n_\beta(r') = n(w)H(w) \quad . \tag{2.42}$$

One then assumes that the major portion of the optical depth integral is in a region such that $\chi' \sim \chi$, and defines the path length for the optical depth integral

$$ds' \cong \sec\chi dr' \quad .$$

Then

$$\int_{s(w)}^{\infty} ds'\, n_\beta(r') = n(w)H(w)\, \sec\chi \tag{2.43}$$

which implies that in the regions $\chi < \frac{\pi}{2}$

$$F_\beta(\chi) = \sec\chi \quad . \tag{2.44}$$

The approximation (2.44) is very accurate only for small zenith angles, but it can be applied with fair accuracy (5%) up to an angle, $\chi = 80°$. For the case $\beta = 0$ it is easy to show, using Equations (2.17) and (2.38a) that

$$F_0(X) = \sec\chi \left\{1 - \sec^2\chi \, \frac{\sin^2\chi}{X} + O\left(\frac{1}{X^2}\right)\right\} \quad . \tag{2.45}$$

These approximations are insufficient for sunrise analysis since $\sec\chi$ will become very large. Away from sunrise a host of approximations similar to those given above exist. But near sunrise more careful consideration is necessary. This is done in the work of Swider (1964). In order to describe the atmosphere accurately, Equation (2.38b) represents a theoretical refinement over Equation (2.38a) in that the scale height is included. Swider calculated the optical depth factor for this case assuming the atmosphere was uniform. His results will be quoted here for completeness, and are valid for $\chi \leq \frac{\pi}{2}$

$$F_1 = \frac{b}{b^2 - \sin^2\chi}\left[\cos\chi - \frac{1}{X}\right] + \frac{2\sin^2\chi}{X|b^2 - \sin^2\chi|^{3/2}} \left\{ \left\{\begin{matrix}\coth^{-1}\\ \tan^{-1}\end{matrix}\right. \left(\frac{b}{\sqrt{|b^2 - \sin^2\chi|}}\right) - \left.\begin{matrix}\coth^{-1}\\ \tan^{-1}\end{matrix}\right. \left(\frac{\cos\chi - \frac{1}{X}}{\sqrt{|b^2 - \sin^2\chi}}\right) \right\} \tag{2.46a}$$

where $\beta = 1$, $b = 1 - \frac{1}{X}$, $(\tan^{-1})$ is applied when $\sin\chi > b$, $(\coth^{-1})$ when $\sin\chi < b$. For $\sin\chi = b$

$$F_1 = \frac{1}{X-1}\left[\frac{1}{2}\cot\left(\frac{\pi}{4} - \frac{\chi}{2}\right) + \frac{1}{6}\cot^3\left(\frac{\pi}{4} - \frac{\chi}{2}\right) - \frac{2}{3}\right]$$

and,
$$F_{\frac{1}{2}} = \frac{1}{G(\sin^2\chi - d^2)}\left[1 - \frac{3\sin^2\chi}{\sin^2\chi - d^2}\right]\left[\cos\chi - \frac{1}{G}\right] - \frac{d\cos\chi}{\sin^2\chi - d^2}$$

$$+ \frac{6d\sin^2\chi}{(\sin^2\chi - d^2)\,|\sin^2\chi - d^2|^{3/2}}\left\{\begin{matrix}\coth^{-1}\\ \\ \tan^{-1}\end{matrix}\left(\frac{d}{\sqrt{|\sin^2\chi - d^2|}}\right)\right.$$

$$\left. - \begin{matrix}\coth^{-1}\\ \\ \tan^{-1}\end{matrix}\left(\frac{\cos\chi - \frac{1}{G}}{\sqrt{|\sin^2\chi - d^2|}}\right)\right\} \qquad (2.46b)$$

where $\beta = \frac{1}{2}$, $G = \frac{X}{2}$, $d = 1 - \frac{2}{X}$, and $(\tan^{-1})$ is used for $\sin\chi > d$. To get results for $\chi \geq \frac{\pi}{2}$ one uses the forms for $\chi \leq \frac{\pi}{2}$ by dividing the absorption integral into parts, using the symmetry properties of a uniform atmosphere.

To be consistent with previous work, and that of Swider, one writes

$$F_\beta(\bar{r}) = \begin{cases} F_\beta(\chi, X) & ; \quad \chi < \frac{\pi}{2} \\ \\ \bar{F}_\beta(\chi, X) & ; \quad \chi \geq \frac{\pi}{2} \end{cases} \qquad (2.47)$$

where it can be shown that

$$\bar{F}_\beta(\chi, X) = 2F_\beta(\tfrac{\pi}{2}\ ;\ X_{0h}) - \frac{n(w)H(w)}{n(h)H(h)}\,F_\beta(\pi - \chi, X) \qquad (2.48)$$

and where the ratio in the second term is

$$\frac{n(w)H(w)}{n(h)H(h)} = \begin{cases} e^{-X_h(1-\sin\chi)} & ; \quad \beta = 0 \\ \\ [1 + \beta X_h(1-\sin\chi)]^{-\frac{1}{\beta}} & ; \quad \beta > 0 \end{cases} \quad . \qquad (2.49)$$

Then, $N = n(h)H(h)\bar{F}_\beta$.

Equation (2.48) can be utilized in conjunction with Equations (2.46a) and (2.46b) to give the optical depth factors for scale height gradients of $\frac{1}{2}$ and 1. When the scale height is considered constant, one obtains the Chapman function, $C_h(\chi,X) = F_0(\chi,X)$. Its values near sunrise can be calculated from any number of analytical approximations that are available for a uniform atmosphere. Swider and Gardner (1967) have listed these approximations and evaluated their accuracy and usefulness. Two approximations are repeated here for reference: when $\chi \leq \frac{\pi}{2}$ (due to Swider)

$$F_0(\chi,X) = -X\cos\chi + \sqrt{1+2X-W}\left\{\sqrt{W} + \frac{\sqrt{\pi}}{2}(1 - \mathrm{erf}\sqrt{W})e^{W}\right\} \quad ; W < 9.5 \qquad (2.50)$$

$$F_0(\chi,X) = -X\cos\chi + \sqrt{1+2X-W}\left\{\sqrt{W} + \frac{1}{2\sqrt{W}}(1 - \frac{1}{2W} + \frac{3}{4W^2} - \frac{15}{8W^3})\right\} \quad ; W \geq 9.5$$

where $W \equiv X(1-\sin\chi)$;

(Green and Barnum, 1964) (cited by Swider and Gardner, 1967)

$$F_0(\chi,X) = \exp\left\{\frac{\chi^2}{2}(1 - 0.115\chi^2 - \alpha\chi^4)^{-1}\right\} \qquad (2.51)$$

where $\alpha = \left\{1 - 0.115\left(\frac{\pi}{2}\right)^2 - \left(\frac{\pi}{2}\right)^2/\ell n\left(\frac{\pi}{2}X\right)\right\}\left(\frac{\pi}{2}\right)^{-4}$.

In addition to these approximations, which may be used in conjunction with Equations (2.48), Swider (1964) also lists an approximation, originally calculated by Nicolet (1945) for $\pi \geq \chi \geq \frac{\pi}{2}$

$$\bar{F}_0(\chi \geq \frac{\pi}{2}, X_h) = \sqrt{\frac{\pi X_h \sin\chi}{2}}\left\{1 + \mathrm{erf}\left[-(\mathrm{ctn}\chi)\sqrt{\frac{X_h \sin\chi}{2}}\right]\right\} \qquad (2.52)$$

For negative scale height gradients exact solutions can be obtained in a manner similar to Swider (1964). Equation (2.17) for $\chi \leq \pi/2$ can be transformed into

$$F_{-\beta}(\chi,X) = \frac{(1+\beta X)^{1/\beta}}{\beta} \int_{c}^{\sqrt{1-s^2}} dz\left(1 - \sqrt{z^2+s^2}\right)^{1/\beta-1} \tag{2.53}$$

$$c = \frac{\beta X\cos\chi}{1+\beta X} \quad , \quad s = \frac{\beta X\sin\chi}{1+\beta X} \quad .$$

Particular values of β are easily evaluated. Thus

$$F_{-1}(\chi,X) = -X\cos\chi + \sqrt{1+2X+X^2\cos^2\chi} \tag{2.54a}$$

$$F_{-\frac{1}{2}}(\chi,X) = -X\cos\chi+\frac{1}{2}(1+\frac{X}{2})\sqrt{4+4X+X^2\cos^2\chi}$$

$$+\frac{1}{4}X^2\left[\sin^2\chi\ \ln\left(\frac{X(1+\cos\chi)}{X+2+\sqrt{4+4X+X^2\cos^2\chi}}\right) - \cos\chi\right] \quad . \tag{2.54b}$$

Equations (2.54a) and (2.54b) can then be used in Equation (2.48) with β negative in Equation (2.49) to give the optical depth factor for $\chi > \pi/2$.

In utilizing the equations of this section Swider's pertinent remarks concerning their applicability will be invoked when necessary. He has also tabulated values of F_0, F_1 and $F_{1/2}$ in his (1964) paper.

2.3.2 An expansion solution for a more general atmosphere

To analyze the more general problem of a nonuniform atmosphere several approaches will be taken. In this section an expansion solution for the optical depth factor will be developed. Later other methods will be used.

In order to utilize any of these solutions the atmosphere must first be sufficently modelled. Because some error is certainly tolerable in this type of calculation, some freedom can be exercised in choosing a model.

As a first step consider the density of a species to have the separable form

$$n(r',\phi') = n(\frac{r'}{H})\ f_{r'}(\phi')$$

where $\phi' \equiv \tilde{\phi}'$, n is a radial distribution, and for the type of specie considered here, f has the following properties:

a) $f_{r'}(\phi') \to 1$ rapidly in the daytime regime

b) $f_{r'}(\phi') \to$ night-to-day density ratio at r' in the nighttime regime.

$f_{r'}$ is parametrically dependent on the altitude. Since $f \to 1$ outside the sunrise region regardless of the altitude, and since the sunrise region is confined to a small region of space, presumably near $\phi' \sim \pi/2$ in most cases, we can assume that an accurate model will result by choosing the f at the fixed altitude r of the end point of the ray path. That is

$$f_{r'}(\phi') \to f_w(\phi') \quad .$$

A criterion for the validity of this assumption might be that

$$\left|\frac{1}{a(\phi-\pi/2)}\ \frac{\partial f}{\partial \phi}\right| >> \left|\frac{\partial f}{\partial w}\right| \quad .$$

Using the arc length parameter of Section 2.1.3, one defines the functions

$$\begin{aligned} g(\phi') &= f_w(\phi') - 1 = f(\xi) - 1 \\ f(\xi) &= f_w[\phi'(\xi)] \quad . \end{aligned} \qquad (2.55)$$

In calculating the optical depth factor Equation (2.55) will be used, where $f(\xi) - 1$ is described by

$$f(\xi) - 1 = \begin{cases} f(\xi) - 1 & , \quad \xi \leq \xi_1 \\ 0 & , \quad \xi > \xi_1 \end{cases} \quad . \tag{2.56}$$

The limit ξ_1 may be extended to infinity if f is defined as a continuous function which converges strongly after sunrise. In any case, ξ_1 may be taken to be of a size characteristic of the sunrise, i.e. relatively small. The following inequalities hold in the sunrise regime, especially in the D region

$$\xi/\eta << 1 \quad ; \quad \tau \sim \eta \quad ; \quad \xi/\tau << 1 \quad . \tag{2.57}$$

Using these facts, one can then expand (f-1) about $\xi = 0$

$$f(\xi)-1 = g(\phi_\varepsilon) + \xi\, g'(\phi_\varepsilon)\left(\frac{d\phi'}{d\xi}\right)_{\xi=0} + \frac{1}{2}\xi^2 \left[g''(\phi_\varepsilon)\left(\frac{d\phi'}{d\xi}\right)^2 + g'(\phi_\varepsilon)\frac{d^2\phi'}{d\xi^2}\right]_{\xi=0} + \ldots \tag{2.58}$$

where

$$\left(\frac{d^m\phi'}{d\xi^m}\right)_{\xi=0} = (-1)^m(m-1)!\,\frac{1}{\tau^m}\sin^m\phi_\varepsilon\,\sin m\phi_\varepsilon \tag{2.59}$$

and

$$\cos\phi_\varepsilon = \frac{\varepsilon}{\sqrt{\varepsilon^2+\tau^2}} \tag{2.60}$$

or, alternatively

$$\sin\phi_\varepsilon = \left\{1 + \frac{\sin^2\delta}{\sin^2\phi}(\cos\phi\,\sin\delta + \tan\tilde{\theta}\,\cos\delta)^2\right\}^{-\frac{1}{2}} \quad .$$

Equation (2.58) will be written in the form

$$f(\xi)-1 = \sum_{\ell=0} a_\ell \left(\frac{\xi}{\tau}\right)^\ell \qquad (2.61)$$

where the a_ℓ are easily defined using Equations (2.58) to (2.60).

Now the optical depth factor may be written

$$\overline{F}'_\beta(\chi,X) = \overline{F}_\beta(\chi,X) + \frac{1}{n(h)} \int_{\xi_0}^{\xi_1} d\xi\, n_\beta(X'_h)[f(\xi) - 1] \qquad (2.62)$$

where the prime on F indicates the nonuniform case. To evaluate Equation (2.62) the following density expansions are derived (in each case $u \equiv \xi/\sqrt{2\eta}$)

$$\frac{n_1(X'_h)}{n(h)} = \left[1 + \sqrt{\xi^2 + \eta^2} - \eta\right]^{-2}$$

$$\frac{n_1(u)}{n(h)} = \frac{1}{(1+u^2)^2} + \frac{1}{\eta}\frac{u^4}{(1+u^2)^3} - \frac{1}{\eta^2}\frac{u^6(1+\frac{1}{4}u^2)}{(1+u^2)^4} + \ldots \qquad (2.63a)$$

$$\frac{n_{1/2}(X'_h)}{n(h)} = \left[1 + \frac{1}{2}\sqrt{\xi^2+\eta^2} - \eta/2\right]^{-3}$$

$$\frac{n_{1/2}(u)}{n(h)} = \frac{1}{(1+\frac{u^2}{2})^3} + \frac{1}{\eta}\frac{\frac{3}{4}u^4}{(1+\frac{u^2}{2})^4} - \frac{1}{\eta^2}\frac{\frac{3}{4}u^6}{(1+\frac{u^2}{2})^5} + \ldots \qquad (2.63b)$$

$$\frac{n_0(X'_h)}{n(h)} = \exp\left\{-\sqrt{\xi^2 + \eta^2} + \eta\right\}$$

$$\frac{n_0(u)}{n(h)} = e^{-u^2}\left\{1 + \frac{u^4}{2\eta} - \frac{u^6}{2\eta^2}\left(1 - \frac{1}{4}u^2\right) + \ldots\right\} . \qquad (2.63c)$$

The density functions were taken from Equations (2.41) using Equations (2.16). One can also write

$$\begin{aligned} \overline{F}'_\beta(\chi,X) &= \overline{F}_\beta(\chi,X) + \sum_{\ell=0} F_\beta^{(\ell)}(\chi,X) \\ F_\beta^{(\ell)}(\chi,X) &= \sqrt{2\eta}\, b_\ell(\phi_\varepsilon)\left(\frac{2\eta}{\tau^2}\right)^{\ell/2} I_\beta^{(\ell)} \end{aligned} \tag{2.64}$$

where,

$$b_\ell(\phi_\varepsilon) = \frac{\tau^\ell}{\ell!}\left(\frac{d}{d\xi}\right)^\ell g(\phi')\bigg|_{\xi=0} = a_\ell$$

$$I_\beta^{(\ell)} = \int_{u_0}^{u_1} du\, u^\ell\, \frac{n_\beta(u)}{n(h)} \quad ; \quad u = \xi/\sqrt{2\eta} \quad .$$

The integrals $I^{(\ell)}$ are evaluated according to whether u_1 and u_0 are positive or negative. For $\chi > \pi/2$, Equations (2.64) have ξ, η, τ normalized to H(h). For $\chi < \pi/2$, $\overline{F} \to F$, and ξ, η, τ are normalized to H(ω). All the $I_\beta^{(\ell)}$ can be constructed from the integral forms

$$\begin{aligned} J_0^{(m)}(u_i) &= \int_0^{u_i} du\, u^m\, e^{-u^2} \\ J_\beta^{(m,q)}(u_i) &= \int_0^{u_i} du\, \frac{u^m}{(1+\beta u^2)^q} \quad ; \quad \beta = 1,\ 1/2 \end{aligned} \tag{2.65}$$

and these integrals are solvable in closed form in terms of elementary functions (including the error function).

The expansions used above could be truncated at order η^{-2} when (as in the sunrise region) $\xi^2/2\eta \lesssim 1$. The resulting Equations (2.64) will still be quite cumbersome to work with, but might be applicable for numerical analysis. They are useless to an analytical study, however, because of their complexity.

A simple model which one could analyze using this approach is the ramp model illustrated in Figure 2.2. The evaluation of the expansion coefficients is straightforward in this case, and the model is easily parameterized. The ramp model is a realistic represention of sunrise, and will be referred to again. The details relevant to an application of this section for the ramp model are not reproduced here.

2.3.3 A perturbation solution for the sunrise region

The ultimate purpose of these calculations is to solve the complete continuity equations over the sunrise region. In this section a simple, self-consistent method of determining the optical depth for a nonuniform atmosphere will be developed by considering the nonuniformity as a perturbation from the photoequilibrium density distribution, and solving for the perturbation using a simplified continuity equation. To this end one defines the angular function as

$$f(r,\phi) = 1 + [f_B(r) - 1]g(\phi)$$

or (2.66)

$$n(r,\phi) = n(r) + [f_B(r) - 1]g(\phi)n(r)$$

where $f_B(r)$ is a boundary condition at the night-day interface such that $n(r)f_B(r)$ is the nighttime photoequilibrium distribution, ϕ is being used rather than ϕ' for ease, ϕ_s is the sunrise hour angle at the altitude r, and g is the angular distribution at altitude r satisfying

$$g(\phi) = \begin{cases} g(\phi) \rightarrow 0 & ; \quad \phi < \phi_s \\ g(\phi) \underset{\sim}{\rightarrow} 1 & ; \quad \phi \geq \phi_s \end{cases} . \tag{2.67}$$

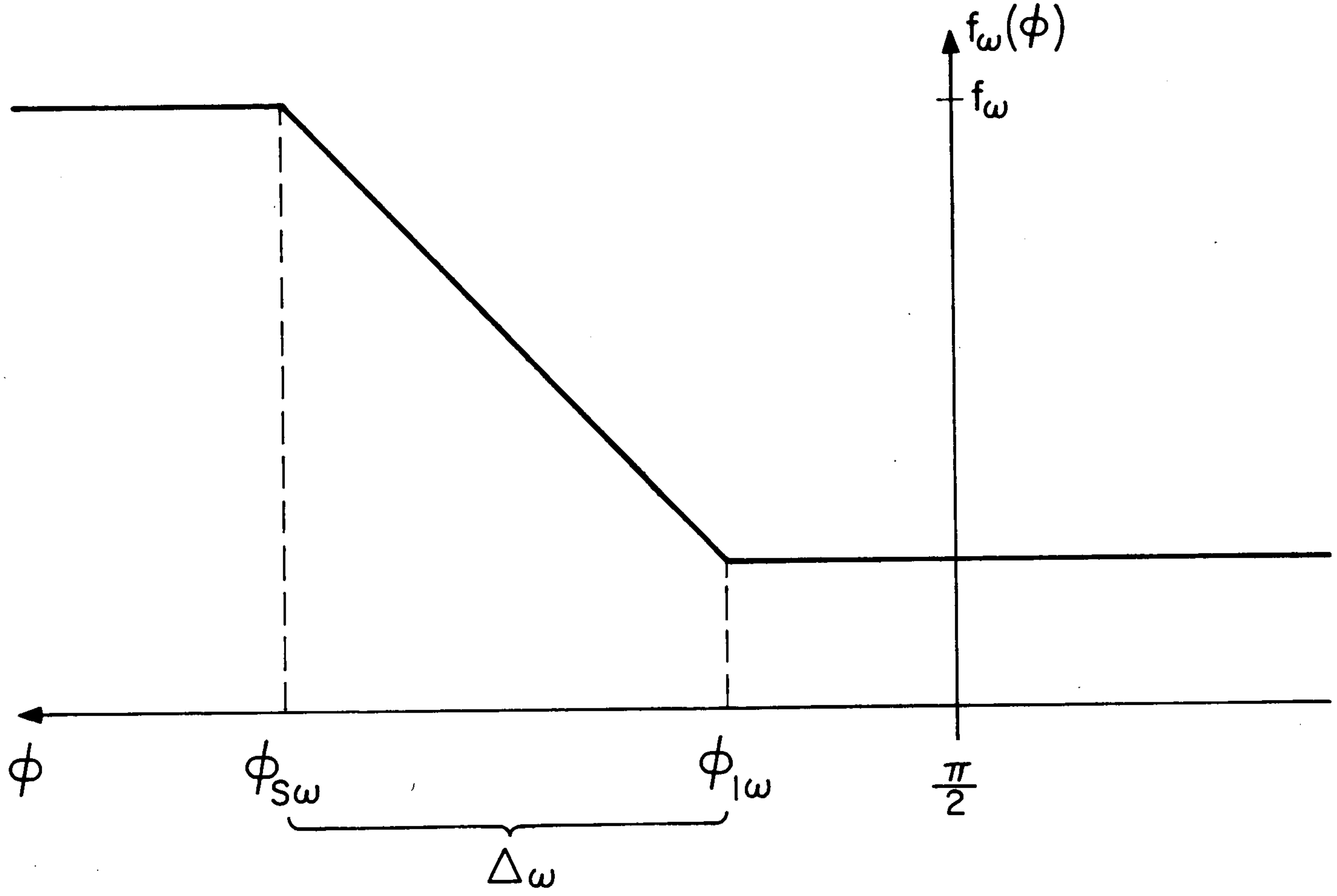

Figure 2.2 Ramp sunrise model.

This is similar to the distributions already mentioned. One also defines the perturbation density

$$\Delta n(r,\phi) \equiv n(r,\phi) - n(r) = [f_B(r) - 1]n(r)g(\phi) \quad . \tag{2.68}$$

To facilitate a determination of $g(\phi)$ one can make the assumption that only photoprocesses act on the perturbation density. This approximation has only limited validity, where competitive chemical production and loss mechanisms are slow and the perturbation is relatively large. For the cases of ozone and atomic oxygen at sunrise this is a good assumption, and is useful for obtaining a general behavior for $g(\phi)$. One also assumes that the atmosphere is rigidly fixed to the earth's rotation. In this case,

$$\frac{\partial n}{\partial t} = - \omega_e \frac{\partial n}{\partial \phi} \tag{2.69}$$

since the local time and hour angle of a fixed point in the atmosphere are not independent, and n is assumed to be a function of only two variables, either (w,ϕ) or (w,t), i.e. there is no local variation in n from day to day. ω_e is the angular velocity of the earth's rotation. The continuity equations for the two photoprocesses of possible interest over sunrise are then written,

$$-\omega_e \frac{\partial \Delta n_j}{\partial \phi} = - J_j(r,\phi)\Delta n_j(r,\phi) \tag{2.70}$$

$$-\omega_e \frac{\partial \Delta n_j}{\partial \phi} = c_j J_i(r,\phi)\Delta n_i(r,\phi) \quad (c_j = 1,2 \text{ in general}) \tag{2.71}$$

where J_j is the photodissociation rate for the jth specie due to solar radiation. and Equation (2.70) represents a simple dissociative loss of specie j, while Equation (2.71) shows the formation of j by the dissociation of i. Clearly several processes may occur simultaneously for any specie, but only the fundamental cases are described above.

To get the dissociation rate, one starts by looking at the total differential rate loss due to dissociation, which is the number of dissociative 'collisions' (i.e. absorptions of photons which lead to dissociation) occurring per second per unit volume between the specie n_j and the flux of solar photons in a wavelength range $\lambda \rightarrow \lambda+d\lambda$. This must be proportional to specie density, to the dissociative cross section of the specie at wavelength λ, and to the flux of incident photons in the range $d\lambda$. Thus,

$$d\mathcal{J}_j = n_j \sigma_j^d(\lambda) I(\lambda) d\lambda \quad ,$$

or the total number of dissociations per second per unit volume is, at a point $\bar{r}$ in space

$$\mathcal{J}_j(\bar{r}) = n_j(\bar{r}) \int d\lambda \; \sigma_j^d(\lambda) I(\lambda,\bar{r}) \quad . \tag{2.72}$$

Here σ_j^d is the dissociative cross section which one can usually assume is equal to the absorption cross section in the appropriate energy range. Defining the dissociation rate, $J_j = \mathcal{J}_j/n_j$

$$J_j(r,\phi) = \int d\lambda \; \sigma_j^d(\lambda) I_0(\lambda) \exp\{-\tau(\lambda;r,\phi)\} \quad . \tag{2.73}$$

Now the dissociation rate may be inserted into Equations (2.70) and (2.71) for analysis. First, Equation (2.70) is considered and yields immediately

$$\frac{dg(\phi)}{d\phi} = \frac{J(\phi,r)}{\omega_e} g(\phi) \tag{2.74}$$

$$g(\phi) = g(\phi_k) \exp \left\{ \int_{\phi_k}^{\phi} d\phi' \, \frac{J(\phi',w)}{\omega_e} \right\} \tag{2.75}$$

where ϕ_k, the initial angle, could lie somewhere near or before sunrise. The boundary conditions given by Equation (2.67) are satisfied by setting $g(\phi_k) \to 1$ for ϕ_k near or before sunrise.

It is interesting to investigate some of the qualitative aspects of the form of Equation (2.75). Figure 2.3 illustrates three curves. Since $J(\phi)$ increases fairly rapidly with decreasing ϕ initially, then becomes more stable as sunrise ends, one expects $g(\phi)$ to have the form of curve a); that is, a small initial slope with a very rapidly decreasing exponential tail. Curve a) can be deduced from an incremental model where J increases with decreasing ϕ. Note that if $J(\phi)$ is proportional to $(\phi_s-\phi)$, curve a) will be Gaussian. In comparison, curve b) is a pure exponential evaluated for some intermediate value of $J(\phi<\phi_s)$. Curve c) represents a linear model of g whose slope is again evaluated for some intermediate value of $J(\phi<\phi_s)$. It can be seen that the simple linear model gives a good representation of the distribution.

The function $g(\phi)$ can be obtained in several ways. First, expansions of either g or J in powers of ϕ could be used to generate solutions. Or analytical models of J could be proposed and solved. Finally, an analytical model for g could be set up empirically. The solutions will be investigated in the order they were introduced here.

By expanding either $g(\phi)$ or $J(\phi)$ about some arbitrary angle ϕ_0 at a height w, and retaining the second and first order terms respectively, one can obtain two solutions of $g(\phi)$ valid near $\phi = \phi_0$ (note, j suppressed)

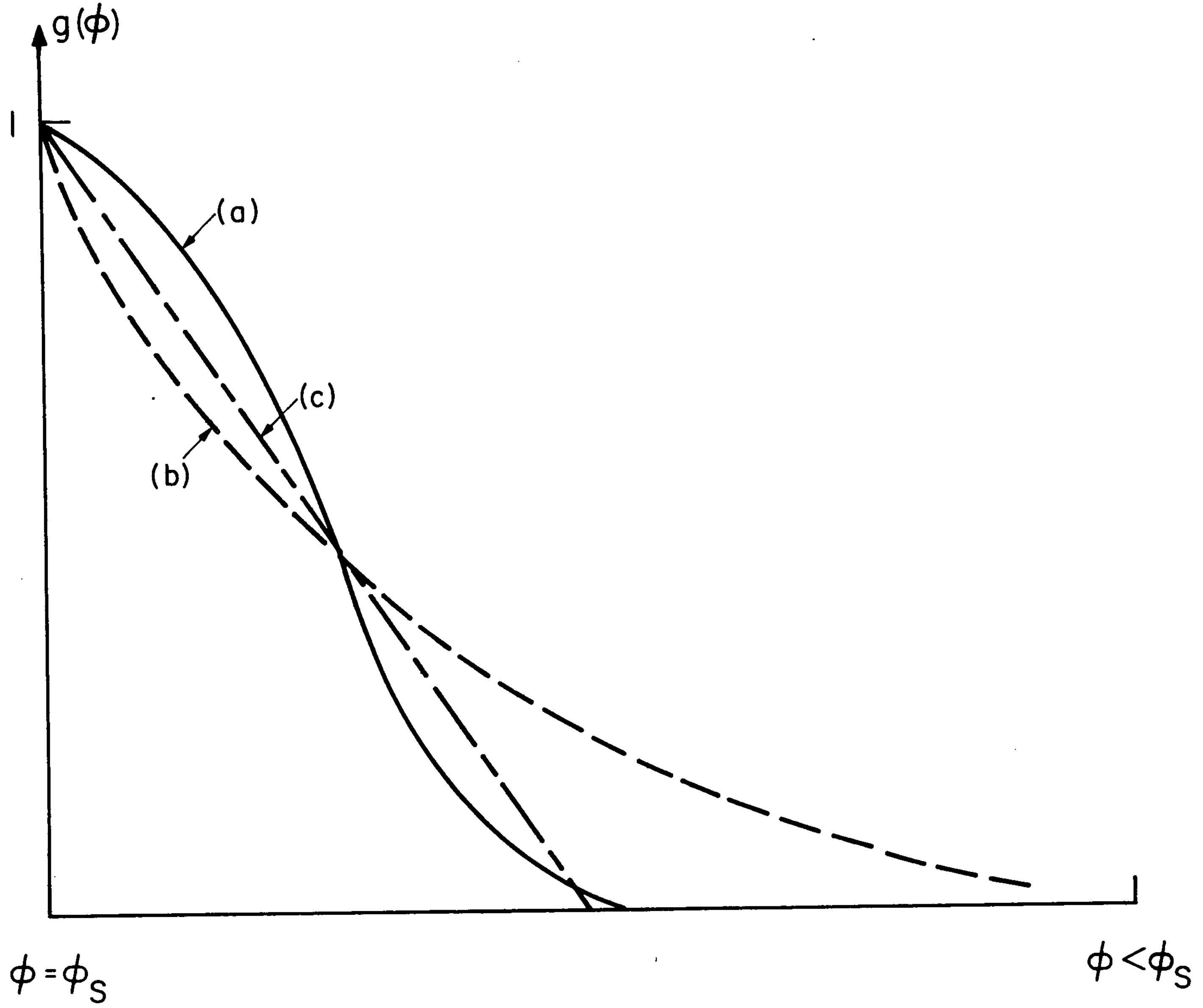

Figure 2.3 Qualitative behavior of the sunrise angular distribution.

$$g(\phi) = g_0\left\{1 + \frac{(\phi-\phi_0)}{\Delta_0} + \frac{1}{2}\frac{(\phi-\phi_0)^2}{\Delta_0^2}\left(1 - \frac{\Delta_0}{\delta_0}\right)\right\} \tag{2.76}$$

$$g(\phi) = \bar{g}_0 \exp\left\{- \frac{1}{2\Delta_0\delta_0}\,[\phi-(\phi_0+\delta_0)]^2\right\} \tag{2.77}$$

where the following definitions hold

$$g_0 = g(\phi_k) \exp\left\{\int_{\phi_k}^{\phi_0} d\phi' \, \frac{J(\phi',w)}{\omega_e}\right\} \tag{2.78}$$

$$\bar{g}_0 = g(\phi_k) \exp\left\{\frac{1}{2\Delta_0\delta_0}\,[\phi_k-(\phi_0+\delta_0)]^2\right\} \tag{2.79}$$

and where one defines the sunrise angular width at ϕ_0 for the jth specie as

$$\Delta_{j0}(\phi_0,w) \equiv \frac{\omega_e}{J_j(\phi_0,w)} \tag{2.80}$$

and the angular depth of J_j at ϕ_0

$$\frac{1}{\delta_{j0}} = -\left[\frac{1}{J_j(\phi_0,w)}\,\frac{\partial J(\phi,w)}{\partial\phi}\right]_{\phi=\phi_0} . \tag{2.81}$$

Equation (2.77) is an approximation to curve a) of Figure 2.3, while Equation (2.76), to first order, represents a ramp approximation c) for the perturbation distribution.

The ramp approximation for Equation (2.76) may then be written

$$g_j(\phi) = g_j(\phi_k)\left[1 - \frac{\phi_k-\phi}{\tilde{\Delta}_{j0}}\right] \tag{2.82}$$

where

$$\tilde{\Delta}_{j0} \equiv \phi_k + \Delta_{j0} - \phi_0 \quad . \tag{2.83}$$

One can also use an empirical approach. In some cases the behavior of J at sunrise can be closely fitted using a Fermi-like function. So in these cases one chooses for J

$$J(\phi,w) = \frac{J_D}{1+e^{(\phi-\phi_{0p})/\delta_p}} \tag{2.84}$$

where J_D is the daytime value of J, ϕ_{0p} is the angle where $J/J_D = 1/2$, δ_p is a measure of the width of the J transition from night to day, and J_D, ϕ_{0p}, and δ_p are all altitude dependent parameters. By inserting this J into Equation (2.75), and taking the appropriate limit of ϕ_k, one has

$$g(\phi) = [1 + e^{-(\phi-\phi_{0p})/\delta_p}]^{-\frac{\delta_p J_D}{\omega_e}} \quad . \tag{2.85}$$

The ϕ_k dependence can be left in so that a certain amount of curve fitting can be done. The solution of (2.75) is then

$$g(\phi) = g(\phi_k)\left(\frac{1+e^{-(\phi_k-\phi_{0p})/\delta_p}}{1+e^{-(\phi-\phi_{0p})/\delta_p}}\right)^{\frac{\delta_p J_D}{\omega_e}} \quad . \tag{2.86}$$

Alternatively, one can simply propose an empirical form for g. The Fermi distribution has the proper sunrise behavior, and leads to the definition,

$$g(\phi) = [1 + e^{-(\phi-\phi_{0g})/\delta_g}]^{-1} \quad . \tag{2.87}$$

Equations (2.85) and (2.87) are functionally very similar. Other continuous functions could likewise be proposed to describe the sunrise. This will not be done here.

In all of the above solutions for g certain parameters must be specified or calculated before the solution can be used. In this sense all the equations are equivalent since the parameters in them are either very similar or related to one another.

Now consider the solution for the optical depth problem by calculating the absorption due to the jth specie of the type being discussed. In notation which can later be adopted to an iterative procedure, this can be written

$$\tau_j^{(1)}(\lambda;r,\phi) = \tau_j^{(0)}(\lambda;r,\phi) + \Delta\tau_j^{(1)}(\lambda;r,\phi) \quad . \tag{2.88}$$

Here $\tau_j^{(1)}$ is the first iterative correction to $\tau_j^{(0)}$ because of the perturbation density. $\Delta\tau_j^{(1)}$ is the perturbation correction. $\tau_j^{(0)}$ is related to $F_\beta(\chi,X)$ for a uniform atmosphere (as in the previous sections), where the correspondence, $r \leftrightarrow X$; $\phi \leftrightarrow \chi$, is known, and (χ,X) is the point of observation. Obviously one may define, assuming $\chi > \frac{\pi}{2}$

$$\Delta\tau_j^{(1)}(\lambda;r,\phi) = \sigma_j(\lambda)n_j(h)H_j(h)\ \Delta F_j^{(1)}(\chi,X) \quad (\beta \text{ suppressed}) . \tag{2.89}$$

Thus, the perturbation optical depth factor is

$$\Delta F_j^{(1)}(\chi,X) = \int_{\xi_0(\chi,X)}^{\infty} d\xi[f_{Bj}(r') - 1] \frac{n_j(r')}{n_j(h)} g_j^{(1)}(\phi') \tag{2.90}$$

where ξ is normalized to $H_j(h)$, $g_j^{(1)}$ is g_j with the parameters specified as best as can be done from available data.

One can write an approximation to Equation (2.90) in the form

$$\Delta F_j^{(1)}(\chi,X) = \bar{g}_j^{(1)} \int_{s_0}^{s_1} \frac{ds'}{H_j} [f_{Bj}(w') - 1] \frac{n_j(w')}{n_j(h)} \tag{2.91}$$

where the definition of $\bar{g}$ is

$$\bar{g}_j^{(1)} = \int ds' g_j^{(1)}(\phi') / \int ds' \quad . \tag{2.92}$$

These equations will be used in evaluating the perturbation for ozone in particular. The rationale for this case is that (f-1) has a large, rapid local variation, and so an average value of g over the range of this variation can be substituted into the integral. Equation (2.92) is an arc-length weighted average for g, a proper one for the integral (2.90). The case where (f-1) varies slowly will be treated later.

For ozone, (f-1) will be approximated by a Gaussian

$$f_{B3}(w')-1 = f_3 \exp\left\{- \left(\frac{w'-w_3}{\delta_3}\right)^2\right\} \tag{2.93}$$

and Equation (2.87) will be used to describe $g(\phi')$. Also define

$$U = \phi - \pi/2 \quad . \tag{2.94}$$

Furthermore, a low latitude correspondence between χ and ϕ is assumed. That is

$$\phi \equiv \chi \quad . \tag{2.95}$$

For the D-region it can be shown that

$$ds' \cong \pm\, dw'/\sqrt{\frac{2(w'-h)}{a}} \tag{2.96}$$

and in Equation (2.92) one uses $ds' \to -d\phi'$ for evaluation, since it can also be shown that

$$U' \cong \pm\sqrt{\frac{2(w'-h)}{a}} \quad . \tag{2.97}$$

The upper sign in Equations (2.96) and (2.97) is for $\phi' > \pi/2$, the lower sign for $\phi' < \pi/2$. If $\phi > \frac{\pi}{2}$, integral (2.90) must be considered in two parts.

To solve (2.92) one must decide on a range for s'. Choosing $w_3 \pm \delta_3$, and $\phi' = \pi/2$ as boundaries, the solutions become (with subscripts and superscripts left off the g's, δ_g's and ϕ_{0g}'s)

$$h < w_3 - \delta_3: \quad \bar{g} = \frac{\delta_g}{U_a - U_b} \ln\left(\frac{1+\alpha_g e^{U_a/\delta_g}}{1+\alpha_g e^{U_b/\delta_g}}\right) \quad ;$$

$$\cos U_a = \frac{a+h}{a+w_3+\delta_3} \quad ; \quad \cos U_b = \frac{a+h}{a+w_3-\delta_3}$$

$$w_3-\delta_3 \leq h < w_3+\delta_3: \quad \overline{g} = \frac{\delta_g}{U_a} \ln\left(\frac{1+\alpha_g e^{U_a/\delta_g}}{1+\alpha_g}\right) \quad ; \; U_b = 0$$

$$h \geq w_3+\delta_3: \quad \overline{g} = \frac{\alpha_g}{1+\alpha_g} \tag{2.98}$$

$$\alpha_g = e^{-(\phi_{0g}-\pi/2)/\delta_g} \quad .$$

One also defines the average values, $\overline{g}^*$ in the following sequence

$$h<w_3-\delta_3: \quad \overline{g}^* = \overline{g} \text{ with } U_b \rightarrow -U_a \quad ; \quad U_a \rightarrow -U_b$$

$$w_3-\delta_3 \leq h<w_3+\delta_3: \quad \overline{g}^* = \overline{g} \text{ with } U_b = 0 \tag{2.99}$$

$$h \geq w_3+\delta_3: \quad \overline{g}^* = \alpha_g/(1+\alpha_g) = \overline{g} \quad .$$

From Equation (2.41) for $\beta=0$

$$\frac{n_j(w')}{n_j(h)} = e^{-(w'-h)/H_j(h)} \tag{2.100}$$

where the variation of H with h will no longer be considered. Using (2.93), (2.96), and (2.100), Equation (2.91) is

$$\Delta F(\chi,X) = \overline{g}_3 \int_{w}^{w_1} \frac{\mp dw'}{\sqrt{\frac{2(w'-h)}{a}}} \frac{f_3}{H_3} e^{-\left(\frac{w'-w_3}{\delta_3}\right)^2} e^{-\frac{(w'-h)}{H_3}} \quad . \tag{2.101}$$

Applying the partition at $\phi' = \pi/2$, or $w' = h$, one has the following solutions for Equation (2.101)

$$\Delta F(\chi,X) = \frac{f_3}{H_3}\sqrt{2a}\,\exp\left[-(w_3-h-\delta_3^2/4H_3)/H_3\right]\left\{\bar{g}_3 I(c,b_0)\sqrt{w-h} + \bar{g}_3^* I(c,b_1)\sqrt{w_1-h}\right\} \tag{2.102}$$

where $\bar{g}$ must be replaced by $-\bar{g}^*$, and $H(h) \rightarrow H(w)$ for $\chi < \pi/2$, and

$$\begin{aligned} I(c,b) &= \int_0^1 dz\; e^{-(bz^2+c)^2} \\ c &= -(w_3-h-\delta_3^2/2H_3)/\delta_3 \\ b_0 &= (w-h)/\delta_3 \\ b_1 &= (w_1-h)/\delta_3 \end{aligned} \tag{2.103}$$

and where w_1 = 90 km is chosen here. The subscript "3" in Equations (2.102) and (2.103) are to indicate that ozone is being considered, although the results could be applied to other similar cases.

Integral (2.103) can be readily solved if one approximates (bz^2+c) by $(bz+c)$. Then

$$I(c,b) = \frac{\sqrt{\pi}}{2b}\begin{cases} \gamma-\beta \; ; & c \geq 0 \\ \gamma+\beta \; ; & c<0 \;, \quad c+b \geq 0 \\ \beta-\gamma \; ; & c<0 \;, \quad c+b<0 \end{cases} \tag{2.104}$$

where

$$\begin{aligned} \beta &= \mathrm{erf}(|c|) \\ \gamma &= \mathrm{erf}(|c+b|) \end{aligned}$$

and for $b = 0$; $I(c,b) = e^{-c^2}$.

Since $0 \leq z \leq 1$, the above approximation gives a larger value for I.

Equation (2.102) with (2.103) or (2.104) and (2.98) and (2.99) gives the perturbation absorption for ozone. For the cases of species where (f-1) varies slowly with altitude Equation (2.90) may be written

$$\Delta F(\chi,X) = \frac{\overline{(f_B-1)}}{H} \int_{w}^{w_1} \frac{\mp dw'}{\sqrt{\frac{2(w'-h)}{a}}} \, e^{-\frac{(w'-h)}{H}} \, g(\phi') \tag{2.105}$$

where $\overline{(f_B-1)}$ is a suitable average value of (f-1) and may be taken to be (f_B-1) evaluated at either w or h, depending on whether f_B is increasing or decreasing with altitude. If the ramp model, Equation (2.82), is used for g Equation (2.105) becomes

$$\Delta F = g(\phi_k) \frac{(f_B(w)-1)}{H\tilde{\Delta}_0} \int_{w}^{w_1} \frac{\mp dw'}{\sqrt{\frac{2(w'-h)}{a}}} \, e^{-\frac{w'-h}{H}} \, [\phi' - (\phi_k - \tilde{\Delta}_0)] \tag{2.106}$$

and the limit w_1 is determined from: $\phi_1 = \phi_k - \tilde{\Delta}_0$. Using approximation (2.97) this can be integrated to yield

$$\Delta F(\chi,X) = g_k \frac{f_B(w)-1}{\tilde{\Delta}_0} \left\{ e^{-c_1^2} - e^{-c^2} + \sqrt{\pi}\, c_1 \left[\mathrm{erf}(c_1) \mp \rho\, \mathrm{erf}(c) \right] \right\} \tag{2.107}$$

where

$$c = \sqrt{\frac{w-h}{H}} \, , \quad c_1 = \sqrt{\frac{w_1-h}{H}} \, , \quad \sin\chi_1 = \frac{a+h}{a+w_1}$$

$$\rho = \begin{cases} +1 \; ; & \phi \geq \pi/2 \; ; \quad H=H(h) \\ -1 \; ; & \phi < \pi/2 \; ; \quad H=H(w) \end{cases}$$

and the upper sign is used when $\phi_1 \geq \frac{\pi}{2}$, the lower sign when $\phi_1 < \pi/2$. Equation (2.107) is to be used for $\phi \geq \phi_1$. When $\phi < \phi_1$, $\Delta F = 0$. Also, Equation (2.107) is not strictly correct for $\phi > \phi_k$, but can be used. Subscripts "j" and superscripts "1" may be added.

Equations (2.102) and (2.107) represent the first order solutions which will be used later in the analysis of the sunrise region. They can be used in Equations (2.88) and (2.89) to find the perturbation optical depth. One then completes the calculation by finding the total optical depth

$$\tau^{(1)}(\lambda;\chi,X) = \sum_j \tau_j^{(1)}(\lambda;\chi,X_j) = \tau^{(0)}(\lambda;\chi,X) + \sum_j \Delta\tau_j^{(1)}(\lambda;\chi,X_j) \cdot \tag{2.108}$$

An iterative scheme can be developed which would proceed according to the scheme

$$\tau^{(1)}(\chi,X) \rightarrow \left\{J_j^{(1)}(\chi,X)\right\} \rightarrow \left\{n_j^{(1)}(\chi,X)\right\} \rightarrow \left\{\delta_j^{(2)}(X)\right\} \rightarrow \left\{\Delta F_j^{(2)}(\chi,X)\right\} \rightarrow \tau^{(2)}(\chi,X) \tag{2.109}$$

with 1→2, 2→3 for the second iteration, and so forth. The $\left\{\delta_j\right\}$ represents the set of parameters used in specifying the altitude and angular behavior of the species over sunrise, and are the parameters of the equations developed in this section. The $\left\{\delta_j\right\}$ are calculated from the distribution solutions, $\left\{n_j\right\}$. This iterative scheme is regenerative in the following sense: an increase in τ will decrease J, shifting the sunrise forward, thus decreasing τ again. Presumably the process is stable in all the cases of interest. In fact it will be assumed here that the iteration converges so rapidly that higher order corrections to $\tau^{(1)}$ will be very small for a good initial model, and $\tau^{(1)}$ is therefore a good solution itself. Actual computations have shown that the parameter reproduction is excellent for this approximation, although the iteration was repeated many times in the determination of the O and O_3 distributions of Section 3.2.1.

Now Equation (2.71) will be investigated. This represents specie production by the dissociation of another specie. Assuming that only this process is important for the specie, $f_B<1$. The solution of Equation (2.71) is easily found to be

$$\begin{aligned} g_j(\phi) &= g_j(\phi_k) + \alpha_{ji}[g_i(\phi) - g_i(\phi_k)] \\ \alpha_{ji}(r) &= c_j \frac{(f_{Bi}-1)}{(1-f_{Bj})} \frac{n_i}{n_j} \quad . \end{aligned} \tag{2.110}$$

In order to solve Equation (2.110) something must be known about the daytime photoequilibrium values n_i and n_j. For the solutions of Equation (2.110) to be useful $\alpha_{ji} \simeq 1$. The values of n_i and n_j obtained from the usual photochemical equilibrium analysis do not generally satisfy this criterion, which simply indicates that a more complex relationship exists between n_i, n_j, and the other species than is expressed by Equation (2.71). One can set $\alpha_{ji} = 1$. Then the solutions of (2.110) are the solutions of g_i already obtained. The perturbation calculation goes through exactly as before except that now ΔF will be negative.

The results of this section can be readily applied to numerical calculations. In addition, the models analyzed can be discussed on a physical basis in relation to the physics of the sunrise.

3. APPLICATION OF THE ABSORPTION ANALYSIS TO THE OZONE AND ATOMIC OXYGEN PROBLEM AT SUNRISE

3.1 Definition of the Sunrise Region

Before proceeding to apply the analysis already developed, it is important to clarify exactly where sunrise is occurring for different wavelengths of radiation. For example, visible wavelengths are refracted and scattered but suffer very little absorption, while the ultraviolet radiation is highly attenuated by the atmosphere while showing little refraction. If "sunrise" is defined by an extinction region for the incident flux, $I(\lambda) < I_{min}(\lambda)$, at low altitudes different wavelengths will have very different sunrise zeniths. Figure 3.1 shows where sunrise is occurring for different wavelengths. Optical waves extend far beyond the horizon because of low altitude refraction. The ultraviolet will exhibit an extinction altitude, h_0, in general, where h_0 will be characteristic of the wavelength considered. For altitudes above h_0 the extinction curve for the ultraviolet is illustrated. In parametrizing the sunrise one might use the approximation of an ideal shadow height h_0, where h_0 is determined as a mean value for the penetration of the band of frequencies which are being considered for the process undergoing analysis ($h_0 \simeq 0$ for optical wavelengths). In this case the sunrise zenith is given by

$$\chi_s(w) = \pi - \sin^{-1}\left(\frac{a+h_0}{a+w}\right) . \qquad (3.1)$$

When the absorption in a certain band of wavelengths is due primarily to the absorption by one constituent, it is possible to obtain an approximate expression for the sunrise zenith, that is, a sunrise zenith which has been averaged over all pertinent wavelengths while being weighted by the cross section for the absorption process, by first defining the extinction ratio

C.2.

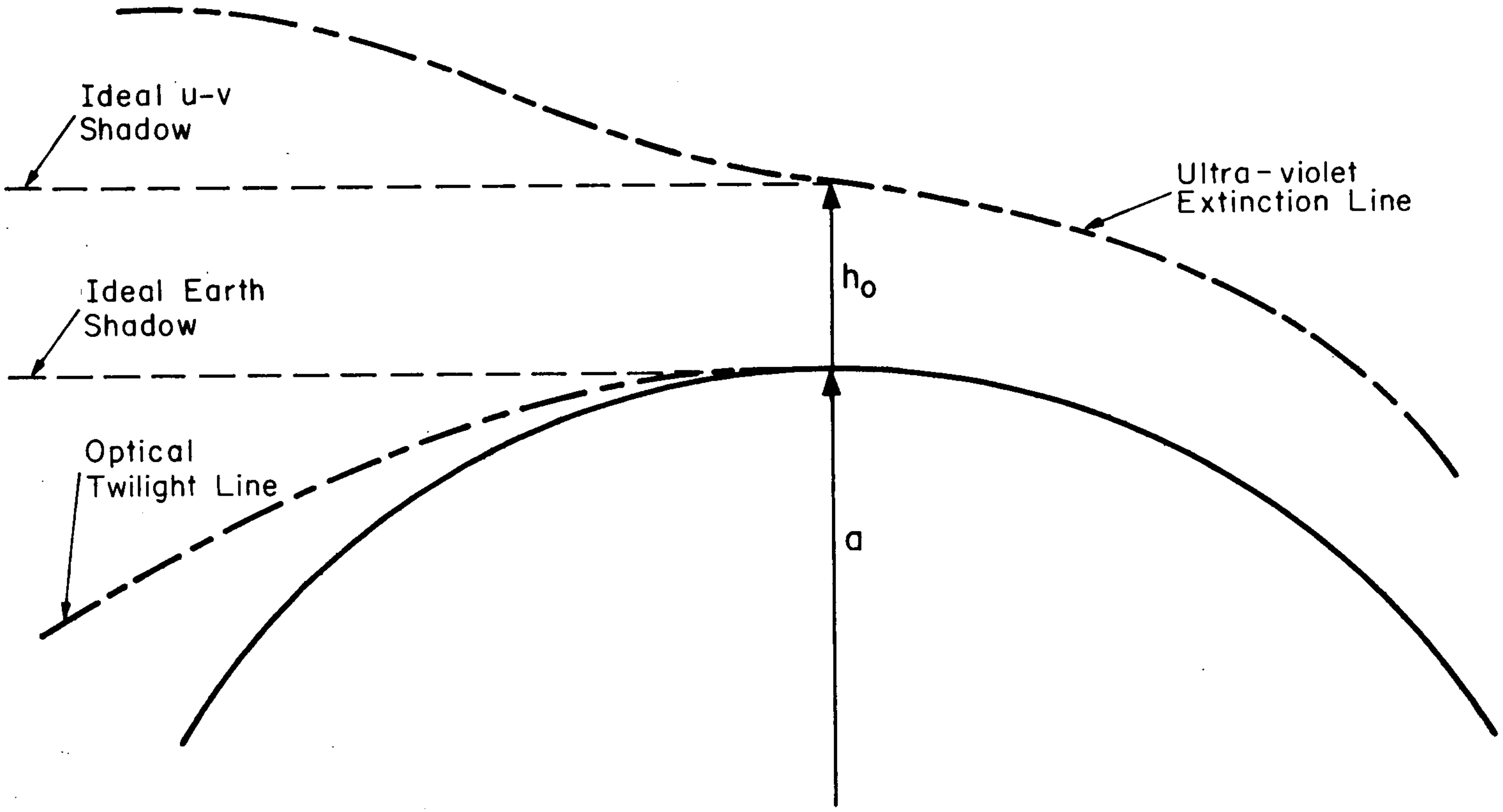

Figure 3.1 Sunrise lines defined by the atmospheric extinction of solar radiation.

$$\alpha_s = \frac{I_\lambda(\chi_{s\lambda},w)}{I_{\lambda 0}} = \text{constant} \quad . \tag{3.2}$$

For a uniform, exponential atmosphere one then obtains

$$U_s(w) = \frac{90°}{F_0\bar{\tau}_0}\left[\ell n \frac{1}{\alpha_s} - \bar{\tau}_0\right]$$

where

$$U_s = \chi_s - \frac{\pi}{2}$$

$$F_0 = F(\tfrac{\pi}{2}\,;w,h) \quad ; \quad \text{for } \beta=0 \tag{3.3}$$

$$\bar{\tau}_0 = n(h)H(h)F_0\,\bar{\sigma}$$

$$\bar{\sigma} = \frac{1}{(\Delta\lambda)}\int_{\lambda}^{\lambda+\Delta\lambda} d\lambda\ \sigma_\lambda = \frac{\sigma_{\text{TOT Band}}}{(\Delta\lambda)} \quad .$$

This expression is good for sunrise zeniths near 90°.

Another way to obtain data on the sunrise would be to study experimental results of probes around the sunrise region. When direct experimental information is available the most fruitful course would be to apply this data to the problem initially, checking later the consistency of the theory and experiment. This approach will be used when possible.

It should be noted that for optical wavelengths Equation (3.1) would be appropriate for sunrise when refraction and tropospheric hazing are ignored. However, for optical wavelengths, Rayleigh scattering should not be ignored. To include the effects of Rayleigh scattering, one can consider the following hypothetical situation: an infinite medium with a plane wave of energy incident. The absorption can be defined, to first order, as the scattering of radiation into lossy angles. The form of the cross section is discussed in Appendix I.

One can also make corrections for the finite size of the sun in a very straightforward manner (see Appendix VI). Consider the sun as a finite, uniform source of radiation. Along any particular ray, the optical depth will be a function of the elevation from the sun's center primarily through the density at the minimum ray height. For a complete discussion of these ideas refer to Appendix VI where the expression

$$\tau_c = \tau \left\{ 1 + \frac{\alpha_o^2}{8} \left[X_o + (X^2 - X_o^2)(1 - \tau) \right] \right\} \tag{3.4}$$

is derived. τ_c is the corrected optical depth, and α_o is half the angle subtended by the sun at the earth. Equation (3.4) is valid for χ near $\pi/2$. If the radiation intensity is peaked near the center of the solar disc, Equation (3.4) represents a maximum correction, as a uniform solar disc was assumed.

3.1.1 A discussion of some special problems associated with the D region

For analysis of the upper atmosphere, the work of Swider (1964) contains all the necessary details. As Swider points out, evaluation of the optical depth factor should be relative to the point of maximum density along the ray. For monotonically increasing distributions (such as are generally found above 120 km) this corresponds to the minimum ray height. Furthermore, Swider demonstrates that the optical depth factor is very insensitive to the exact scale height gradient adopted. For the atmosphere above 120 km he shows that, $0 \leq \beta \leq 1$. Based on Swider's (1964) arguments the optical depth factor for $\beta=0$ can be used. The work of the previous sections was done for scale height gradients, $0 \leq \beta \leq 1$, where the density at the minimum ray height was used to define the optical depth.

In the lower atmosphere one finds negative scale height gradients for some species because of either their local distribution or the mesospheric temperature structure. However, in most cases, $|\beta| \lesssim 1$, and the results for $\beta = 0$ can be utilized with small errors, just as is done for positive scale height gradients in the upper atmosphere. Physically a negative scale height gradient will tend to concentrate the absorption at lower altitudes, whereas a positive gradient has the opposite effect. This is so because a distribution with a negative scale height gradient decreases more and more rapidly with increasing height, thereby maximizing the absorption at lower altitudes. The optical depth is formulated in terms of the local scale height of the lowest point along the ray path, and for small negative gradients, the excess absorption which the approximate analytical expressions will include is negligible. In fact the results may be more accurate than those for a positive scale height gradient using this formulation.

The maximum density along the ray path for the nonuniform atmosphere case will generally not be at the minimum ray height. Its position along the ray depends on the magnitude of f_B, on the proximity of sunrise to $\phi = \frac{\pi}{2}$, and on the form of $g(\phi)$. Qualitatively one expects that for a relatively large perturbation near $\phi = \pi/2$ the maximum density will be at a point along the ray somewhere in the sunrise region. However, the perturbation optical depth calculation is not susceptible to the sensitivity of the maximum density normalization as are the usual uniform atmosphere calculations. This is because: a) the whole approach is approximate, and b) the resulting ray integrals extend only over a limited region of space. The formulation of the absorption problem in terms of the density at the minimum ray height will therefore be considered valid.

Great effort has been spent here on evaluating the optical depth problem when, in fact, the optical depth formalism and the data necessary for the evaluation of the optical depth formulas are only approximate themselves. Furthermore, the primary absorption of ultraviolet radiation in the atmosphere is by the major constituents which are nearly uniform over the sphere. Of the many minor constituents which undergo large sunrise transitions, practically all are optically very thin. However, in the formation of the D region, ozone is very important. It is the ozone which controls the amount of ultraviolet radiation which is available for photoprocesses at sunrise via absorption in its Hartley band. The ozone density decreases at sunrise by a factor of around 10 between 60-80 km. This means there is an optically thick transient layer near sunrise. Using a crude model, Thomas and Bowman (1969) have illustrated that ozone absorption is critical in determining the extinction of ultraviolet radiation in the D region.

Even so, the result of this study could be applied to problems other than a detailed description of ozone absorption.

3.2 The All-Oxygen Atmosphere Model

As a first application to the D-region, and for the purposes of illustration here, an all oxygen atmosphere and its response to sunrise will be studied. This means that only the oxygen allotropes O, O_2, O_3, have to be considered when constructing the photochemical scheme. The oxygen model, however, presents some special problems which, when analyzed, lend a general insight into the solutions for similar cases.

Many species in the atmosphere do not have normal radial distributions because of the mechanisms which produce, transport, and destroy them. Both atomic oxygen and ozone display a peak in their distributions. The atomic oxygen peak density occurs in the vicinity of 100 km and decreases more rapidly at lower than at greater altitudes. This suggests modelling the distribution as the difference of two exponential distributions. Such a model is outlined in Appendix II. However, since atomic oxygen is a negligible absorber of important D-region wavelengths its absorption can be ignored in this work.

The ozone peak at about 25 km is more easily modeled using a parabolic approximation because of its sharp narrow character. Above the peak a normal distribution of ozone exists. Below the peak the ozone can be ignored because the contribution to the total absorption from this region will be much smaller than the absorption of the peak. This ozone model is discussed in Appendix III.

Another problem which arises for the oxygen system, but which is found quite generally in all chemical systems, is the presence of excited species of the constituent gases. Each excited specie will have its own reaction scheme, sometimes with important consequences. Atomic oxygen is found primarily in two states, the ^3P ground state and ^1D first excited state. Hunt (1966) has shown that the concentration of excited atomic oxygen is about 6 orders of magnitude below that of the ground state in the D region. His results are based on an oxygen-hydrogen model but are valid here. Molecular oxgyen has two excited states which are known to be important. They are the $^1\Sigma_g^+$ and $^1\Delta_g$ states. Molecular oxygen is normally found in the $^3\Sigma_g^-$ ground state. The excited species of the oxygen allotropes are produced by the photodissociation of molecular oxygen and ozone. Depending on the energy of the excited state, there is a threshold wavelength for which the production of the excited state is possible. The excited states of O_2 are important in several respects. The singlet Σ state vigorously attacks ozone and may represent a potentially strong ozone dissociation process (Hunt 1965a). The singlet Δ state also dissociates ozone, but more importantly, it effectively detaches O_2^-. This reaction has recently been considered as significant in the formation of the D-region ionosphere. In airglow studies, the infrared band of O_2, ${}^1\Delta_g - {}^3\Sigma_g^-$, is used to measure the quantities of $O_2({}^1\Delta_g)$ present in the atmosphere due to ozone photolysis or other reaction sources. As mentioned, the amount of ${}^1\Delta_g$ in the D region helps determine the ionization there. However, the excited species will be ignored in the determination of the O and O_3 concentrations at this point because of the additional complexity. Since their quantity is generally a very small part of the ground state concentration, excited species will be important only in reactions where the excitation produces a large enhancement in the reaction cross section, such as in several reactions with ionized species. Examples of such reactions have been mentioned above. It will be assumed that corrections to the O and O_3 densities, where necessary, can be made to the simpler analysis. Hunt (1965a) has shown that the $O_2({}^1\Delta)$ is unimportant in determining ozone concentration, and this would be especially true in the sunrise region where the $O_2({}^1\Delta)$ densities are smaller.

In the work that follows, the oxygen allotropes O, O_2, O_3 will be referred to with the subscripts 1, 2, 3 respectively; and the entire neutral atmosphere by the subscript 0. Hunt (1965b) in a study of the nonequilibrium behavior of an oxygen atmosphere used the reactions which are important for this model. They are

$$
\begin{aligned}
&O_2 + h\nu \xrightarrow{J_2} O + O \\
&O_3 + h\nu \xrightarrow{J_3} O + O_2 \\
&O + O + M \xrightarrow{k_1} O_2 + M \\
&O + O_2 + M \xrightarrow{k_2} O_3 + M \\
&O + O_3 \xrightarrow{k_3} O_2 + O_2 \quad .
\end{aligned}
\qquad (3.5)
$$

Here the k's are the appropriate reaction rate constants. Note: all rate constants in this text are given in cm sec units. For two-body reactions the units are cm^3 sec^{-1}, and for three-body reactions, cm^6 sec^{-1}. The continuity equations which follow from Equation (3.5) are (ignoring transport terms)

$$
\begin{aligned}
\frac{\partial n_1}{\partial t} &= 2J_2n_2 + J_3n_3 - k_2n_0n_1n_2 - k_3n_1n_3 - 2k_1n_0n_1^2 \\
\frac{\partial n_2}{\partial t} &= -J_2n_2 + J_3n_3 + k_1n_0n_1^2 + 2k_3n_1n_3 - k_2n_0n_1n_2 \\
\frac{\partial n_3}{\partial t} &= -J_3n_3 + k_2n_0n_1n_2 - k_3n_1n_3 \quad .
\end{aligned}
\qquad (3.6)
$$

The transport terms will be ignored based on the following argument. Only the sunrise region is being analyzed. And the sunrise region is very narrow, and certainly less than 10° arc. Thus, any local phenomena whose time constant is greater than about 1/2 hour will not be an important factor in the dynamics of the sunrise. Now the principle transport phenomena in the D region is eddy diffusion or diffusion via turbulent mixing. The eddy diffusion time constant is defined roughly by

$$\tau_e \sim H_0^2/D_e \tag{3.7}$$

where H_0 is the D-region neutral atmospheric scale height, and D_e is the eddy diffusion coefficient there. For the D region $\tau_e \sim$ hours, and so eddy diffusion can be ignored. If more detail is desired, one can also include the eddy diffusion term in the continuity equation. It is important to note that if the analysis is to continue through the sunrise into the daytime regime, then the effects of diffusion will become important in solving for the neutral atmosphere, e.g. Hesstvedt (1968, 1969). In general, many of the neutral species will be in a nonequilibrium state during most, or all of the daytime or nighttime even after a stable diurnal cycle has been established (Hunt, 1965b). Assuming that the effects of the detailed behavior of the sunrise (and sunset) region will be washed out over a diurnal cycle, such long-term analyses as Hesstvedt (1968, 1969), which include the influence of eddy diffusion while utilizing a greatly simplified sunrise (and sunset) model, can be used to establish boundary conditions for the sunrise problem. Of course, to be completely consistent one should solve the entire problem continuously over many days until a stable diurnal cycle is achieved.

3.2.1 Data and data acquistion for the all-oxygen model

In order to carry out any numerical analysis a host of data concerning reaction rates, solar fluxes, cross sections, atmospheric densities, scale heights and scale height gradients, and thermal structure must be known. The neutral atmosphere acts as a background for the evolution of the minor constituent chemistry. Table 3.1 lists the properties of the neutral atmosphere

Table 3.1 The neutral atmosphere

Alt. km	Temp. °K	Atmospheric Scale Height km	n(M) cm^{-3}	Atmospheric Scale Height Gradient, β
50.0	270.7	8.05	2.135 (16)	+.0017
52.5	270.5	8.05	1.566 (16)	-.0276
55.0	265.6	7.91	1.166 (16)	-.0561
57.5	260.7	7.77	8.636 (15)	-.0561
60.0	255.8	7.63	6.361 (15)	-.0668
62.5	249.1	7.44	4.690 (15)	-.0961
65.0	239.3	7.15	3.465 (15)	-.115
67.5	229.5	6.86	2.528 (15)	-.115
70.0	219.7	6.47	1.820 (15)	-.115
72.5	209.9	6.29	1.291 (15)	-.115
75.0	200.2	6.00	9.013 (14)	-.115
77.5	190.4	5.71	6.181 (14)	-.115
80.0	180.7	5.42	4.157 (14)	-.057
82.5	180.7	5.43	2.622 (14)	+.0016
85.0	180.7	5.43	1.654 (14)	+.0016
87.5	180.7	5.43	1.044 (14)	+.0018
90.0	180.7	5.44	6.591 (13)	+.047

and was taken from the U. S. Standard Atmosphere (1962). Note: all data which are listed in the form, e.g. 1(10) are to be interpreted as 1×10^{10} throughout the text. The data given in Table 3.1 are for the D region. The scale height gradient, β, was calculated from the scale height data in a straightforward way. Other data to supplement Table 3.1 can be found using

$$\begin{aligned} M &= 28.964 = \text{mean molecular mass} \\ n(N_2) &= .7808\ n(M) \\ n(O_2) &= .2095\ n(M) \quad . \end{aligned} \tag{3.8}$$

In order to obtain ozone data a graph was plotted which was based on both theoretical and experimental high altitude ozone distributions. The day and nighttime ozone curves are shown in Figure 3.2. From Figure 3.2, Table 3.2 was derived, and is the source of high altitude ozone data for this paper. The data used to plot Figure 3.2 were obtained from various sources including Hunt (1966), Weeks and Smith (1968), Smith (1969), Hesstvedt (1968, 1969) and Carver *et al*. (1966). Also included in Table 3.2 are representative values for the atomic oxygen densities in the D region at night near dawn based on the works of Hunt (1966) and Hesstvedt (1969). (In this case $O(^3P)$ is assumed, and the $O(^1D)$ is being ignored.)

Tables 3.3 and 3.4 contain the necessary information on the solar radiation fluxes, and the absorption cross sections for O_2 and O_3 as well as Rayleigh scattering for wavelengths between 1400 and 7500 Å. The data were taken from a report by Radicella and Stowe (1970), Inn and Tanaka (1959), *Handbook of Geophysics* (1961), and Goody (1964). The original sources for most of the data are cited in Radicella and Stowe (1970).

Table 3.5 lists supplemental data on the low altitude (0-50 km) ozone and neutral atmosphere densities. These data are necessary for calculating

RC

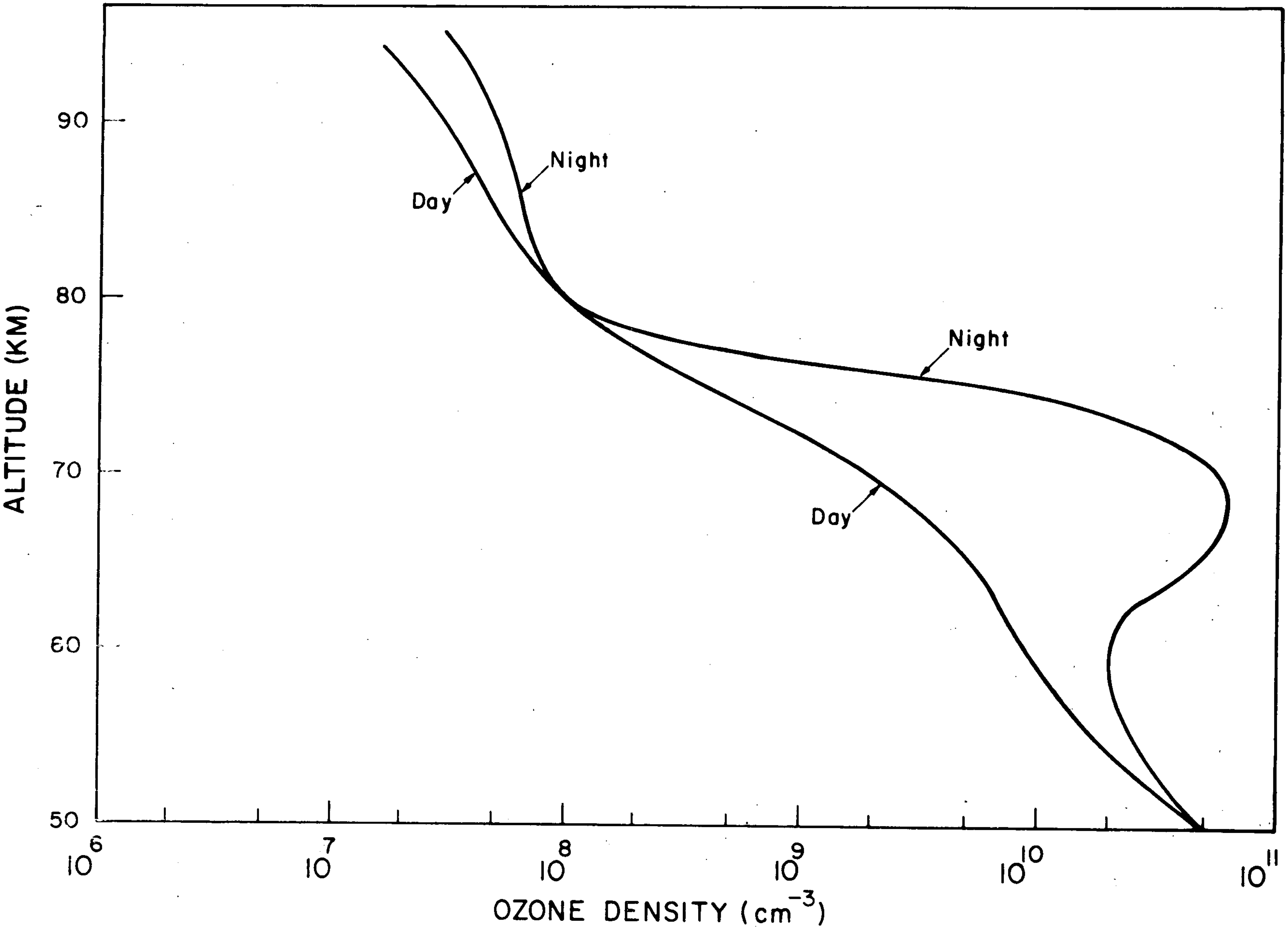

Figure 3.2 Daytime and nighttime ozone distributions in the D region.

Table 3.2 Ozone and atomic oxygen data

Alt. km	$n(O_3)$- cm^{-3} daytime	$n(O_3)$-cm^{-3} night	$f_B = \frac{n_{night}}{n_{day}}$	H_{O_3} km	β	$n(O)$-cm^{-3}
50.0	5.0 (10)	5.0 (10)	1.0	3.2	.62	0
52.5	2.8 (10)	3.4 (10)	1.2	4.8	.54	0
55.0	1.8 (10)	2.6 (10)	1.4	6.1	.59	0
57.5	1.2 (10)	2.1 (10)	1.8	7.6	.50	0
60.0	9.0 (9)	2.0 (10)	2.2	8.9	.46	1.0 (0)
62.5	7.0 (9)	2.5 (10)	3.6	10.0	-1.10	2.0 (0)
65.0	5.3 (9)	4.7 (10)	8.9	7.3	- .83	5.0 (0)
67.5	3.5 (9)	6.2 (10)	18.0	5.2	- .62	1.0 (1)
70.0	2.0 (9)	6.0 (10)	30.0	3.7	- .25	1.0 (3)
72.5	9.4 (8)	3.0 (10)	32.0	3.0	- .04	1.0 (6)
75.0	4.0 (8)	6.0 (9)	15.0	3.0	.23	1.0 (7)
77.5	1.8 (8)	3.3 (8)	1.8	3.5	.53	1.1 (8)
80.0	1.0 (8)	1.0 (8)	1.0	4.8	.86	9.0 (9)
82.5	6.8 (7)	7.4 (7)	1.1	7.1	.91	7.0 (10)
85.0	5.0 (7)	6.5 (7)	1.3	9.4	.26	1.0 (11)
87.5	3.9 (7)	5.7 (7)	1.5	10.0	- .62	3.5 (11)
90.0	3.0 (7)	5.0 (7)	1.7	8.5		7.5 (11)

Table 3.3 Solar radiation and absorption cross sections

Central Wavelength, Å	Wavelength Interval, Å	Average Solar Photon Flux in the Interval Phot-cm^{-2}-sec^{-1}-Å^{-1}	$\sigma(O_2)$ cm^2	$\sigma(O_3)$ cm^2
1215	1.0	2.70 (11)	1.10 (-20)	3.50 (-17)
1400	50.0	3.66 (8)	1.45 (-17)	7.00 (-18)
1450	50.0	7.40	1.48	4.50
1500	50.0	1.46 (9)	1.28	3.50
1550	50.0	2.66	8.80 (-18)	2.50
1600	50.0	5.20	4.87	1.10
1650	50.0	8.40	2.37	9.00 (-19)
1700	50.0	1.40 (10)	1.02	9.00
1750	50.0	2.12	3.08 (-19)	8.50
1775	2.5	2.44	2.53 (-20)	8.00
1780	5.0	2.55	1.70	7.90
1785	5.0	2.66	1.63	7.90
1790	5.0	2.79	1.77	7.80
1795	5.0	2.81	2.08	7.80
1800	5.0	3.03	1.20	7.70
1805	5.0	3.17	2.67	7.70
1810	5.0	3.32	1.17	7.60
1815	5.0	3.47	1.19	7.50
1820	5.0	3.61	1.18	7.40
1825	5.0	3.76	4.50 (-21)	7.30
1830	5.0	3.95	7.04	7.20
1835	5.0	4.12	6.34	7.10
1840	5.0	4.30	1.43	7.00
1845	5.0	4.50	5.63	6.90
1850	5.0	4.69 (10)	6.64 (-21)	6.80 (-19)
1855	5.0	4.89	1.48	6.70
1860	5.0	5.14	1.57	6.55
1865	5.0	5.34	5.07	6.40
1870	5.0	5.64	2.03	6.25
1875	5.0	5.84	4.40 (-22)	6.10
1880	5.0	6.14	1.45 (-21)	5.95
1885	5.0	6.39	1.77	5.80
1890	5.0	6.70	3.56 (-22)	5.65
1895	5.0	7.00	2.06	5.50
1900	5.0	7.26	6.37	5.30
1905	5.0	7.56	8.28	5.20
1910	5.0	7.87	3.98	5.10
1915	5.0	8.28	1.88	5.00
1920	5.0	8.59	4.30	4.80
1925	5.0	8.90	6.45	4.70
1930	5.0	9.31	2.28	4.60
1935	5.0	9.72	1.20	4.50
1940	5.0	9.94	9.44 (-23)	4.40
1945	5.0	1.06 (11)	1.80 (-22)	4.30
1950	5.0	1.09	1.98	4.20
1955	5.0	1.13	8.87 (-23)	4.10
1960	5.0	1.17	5.85	3.90
1965	5.0	1.20	5.97	3.75
1970	5.0	1.26	1.03 (-22)	3.60
1975	2.5	1.30	8.85 (-23)	3.45

Table 3.4 Solar radiation and absorption cross sections

Central Wavelength, Å	Wavelength Interval, Å	Average Solar Photon Flux in the Interval Phot-cm^{-2}-sec^{-1}-Å^{-1}	Absorption $\sigma(O_2)$ cm^2	Cross sections $\sigma(O_3)$ cm^2	Rayleigh Total Scattering Cross sections σ_R cm^2
2000	50.0	1.407 (11)	1.30 (-23)	3.30 (-19)	3.12 (-25)
2050	50.0	1.854	1.10	3.52	2.84
2100	50.0	3.060	9.60 (-24)	5.49	2.57
2150	50.0	5.186	7.90	9.86	2.33
2200	50.0	6.854	6.40	1.75 (-18)	2.12
2250	50.0	7.914	4.60	2.89	1.95
2300	50.0	8.322	3.10	4.45	1.77
2350	50.0	7.558	1.80	6.25	1.63
2400	50.0	8.200	1.00	8.05	1.50
2450	50.0	9.604	0.0	9.80	1.39
2500	50.0	9.548	0.0	1.09 (-17)	1.27
2550	50.0	1.435 (12)	0.0	1.13	1.18
2600	50.0	1.829	0.0	1.08	1.10
2650	50.0	2.664	0.0	9.56 (-18)	1.01
2700	50.0	3.392	0.0	7.77	9.35 (-26)
2750	50.0	3.04	0.0	5.70	8.70
2800	50.0	3.376	0.0	3.84	8.05
2850	50.0	4.870	0.0	2.44	7.30
2900	50.0	7.578	0.0	1.39	6.55
2950	50.0	9.340	0.0	7.44 (-19)	5.95
3000	50.0	9.196	0.0	3.84	5.40
3050	50.0	1.027 (13)	0.0	1.96	5.05
3100	50.0	1.184	0.0	1.02	4.75
3150	50.0	1.298	0.0	5.36 (-20)	4.44
3200	50.0	1.367 (13)	0.0	2.94 (-20)	4.20
3250	50.0	1.666	0.0	1.46	3.90
3300	50.0	1.907	0.0	7.04 (-21)	3.67
3350	50.0	1.869	0.0	3.82	3.50
3400	50.0	1.896	0.0	1.94	3.24
3450	50.0	2.028	0.0	7.04 (-22)	3.08
3500	25.0	2.076	0.0	2.74	2.93
3750	500.0	2.663	0.0	0.0 10^{-23}	2.20
				or	
4250	500.0	4.138	0.0	0.0 10^{-24}	1.28
4750	500.0	5.012	0.0	4.80 (-22)	8.29 (-27)
5250	500.0	5.150	0.0	2.06 (-21)	5.55
5750	500.0	5.514	0.0	3.98	3.86
6250	500.0	5.396	0.0	3.66	2.77
6750	500.0	5.204	0.0	1.53	2.04
7250	500.0	4.948	0.0	5.23 (-22)	1.53

Table 3.5 The low altitude ozone and neutral atmosphere densities and scale heights

Alt. km	n(M) cm^{-3}	H_M km	$n(O_3)$ cm^{-3}	H_{O_3} km
0	2.547(19)	8.43	1.5(10)	--
2.5	1.990(19)	7.97	3.0(10)	--
5.0	1.531(19)	7.45	6.5(10)	--
7.5	1.159(19)	7.03	8.5(10)	--
10.0	8.598(18)	6.56	1.0(11)	--
12.5	5.996(18)	6.37	8.0(11)	--
15.0	4.050(18)	6.37	2.0(12)	--
17.5	2.736(18)	6.38	4.5(12)	--
20.0	1.849(18)	6.38	6.0(12)	--
22.5	1.239(18)	6.46	7.0(12)	--
25.0	8.335(17)	6.54	7.5(12)	--
27.5	5.636(17)	6.61	4.5(12)	--
30.0	3.828(17)	6.69	3.5(12)	3.1
32.5	2.602(17)	6.79	1.8(12)	3.1
35.0	1.760(17)	7.00	1.0(12)	3.1
37.5	1.580(17)	7.06	6.0(11)	3.1
40.0	8.308(16)	7.42	2.5(11)	3.1
42.5	5.800(16)	7.63	1.5(11)	3.1
45.0	4.089(16)	7.84	9.0(10)	3.1
47.5	2.914(16)	8.04	6.5(10)	3.1
50.0	2.135(16)	8.05	5.0(10)	3.2

the absorption at low grazing heights, and were obtained from the U. S. Standard Atmosphere (1962), and Hunt (1965b).

The reaction rate constants for Equations (3.5) are given in Table 3.6. They are the result of a study by Kaufman in DASA (1967), Chapter 14. In each case the temperature is in degrees Kelvin. For the three-body reactions the rates are adopted from data using molecular nitrogen as the third body.

Yet to be specified are the height dependent parameters describing the various models proposed in this study. These parameters are initially set by the ozone sunrise distributions found from the uniform dissociation rates. The parameters are then corrected after each calculation. One parameter, the ozone sunrise angular width, could be initially estimated from the theoretical diurnal studies of Hunt (1967b, 1966) and Hesstvedt (1969). A reasonable value would be

$$\Delta(O_3) \sim 7^\circ \quad . \tag{3.9}$$

Data for the other ozone models used in Equation (2.102) and Appendix III can be derived from Tables 3.2 and 3.4.

3.2.2 Method of solution of the model

In Figure 3.3 the numerical solution scheme is block-diagramed. Since the radiation rates, J, are spatially dependent through the optical depth, at each point in the numerical calculation the various J's must be calculated using the radiation data. If one writes the optical depth in the form

$$\tau(\lambda; \bar{r}) = \sigma^a(\lambda)\hat{\tau}(\bar{r}) \tag{3.10}$$

then the numerical analog of Equation (2.73) will be

$$J_j(\bar{r}) = \sum_p \Delta\lambda_p \; \sigma_j{}^d(\lambda_p)\bar{I}_0(\lambda_p)\exp\left\{-\sum_q \sigma_q^a(\lambda_p) \; \hat{\tau}_q(\bar{r})\right\} \tag{3.11}$$

Table 3.6 Reaction rate constants for the oxygen atmosphere model

Reaction	Rate Coefficient
$O + O + M \rightarrow O_2 + M$	$k_1 = 3.0 \times 10^{-33} \left(\frac{T}{300}\right)^{-2.9\pm0.4}$
$O + O_2 + M \rightarrow O_3 + M$	$k_2 = 5.5 \times 10^{-34} \left(\frac{T}{300}\right)^{-2.6\pm0.4}$
$O + O_3 \rightarrow O_2 + O_2$	$k_3 = (1.4\pm0.3) \times 10^{-12} \exp\left(-\frac{3000\pm400}{RT}\right)$

$R = 1.987$ cal./°K - mole

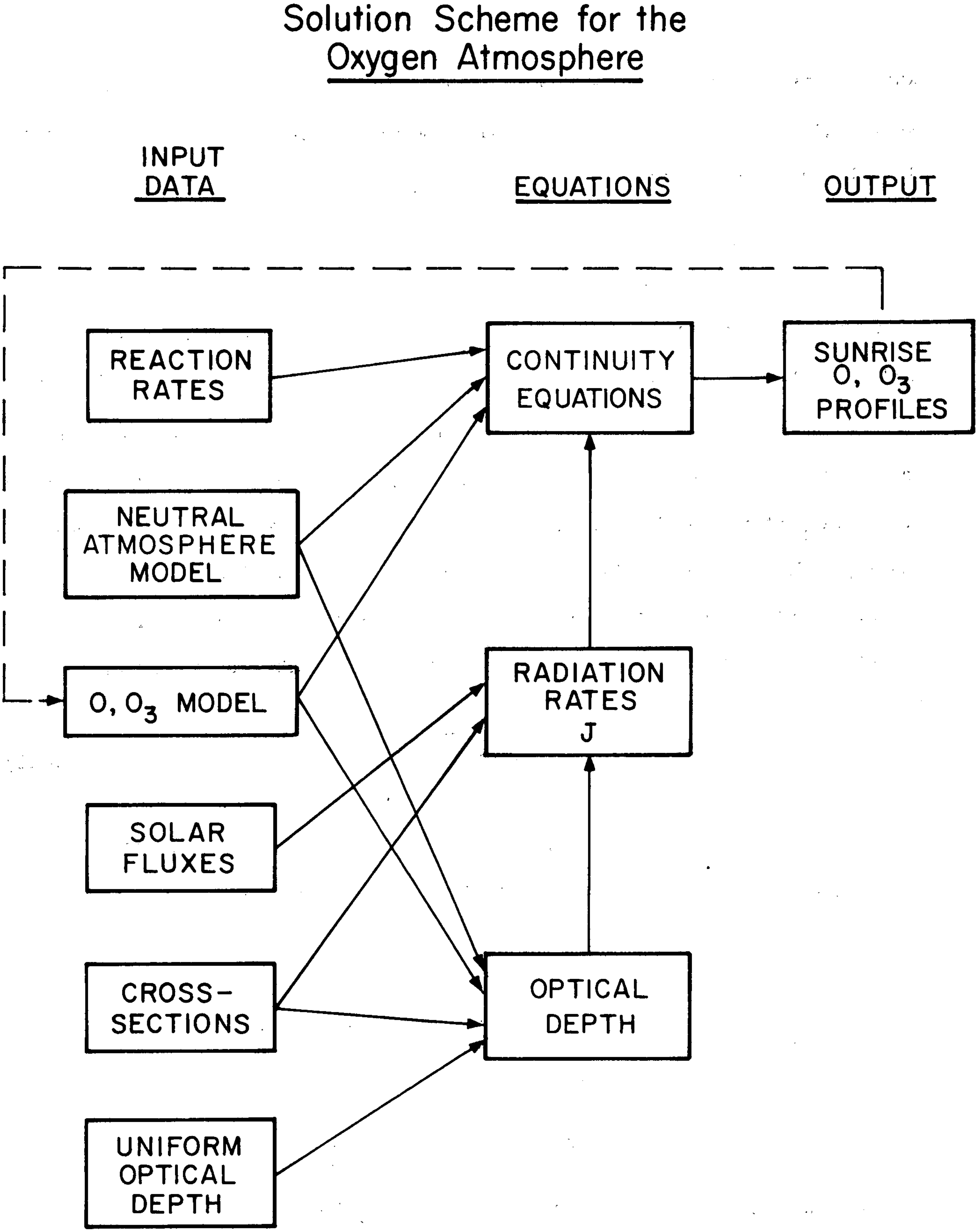

Figure 3.3 Solution scheme for the oxygen atmosphere.

where $\overline{I}_0$ is a suitable average photon flux, the sum 'p' is extended over the wavelength range of importance, and the sum 'q' is over the absorbing species. It will be assumed that

$$\sigma_i^a = \sigma_i^d = \sigma_i \qquad (3.12)$$

which is nearly exactly correct since the dissociation thresholds are quite low, and dissociation is the primary channel for the wavelengths of interest here.

To solve the continuity equations the photorates J are first determined as functions of χ at equal time intervals over the sunrise with all calculations commencing at $\chi = 100°$ and continuing for two hours. The J's are then used as input data for the continuity equations, as in Figure 3.3, with the same time step. It should be noted that for zenith angles near 90° the continuity equations could be transformed into equations in χ rather than time by

$$\frac{\partial n}{\partial t} \to -\omega_e \frac{\partial n}{\partial \chi} \sqrt{\cos(\tilde{\theta}+\delta)\ \cos(\tilde{\theta}-\delta)} \quad . \qquad (3.13)$$

The relationship between the time base and the various parameters of the problem can be defined by the following set of equations

$$\begin{aligned} \phi &= \phi_0 - \omega_e t \\ \cos\chi &= \cos\delta \cos\tilde{\theta} \cos\phi + \sin\delta \sin\tilde{\theta} \\ h &= (a+w) \sin\chi - a \\ X_h &= (a+w)/H(h) \quad . \end{aligned} \qquad (3.14)$$

These equations have already been quoted in the text.

The calculation of the J's is done using Equation (3.11) once the $\hat{\tau}_q$ are known (i.e., τ). The optical depth must take into account the absorption due to molecular oxygen, ozone, and Rayleigh scattering. For the wavelengths of interest here atomic oxygen and molecular nitrogen absorption may be ignored. So, for the sunrise region

$$\tau = \sigma_2 n_2(h)\ H_0(h)F_2 + \sigma_3 n_3(h)H_3(h)F_3 + \sigma_{Re} n_0(h)H_0(h)F_0\ . \tag{3.15}$$

From Appendix I, $\sigma_{Re} \doteq \sigma_R$, and Equation (3.8) gives $n_2(h) = .2095 n_0(h)$. Since both O_2 and the total neutral atmosphere are essentially uniform and have the same scale height, $F_2 = F_0 \equiv F_M$, from which

$$\tau = (\sigma_R + .21\sigma_2)n_0(h)H_0(h)F_M(X_0,\chi)c_M + \sigma_3 n_3(h)H_3(h)F_3(X_3,\chi)c_3 \tag{3.16}$$

where the c's are factors due to the finite size of the sun and are given by Equation (3.4). For $\chi < \frac{\pi}{2}$ the c's can be evaluated using Equation (3.4) with $X_o = X$ (i.e., a constant factor at any altitude which may be taken as approximately unity). For $\chi \geq \pi/2$ one uses Equation (2.52) for F_M. If $\chi < \pi/2$ one has Equations (2.50) or (2.51). To calculate F_3 the absorption of the nighttime ozone layer can be included, after the necessary ozone model parameters (i.e., ϕ_{og} and δ_g) have been ascertained, by utilizing all of the Equations (2.98), (2.99), (2.102), (2.103), (III.8), and (III.11).

Once the J's are determined the sunrise problem can easily be solved by performing a free running integration of the continuity equations starting with the nighttime boundary conditions using a Runge-Kutta integration scheme. The Runge-Kutta method is most applicable here since long diurnal cycles are not being considered and short integration intervals can be used to overcome any rapid variations or 'stiffness' in the continuity equations without costing a lot of machine time. The Runge-Kutta method has the advantages of being straightforward with simple error detection built in, quite accurate, and conserving mass in the continuity equations automatically (when stoichemistry is being considered).

With an initial set of ozone distributions calculated for the case of uniform absorption, the nonuniform parameters needed above for $\dot{F}_3$ can be determined from these plots (see Appendix V). This process can then be iterated as in Equation (2.109). At the end of each iteration step the calculated ozone distributions, the previously calculated ozone distributions, and the ozone sunrise models are compared and adjusted. The process is repeated until the differences in the calculated ozone densities are minimal, and the ozone distributions compare favorably with the ozone models.

For the set of continuity Equations (3.6) it should be noted that the fractional change in $n(O_2)$ over any part of the sunrise will be many orders of magnitude less than one, so that the equation for O_2 can be ignored and $n(O_2)$ can be held constant in the equations for O and O_3. Strictly speaking this is incorrect since mass will not then be conserved. But the error is certainly negligible in this case.

In solving the continuity Equations (3.6) it was found that an additional loss term was needed in the equation for $\dot{n}_3$. This resulted because the initial conditions which were placed on the solutions (predawn) were derived from analyses that included many more constituents than were used here as well as transport effects. The additional term was incorporated in the computer program to make $\dot{n}_3 \sim 0$ for the predawn region. Also, this additional loss term was needed only at the three highest altitudes studied, where the atomic oxygen densities were relatively much larger than the ozone densities. This effect merely indicates that the equilibrium densities for an all-oxygen atmosphere model are inaccurate.

The computer program that was used to solve for the photorates is outlined in Appendix IV. The results of the computations are given in Figures 3.4-3.10. Figure 3.4 illustrates the molecular oxygen photodissociation rate for the nonuniform atmosphere (i.e. with the night-to-day ozone absorption included). Figures 3.5 and 3.6 are the ozone photodissociation rates for the uniform and nonuniform cases respectively. Figure 3.7 shows the ozone distributions over sunrise for both cases, with solid lines indicating the values for nonuniform absorption. The atomic oxygen sunrise densities are given in Figures 3.8 and 3.9 for the uniform and nonuniform cases respectively. And Figure 3.10 illustrates the O-to-O_3 ratio during sunrise, again with the results for the nonuniform atmosphere being shown by solid lines. In each figure there are plots for each of nine altitudes in 5 km steps from 50-90 km.

3.2.3 Discussion of the results for the oxygen atmosphere model

All the calculations shown in Figures 3.4-3.10 were done at 38°N latitude using the absorption formulation of the previous sections and are shown as functions of the solar zenith angle. That formulation was made at 0° latitude with $\delta = 0°$. It is argued here that the plots of the ozone and atomic oxygen densities, as well as the photodissociation rates, as functions of the solar zenith angle, χ, are relatively insensitive to changes in latitude for low latitudes. Two effects take place when $\tilde{\theta}$ is increased from zero with $\delta = 0°$. Referring to Equation (3.13) one can see that the continuity equations are nearly invariant for different latitudes except for a multiplicative constant, dependent on $\tilde{\theta}$ and δ, which is close to unity at low latitudes. Distributions of O and O_3

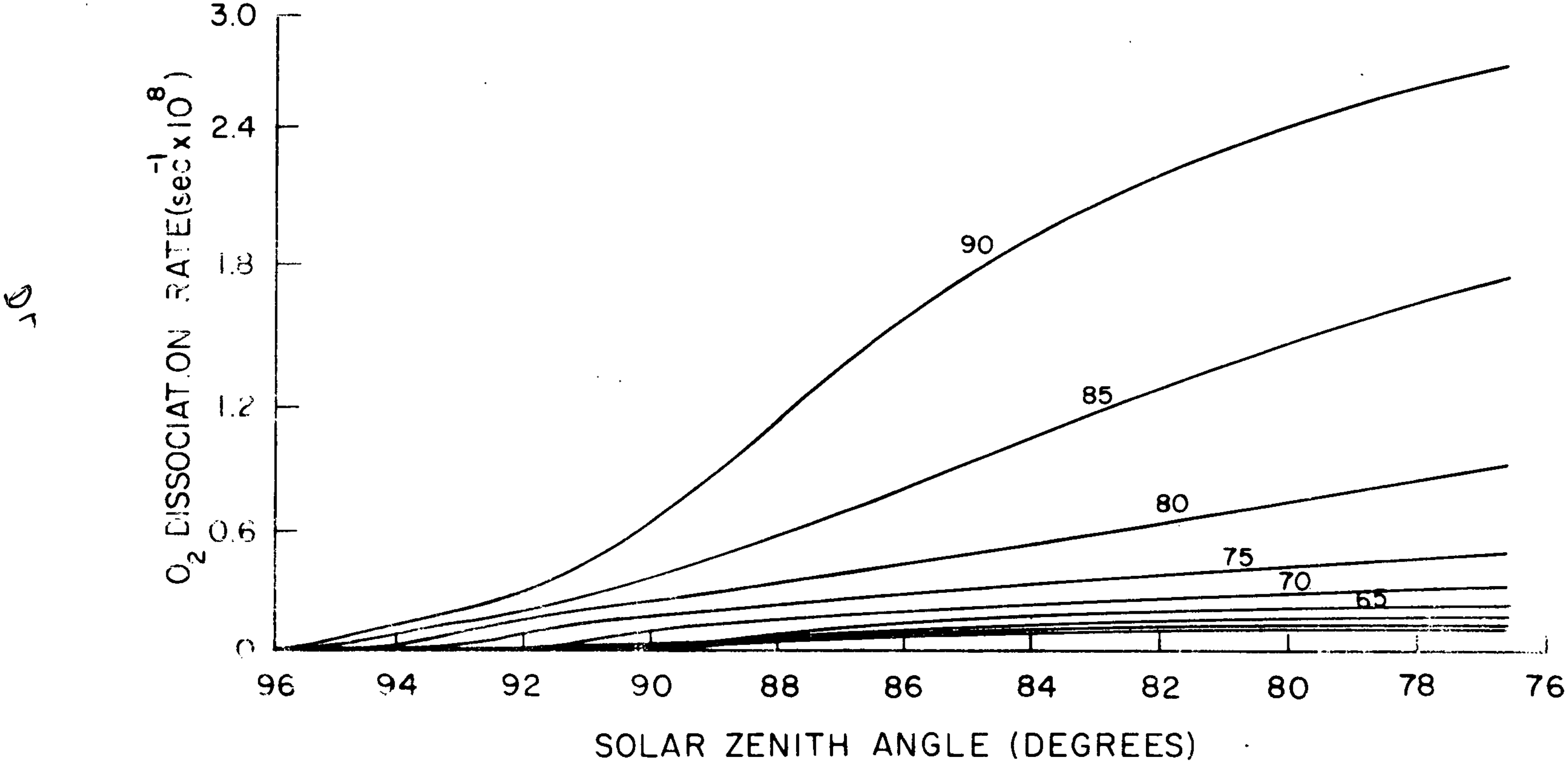

Figure 3.4 Molecular oxygen photodissociation rates over sunrise.

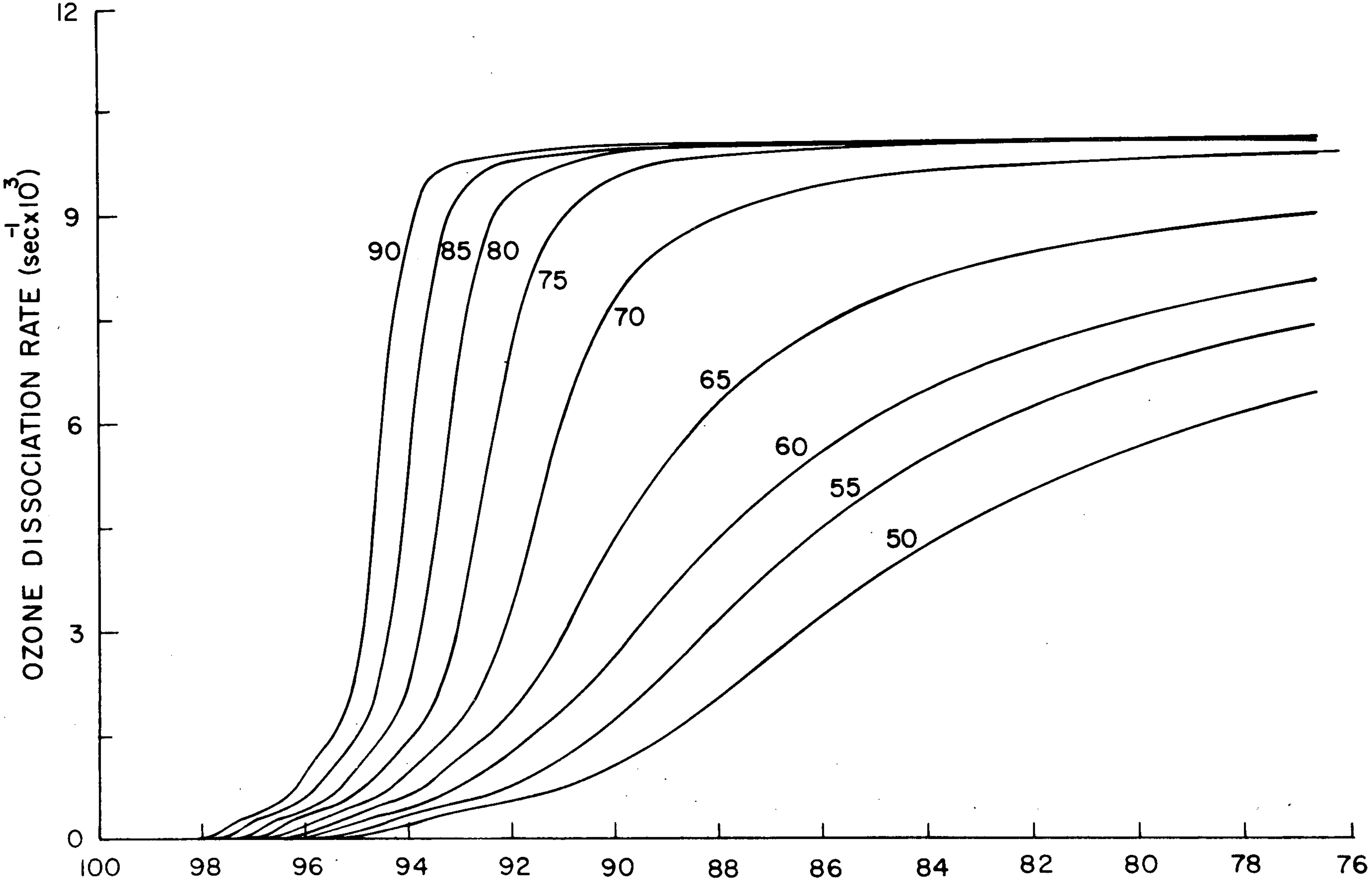

Figure 3.5 Ozone photodissociation rates over sunrise for the uniform absorption case.

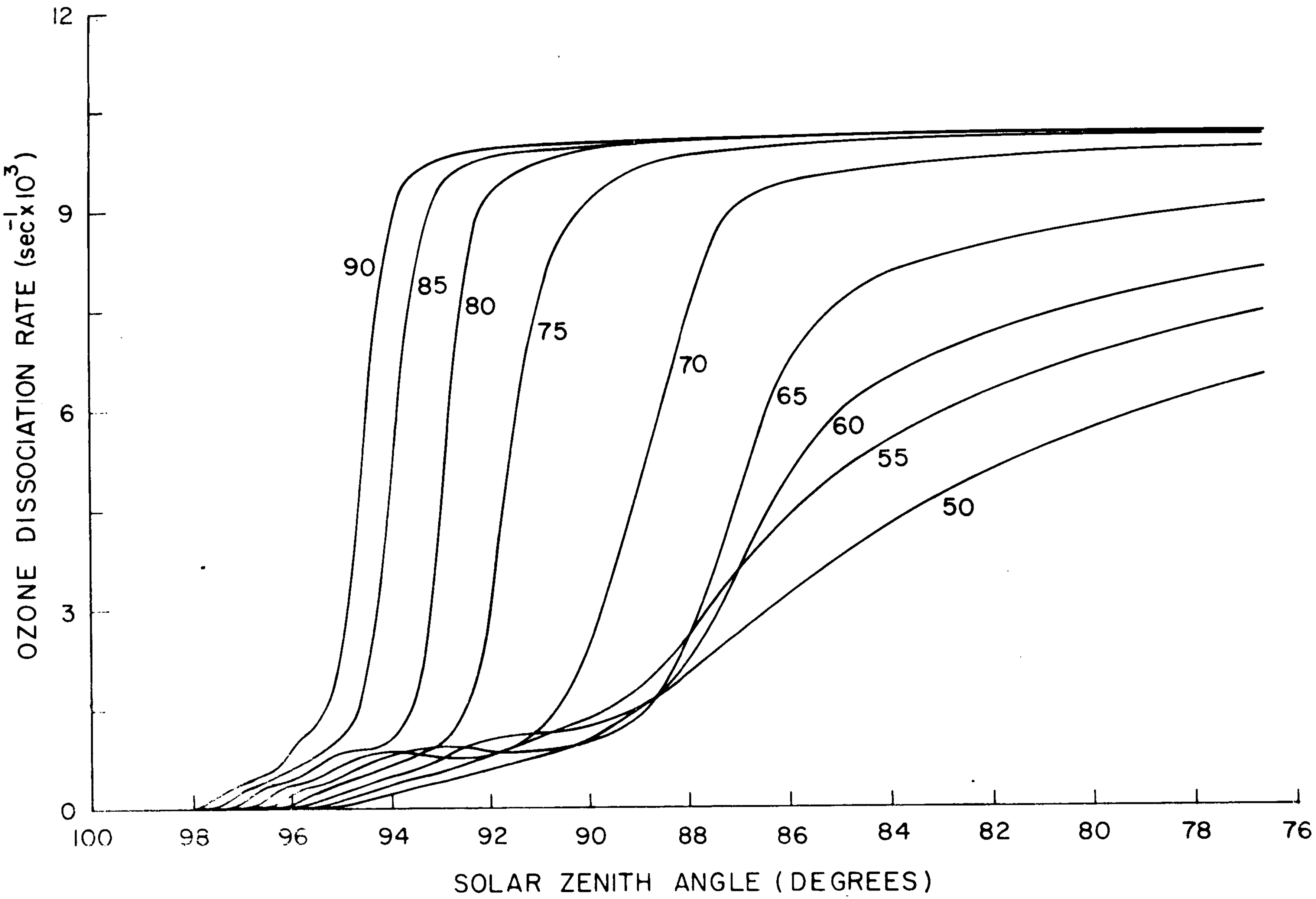

Figure 3.6 Ozone photodissociation rates over sunrise for the nonuniform absorption case.

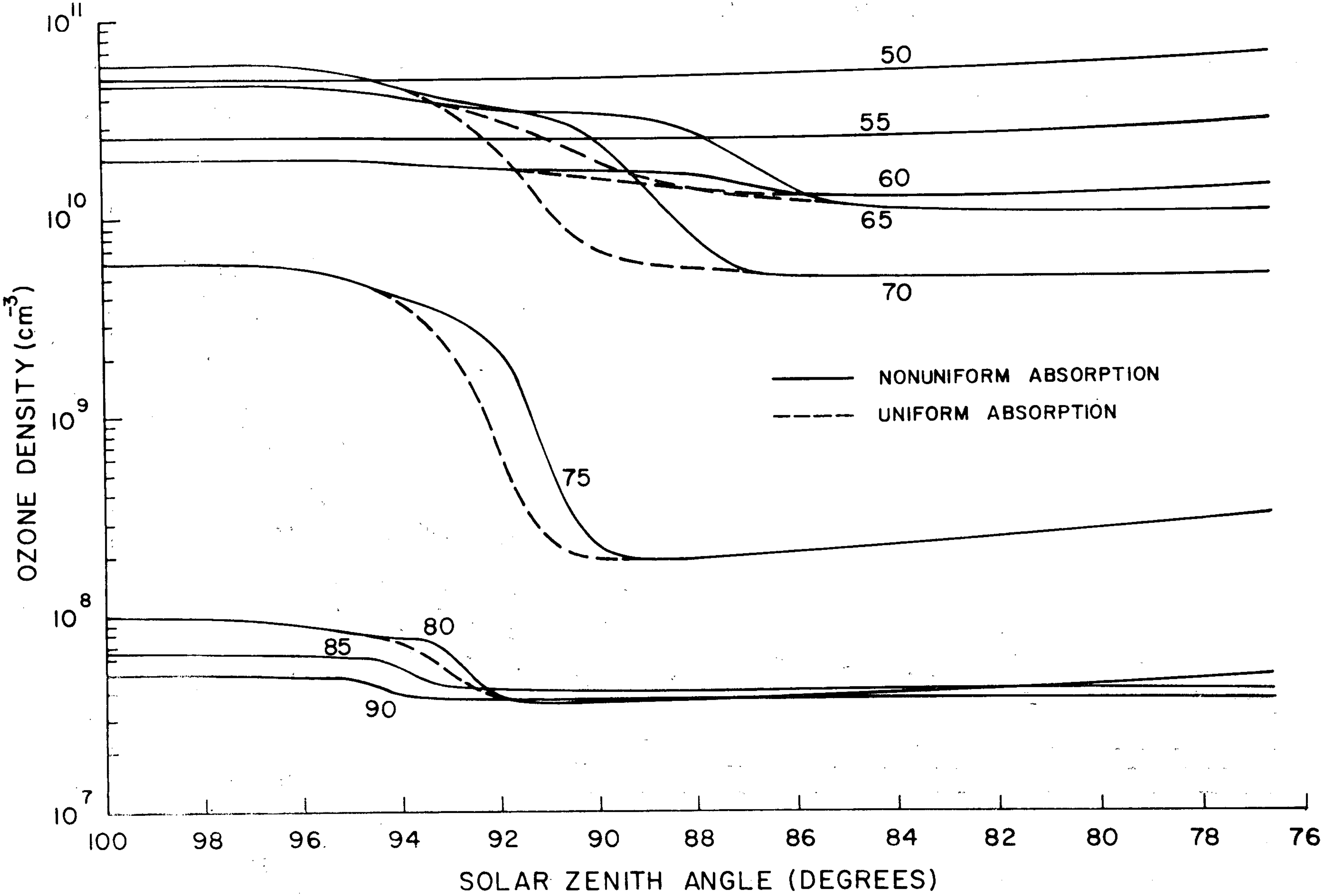

Figure 3.7 Ozone distributions during sunrise for both the uniform and nonuniform absorption cases.

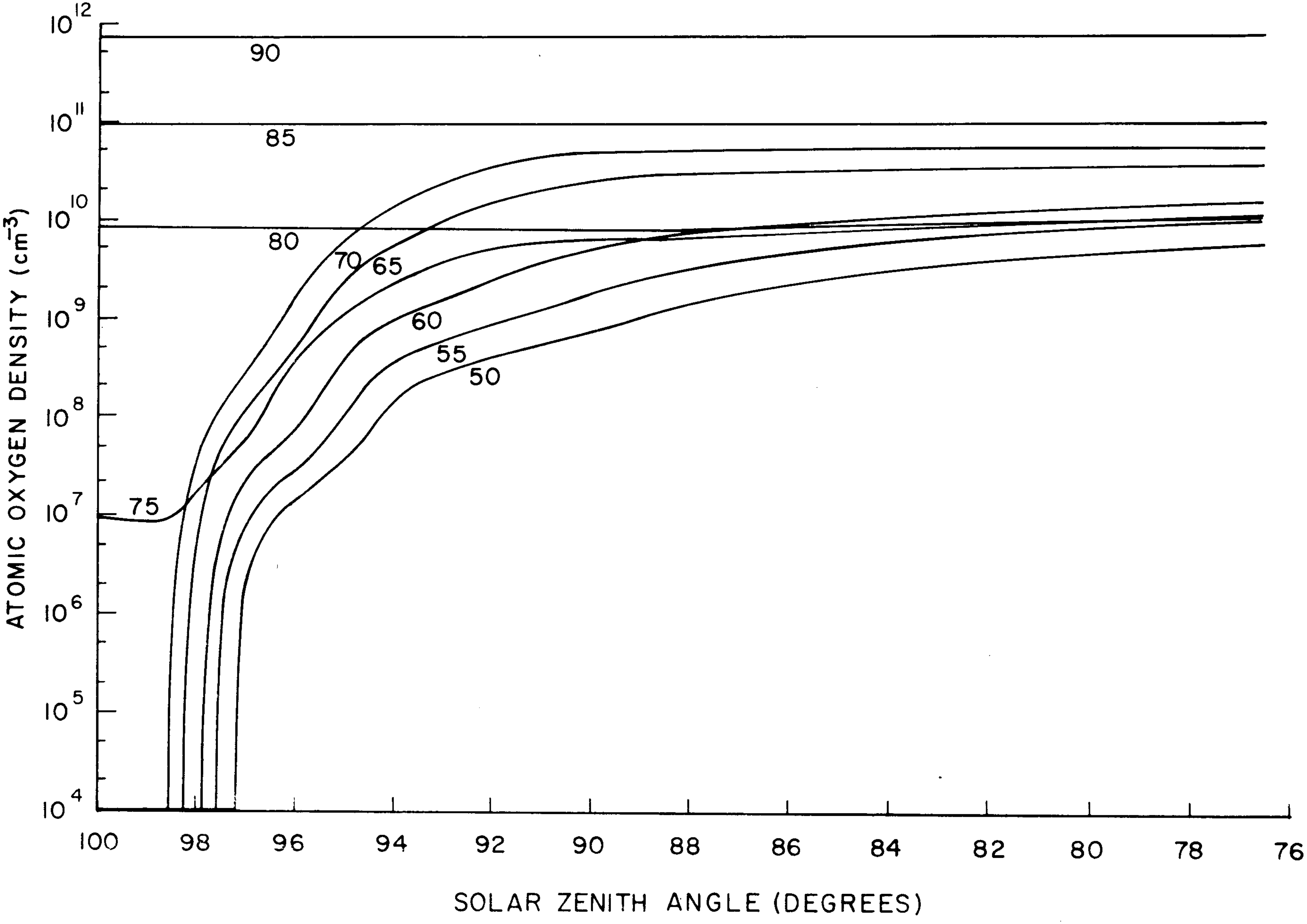

Figure 3.8 Atomic oxygen distributions during sunrise for the uniform absorption case.

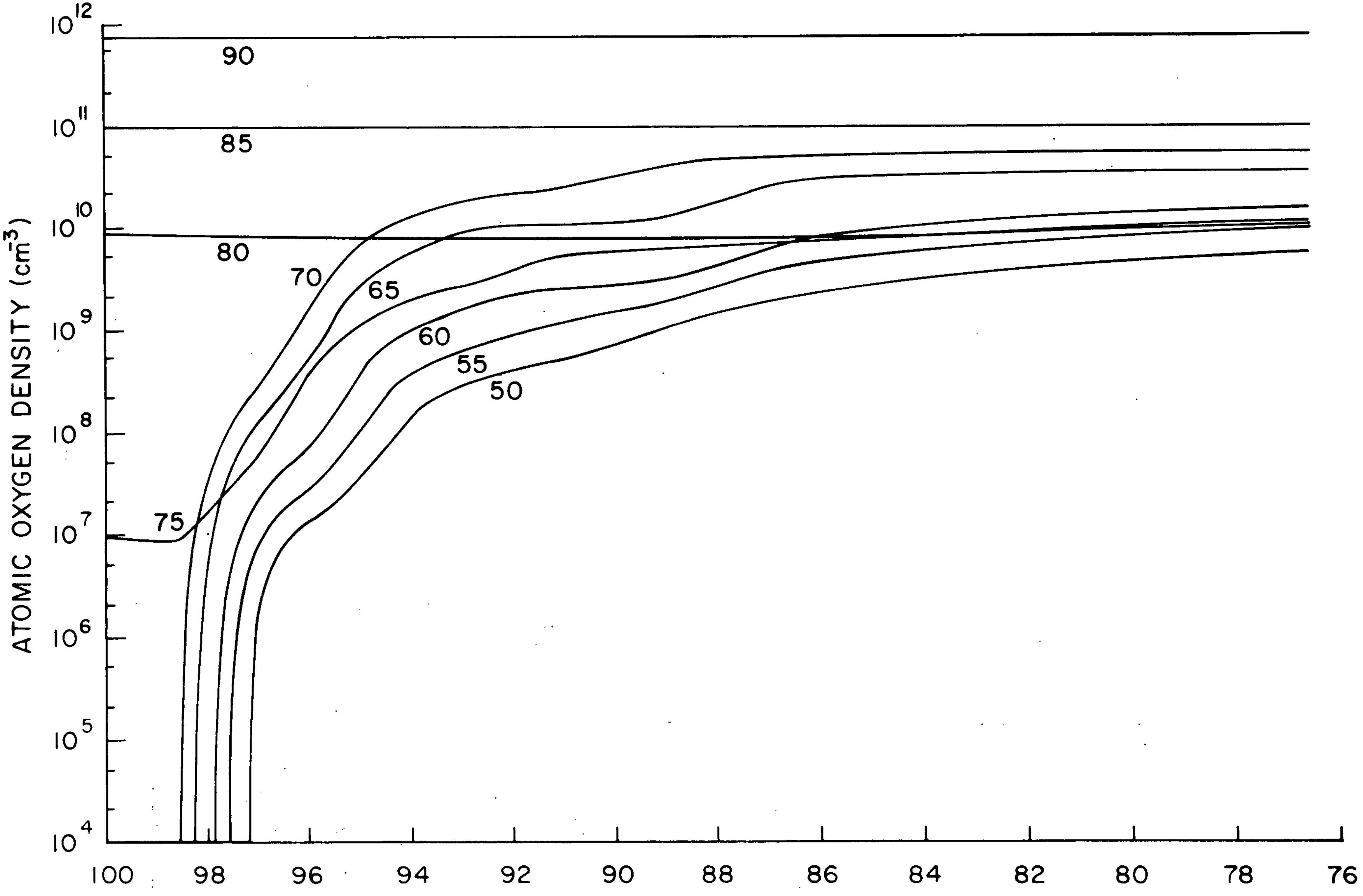

Figure 3.9 Atomic oxygen distributions during sunrise for the nonuniform absorption case.

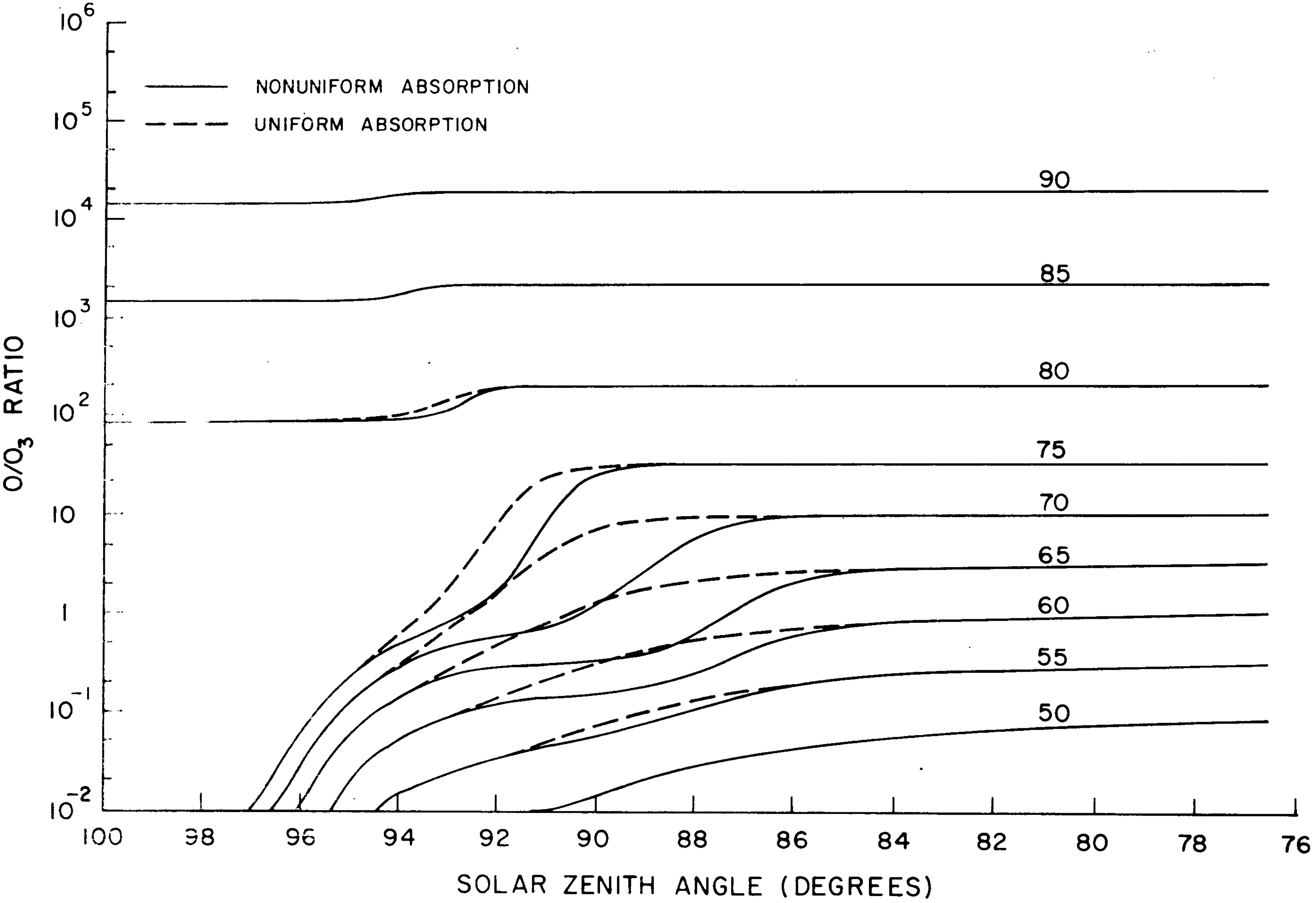

Figure 3.10 The O/O_3 density ratios over sunrise for both the uniform and nonuniform absorption cases

were calculated for 0° and 38° latitude and compared. They showed that at the larger latitude the O and O_3 changes lead those at 0° latitude because the rates of change in the continuity equations are larger. However, the difference (on a χ-plot) was never more than a small fraction of a degree ($\lesssim .1°$). Also, for ray paths with $\tilde{\theta} > 0$ the ray passes over other higher latitudes, and so through sunrise transition regions which are theoretically shorter. This would reduce the absorption along the ray path and enhance an earlier sunrise effect.

If δ is changed from 0° the ray path passes obliquely through the sunrise region which (although the region can be expected to be less wide) would augment the absorption along the ray path. This could compensate for the decrease of absorption at higher latitudes. However, since δ and $\tilde{\theta}$ are small, and the whole analysis is only approximate, the net effect on the O and O_3 sunrise distributions of a change in $\tilde{\theta}$ or δ will be unimportant. This effect will be even less noticeable in the dissociation rates. All the variables plotted in Figures 3.4-3.10 will therefore be taken as pure functions of χ.

First consider the molecular oxygen photodissociation rates, J_2, plotted in Figure 3.4 which are for the nonuniform atmosphere and are nearly identical to the rates for the case of a uniform atmosphere (which are not illustrated). Indeed, since only the ozone absorption in the nearest uv wavelength range for the perturbation ozone density is different for the two J_2's, the difference will be minimal. The rates illustrated in Figure 3.4 begin at very small values, then slope upward from sunrise, and finally bend over and level out toward their noon values. At higher altitudes the daytime rates are of the order of 10^{-8} sec^{-1}, while below 80 km $J_2 \lesssim 10^{-9}$ sec^{-1}. At D-region altitudes the sunrise for J_2 is not abrupt, but extends over many degrees (and might even be approximated by a ramp). If a step function is used for J_2, the error can be minimized by placing the step symmetrically in the sunrise.

The photodissociation rates of ozone at sunrise in a uniform atmosphere are shown in Figure 3.5. At the largest solar zenith angles ($h \simeq 0$) there is a small amount of residual photodissociation due mainly to the penetration of optical radiation. The photorate J_3 then increases slowly until the ozone peak at 25 km, which effectively blocks most of the uv radiation, is overcome. A rapid increase in J_3 then ensues toward a stable daytime rate. At the lowest altitudes this increase in J_3 is fairly slow because the scale height·density produce of ozone is large. However, since ozone has a negative scale height gradient over portions of the D region, the sharpness of this increase is enhanced at higher altitudes because the density is falling off rapidly with altitude.

One can see from Figure 3.5 that ozone is ineffective as an absorber above 65 km in the daytime regime. This follows because J_3 is nearly independent of altitude in this region, which indicates that the radiation intensity is unattenuated there. The daytime values of J_3 are about 10^{-2} $\sec^{-1}$. The initial sunrise values are at least three orders of magnitude smaller, and so are not clearly defined on the linear plots of Figures 3.5 and 3.6.

In Figure 3.6 the excess absorption of the ozone night-to-day transition has been included in the calculation for J_3. At large solar zenith angles J_3 at any altitude is not affected by the ozone nighttime peak, as the absorption by the 25 km peak is much larger. Also, for smaller solar zenith angles, past sunrise, the J_3 quickly approach the uniform rates of Figure 8a already discussed. One also notes that at low altitudes, below 60 km, the rates are practically unaffected for all angles; and at high altitudes, above the 80 km, the principle effect is a slight sharpening of the main rise in J_3.

For the intermediate altitudes the extra absorption has a strong influence on J_3. In Figure 3.6 one sees that the main sunrise increase in J_3 is delayed at these altitudes, and an earlier ledge of dissociation is established. Although this ledge has a typical value only of the order of 10^{-3} sec^{-1}, it is large enough to produce (over several degrees) a noticeable early decrease in the ozone distribution and large quantities of atomic oxygen (even though the relative change in the ozone density may be small, its absolute value can be large). The longest delays in J_3 occur for the altitudes from around 65-75 km where the added nighttime ozone layer is most prominent. At these altitudes the morning decay of ozone may be delayed several degrees. The daytime photochemistry will not be affected by this delay, but any chemical effects produced directly by the sunrise ozone change will lag somewhat at sunrise.

The ozone densities calculated using the data of Figures 3.4, 3.5 and 3.6 are plotted in Figure 3.7. The sunrise is clearly depicted at each altitude above 55 km. Below 55 km sunrise does not occur for ozone. One can also see the nonequilibrium behavior of the ozone after sunrise, and how small this variation is compared to the sunrise changes for the range of solar zenith angles shown.

Figures 3.2 and 3.7 can be compared to see if the static and dynamic ozone models are compatible. Several differences are evident. The greatest relative change in the ozone density occurs at 75 km in Figure 3.7 as compared to 70 km in Figure 3.2. There is also a sunrise variation at 80 km which is not indicated in Figure 3.2, and the variation becomes smaller at altitudes above 80 km. In all, the general difference from Figure 3.2 in Figure 3.7 is a upward shift of several kilometers of the nighttime ozone peak (relative to the postsunrise ozone densities). In Figure 3.2 the ozone distributions represent presunrise and 'noon' values, which will be different from the postsunrise values of Figure 3.7 because of the nonequilibrium behavior of the ozone after sunrise. Continuing the calculation to noon in Figure 3.7 would probably not reproduce the noon values of Figure 3.2 because the oxygen chemistry, although sufficient for a sunrise calculation (Section 4.2), cannot adequately describe the long-term behavior of the ozone. A correction for this effect has been incorporated in the $O_2(^1\Delta)$ density calculations of Section 4.5 where the ozone distributions of Figure 3.7 were used. One shortcoming of this work is that the daytime nonequilibrium ozone behavior is not fully accounted for in the absorption model. But this can be compensated to a great degree by adjusting the ozone model parameters used in the calculations.

In Figures 3.8 and 3.9 the atomic oxygen densities for uniform and nonuniform absorption respectively are shown. There are no drastic differences in the two sets of curves. However, the atomic oxygen rise is slower for the nonuniform case, Figure 3.9. At altitudes below 80 km the nonuniform O density will be as much as 60% below its equivalent uniform value, and these smaller values of n(O) can last for many degrees. In effect, with the reduced ozone dissociation rates during sunrise the O densities build toward smaller postsunrise equilibrium values in the nonuniform case.

At the highest altitudes, 80 km and above, there is hardly any change in the O densities over sunrise. Below 80 km the sunrise O densities are very sensitive to the O_3 dissociation rates, J_3. Even for the smallest values of J_3 at the largest zenith angles near geometrical sunrise, the density of O is greater than 10^6 cm^{-3} early in the sunrise for altitudes below 75 km. After a very rapid initial rise, the atomic oxygen increases more slowly with J_3 and J_2 until the photoequilibrium values are achieved. The fine structure in the curves is due primarily to the structure of the photorates J_3. Although some of these details are probably model-induced, the general behavior of the curves is clearly delineated.

Below 75 km if one desires to completely specify the atomic oxygen densities at sunrise for values less than about 10^6 cm^{-3}, the ozone photodissociation rates have to be specified over a greater range of zenith angles, well into the presunrise region. Molecular oxygen dissociation is unimportant in this region as it is over much of the sunrise. Several effects could be considered. First, refraction should be included in the calculation at low grazing heights (minimum ray heights). Secondly, near h = 0 there is a geometrical effect due to the finite size of the sun, as it rises above the horizon. In the solution, about one degree of arc will be affected by this geometrical effect. Finally, the scattered twilight radiation densities should be estimated in order to obtain the photorates in the presunrise region. Since the dissociating radiation in this part of the sunrise is very low energy, the atomic and molecular oxygen produced will be primarily in the ground state. In addition, the atomic oxygen densities in the presunrise region will be very small, and will increase rapidly near the geometrical sunrise. In fact, the curves of Figures 3.8 and 3.9 could probably be extrapolated to the presunrise values without too much difficulty.

It is clear from Figure 3.10 that the differences in the O/O_3 density ratio between the uniform and nonuniform absorption cases is more pronounced than the corresponding O density differences. The O/O_3 ratio is a parameter which can be useful in determining the electron density under certain conditions, where the processes of associative detachment by O and charge exchange with O_3 compete in the destruction of O_2^-. If $O/O_3 < 1$ it has only a small effect on the electron density. Below 65 km in Figure 3.10 the O/O_3 ratio is less than one at all solar zenith angles. At 65 km and above the ratio does attain values greater than one. In the nonuniform case the points at which $O/O_3 = 1$ are delayed by about 1° at 75 km to about 3° at 65 km. At 80 km and above there is little variation in the O/O_3 ratios, which have large values.

It can be concluded that for altitudes from 60 to 80 kilometers at sunrise some important D-region processes will be affected by the extra absorption of the night-to-day ozone layer. At large solar zenith angles the direct absorption of u.v. radiation by the ozone in its Hartley band will influence the photodetachment of D-region negative ions, especially those with electron affinities in the 3-4 e.v. range. The 'softening' of the atomic oxygen sunrise increase discussed above will result in a slower initial production of electrons by associative detachment at sunrise. The importance of atomic oxygen with respect to its other reactions will likewise be altered. In particular, the conversion of CO_3^- to O_2^- (a significant D-region reaction) will be dampened at sunrise. There will also be an alteration in the production of the metastable excited specie $O_2(^1\Delta_g)$ because the sunrise variations in O_3 and J_3 are greatly changed by the extra ozone absorption (see Section 4.5 where the $O_2(^1\Delta)$ problem is formulated). All these effects are included in the analysis of the D region which follows.

4. MINOR CONSTITUENTS IN THE D REGION

The development of the lower D-region ionization at sunrise can be attributed to the presence of solar radiation both through its direct effects of ionization and detachment and its indirect effect on the minor constituents which react with the charged species. A study of the behavior of the minor constituents over sunrise is therefore necessary. In the previous sections a detailed investigation of O and O_3 was carried out. However, a complete description of the sunrise should account for the behavior of other minor constituents such as NO and H_2O, and excited species such as $O_2(^1\Delta)$.

4.1 Oxygen Species

The excited metastable oxygen species can play a significant role in the formation of the D region as well as in its investigation. Excited oxygen species give rise to dayglow and nightglow radiation bands which can be used to measure their abundance, and so provide an experimental link to the oxygen chemistry. Even though the density ratio of excited to unexcited states for a specie is very small, excited atoms and molecules are chemically very active and may provide important channels for atmospheric processes. The most important ground state and metastable oxygen species which will be considered here are, in spectroscopic notation, $O(^3P)$, $O(^1D)$, $O_2(X\ ^3\Sigma_g^-)$, $O_2(a^1\Delta_g)$, and $O_2(b^1\Sigma_g^+)$. The left superscript in each case is the spin degeneracy, 2S+1, where S is the total electron spin of the state. For the O_2 states the capital Greek letter indicates the component of the total orbital angular momentum along the internuclear axis. In addition, for homonuclear diatomic molecules the - or + indicates whether or not the wave function changes sign upon an inversion through any plane which contains the internuclear axis, and a g or u (for 'gerade' or 'ungerade') indicates whether the state is even or odd under a reflection through the plane which perpendicularly bisects the internuclear axis. The molecular notation orders the electronic states with the letters X, A, B,... Thus, X $^3\Sigma_g^-$ is the ground state, and a $^1\Delta_g$ and b $^1\Sigma_g^+$ are the first two excited singlet states of molecular oxygen. In atomic notation, ^3P and ^1D are the ground and first excited states of atomic oxygen. For molecular species each electronic state also has a vibrational and rotational spectrum, vibrational excitations generally being in the near infrared and rotational in the far infrared.

Hunt (1965a) argued that the net loss of ozone in the D region through the action of the O_2 excited species was negligible because these reactions are nonterminating and are slow relative to the photolysis of ozone. Thus the reactions

$$\begin{aligned} O_2(^1\Delta) + O_3 &\xrightarrow{k_{4a}} 2O_2 + O \\ O_2(^1\Sigma) + O_3 &\xrightarrow{k_{4b}} 2O_2 + O \end{aligned} \qquad (4.1)$$

(where the simplified notation $O_2 \equiv O_2(^3\Sigma)$, $O \equiv O(^3P)$ is being used) destroy ozone much slower than photolysis, and produce atomic oxygen which then regenerates ozone. Hunt let the prefactor values of k_{4a} and k_{4b} range between 10^{-14} and 10^{-12} (k_{4a} also exhibits an activation energy of 2.6 kcal in Hunt's work). Note: as previously mentioned all reaction rate constants are in the cm-sec units. A value of k_{4b} as large as $7\text{x}10^{-12}$ has been quoted in Snelling and Hampson (1968). However, since Hunt (1965a) may have overestimated the densities of excited species of O_2 his conclusions remain essentially correct. Then reactions (4.1) may be ignored in the photochemistry of ozone. Snelling and Hampson (1968) further showed that reaction k_{4b} is unimportant in the atmosphere as a quenching reaction for $O_2(^1\Sigma)$.

The important sources of oxygen metastables are listed below

$$\begin{aligned}
&O_3 + h\nu \xrightarrow{J_{3b}} O_2(^1\Delta) + O(^1D) \;;\; \lambda < 3100\text{Å} \\
&O_3 + h\nu \xrightarrow{J'_{3b}} O_2(^1\Sigma) + O(^1D) \;;\; \lambda < 2670\text{Å} \\
&O(^1D) + O_2 \xrightarrow{k_{5b}} O + O_2(^1\Delta) \\
&O(^1D) + O_2 \xrightarrow{k_{5c}} O + O_2(^1\Sigma) \\
&O_2(^1\Sigma) + M \xrightarrow{k_{6b}} O_2(^1\Delta) + M \\
&O + O + M \xrightarrow{k'_1} O_2(^1\Delta) + M \\
&O_2 + h\nu \xrightarrow{J_{2b}} O + O(^1D) \;;\; \lambda < 1750\text{Å} \;.
\end{aligned} \tag{4.2}$$

The excited species are quenched by the following set of reactions

$$\begin{aligned}
&O_2(^1\Sigma) + M \xrightarrow{k_6} O_2 + M \\
&O_2(^1\Delta) + M \xrightarrow{k_7} O_2 + M \\
&O_2(^1\Delta) \xrightarrow{A_1} O_2 + h\nu \;;\; \lambda = 12{,}700\text{Å} \\
&O_2(^1\Sigma) \xrightarrow{A_2} O_2 + h\nu \;;\; \lambda = 7710\text{Å} \\
&O_2(^1\Delta) + O \xrightarrow{k_{7a}} O_2 + O \\
&O_2(^1\Delta) + O_3 \xrightarrow{k_{7b}} O_2 + O_3 \\
&O_2(^1\Sigma) + O_3 \xrightarrow{k_{6a}} O_2 + O_3
\end{aligned} \tag{4.3}$$

$$O(^1D) + M \xrightarrow{k_{5a}} O + M$$

$$O(^1D) + O_3 \xrightarrow{k_8} 2O_2 \quad .$$

The values of the Einstein spontaneous emission coefficients are $A_1 = 2.6\text{x}10^{-4}$ $\sec^{-1}$ and $A_2 = .14 \sec^{-1}$. The rate constants for the above reactions are discussed in Hunt (1965a), Gattinger (1968), Snelling and Hampson (1968), Evans et al. (1968), and DASA (1967). Figure 4.1 illustrates the daytime distributions of the excited species in the D region and is based on the work of Evans et al. (1968), Gattinger (1968), Wallace and Hunten (1968), and Hunt (1966), with a correction factor for Evan's data as quoted in Hunten and McElroy (1969). Even though the $O(^1D)$ concentration is quite small, Hesstvedt (1968) shows values smaller still by two orders of magnitude. At night in the D region there is virtually no $O(^1D)$, and the densities of $O_2(^1\Delta)$ and $O_2(^1\Sigma)$ are extremely small below 85 km.

In the daytime the principle source of excited species is the photodissociation of ozone in its Hartley band. At higher altitudes, the dissociation of molecular oxygen in the Schumann-Runge bands and continuum also produces $O(^1D)$. The loss rates for the excited molecules are determined by their radiative lifetimes and collisional de-excitation. At night the main sources of oxygen excitation are through O-O and O-O_3 recombination, whereas the quenching remains almost unaffected. In the presunrise D region one would therefore expect to find only small quantities of excited species.

Referring to Figures 3.6 and 3.7, and nothing that the bulk of the ozone dissociation is in its Hartley band $\lambda < 3000$Å, one might conclude that excited

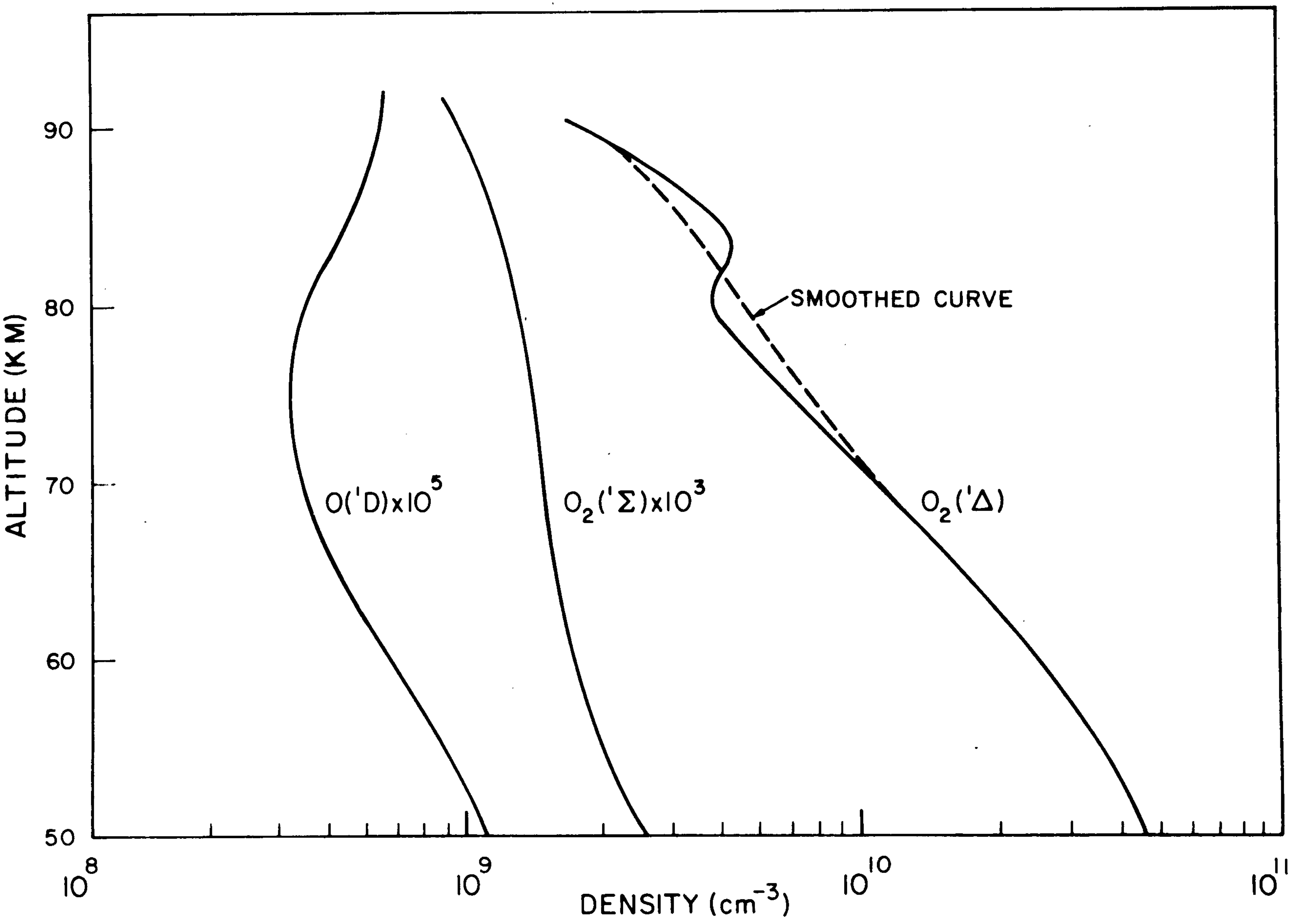

Figure 4.1 Daytime distributions of excited species in the D region.

species will not be produced in the D region until the O_3 dissociation rate jumps to near its daytime value. In Figure 3.7 this corresponds to the time when the ozone distribution begins to decrease rapidly. However, such a conclusion may not be true at some altitudes, and will be discussed in Section 4.5 (see Figures 4.5 and 4.6).

Hunten and McElroy (1968) suggest that excited oxygen molecules can be a source of electrons and O_2^+ ions in the D region comparable to the source of ionization of NO by Lyman α. $O_2(^1\Delta)$ has an ionization threshold which is about 1 eV lower than that of ground state O_2. This extends the ionization spectrum from 1027 to 1118Å. Some very recent measurements by Huffman et al. (1970) of the absorption by CO_2 in the O_2 windows implies, however, that the $O_2(^1\Delta)$ source of ionization is not as important in the D region. Hunten and McElroy (1968) assumed a constant ionization cross section of 10^{-18} cm^2. As Huffman points out this oversimplification will lead to an over estimation of the $O_2(^1\Delta)$ ionization rate. It would appear that the ionization of $O_2(^1\Delta)$ will not compete with NO ionization as a source of electrons during the day, and will not produce large quantities of O_2^+ in the D region. Hunten and McElroy also suggest that $O_2(^1\Delta)$ is important in the chemistry of NO (see Equation 4.22).

Krassovsky (1969) points out that vibrationally excited ground state O_2 molecules (denoted O_2^*) might be an important ionization source. O_2^* is produced in the reaction

$$O_3 + O \xrightarrow{k_3^*} O_2(^1\Delta) + O_2^* \qquad (4.4)$$

and is partially responsible for the observed hydroxyl emission by the transfer of excitation in its reaction with atomic hydrogen (see (4.18)). O_2^* may be ionized by wavelengths as long as 1540Å, and O_2^* densities predicted on the bas of hydroxyl emissions are not less than 10^8 cm^{-3}. However, because of the lack of data for the chemistry of vibrationally excited species their role in D-region behavior is questionable, although potentially important. Even if the presunrise densities of O_2^* are large it is doubtful that any substantial ionization would result early in sunrise because the short wavelength radiation is strongly attenuated. However O_2^* would lead to an earlier production of electrons than $O_2(^1\Delta)$ could even though $O_2(^1\Delta)$ is produced from ozone in the 2000-3000Å range since its ionization threshold is at 1118Å, and that of O_2^* is at 1540Å.

It has recently been found by Hudson et al. (1969) that predissociation of O_2 in the Schumann-Runge bands can effectively increase the atomic oxygen production above 70 km. The process is

$$O_2(^3\Sigma) + h\nu \rightarrow O_2(B\ ^3\Sigma_u^-)_{v'>2} \xrightarrow{J'_{2b}} O + O(^1D) \qquad (4.5)$$

with $\lambda > 1750$Å, and the vibrational levels indicated by v'. The effect of this additional atomic oxygen production is largest at 85 km and very much smaller at other altitudes. Since above 80 km there is very little diurnal variation in the atomic oxygen concentrations one would not consider this process important in this analysis, especially at sunrise. However, it should be included in any photochemical scheme for atomic oxygen since it effectively increases the diurnal average O quantities. No correction factors will be assumed here for the presunrise O and O_3 densities of Hunt (1966) or Hesstvedt (1968) for example, since their results are at least in fair agreement with experimental measurements (Smith, 1969).

Excited molecular oxygen leads to the airglow emissions

$$O_2(^1\Delta) \rightarrow O_2(^3\Sigma)_{v'=0} + h\nu \ ; \ \lambda = 12{,}700\text{Å},\ 1.27\mu$$
$$O_2(^1\Delta) \rightarrow O_2(^3\Sigma)_{v'=1} + h\nu \ ; \ \lambda = 15{,}800\text{Å},\ 1.58\mu \qquad (4.6)$$

which have been used to measure the densities of $O_2(^1\Delta)$ in the atmosphere (Gattinger 1968; Evans et al. 1968). Atomic oxygen emissions are

$$O(^1D) \xrightarrow{A_3} O(^3P) + h\nu \ ; \ 6300,\ 6364\text{Å (Red line multiplet)}$$
$$O(^1S) \xrightarrow{A_4} O(^1D) + h\nu \ ; \ 5577\text{Å (Green line)} \qquad (4.7)$$

where $A_3 = 9.1 \times 10^{-3}$ sec^{-1} and $A_4 = 1.4$ sec^{-1}. The ^1S atomic oxygen can be formed by

$$O + O + O \xrightarrow{k_{9a}} O_2 + O(^1S) \qquad \text{(Chapman Process)}$$
$$N + O + O \xrightarrow{k_{9b}} NO + O(^1S) \qquad (4.8)$$
$$\left.\begin{array}{l} O + O + M \longrightarrow O_2(A\ ^3\Sigma_u^+) + M \\ O_2(A\ ^3\Sigma_u^+) + O \longrightarrow O_2 + O(^1S) \end{array}\right\} \text{(Barth Process)}\ .$$

There is still much controversy as to which source of $O(^1S)$ is most important or if others exist. Hesstvedt (1968) showed that the Chapman process agreed well with green line emission observations. The ^1S state is almost exclusively radiatively deactivated.

In Table 4.1 the 'oxygen' reactions introduced to this point are tabulated. The reference they were obtained from (not necessarily the original source)

Table 4.1 Reaction rates for neutral oxygen reactions

REACTION	RATE CONSTANT	SOURCE
$O_2 + h\nu \rightarrow O + O$	J_2 ; $\lambda < 2424$ Å	
$O_3 + h\nu \rightarrow O_2 + O$	J_3 ; $\lambda < 11{,}800$ Å	
$O + O + M \rightarrow O_2 + M$	$k_1 = 3.3\text{x}10^{-33}(\frac{T}{300})^{-2.9}$	DASA (1967)
$\rightarrow O_2(^1\Delta) + M$	$k_1' = k_1/5$	Gattinger (1968)
$O + O_2 + M \rightarrow O_3 + M$	$k_2 = 5.5\text{x}10^{-34}(\frac{T}{300})^{-2.5}$	DASA (1967)
$O + O_3 \rightarrow O_2 + O_2$	$k_3 = 1.4\text{x}10^{-12}e^{-1500/T}$	DASA (1967)
$O_2(^1\Delta) + O_3 \rightarrow 2O_2 + O$	$k_{4a} = 2.5\text{x}10^{-15}$	Snelling & Hampson (1968)
$O_2(^1\Sigma) + O_3 \rightarrow 2O_2 + O$	$k_{4b} = 6.0\text{x}10^{-13}$	DASA (1967)
$O(^1D) + M \rightarrow O + M$	$k_{5a} = 5.0\text{x}10^{-11}$	DASA (1967)
$O(^1D) + O_2 \rightarrow O + O_2(^1\Delta)$	$k_{5b} = 1.0\text{x}10^{-12}$	DASA (1967)
$O(^1D) + O_2 \rightarrow O + O_2(^1\Sigma)$	$k_{5c} = 1.5\text{x}10^{-11}$	Snelling & Hampson (1968)
$O_2(^1\Sigma) + M \rightarrow O_2 + M$	$k_6 = 10^{-14}$	Text
$O_2(^1\Sigma) + O_3 \rightarrow O_2 + O_3$	$k_{6a} = 1.7\text{x}10^{-14}$	Gattinger (1968)
$O_2(^1\Sigma) + M \rightarrow O_2(^1\Delta) + M$	$k_{6b} = 2.0\text{x}10^{-15}$	Snelling & Hampson (1968)
$O_2(^1\Delta) + M \rightarrow O_2 + M$	$k_7 = 1.0\text{x}10^{-19}$	DASA (1967)
$O_2(^1\Delta) + O \rightarrow O_2 + O$	$k_{7a} = 2.0\text{x}10^{-14}$	DASA (1967)
$O_2(^1\Delta) + O_3 \rightarrow O_2 + O_3$	$k_{7b} < 1.7\text{x}10^{-14}$	Gattinger (1968)
$O(^1D) + O_3 \rightarrow O_2 + O_2$	$k_8 = 1.0\text{x}10^{-11}$	Text
$O + O + O \rightarrow O_2 + O(^1S)$	$k_{9a} = 1.5\text{x}10^{-34}$	DASA (1967)
$N + O + O \rightarrow NO + O(^1S)$	$k_{9b} = 3.0\text{x}10^{-33}$	DASA (1967)
$O_2(^1\Delta) \rightarrow O_2 + h\nu$	$A_1 = 2.6\text{x}10^{-4}$ sec^{-1}	Evans _et al_. (1968)
$O_2(^1\Sigma) \rightarrow O_2 + h\nu$	$A_2 = .14$ sec^{-1}	DASA (1967)
$O(^1D) \rightarrow O + h\nu$	$A_3 = 9.1\text{x}10^{-3}$ sec^{-1}	DASA (1967)
$O(^1S) \rightarrow O(^1D) + h\nu$	$A_4 = 1.4$ sec^{-1}	DASA (1967)

is also shown. In the cases where 'Text' is written after the rate constant it indicates that an average value, based on those quoted by several authors, has been selected because of a large disparity in the rates.

With the exception of reaction (9b) only reactions involving oxygen allotropes have been introduced here. In subsequent sections the oxygen-hydrogen and oxygen-nitrogen reaction schemes will be discussed. Basically, the chemistry of the excited oxygen species is described by the reactions in Table 4.1. The effect of a more complex chemistry is primarily an increase in the quenching of the excited species, since more reaction channels are inevitably added. The relative importance of excited specie reactions in the formation of the ionized D region will be discussed further.

4.2 Oxygen-Hydrogen Reactions

When one considers the many possible reactions between oxygen and hydrogen compounds, as well as excited species and radiation interactions, the oxygen photochemistry becomes quite involved (Hunt 1966; Hesstvedt 1968; Shimazaki and Laird 1969, 1970). In some altitude ranges only certain reactions need to be considered, and the day and nighttime chemistries may be quite different. In a few cases a reaction will be unimportant under all achievable conditions (Hesstvedt 1969). Some researchers have also found that entire chemical systems may be analyzed independently, such as the oxygen-hydrogen, oxygen-nitrogen systems (Hesstvedt and Jansson 1969; Nicolet 1965a).

In Table 4.2 the important hydrogen reactions for a wet ozone photochemical theory are listed. The photodissociation of H_2 and OH is not included since the wavelength limit for this process is about 1100Å in both cases. No cross section data are available for HO_2, but it is assumed that HO_2 and H_2O_2 have approximately the same dissociation rate (Hunt 1966). The altitude

Table 4.2 Oxygen-hydrogen reactions

REACTION	RATE CONSTANT	SOURCE
$H_2O + h\nu \rightarrow OH + H$	J_4 ; $\lambda < 2390\text{Å}$ + Lyα	
$H_2O_2 + h\nu \rightarrow OH + OH$	J_5 ; $\lambda < 5650\text{Å}$	
$HO_2 + h\nu \rightarrow OH + O$	J_6	
$H + O_3 \rightarrow OH + O_2$	$k_{10a} = 2.6\text{x}10^{-11}$	Hunt (1966)
$\rightarrow HO_2 + O$	$k_{10b} = 2.0\text{x}10^{-10}\ e^{-2000/T}$	Hesstvedt (1969)
$OH + O \rightarrow H + O_2$	$k_{11} = 5.0\text{x}10^{-11}$	Hunt (1966)
$OH + O_3 \rightarrow HO_2 + O_2$	$k_{12} = 5.0\text{x}10^{-13}$	Hunt (1966)
$OH + OH \rightarrow H_2O + O$	$k_{13} = 2.0\text{x}10^{-12}$	Hesstvedt (1969)
$OH + HO_2 \rightarrow H_2O + O_2$	$k_{14} = 1.0\text{x}10^{-11}$	Hunt (1966)
$OH + H \rightarrow H_2 + O$	$k_{15} = 3.0\text{x}10^{-11}e^{-4150/T}$	Hesstvedt (1969)
$OH + H_2 \rightarrow H_2O + H$	$k_{16} = 1.0\text{x}10^{-10}e^{-2950/T}$	Hesstvedt (1969)
$OH + H_2O_2 \rightarrow H_2O + HO_2$	$k_{17} = 4.0\text{x}10^{-13}$	Hunt (1966)
$H + HO_2 \rightarrow H_2 + O_2$	$k_{18a} = 3.0\text{x}10^{-12}$	Hesstvedt (1969)
$\rightarrow OH + OH$	$k_{18b} = 3.0\text{x}10^{-12}$	Hesstvedt (1969)
$\rightarrow H_2O + O$	$k_{18c} = 2.0\text{x}10^{-10}e^{-2000/T}$	Hesstvedt (1969)
$H + H_2O_2 \rightarrow H_2 + HO_2$	$k_{19a} = 1.0\text{x}10^{-13}$	Hunt (1966)
$\rightarrow H_2\ O + OH$	$k_{19b} = 5.0\text{x}10^{-12}\sqrt{T}e^{-3000/T}$	Gattinger (1968)
$H + O_2 \rightarrow OH + O$	$k_{20} = 1.0\text{x}10^{-9}e^{-8400/T}$	Hesstvedt (1969)
$H + O_2 + M \rightarrow HO_2 + M$	$k_{21} = 3.0\text{x}10^{-32}(\frac{273}{T})^{1.3}$	Hesstvedt (1969)
$H + OH + M \rightarrow H_2O + M$	$k_{22} = 2.5\text{x}10^{-31}$	Hunt (1966)
$H + H + M \rightarrow H_2 + M$	$k_{23} = 1.2\text{x}10^{-32}(\frac{273}{T})^{.7}$	Hesstvedt (1969)
$H + O + M \rightarrow OH + M$	$k_{24} = 8.0\text{x}10^{-33}$	Hesstvedt (1969)
$HO_2 + O \rightarrow OH + O_2$	$k_{25} = 1.0\text{x}10^{-11}$	DASA (1967)
$HO_2 + O_3 \rightarrow OH + O_2 + O_2$	$k_{26} = 1.0\text{x}10^{-14}$	Hunt (1966)
$HO_2 + HO_2 \rightarrow H_2O_2 + O_2$	$k_{27} = 1.5\text{x}10^{-12}$	Hesstvedt (1969)

Table 4.2 Oxygen-hydrogen reactions (continued)

REACTION	RATE CONSTANT	SOURCE
$H_2O_2 + O \rightarrow OH + HO_2$	$k_{28a} = 1.0 \times 10^{-15}$	Hunt (1966)
$\rightarrow H_2O + O_2$	$k_{28b} = 1.0 \times 10^{-15}$	Gattinger (1968)
$H_2 + O \rightarrow OH + H$	$k_{29} = 7.0 \times 10^{-11} e^{-5100/T}$	Hesstvedt (1969)
$OH + O + M \rightarrow HO_2 + M$	$k_{30} = 1.4 \times 10^{-31}$	Hunt (1966)
$O(^1D) + H_2 \rightarrow OH + H$	$k_{31} = 2.0 \times 10^{-10}$	Snelling & Hampson (1968)
$O(^1D) + H_2O \rightarrow OH + OH$	$k_{32} = 2.0 \times 10^{-10}$	Snelling & Hampson (1968)

FR

behavior of the hydrogen species for day and night conditions (solid and dashed lines) is illustrated in Figure 4.2. The data were obtained from the theoretical work of Hunt (1966), Hesstvedt (1969), and Shimazaki and Laird (1969, 1970) who used essentially the chemical scheme of Table 4.2 as well as eddy transport effects (Hesstvedt, Shimazaki and Laird). Hunt incorporated a humidity mixing ratio of $2.5\text{x}10^{-6}$ gms/gm (that is, grams of H_2O when all hydrogen compounds are reduced to water, to grams of atmosphere, per unit volume) and Hesstvedt used a ratio of $5.0\text{x}10^{-6}$ g/g. These correspond approximately to number density mixing ratios of $5\text{x}10^{-6}$ and 10^{-5} respectively. Shimizaki and Laird (1969,1970) appear to have used a mixing ratio about one order of magnitude smaller, and consequently their calculated hydrogen compound densities are generally smaller than those of Hunt and Hesstvedt.

Since the sunrise behavior is being studied in this work, one only needs to consider those species which will be significant to the D-region neutral or ion chemistry at sunrise. Of particular importance is the effect of the hydrogen chemistry on atomic oxygen and ozone. One notes that the hydrogen reactions provide an additional loss mechanism for ozone which will not vary much from night through sunrise, and which will be small in the daytime compared to ozone photolysis. Some atomic oxygen will be produced early in the sunrise by the dissociation of HO_2 because of its long wavelength limit, but again the amount will be much smaller than that produced by ozone photodissociation at long wavelengths since at low altitudes $n(O_3) >> n(HO_2)$ and at high altitudes neither process is important.

In order to assess further the effects of the hydrogen chemistry on the O and O_3 sunrise behaviors that were determined using a simple all-oxygen model, one can study the time constants for the important oxygen-hydrogen

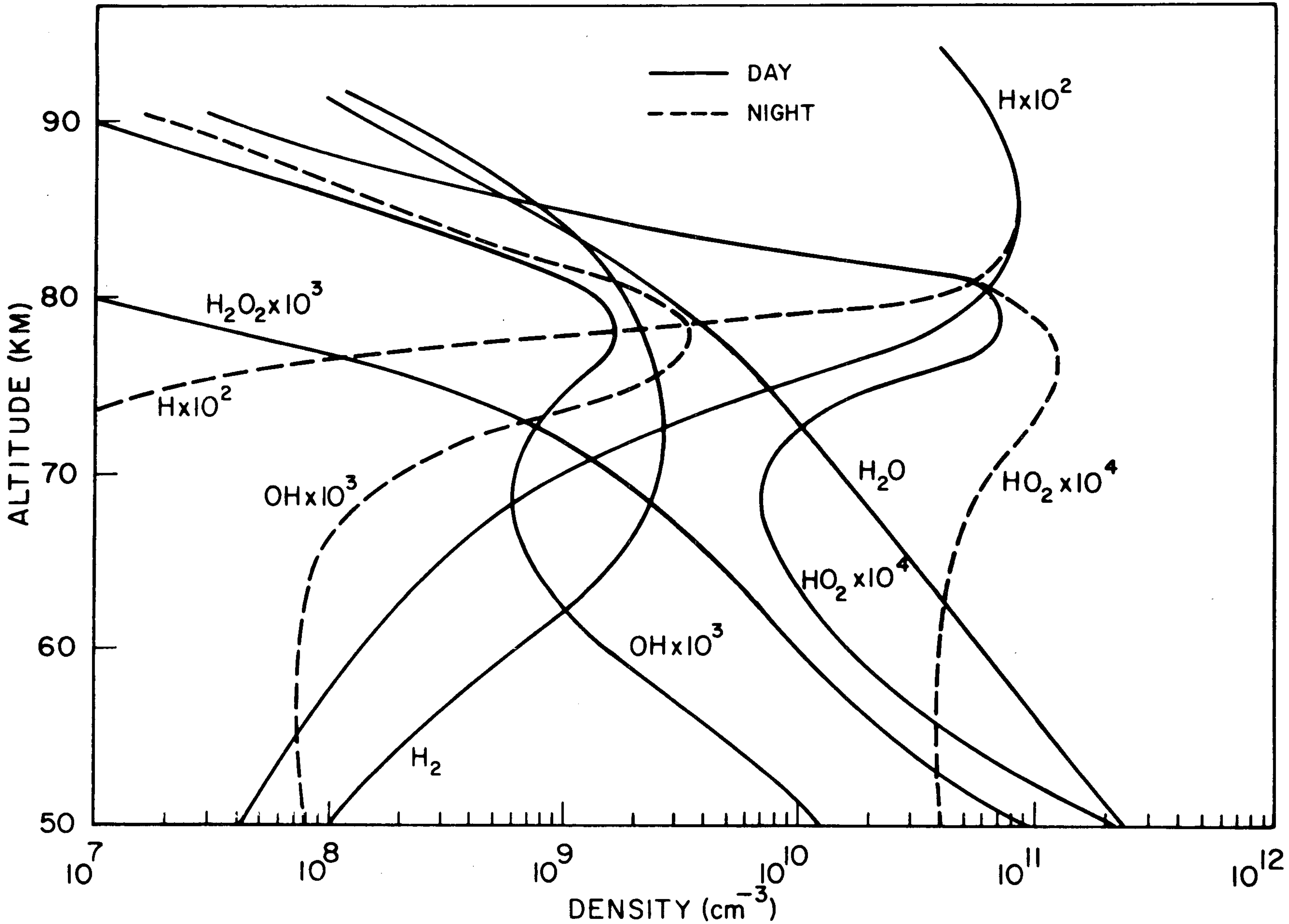

Figure 4.2 Distribution of hydrogen compounds in the D region.

reactions in the D region. First, consider the continuity equation for the ith constituent in a chemical system consisting of the set of species $\{n_j\}$

$$\dot{n}_i = P_i(n_j) - L_i(n_j) \tag{4.9}$$

where it will be assumed that an equilibrium or quasi-equilibrium state exists such that the set of values $\{n_j^{(0)}\}$ satisfies: $P_i(n_j^{(0)}) = L_i(n_j^{(0)})$. Under these conditions one defines the 'exponential' lifetime or time constant for a small perturbation in n_i by

$$\frac{1}{\tau_i} = \left.\frac{\partial L_i}{\partial n_i}\right|_{\{n_j^{(0)}\}} \quad . \tag{4.10}$$

The time constant for a particular loss process for the specie i involving the specie k is

$$\frac{1}{\tau_{ik}} = \left.\frac{\partial L_{ik}}{\partial n_i}\right|_{\{n_j^{(0)}\}} \tag{4.11}$$

where L_{ik} is the particular loss process, and where

$$\frac{1}{\tau_i} = \sum_k \frac{1}{\tau_{ik}} \tag{4.12}$$

when

$$L_i = \sum_k L_{ik} \quad .$$

To describe roughly the transient behavior of n_i if another specie, n_k, is perturbed one uses the definition

$$\frac{1}{\tau_i^k} = \frac{\partial}{\partial n_k} (P_i - L_i) \left.\vphantom{\frac{1}{1}}\right|_{\{n_j^{(0)}\}} \tag{4.13}$$

where $|\tau_i^k|$ is the time it would take the change in n_i (+ or -) to equal the perturbation of n_k if the transition proceeded at its initial rate.

One can now determine the dominant sunrise processes by using the density and rate data in Tables 3.1, 3.2, 3.6 and 4.2 and Figure 4.2 during sunrise the atomic oxygen production is dominated by ozone, and then O_2, photodissociation Below 75 km the loss rates for O and O_3 due to the oxygen-only reactions are more than an order of magnitude faster than the oxygen-hydrogen loss rates (the three-body recombination of atomic oxygen, $O + O_2 + M$, is of the order of minutes while the two-body reactions of O with O_3, OH, and HO_2 and of O_3 with H are at least of the order of hours).

Above 75 km the oxygen-only and oxygen-hydrogen atmosphere loss rates can be comparable. But at these altitudes both the O and O_3 have a very small or negligible sunrise variation. The O loss rates here have time constants of at least several hours so that any change in the O densities will be sluggish. The total ozone-hydrogen loss rate is nearly constant over the sunrise and can be simply corrected in the continuity equations by including an additional loss term (as in Section 3.2.2). These loss rates are chosen so that the pre-sunrise ozone densities are in equilibrium since they are certainly in quasi-equilibrium. Around 75 km the following conditions hold: The atomic oxygen loss rate due to oxygen reactions (on the order of an inverse hour) represents 60 to 80% of the total O loss rate over sunrise. The ozone loss rate (and an even greater percentage of the total loss rate during sunrise) by photolysis is about 85% of the total O_3 daytime loss rate.

The hydrogen species will have definite long-term effects on the atomic oxygen and ozone distributions, but at sunrise in the D region the all-oxygen model represented by Equations (3.5) is quite adequate. The greatest error, near 75 km, will cause a slight overestimation in the O and O_3 densities but will not significantly alter their sunrise behavior. The results of Chapter 3 are therefore valid and need not be amended by introducing a more complicated chemical scheme.

One can estimate the maximum change in the equilibrium value of a specie n_i, δn_i, that would result from a change in the equilibrium value of a specie n_k, δn_k, when δn_k is known and fixed, say, as the measured or calculated difference in the night and day equilibrium values of n_k. One first defines

$$\frac{1}{\bar{\tau}_i^k} = \frac{1}{\tau_i} + \frac{\delta n_k}{n_i^{(0)}} \frac{\partial L_i}{\partial n_k}\bigg|_{\{n_j^{(0)}\}} \quad . \tag{4.14}$$

Then

$$\delta n_i = \frac{\bar{\tau}_i^k}{\tau_i^k}\, \delta n_k \tag{4.15}$$

unless an important n_i^2 recombination process exists, in which case

$$\delta n_i = \frac{1}{2\alpha\bar{\tau}_i^k}\left\{\left[1 + 4\alpha\bar{\tau}_i^k \frac{\bar{\tau}_i^k}{\tau_i^k}\,\delta n_k\right]^{1/2} - 1\right\} \tag{4.16}$$

where α is the coefficient of the process. These equations hold for any size perturbation. If the change δn_i is to be significant compared to δn_k, $|\bar{\tau}_i^k| \sim |\tau_i^k|$. For $|\bar{\tau}_i^k| << |\tau_i^k|$ the specie k does not affect the chemistry of i very much. In addition, when one considers the photodissociation rates (by setting $n_k \rightarrow J_k$) it is found that for species such as O and O_3 the sunrise change in the photochemistry is dominated by this process rather than by the purely chemical changes involving the hydrogen reactions. In Appendix VII an example showing the effects of the various time constants on the atomic oxygen growth at sunrise is given. These calculations substantiate the arguments presented here.

It may be concluded from the discussion above that hydrogen plays only a minor role in the sunrise formation of the neutral D region. Most studies of the ionized mesosphere such as Radicella (1968a) and Gunton (1969) also show hydrogen to have little direct effect on the ionized constituents. However, water-derived compounds will be considered again when the formation of D-region positive ions is outlined. It is also believed to be important that water vapor can lead to the production of hydrated negative ions.

Of all the reactions in Table 4.2 a few are more important than the others. Among these are the reactions described by the rates k_{10a}, k_{11}, k_{20}, k_{21}, k_{25} and k_{26}, which include the reactions just discussed above. In essence, one does not consider the slower oxygen-hydrogen reactions in this scheme (Radicella and Stowe, 1970). The hydroxyl excitation mechanisms are a part of these reactions though, and are,

$$\begin{aligned} H + O_3 &\xrightarrow{k_{10a}} OH^* + O_2 \\ O_2^* + H &\xrightarrow{k'_{20}} OH^* + O \text{ (Krassovsky process)} \end{aligned} \tag{4.17}$$

where each vibrationally excited hydroxyl molecule emits several photons in the Meinel airglow bands (Hunt, 1966, assumes 6 photons; Hesstvedt, 1968, 4 photons). Because of the uncertainties in the O_2^* excitation-de-excitation reactions however, it is difficult to evaluate the importance of the Krassovsky process to the hydroxyl airglow. Hesstvedt (1968) concludes that it is negligible in the D region.

4.3 Oxygen-Nitrogen Reactions

Nitrogen compounds are of great importance in the D region. Uncertainties in their densities and reaction schemes can lead to ambiguities in the behavior of the D region. The reactions between oxygen and nitrogen species have only a small effect on the distribution of the oxygen allotropes (Hesstvedt and Jansson, 1969), but the ion chemistry of the mesosphere is critically dependent on species such as NO and NO_2. However, experimental and theoretical nitric oxide distributions have not yet been completely resolved. Figure 4.3 illustrates some of the proposed and measured NO densities. Nicolet's (1965b) values include the effects of the positive ion chemistry at higher altitudes, which increases the NO content significantly (and more so at greater altitudes). The Mitra (1968) distribution might be erroneously small for the D region. As proposed by Mitra, it is

$$n(NO) = 4\times10^{-1} e^{-\frac{3700}{T}} n(O_2) + 5\times10^{-7} n(O) \tag{4.18}$$

and was designed to fit the results deduced from several measurements of positive ion densities as well as a limited version of the photochemistry of nitric oxide. The values of Barth (1966b), Nicolet (1965b), and Hesstvedt and Jansson (1969) agree quite well, but Shimazaki and Laird's (1969) results are smaller. Pearce's (1969) revised (i.e. decreased by a factor of 5) measurements are larger, and may reflect some seasonal variation in the nitric oxide. The profile defined by Barth's 85 km value of 4.0×10^{7} cm^{-3} with a constant mixing ratio is larger than any of the other distributions.

Also illustrated in Figure 4.3 is a very recent measurement of nitric oxide by Meira (1970) who used the same NO detection technique as Barth and Pearce (i.e. airglow intensity) but a much more detailed data reduction scheme. The results show a marked depression in the NO density near 85 km, and subsequently lower values of NO below 85 km. Above 85 km the distribution appears to be

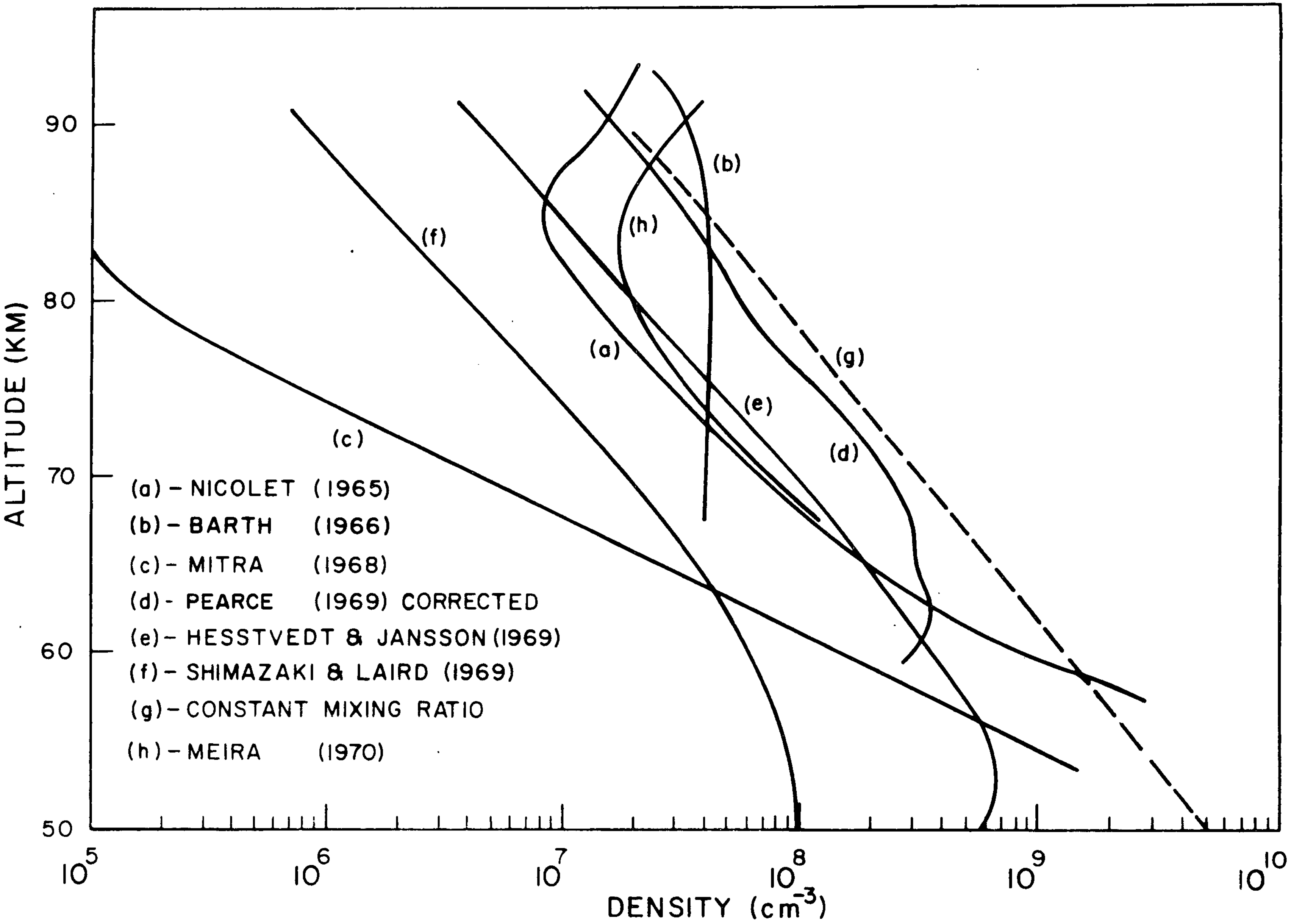

Figure 4.3 Distribution of nitric oxide in the D region.

in photochemical equilibrium while below 85 km mixing would seem to predominate (Meira, 1970). The distribution can be compared to Nicolet's (1965b) values. Meira's (1970) NO values are presumed to be more reliable than Barth's or Pearce's.

The nitrogen compounds in the atmosphere are dissociated by solar radiation as follows

$$\begin{aligned} &N_2 + h\nu \xrightarrow{J_7} N + N \ ; \ \lambda < 1260\text{Å} \\ &NO + h\nu \xrightarrow{J_8} N + O \ ; \ \lambda < 1910\text{Å} \\ &NO_2 + h\nu \xrightarrow{J_9} NO + O \ ; \ \lambda < 3975\text{Å} \\ &N_2O + h\nu \xrightarrow{J_{10a}} N_2 + O \ ; \ \lambda < 7360\text{Å} \\ &\qquad\qquad \xrightarrow{J_{10b}} NO + N \ ; \ \lambda < 2500\text{Å} \ . \end{aligned} \tag{4.19}$$

There are several processes with long wavelength limits, for NO_2 and N_2O, which could be important at sunrise if their zero optical depth rates were large. Atomic nitrogen production will be delayed from sunrise since it is a high energy process. In the nighttime D region there is little atomic nitrogen so that N can have little effect early in sunrise. Some of the reactions of atomic nitrogen which are pertinent to the photochemistry of the mesosphere are

$$\begin{aligned} &N + NO \xrightarrow{k_{33}} N_2 + O \\ &N + O_2 \xrightarrow{k_{34}} NO + O \\ &N + O_3 \xrightarrow{k_{35}} NO + O_2 \\ &N + O + M \xrightarrow{k_{36}} NO + M \ . \end{aligned} \tag{4.20}$$

Hunten and McElroy (1968) have also suggested reaction (34) with excited oxygen molecules

$$N + O_2(^1\Delta) \xrightarrow{k'_{34}} NO + O \quad . \tag{4.21}$$

They argue that k'_{34} is large since the extra 1 ev of energy carried by the $O_2(^1\Delta)$ will effectively overcome the activation energy of k_{34}. This reaction has recently been shown to be unimportant (Strobel et al., 1970), with the reaction of molecular oxygen and excited nitrogen atoms being dominant.

Other reactions of known importance are

$$\begin{aligned} &NO + O + M \xrightarrow{k_{37}} NO_2 + M \\ &NO + O_3 \xrightarrow{k_{38}} NO_2 + O_2 \\ &NO_2 + O \xrightarrow{k_{39}} NO + O_2 \quad . \end{aligned} \tag{4.22}$$

The following radiative recombination processes also occur

$$\begin{aligned} &N + O \xrightarrow{k_{40}} NO + h\nu \\ &NO + O \xrightarrow{k_{41}} NO_2 + h\nu \\ &N_2 + O \xrightarrow{k_{42}} N_2O + h\nu \quad . \end{aligned} \tag{4.23}$$

Some other reactions of less aeronomic importance, as well as those listed above, are summarized with their rate constants in Table 4.3 . Nicolet (1965a) has also discussed reactions of the higher order oxides of nitrogen (NO_3, N_2O_5, etc.) and concludes that they may have some stratospheric significance at night. These compounds are ignored here.

Figure 4.4 shows the day and nighttime distributions of nitrogen compounds in the D region (solid and dashed curves). These data are essentially from

Table 4.3 Oxygen-nitrogen reactions

REACTION	RATE CONSTANT	SOURCE
$N_2 + h\nu \rightarrow N + N$	J_7 ; $\lambda < 1260\text{Å}$	
$NO + h\nu \rightarrow N + O$	J_8 ; $\lambda < 1910\text{Å}$	
$NO_2 + h\nu \rightarrow NO + O$	J_9 ; $\lambda < 3975\text{Å}$	
$N_2O + h\nu \rightarrow N_2 + O$	J_{10a} ; $\lambda < 7360\text{Å}$	
$\rightarrow NO + N$	J_{10b} ; $\lambda < 2500\text{Å}$	
$N + NO \rightarrow N_2 + O$	$k_{33} = 2.2\text{x}10^{-11}$	DASA (1967)
$N + O_2 \rightarrow NO + O$	$k_{34} = 1.0\text{x}10^{-16}T^{3/2}e^{-3300/T}$	Hesstvedt & Jansson (1969
$N + O_2(^1\Delta) \rightarrow NO + O$	$k'_{34} = 1.0\text{x}10^{-13}$(estimate)	Hunten & McElroy (1968)
$N + O_3 \rightarrow NO + O_2$	$k_{35} = 2.0\text{x}10^{-12}T^{1/2}e^{-1200/T}$	Nicolet (1965a)
$N + O + M \rightarrow NO + M$	$k_{36} = 1.1\text{x}10^{-32}(\frac{T}{300})^{-0.5}$	DASA (1967)
$NO + O + M \rightarrow NO_2 + M$	$k_{37} = 1.0\text{x}10^{-31}(\frac{T}{300})^{-2.5}$	DASA (1967)
$NO + O_3 \rightarrow NO_2 + O_2$	$k_{38} = 8.0\text{x}10^{-13}e^{-1200/T}$	Hesstvedt & Jansson (196
$NO_2 + O \rightarrow NO + O_2$	$k_{39} = 3.0\text{x}10^{-11}e^{-530/T}$	Hesstvedt & Jansson (196
$N + O \rightarrow NO + h\nu$	$k_{40} = 2.0\text{x}10^{-17}$	DASA (1967)
$NO + O \rightarrow NO_2 + h\nu$	$k_{41} = 6.4\text{x}10^{-17}$	Hesstvedt & Jansson (196
$N_2 + O \rightarrow N_2O + h\nu$	$k_{42} = 1.0\text{x}10^{-24}$	Hesstvedt & Jansson (196
$N + NO_2 \rightarrow N_2 + O_2$	$k_{43a} = 1.5\text{x}10^{-11}$	DASA (1967)
$\rightarrow NO + NO$	$k_{43b} = 3.0\text{x}10^{-12}$	DASA (1967)
$\rightarrow N_2O + O$	$k_{43c} = 1.5\text{x}10^{-13}$	DASA (1967)
$N + N + M \rightarrow N_2 + M$	$k_{44} = 5\text{x}10^{-33}(\frac{T}{300})^{-2.0}$	DASA (1967)
$N_2 + O + M \rightarrow N_2O + M$	$k_{45} = 1.0\text{x}10^{-34}e^{-7500/T}$	DASA (1967)

e.3

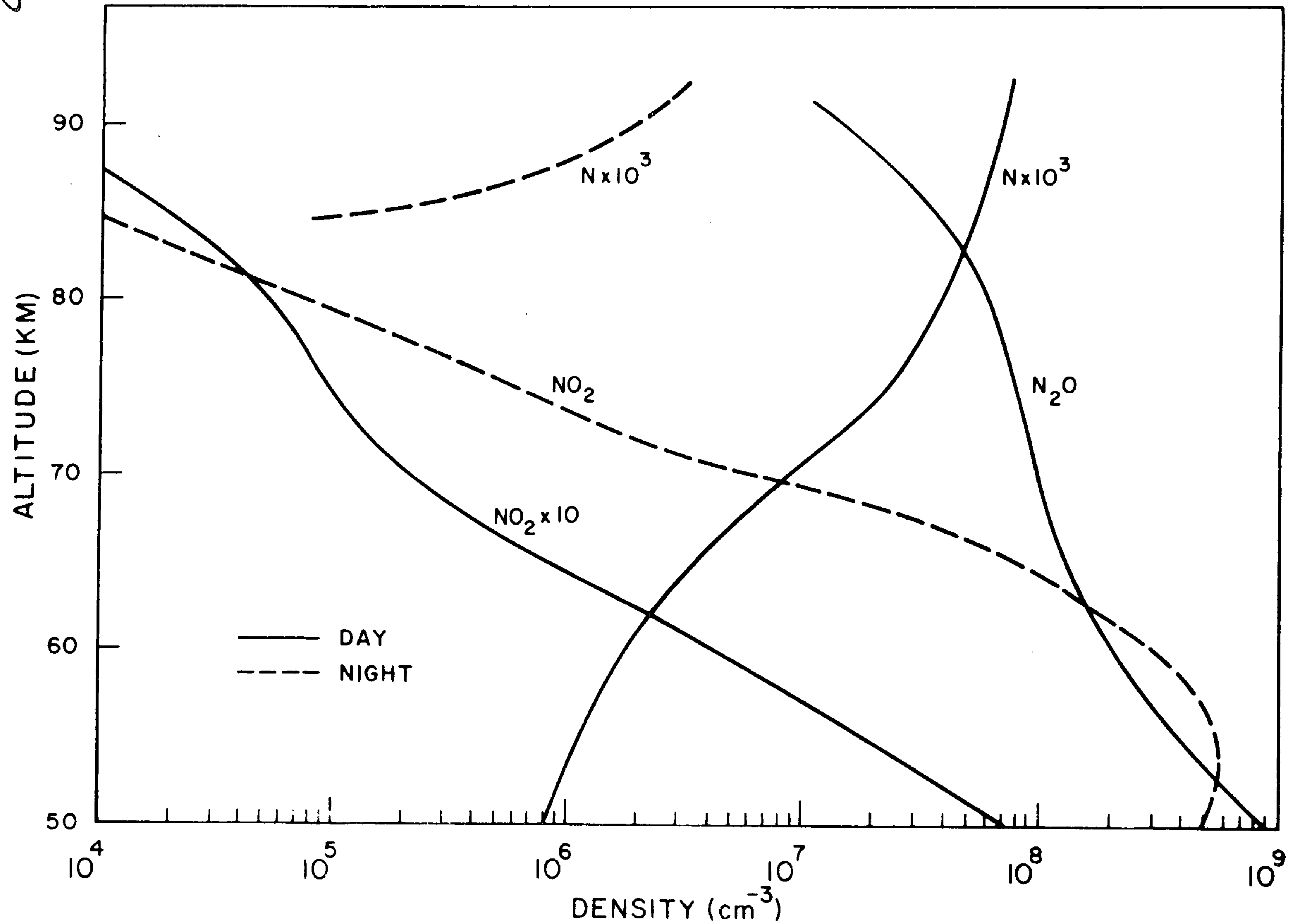

Figure 4.4 Distribution of nitrogen compounds in the D region.

the results of Hesstvedt and Jansson (1969), which agree well with the results of Shimazaki and Laird (1969, 1970). As is expected, only small amounts of atomic nitrogen exist below 90 km. The large amounts of N_2O at low altitudes could serve as an early source of atomic oxygen at sunrise, but the competition with ozone as a source would make it seem insignificant. The reduction in NO_2 during sunrise will only have a small effect on the negative ion chemistry for those times. It is not shown in Figure 4.4 that at the lower altitudes all the NO is converted to NO_2 at night. Because this diurnal effect takes place below 65 km, the NO variation at sunrise has a negligible effect on the formation of the C layer. LeLevier and Branscomb (1968) found that the electron concentration in the D region would be inversely proportional to the NO concentration in the daytime. The nitric oxide, which rapidly converts electrons into terminal ions, competes with atomic oxygen which effectively detaches electrons. It is possible that the form of the C layer is partially produced by this effect of the NO distribution. However, the ion chemistry scheme which will be considered here is more complex than that used by LeLevier and Branscomb, and such a simple result as they obtained will probably not be valid at all altitudes in this case.

The excited nitrogen species could also be studied. Atomic and molecular nitrogen and nitric oxide have numerous electronic and vibrational excitations, but as Nicolet (1965b) points out, these are probably of little aeronomic importance. The airglow of NO lies in the so-called γ bands between 2000-2500Å (vibrational levels of the electronic transition $A^2\Sigma^+ - X^2\Pi$) and can be excited by the pre-association of N and O. This airglow has been used to measure NO in the atmosphere (Barth, 1966a and b; Pearce, 1969; Meira, 1970).

4.4 Other Minor Neutral Constituents in the D Region

Nicolet (1965a) outlined the nitrogen-hydrogen reactions which might be of interest in atmospheric studies. Among these are

$$\begin{aligned} &H + NO_2 \xrightarrow{k_{46}} NO + OH \\ &NO + HO_2 \xrightarrow{k_{47}} OH + NO_2 \\ &NO + H_2O_2 \xrightarrow{k_{48}} HNO_2 + OH \quad . \end{aligned} \tag{4.24}$$

These reactions are all unimportant when compared to the equivalent reactions involving O and O_3. Also, in the reaction cycles

$$\left.\begin{aligned} &N + NO + M \rightarrow HNO + M \\ &H + HNO \rightarrow NO + H_2 \\ &OH + HNO \rightarrow NO + H_2O \\ &HO_2 + HNO \rightarrow NO + H_2O_2 \end{aligned}\right\} k_{49a} - k_{49d}$$

$$\left.\begin{aligned} &NO_2 + H + M \rightarrow HNO_2 + M \\ &NO + OH + M \rightarrow HNO_2 + M \\ &H + HNO_2 \rightarrow H_2 + NO_2 \\ &OH + HNO_2 \rightarrow H_2O + NO_2 \end{aligned}\right\} k_{50a} - k_{50d} \tag{4.25}$$

$$\left.\begin{aligned} &NO_2 + OH + M \rightarrow HNO_3 + M \\ &NO + HO_2 + M \rightarrow HNO_3 + M \\ &H + HNO_3 \rightarrow H_2O + NO_2 \\ &OH + HNO_3 \rightarrow H_2O + NO_3 \end{aligned}\right\} k_{51a} - k_{51d}$$

the loss processes for the hydrogen compounds are negligible compared to the equivalent processes with O, O_2, and O_3; and NO_2 only plays the role of a catalyst, while NO losses from reactions (50) and (51) are recovered from the other nitrogen oxides that are produced. The overall effect is that the chemical schemes of the two previous sections are not severely perturbed by these reactions.

Snelling and Hampson (1968) report that the reaction of excited atomic oxygen and methane is fast

$$O(^1D) + CH_4 \xrightarrow{k_{52}} CH_3 + OH \tag{4.26}$$

with $k_{52} = 2x10^{-10}$. But the complete methane reaction chain is quite complex and incompletely known, and the importance of hydrocarbons in an oxygen-hydrogen atmosphere has yet to be ascertained. In a sunrise analysis this reaction can certainly be ignored.

Carbon dioxide is a plentiful minor constituent whose chemistry is not well known either. A very basic reaction sequence is

$$\begin{aligned} CO_2 + h\nu &\xrightarrow{J_{11}} CO + O \; ; \; \lambda < 1690\text{Å} \\ CO + O + M &\xrightarrow{k_{53}} CO_2 + M \end{aligned} \tag{4.27}$$

where $k_{53} < 8x10^{-35}$ has been determined. In this work a constant mixing ratio will be assumed for carbon dioxide, so that

$$n(CO_2) = 3x10^{-4}\ n(M) \tag{4.28}$$

for day and night.

A potentially important set of minor constituents in the D region are water vapor clusters of the form $(H_2O)_n$. Stable clusters with positive ions attached could act as very effective electron recombination traps. Such a cluster could have a large cross section reacting at the gas kinetic rate. Likewise, negative ion clusters might play the role of terminating ions in the lower mesosphere. The detection of noctilucent clouds in the D region seems to confirm that water vapor condensation is present. However, without a fully developed chemistry for such clusters their real significance cannot be determined.

4.5 Photodissociation and Density Data for the Minor Constituents

In Tables 4.4 and 4.5 the minor constituent densities are tabulated at 2.5 kilometer intervals between 50 and 90 kilometers. These data were obtained from Figures 4.1-4.4. In Table 4.4 for nighttime conditions all the constituents which have little or no diurnal variation are listed rather than in Table 4.5 for daytime conditions. It should be noted that $O(^1D)$ is not present at night, $O_2(^1\Delta)$ is present in very small quantities at night, and N_2O is absent in the daytime. Also, the H_2O_2 nighttime densities will be assumed to be the same as those in Table 4.5, even though the night densities may vary by about ± an order of magnitude from these values. The nitric oxide below 65 km disappears at night, being converted into NO_2. The nitric oxide values in the tables are representative of the higher values of curves (a), (b), (d), and (e) from Figure 4.3. The ambiguity in the NO density can lead to a wide variation in the electron production rate at high altitudes. The nitric oxide density will therefore be considered as variable in this study.

The behavior of $O_2(^1\Delta)$ is a factor in determining the sunrise development of the electron density. Rather than solving the complicated set of coupled continuity equations for the minor constituents including $O_2(^1\Delta)$, a simplified solution will be developed. One assumes that $O_2(^1\Delta)$ is produced primarily by the dissociation of ozone in its Hartley band. Using reactions k_{5b} and

Table 4.4 Nighttime minor constituent distributions in the D region

Alt, km	H_2O	H_2	H	OH	HO_2	NO	N	NO_2	N_2O
50	2.4(11)*	1.0(8)	---	7.8(4)	4.0(6)	---	---	4.8(8)	9.0(8)
52.5	1.7(11)	1.5(8)	---	7.4(4)	3.9(6)	---	---	5.6(8)	6.0(8)
55	1.2(11)	2.3(8)	---	7.2(4)	3.8(6)	---	---	5.7(8)	4.0(8)
57.5	8.3(10)	3.7(8)	---	7.3(4)	3.8(6)	2.0(4)	---	4.7(8)	2.8(8)
60	6.0(10)	6.4(8)	---	7.5(4)	4.0(6)	2.0(5)	---	3.0(8)	2.0(8)
62.5	4.3(10)	1.0(9)	---	7.9(4)	4.1(6)	2.0(7)	---	1.7(8)	1.6(8)
65	3.0(10)	1.7(9)	---	8.9(4)	4.5(6)	8.5(7)	---	8.0(7)	1.3(8)
67.5	2.1(10)	2.2(9)	---	1.2(5)	5.2(6)	1.1(8)	---	3.0(7)	1.1(8)
70	1.5(10)	2.6(9)	---	2.0(5)	6.5(6)	1.2(8)	---	6.5(6)	1.0(8)
72.5	1.1(10)	2.7(9)	---	5.0(5)	9.2(6)	1.0(8)	---	1.6(6)	8.8(7)
75	7.6(9)	2.6(9)	2.0(5)	2.0(6)	1.2(7)	7.0(7)	---	6.0(5)	8.0(7)
77.5	4.8(9)	2.2(9)	6.0(6)	3.5(6)	1.2(7)	4.8(7)	---	2.2(5)	7.4(7)
80	2.8(9)	1.8(9)	3.5(8)	2.4(6)	7.5(6)	3.5(7)	---	7.0(4)	6.4(7)
82.5	1.5(9)	1.3(9)	7.3(8)	7.5(5)	1.2(6)	2.5(7)	---	2.5(4)	5.0(7)
85	7.0(8)	8.0(8)	8.3(8)	2.0(5)	1.0(5)	1.8(7)	1.6(2)	9.5(3)	3.7(7)
87.5	3.2(8)	4.3(8)	7.9(8)	7.0(4)	1.5(4)	1.3(7)	8.0(2)	---	2.4(7)
90	1.5(8)	2.0(8)	6.7(8)	2.0(4)	4.0(3)	1.0(7)	2.0(3)	---	1.5(7)

*2.4(11) $\equiv 2.4 \times 10^{11}$

Table 4.5 Daytime minor constituent distributions in the D region

Alt, km	$O_2(^1\Delta)$	$O(^1D)$	H	OH	HO_2	H_2O_2	NO	N	NO_2
50	4.6(10)	1.0(4)	4.2(5)	1.2(7)	2.1(7)	1.0(8)	1.1(9)	8.0(2)	7.0(6)
52.5	4.2(10)	9.0(3)	5.5(5)	8.0(6)	1.0(7)	4.5(7)	9.6(8)	9.5(2)	3.5(6)
55	3.6(10)	8.0(3)	7.5(5)	5.0(6)	5.0(6)	2.5(7)	8.0(8)	1.2(3)	1.7(6)
57.5	3.1(10)	6.8(3)	1.0(6)	2.7(6)	2.7(6)	1.5(7)	6.5(8)	1.4(3)	9.0(5)
60	2.5(10)	5.8(3)	1.4(6)	1.5(6)	1.6(6)	1.0(7)	5.0(8)	1.8(3)	4.3(5)
62.5	2.1(10)	4.9(3)	2.0(6)	1.0(6)	1.1(6)	7.0(6)	3.8(8)	2.5(3)	2.0(5)
65	1.6(10)	4.2(3)	3.0(6)	7.3(5)	8.5(5)	4.5(6)	2.8(8)	3.5(3)	8.0(4)
67.5	1.3(10)	3.8(3)	4.5(6)	6.0(5)	7.1(5)	2.8(6)	2.0(8)	5.4(3)	4.0(4)
70	1.0(10)	3.5(3)	1.0(7)	6.2(5)	7.1(5)	1.5(6)	1.4(8)	8.5(3)	2.0(4)
72.5	8.2(9)	3.3(3)	2.4(7)	7.3(5)	9.6(5)	8.0(5)	1.0(8)	1.5(4)	1.3(4)
75	6.7(9)	3.2(3)	6.6(7)	1.1(6)	2.5(6)	3.0(5)	7.0(7)	2.3(4)	9.4(3)
77.5	5.5(9)	3.3(3)	2.5(8)	1.6(6)	6.6(6)	6.0(4)	4.8(7)	3.0(4)	7.2(3)
80	4.6(9)	3.5(3)	5.6(8)	1.4(6)	6.8(6)	1.0(4)	3.5(7)	4.0(4)	5.0(3)
82.5	3.9(9)	4.0(3)	7.7(8)	5.4(5)	1.2(6)	---	2.5(7)	4.7(4)	3.5(3)
85	3.2(9)	4.3(3)	8.3(8)	1.5(5)	1.0(5)	---	1.8(7)	5.6(4)	2.0(3)
87.5	2.5(9)	5.1(3)	7.9(8)	5.0(4)	1.5(4)	---	1.3(7)	6.3(4)	1.0(3)
90	1.8(9)	5.5(3)	6.7(8)	1.0(4)	4.0(3)	---	1.0(7)	7.0(4)	---

k_{6b} of Table 4.1 and the densities of Figure 4.1 one can calculate that the $O(^1D)$ and $O_2(^1\Sigma)$ sources of $O_2(^1\Delta)$ would represent 50-80% of the total $O_2(^1\Delta)$ production rate during the daytime, the larger percentage applying at altitudes above 75 km. During sunrise, however, the densities of $O(^1D)$ and $O_2(^1\Sigma)$ will be smaller, and the ozone densities larger, generally, than their respective noon values. It may also be that these rates or the excited specie densities, or both, have been overestimated. For example, Hesstvedt (1968) has calculated $O(^1D)$ densities which are more than an order of magnitude smaller than those of Figure 4.1. For these reasons the assumption that only ozone photolysis produces $O_2(^1\Delta)$ is utilized here. The loss rate of $O_2(^1\Delta)$ by collisional de-excitation and spontaneous emission is essentially constant over sunrise and will be evaluated using the reactions in Table 4.1. One then has,

$$\dot{n}_\Delta = P_\Delta(t) - n_\Delta L_\Delta$$

with

$$L_\Delta = k_7 n_M + A_1 \tag{4.29}$$

$$P_\Delta = \eta_\Delta J_{3b} n_3 + P'_\Delta = \overline{P}_\Delta + P'_\Delta$$

where P'_Δ is the production of $O_2(^1\Delta)$ from the O-O reaction (1) and is important only above 75 km. P'_Δ therefore exhibits little diurnal change, so one can write

$$P'_\Delta = n^N_\Delta L_\Delta \tag{4.30}$$

where the superscript 'N' indicates night, and 'D' daytime values. The ozone and atomic oxygen collisional de-excitation reactions are not included in L_Δ because the large size of these rates is questionable (Zipf, 1969, quotes the values $k_{7a} < 10^{-15}$, $k_{2b} = 2\text{x}10^{-15}$). Since J_{3b} is essentially the dissociation rate of ozone in the Hartley band, and η_Δ can be interpreted as an effective quantum efficiency for $O_2(^1\Delta)$ production. Here it will be determined from the measured daytime densities of $O_2(^1\Delta)$ by

$$\eta_\Delta = \frac{(n_\Delta^D - n_\Delta^N) L_\Delta}{J_{3b}^D n_3^D} \quad . \tag{4.31}$$

The solution of (4.29) is

$$n_\Delta(t) = n_\Delta^N + \int_0^t dx e^{-xL_\Delta} \, \overline{P}_\Delta(t-x) \quad . \tag{4.32}$$

The integration must extend into the presunrise region where $\overline{P}_\Delta \to 0$.

It is interesting to note that the values of η_Δ below 75 km turn out to be about 0.2-0.3. The fact that η_Δ is of the right size and nearly constant at low altitudes indicates that the atmospheric model is probably accurate there, although the values of η_Δ themselves are only approximate. Above 75 km the η_Δ jump to unphysical values of about 1.3. This is partly due to the omission of the $O(^1D)$ and $O_2(^1\Sigma)$ sources of $O_2(^1\Delta)$ which are proportionately largest at these altitudes. In addition there are the possibilities of an error in the high altitude $O_2(^1\Delta)$ measurement, an underestimate in the high altitude ozone, or even another undiscovered source of $O_2(^1\Delta)$, all of which would help to resolve the discrepancies in the η_Δ. In all, the substitution of ozone photolysis as the total source of $O_2(^1\Delta)$ above 75 km is a rough approximation which is useful in calculating the $O_2(^1\Delta)$ behavior at sunrise. At these heights the effects of the $O_2(^1\Delta)$ on the charged species' sunrise will probably be small anyway. For example, as a means of detachment of electrons from O_2^-, $O_2(^1\Delta)$ can not compete with O above 75 km (see rates in Table 7.2). And as a source of ionization, $O_2(^1\Delta)$ will be less than the nitric oxide-Lyman α source (see Section 5.3 and Figure 5.1), and will appear later in the sunrise because of its shorter wavelength limit.

In Figures 4.5 and 4.6 the $O_2(^1\Delta)$ sunrise densities are illustrated for two ozone distributions. In both cases the densities have been normalized to the measurements of Evans et al. (1968) and were calculated using Equation (4.32) and the ozone dissociation rate of Figure 3.6. In Figure 4.5 the ozone distributions of Figure 3.7 were utilized, and in Figure 4.6 a simple ozone model which is presented in Chapter 8 was used.

One important feature of the calculations are the 65-75 km curves. The large rapid rise in the $O_2(^1\Delta)$ density at 70 km is a consequence of the large diurnal ozone variation at this height. The nighttime ozone layer is dense enough to reduce the uv radiation intensity by a factor of 20 or more, which effectively delays the ozone sunrise decay, but there is enough residual dissociation in the Hartley band to produce large quantities of $O_2(^1\Delta)$ from the large nighttime ozone densities. As sunrise progresses J_{3b} rises to its daytime value, the O_3 decays, and the $O_2(^1\Delta)$ density shifts towards the daytime equilibrium value. This behavior will be typical of the altitudes from 65-75 km where the largest diurnal ozone density change occurs.

The early $O_2(^1\Delta)$ rise effect at altitudes between 65 and 75 km partially offsets the delay in the ozone dissociation rate increase that one would expect to control the sunrise $O_2(^1\Delta)$ densities. Thus, excited molecular oxygen will be found in the sunrise region up to 95° (see Figures 4.5 and 4.6) the above discussion excludes any unusual wavelength dependence of the $O_2(^1\Delta)$ production which would invalidate the use of an effective η_Δ.

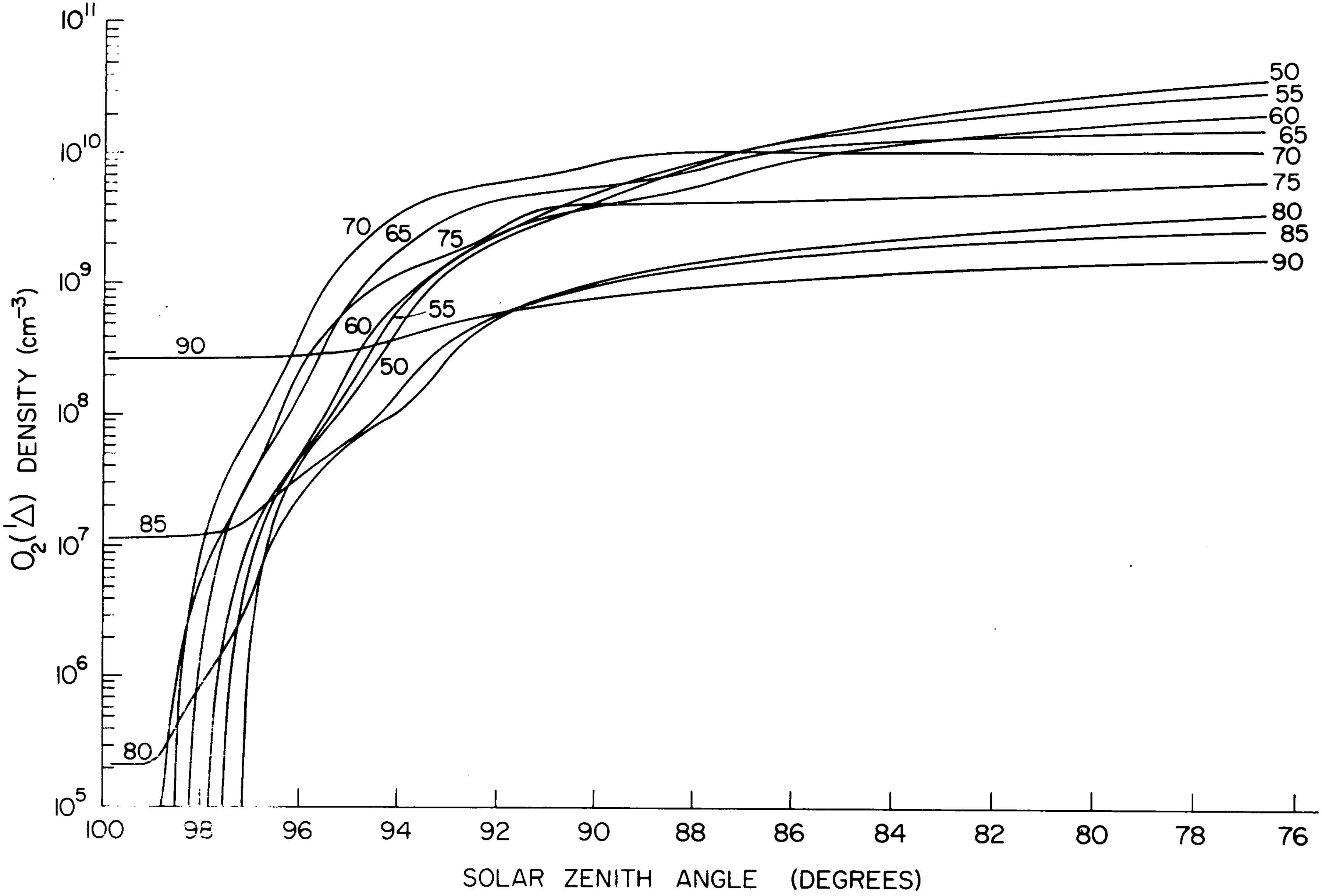

Figure 4.5 $O_2(^1\Delta)$ densities during sunrise.

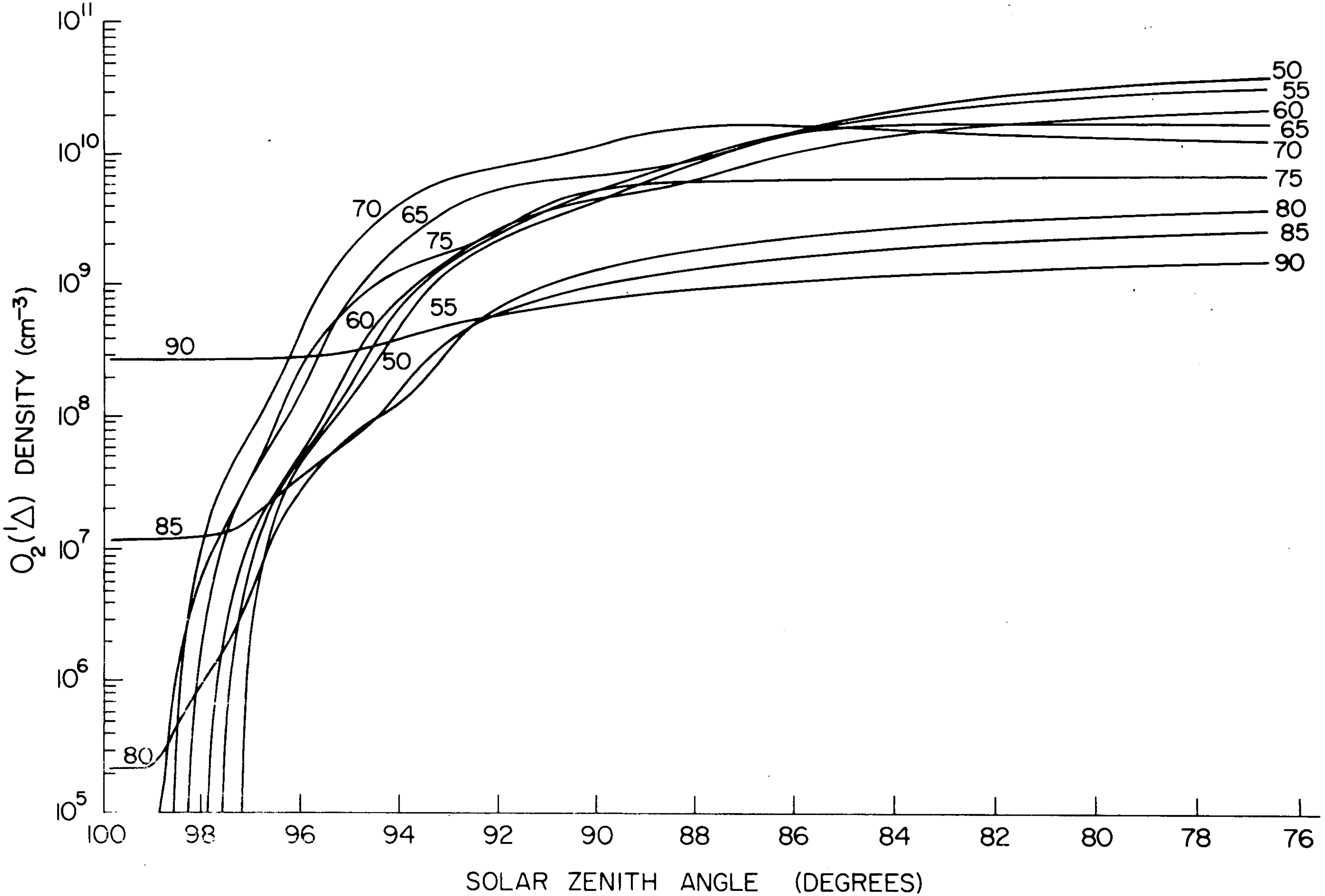

RC

Figure 4.6 $O_2(^1\Delta)$ densities during sunrise calculated using an ozone model.

The dissociation of other minor constituents at sunrise is not as critical in determining the sunrise electron densities. The variation of these constituents at sunrise can be calculated by using their continuity equations and solving a long set of coupled equations. In order to accomplish this the sunrise dissociation rates for these constituents must first be determined. In Table 4.6 the dissociation rates for the important D-region minor constituents are listed. The cross sections that are given (in Megabarns, 1 Mbarn = 10^{-18} cm^2) represent average or typical values for continuums, peak values for absorption bands, or the value of σ^a at a solar line. In Figure 4.7 the absorption cross sections of several minor constituents are reproduced (solid curves) for the wavelength region 1500-3000Å. Also shown is the incident solar flux in this wavelength range. Data has been obtained from Inn _et al_. (1953); Nakayama _et al_. (1959); Watanabe (1958); Nawrocki and Papa (1963); Shimazaki and Laird (1970).

The photodissociation rate of HO_2 in Table 4.6 is assumed to have the same size and spectral composition as that of H_2O_2 (Hunt 1966). For wavelengths longer than 1000Å both NO_2 and N_2 are assumed to have average cross sections of 1 Mbarn (Shimazaki and Laird, 1970). In the case of nitric oxide, the Lyman α ionization rate and photodissociation rate are comparable and are both effective NO loss processes. The long wavelength dissociation process of N_2O is undetermined. In calculating the other rates from the absorption cross sections a dissociation efficiency of 1 is taken.

Also plotted in Figure 4.7 are several differential dissociation rates, $dJ/d\lambda$, for zero optical depth. In the cases of H_2O and N_2O distinct peaks in the spectrum are found, and the dependence of the dissociation rate on zenith angle can be written

Table 4.6 Photodissociation rates for minor constituents

Process	Rate for τ=0, sec^{-1}	Absorption Spectrum, Å	Average cross section Mbarns	References
$J_{2b}: O_2 \rightarrow O + O(^1D)$	5.8×10^{-6}	$\lambda < 1750$	---	Shimazaki & Laird (1970)
$J_4: H_2O \rightarrow OH + H$	4.8×10^{-6}	1216, Line	14	Watanabe (1958) and
	9.8×10^{-6}	1650, band	4.8	Gattinger (1968)
$J_5: H_2O_2 \rightarrow 2OH$	1.7×10^{-4}	1900-2900	$\sim .1$	Gattinger (1968)
$J_6: HO_2 \rightarrow OH + O$	1.7×10^{-4}	---	---	Hunt (1966)
$J_7: N_2 \rightarrow N + N$	1.0×10^{-12}	$\lambda < 1260$	1.0	Shimazaki & Laird (1970)
$J_8: NO \rightarrow N + O$	9.5×10^{-8}	1216, Line	.35	Shimazaki & Laird (1970)
$NO^+ + e$	2.7×10^{-7}	1216, Line	1.0	and this work
$J_9: NO_2 \rightarrow NO + O$	5.0×10^{-3}	$\lambda < 3975$	---	Nicolet (1965a)
$J_{10a}: N_2O \rightarrow N_2 + O$	---	$\lambda < 7360$	---	----
$J_{10b}: N_2O \rightarrow NO + N$	3.0×10^{-6}	1800, band	.14	Shimazaki & Laird (1970)
		$\lambda < 1550$	---	
$J_{11}: CO_2 \rightarrow CO + O$	---	1400, bands	.60	Inn *et al.* (1953)
	---	1216, Line	.074	

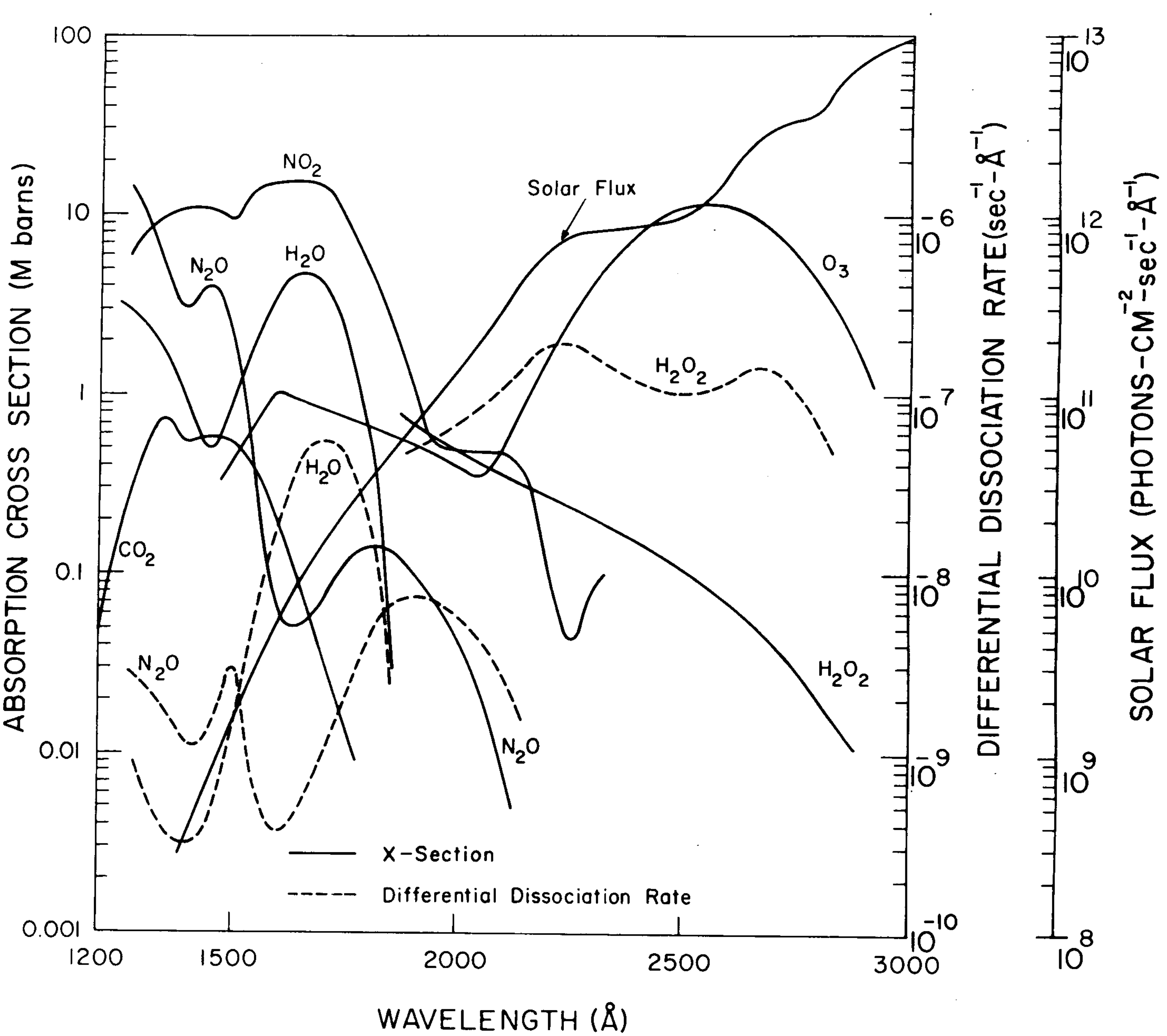

Figure 4.7 Absorption cross sections of the minor constituents in the near ultraviolet.

$$J(\chi) = J(\tau=0)\ e^{-\tau_0(\chi)} \tag{4.33}$$

where τ_0 is evaluated using cross sections for the major absorbers that correspond to average values in the vicinity of the peak in $dJ/d\lambda$. It is assumed that an average cross section can be defined in the vicinity of the peak, otherwise a detailed calculation would be necessary. For H_2O and N_2O the appropriate data are

$$\begin{aligned} H_2O &: \sigma_2 = 1.0\mathrm{x}10^{-18}\ ,\ \sigma_3 = 9.0\mathrm{x}10^{-19}\ ,\ \lambda_0 = 1700\text{Å} \\ N_2O &: \sigma_2 = 6.0\mathrm{x}10^{-22}\ ,\ \sigma_3 = 5.3\mathrm{x}10^{-19}\ ,\ \lambda_0 = 1900\text{Å}\quad . \end{aligned} \tag{4.34}$$

The dissociation spectrum for H_2O_2 is relatively flat. Thus the major contribution to its dissociation rate near sunrise will come where the atmospheric absorption is minimum, or around 2100Å in this case. The dissociation of NO_2 will show a similar dependence on wavelengths near 2100Å. Then Equation (4.33) can be applied for a rough calculation of both of these rates in the modified form

$$J(\chi) = J(\tau=0)\ e^{-\tau_0(\chi)+\tau_0(0)-\tau(0)} \tag{4.35}$$

where $\tau(0)$ is the equivalent optical depth of the total rate for an overhead sun. Equation (4.35) will overestimate the dissociation rate at sunrise.

For a sunrise analysis of the minor constituents the photodissociation rates specified above are sufficient even though they are approximate. It should be noted that the sunrise variation of any minor constituents which are important in the ion chemistry can be empirically specified on the basis of available diurnal studies, e.g. Gunton (1969), and Shimazaki and Laird (1970).

One important feature of the sunrise change in a minor constituent which can be deduced from its dissociation rate is the zenith angle at which the change has its onset. This fact, in conjunction with an empirical behavior during sunrise, can be used to completely determine the minor constituents' variations at sunrise. Applications of these ideas are made later.

5. IONIZATION SOURCES IN THE D REGION

There are several sources of ionization in the D region and they are the result of both radiation and particles penetrating the atmosphere. Solar and galactic cosmic rays are an important ionization source at low altitudes. During solar events solar cosmic rays can greatly perturb the D region even at low altitudes. But normally, it is galactic cosmic rays that produce the ionization of the lower D region both during the day and night (Moler, 1968). It has also been proposed that precipitating energetic electrons will ionize the upper D region, this ionization being significant at night (Radicella, 1968a).

Solar radiation at particular wavelengths ionizes the D region. Hydrogen Lyman-alpha near 1216Å ionizes nitric oxide with a high production rate. Until recently it had also been proposed (Hunten and McElroy, 1968) that $O_2(^1\Delta)$ which can be ionized for $\lambda < 1118$Å is an important ionization source in the upper D region. In addition, Lyman-beta, X-rays, and other ultraviolet radiations all contribute to the ionization of the upper daytime D region.

All of these ionization sources are discussed, and their relative importance for a sunrise analysis is decided. Generally, short wavelengths will not penetrate to the sunrise region, but will have to be included in the analysis to describe the entire night-to-day electron variation. Only the normal D region for quiet sun conditions at middle and low latitudes will be considered. Abnormal or disturbed conditions are not studied in this work.

5.1 Cosmic Ray Ionization

For quiet sun conditions solar cosmic ray ionization is negligible. However, galactic cosmic ray ion-pair production, assumed to have no diurnal variation at any given altitude, is an important D-region source of electrons and O_2^+ and N_2^+. Galactic cosmic rays are composed of about 92% protons (hydrogen nuclei) and 8% alpha particles (helium nuclei) (Nawrocki and Papa, 1963). These corpuscles, having energies >> 1 Bev, strip electrons from all the atmospheric constituents as they penetrate the atmosphere. High energy secondary particles (electrons, neutrons, and protons) produce a cascade of ionization. Detailed calculations of the production of thermalized electrons by galactic cosmic rays based on measured cosmic ray fluxes and cloud chamber yield rates have been done by Webber (1962). If it is assumed that the flux is vertically incident on the atmosphere and has an energy spectrum given by S(E), i.e. number cm^{-2} sec^{-1} $energy^{-1}$, and if one uses an empirical form for the energy loss of a primary with altitude

$$E(z) = Ee^{-\alpha\sigma H n_0(z)} \tag{5.1}$$

one can then proceed to establish the electron production rate

$$q_{CR}(z) = n_0(z) \int dE\ \sigma\ S(E)\ e^{-\frac{\sigma n_0(z)H}{N(E)}} \tag{5.2}$$

by setting $\alpha = 2/N(E)$, where N(E) is the average total electron yield for a primary particle of energy E, and σ is an effective inelastic collisional cross section of the atmospheric constituents with high energy particles for the production of electrons. Equation (5.1) shows that the particle energy decreases exponentially with the number of collisions. It is assumed in arriving at (5.2) that each effective collision leads to a thermal electron. Thus σ will be larger than the collisional cross section for the production of secondaries. The proportionality constant, α, was chosen so that the total electron production rate in a unit column is normalized

$$Q = \int q(z)dz = \int dE\ S(E)N(E)\ . \tag{5.3}$$

At higher altitudes, where $\sigma nH < 1$, one has the result that $q_{CR} \propto n$, which is known to be true. Equation (5.2) also predicts that the electron production profile for each small energy range will be like a Chapman layer.

The cosmic ray production has a magnetic latitude dependence because the earth's magnetic field channels the charged primary and secondary particles along the field lines, away from the equator. The net effect of this magnetoresistance at low latitudes is summarized in an empirical equation quoted by Radicella (1968a)

$$q_{CR} = 1.5\text{x}10^{-18}\ n_0(z)\ [\cos\tilde{\theta}_m]^{-4}[1-\frac{3}{22}(y-1964)] \tag{5.4}$$

where $\tilde{\theta}_m$ is the magnetic latitude and y is the year. The temporal variation is due to normal changes in solar activity, and will be ignored here in favor of Webber's (1962) calculations for solar minimum. The production rates for galactic cosmic rays are illustrated in Figure 5.1. The latitude variation will be assumed to be

$$\frac{q_{CR}(\tilde{\theta}_m)}{q_{CR}(\tilde{\theta}_{m0})} = (\frac{\cos\tilde{\theta}_{m0}}{\cos\tilde{\theta}_m})^n \tag{5.5}$$

with $\tilde{\theta}_{m0} \simeq 60°$ and $n = 4$. Also, for the altitudes of interest here

$$q_{CR}(z) = q_{CR}(z_0)\ \frac{n_0(z)}{n_0(z_0)}\ . \tag{5.6}$$

5.2 Nitric Oxide Ionization by Lyman α

Another important source of ionization in the D region at higher altitudes

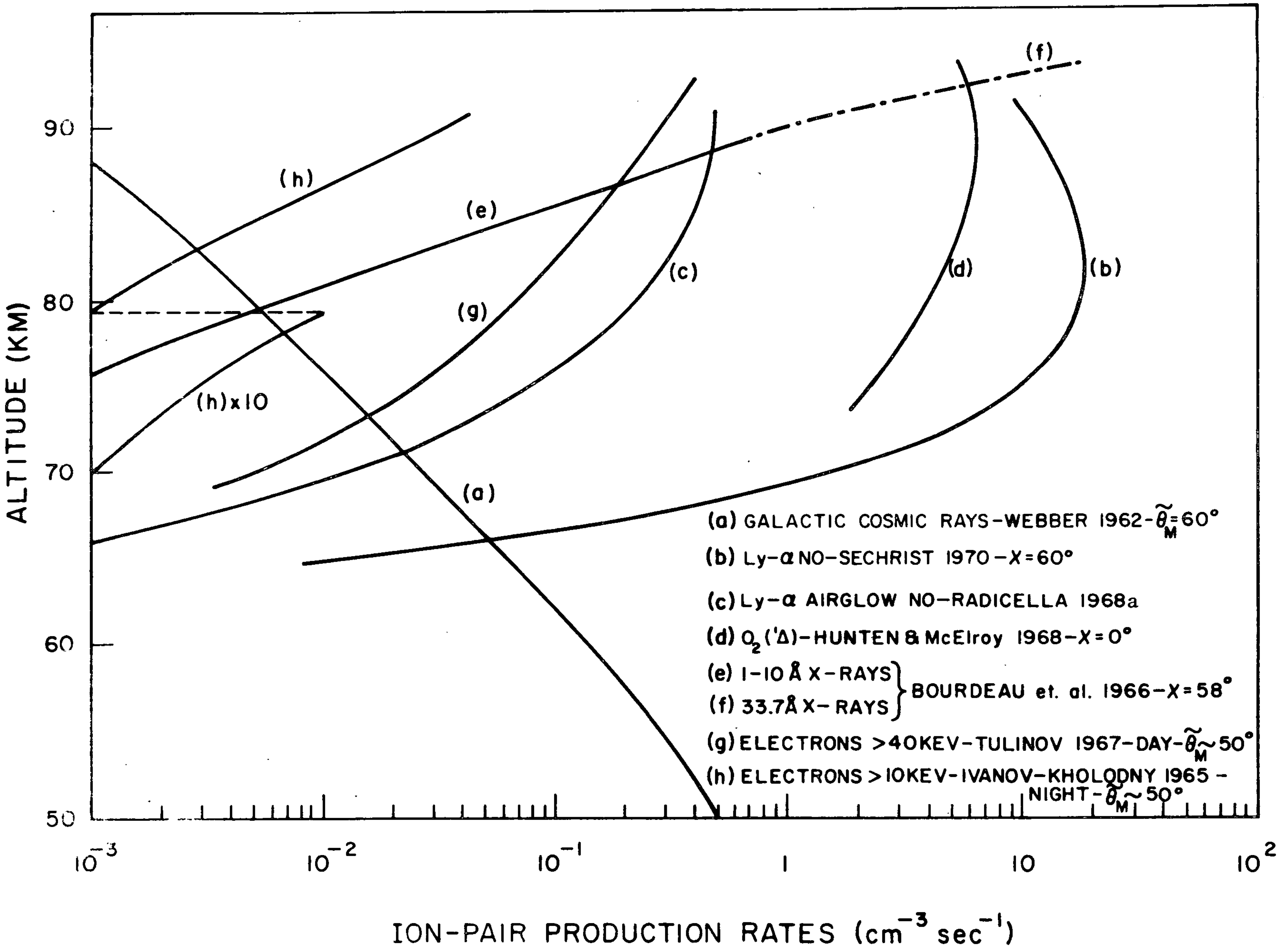

Figure 5.1 Ion-pair production rates in the D region.

in the daytime is the ionization of NO by hydrogen Lyman α radiation. The following ionization thresholds

$$\begin{array}{ll} O,\ O_3,\ N,\ N_2,\ H_2O & < 1000\text{Å} \\ O_2(^3\Sigma_g) & 1028\text{Å} \\ O_2(^1\Delta_g) & 1118\text{Å} \\ NO_2 & 1268\text{Å} \\ NO & 1338\text{Å} \end{array} \tag{5.7}$$

illustrate that nitric oxide is one of the only abundant atmospheric constituents which can be ionized by Ly α. It is a coincidence of nature that there happens to be a strong solar emission at 1216Å, Ly α, where molecular oxygen, the major atmospheric absorber around this wavelength, has a shallow window in its absorption spectrum [$\sigma^a_{O_2} = 1.2\text{x}10^{-20}$ cm^2 according to Blake <u>et al.</u> (1965); $\sigma^a_{O_2} = 1.0\text{x}10^{-20}$ cm^2, DASA (1967); $\sigma^a_{O_2} = 1.48\text{x}10^{-20}$ cm^2, Watanabe (1958)].

A daytime value of the direct solar flux associated with the Ly-α emission will be taken as $2.7\text{x}10^{11}$ photons cm^{-2} sec^{-1}. The ionization cross section of NO at 1216Å has been established as $\sigma^i_{NO} = 2.0\text{x}10^{-18}$ cm^2. Very simply then, the ionization rate of nitric oxide due to direct solar radiation at λ = 1216Å (and considering Ly α as the only important wavelength for this process) is

$$I_{NO} = \sigma^i_{NO}\, I_0\, e^{-\tau_{O_2}} \tag{5.8}$$

$$\tau_{O_2} = \sigma^a_2\, n_2 H_2 F_2 \quad ; \quad \lambda = 1216\text{Å}$$

where I_0 is the total Ly-α solar flux, and I_{NO} is the ionization rate.

The electron-ion production rate due to NO ionization is then

$$q_{NO} = n_{NO} I_{NO} \quad . \tag{5.9}$$

An alternative to Equations (5.8) is to use measured values of the photo flux with altitude, $I_0 e^{-\tau}$, which can be obtained from Bourdeau et al. (1966) or Reid (1970). There is a great limitation to this data though since the measurements apply to only one zenith angle. These experimental values are very close to theoretical predictions anyway. Such measurements would probably be most useful in a coordinated experiment.

The role of NO ionization by direct sunlight at sunrise in the D region must be negligible since τ becomes very large there. However, a large scattered Lyman α flux, due to resonant scattering from the atomic hydrogen content above 120 km, exists both at day and night. This radiation will be considered as a vertical Ly-α photon flux emanating with a zero optical depth from the 120 km level. Its intensity also displays a diurnal cycle which will be represented empirically for the sunrise region by

$$I(\chi) = I(\chi_0) \exp\{-\alpha \sin^{1/n}(\chi-\chi_0)\} \ ; \ n \text{ ODD} \tag{5.10}$$

based on the results of Donahue (1966). From Donahue's paper the conservative values, $\chi_0 = 100°$, $\alpha = 1.5$, $I(\chi_0) = 4$kR (1 kiloRayleigh = 10^9 photons cm^{-2} sec^{-1}), and $n = 1$ are chosen. The production rate of electrons and ions due to scattered Ly α both before and during sunrise is then

$$\begin{aligned} q'_{NO} &= n_{NO}\sigma^i_{NO} \, I(\chi) e^{-\tau'_{O_2}} \\ \tau'_{O_2} &= \sigma^a_2 n_2 H_2 - \tau_{O_2}(120 \text{ km}, \chi=0°) \quad . \end{aligned} \tag{5.11}$$

The total Ly-α ion-pair production is then the sum of Equations (5.9) and (5.11). q is dependent on χ through F_2, and q' through I.

Radicella (1968a) shows a calculation of q'_{NO} assuming a 4kR Ly-α nighttime flux and Barth's (1966b) NO distribution. This is shown in Figure 5.1 along with a typical daytime production rate taken from Sechrist (1970), also based on Barth's (1966b) distribution. No peak is found in Radicella's curve since Barth's NO has a nearly constant density over the altitude range rather than being distributed with a constant mixing ratio from the value at 85 km as is assumed by Sechrist (1970). The adoption of a constant mixing ratio is logical, however, since the lifetime of NO in the D region is very long. Both NO distributions are shown in Figure 4.3.

It should be noted that the resonant scattering by atomic hydrogen, as well as O_2 absorption, has a controlling effect on the direct solar Ly-α flux attenuation. Variations in the H content above 120 km could produce large variations in the Ly α reaching the D region. The effect would be minimal for this study in any case since the direct Ly-α flux is unimportant at sunrise. However, it could be a factor in establishing the daytime equilibrium of the upper D region. Whether or not a change in the attenuation of the direct solar flux is large, or is offset by an increase in the scattered dayglow would determine the importance of this effect in the daytime. Lyman α fluxes are usually measured above the molecular oxygen absorption, but below the atomic hydrogen layer.

5.3 Ionization of $O_2(^1\Delta)$

Hunten and McElroy (1968) have proposed that the ionization of $O_2(^1\Delta)$ with a threshold of 1118Å is an important ionization source in the upper

Dr

D region. The peak production function (for $\chi=0°$) which they derived is based on the $O_2(^1\Delta)$ densities measured by Evans et al. (1968) and an estimate of the $O_2(^1\Delta)$ ionization cross section, and is illustrated in Figure 5.1. The $O_2(^1\Delta)$ densities of Evans et al. (1968), and so the $O_2(^1\Delta)$ ion-pair production rates have been corrected by a multiplicative factor of 1.31 (Hunten and McElroy, 1969).

Since Huffman's et al. (1970) measurements of the absorption by CO_2 in the O_2 windows lead to the conclusion that Hunten and McElroy's (1968) ionization rates are too large, it seems that the $O_2(^1\Delta)$ ionization source is not as competitive with the nitric oxide source in the mesosphere. This is especially true during sunrise. First, $O_2(^1\Delta)$ is not abundant everywhere at sunrise, with an ozone dissociation threshold $\lambda \sim 3100Å$, although its initial production would precede its ionization. More importantly, the penetration of short wavelengths to large zenith angles in the D region is very small.

The $O_2(^1\Delta)$ ionization rate, I_Δ, as determined by Hunten and McElroy will have a noon value that is given approximately by

$$I_\Delta(\tilde{\theta},\delta) = I_\Delta(0)\ \cos(\tilde{\theta}+\delta) \tag{5.12}$$

where $I_\Delta(0)$ is found from Figure 5.1 by taking q_Δ/n_Δ for each height, and δ is the earth's declination angle. The sunrise variation in I_Δ will be discussed in Chapter 8, but its eventual value will have a negligible effect on this study.

5.4 X-Ray and Ultraviolet Ionization of the D Region

Some important ionizing radiations in the uppermost D region and lower E region for quiet solar conditions are, in the order of decreasing penetration, 1-10Å X-rays, X-rays ∿ 33.7Å corresponding to a C VI line, Lyman β at 1026Å, and EUV (extreme ultraviolet radiation) $\lambda < 1000Å$. The resulting ionized constituents are primarily O_2^+ and N_2^+. Nicolet and Aikin (1960), Watanabe and Hinteregger (1962), and Bourdeau, et al. (1966) have made thorough studies of these ionization sources. In Figure 5.1 the X-ray ionization rates have been added together and plotted, but their ranges of importance are indicated. These data are from Bourdeau, et al. (1966) for a solar zenith angle of 58°. Only X-rays penetrate below 90 km, Ly-β and EUV being severely attenuated in the E region.

It is apparent that solar X-rays are not of any consequence during sunrise, and will not directly affect the D region at any altitude for large solar zenith angles say, $\chi > 80°$. They can therefore be ignored in this study. Likewise, Bremsstrahlung X-rays produced by precipitating electrons in the D region can also be ignored because of their small intensity (Rees, 1968).

5.5 Ion-Pair Production in the D Region by Precipitated Electrons

Electrons with energies greater than 40 kev can precipitate into the D region and collisionally ionize the constituents there, mainly O_2 and N_2. These energetic electrons originate in the radiation belts which surround the earth at middle magnetic latitudes. The charged particles in these belts are trapped by the earth's magnetic field and slowly leak out (Zmuda, 1966). Under normal conditions an isotropic daytime flux of 5×10^3 electrons cm^{-2} sec^{-1} is typical for middle latitudes, 40°-60°, according to Manson and Merry (1970). At lower latitudes a residual drizzle flux of about 10^2 can still ionize the D region. At the higher latitudes precipitating protons and electrons are a major source of ionization (Rees, 1968). A large diurnal variation in the precipitated flux also exists, the nighttime fluxes being smaller than the daytime fluxes at the same latitude. For comparison, in Figure 5.1 a daytime ionization rate calculated by Tulinov (1967) and a nighttime ionization rate calculated by Ivanov-Kholodny (1965), both for middle magnetic latitudes, are displayed. The diurnal variation exceeds an order of magnitude. Unfortunately no studies of this variation are available. Neither have any detailed latitudinal descriptions of the electron precipitation been put forward yet.

Depending on how the diurnal change in energetic electron production is distributed, this source may or may not be a factor at sunrise. It must compete with the scattered Lyman α ionization of NO above 70 km in the presunrise region, and with NO and $O_2(^1\Delta)$ ionization above 70 km in the postsunrise region. The precipitated electron source is never important below 70 km. From Figure 5.1 it can be seen that the daytime energetic electron production rate, q_{el}, is comparable to the NO rate for about 90° zenith angle, whereas the nighttime q_{el} is negligible in such a comparison. It is probable that q_{el} at sunrise will be large enough to be included in the calculations.

For the purposes of this work q_{el} will be specified to have the following empirical latitudinal behavior

$$\frac{q_{el}(\tilde{\theta}_m)}{q_{el}(\tilde{\theta}_{m0})} = [1 + A \sin^2 a(\tilde{\theta}_m - \tilde{\theta}_{m0})]^{-1} \tag{5.13}$$

with $\tilde{\theta}_{m0} \sim 50°$, $A \sim 50$, and $a \sim 1$. The diurnal behavior will be assumed to have the simple form (around sunrise)

$$q_{el}(\chi) = \frac{1}{2}(q_{el}^D + q_{el}^N) + \frac{1}{2}(q_{el}^D - q_{el}^N) \cos(\chi - \chi_0) \tag{5.14}$$

where 'D' and 'N' indicate day and night values, and $\chi_0 \sim 0$. These empirical forms display in a general way the behavior q_{el} is expected to have. Since q_{el} is not a dominant source of ionization the errors in calculations will not be notable.

6. POSITIVE ION CHEMISTRY

The past decade has seen a great refinement in the techniques of laboratory measurements of ionic reaction rates. More confidence has also been placed in aeronomic estimates deduced from the observation of atmospheric parameters. The improvement in understanding of the D-region ion chemistry has therefore been dramatic in recent years. Still, a great volume of data has yet to be collected, and many processes contributing to the D-region behavior have yet to be fully described while others are probably waiting to be discovered. At the present state of knowledge one should perhaps place more weight on the laboratory measurements of reaction rates when they are available since aeronomic estimates are usually less certain.

The various types of positive (and negative) ionic reactions are listed in Appendix VIII. The nomenclature for types of reactions is very descriptive and no further explanation of them is needed here. Among the researchers who have contributed to the determination of reaction rates of atmospheric interest since 1960 many papers and reviews have been published. Some of these used as references for this work are Ferguson, et al. (1965), Nicolet (1965b), Ferguson (1967), Ferguson and Fehsenfeld (1969), and Mitra (1968).

A detailed discussion of reaction rate theory is not necessary for the purpose of studying the atmosphere as long as confidence can be placed in the present measurements and estimates of reaction rates. Generally, chemical interactions are described in terms of the formation of an activated complex along a reaction path on a potential energy surface that is defined in an elemental, or minimal, configuration space for the reaction. A formal expression for the rate constant is

$$k = \int\int\cdots\int\prod_{i=1}^{3N} \left(\frac{dq_i dp_i}{h}\right) K \nu P$$

where N is the dimension of the elemental phase space, P is the normalized distribution (in phase space) of activated complexes on a 3N-1 dimensional hypersurface in the configuration space which separates 'products' and 'reactants', ν is the frequency with which complexes pass from one side of the hypersurface to the other, and K is the transmission coefficient, or fraction of the complexes which become 'reactants' or 'products' after passing through the hypersurface, and measures both turnaround and channel efficency. The integration is performed over the hypersurface in the elemental phase space. Absolute reaction rate theory results when the hypersurface is taken at a saddle point on the potential energy curve. In collision theory the surface is placed on the side of the reactants and K, ν, and P are appropriately defined. In addition to the reaction rate calculation, the equilibrium constant for a reaction can be determined by applying statistical mechanics to the chemical system, and yields the ratio of forward to backward rates for the reaction.

Such analyses are usually helpful in determining the order of magnitude of reaction rates and their temperature dependence.

6.1 Positive Ions in the D Region

Positive ions are formed in the D region by the ionization processes described in Chapter 5 and by the subsequent transfer of positive charge from specie to specie. Some of the charge transfer channels are very fast, which explains why there is almost no ionized molecular nitrogen in the mesosphere, and why hydrated species are dominant over much of this region. A careful determination of the positive ion composition of the D region can be important in several respects. Electron densities are controlled to a great extent by their loss through recombination with positive ions. At higher altitudes, where the competitive electron loss process of attachment is negligible, the equilibrium electron density is critically dependent on the recombination coefficient, α. The molecular positive ions, such as O_2^+ and NO^+, which appear in the D region have recombination coefficients of the order of 10^{-7}-10^{-6} cm^3 sec^{-1}. On the other hand it is believed that water-derived clustered positive ions (also referred to here as hydrated or aggregate) have recombination coefficients an order of magnitude greater than this. In a particular altitude range where one positive ion is dominant the recombination coefficient, and so the electron density, is determined by that ion. As long as recombination is the main electron loss process, changes in electron density not attributable to the production rate reflect a change in the positive ion composition, and vice versa.

Determination of positive ion densities is also used in applying the charge neutrality condition on electrons and positive and negative ions. In this way measurements of positive ion and electron densities (and negative ion densities at low altitudes) can be used to cross check theoretical and experimental charge densities. The charge neutrality condition can also be used to simplify the chemical calculations by eliminating a variable from the continuity equations.

Positive ions will recombine with or neutralize negative ions. In the nighttime D region this is the primary loss process for negative ions. Competing processes would be collisional detachment or associative detachment followed by electron-ion recombination. However, for the terminating negative ions found at night in the mesosphere these last two processes are negligible, and one must then determine which ion-ion reactions are neutralizing the charge. It is usually assumed that the negative ions recombine with a general, unspecified positive ion whose density is the total positive ion density, at a rate, ε, of the order of 10^{-8}-10^{-7} cm^3 sec^{-1}. Unfortunately only a few neutralization and recombination reactions have been measured. Again it is possible that hydrated ionic species are present in large quantities in the D region, and that they will have large recombination or neutralization cross sections. An abundance of these aggregated ions at night is even more plausible since they will be more stable in a radiationless environment. For the present work, estimates of the ion-ion reaction rates available at this time will be sufficient. These reactions are discussed in Chapter 7, with negative ions.

In analyzing mass spectrographic data of positive ion measurements made in the D region Narcisi and Bailey (1965); Narcisi et al. (1968) have identified the ion masses based on ionospheric knowledge and isotopic ratios. They are listed in Table 6.1. The dominant mesospheric ions found by Narcisi are NO^+, H_3O^+, and $H_5O_2^+$. In Figures 6.1 and 6.2 the day and nighttime positive ion densities are illustrated. These curves are based primarily on the work of Narcisi and Bailey (1965) and Narcisi et al. (1968). Although they are more qualitative than quantitative, the density profiles illustrate many important features of the D region. As is expected, the ions N_2^+ and H_2O^+ are negligible at all altitudes from 50-90 kilometers. Also absent is O_2^+, which indicates that hydration and charge transfer channels are fast for this ion. In fact, below 83 km hydrated species, and in particular $H_5O_2^+$, are the dominant positive ions for both day and night as detected by mass spectrometers. Above about 83 km NO^+ assumes the role of dominant ion which it retains along with O_2^+ into the E region (except for isolated layers of metallic ions which can have high densities).

Table 6.1 D-region positive ions

Ion Mass	Ion	Ion Mass	Ion	Ion Mass	Ion
18^+	H_2O^+	23^+	Na^+	46^+	$N_2^+ \cdot H_2O$ NO_2^+
19^+	H_3O^+	$24^+, 25^+, 26^+$	Mg^+		
28^+	N_2^+	40^+	Ca^+		
30^+	NO^+	52^+	Cr^+		
		$54^+, 56^+$	Fe^+	48^+	$NO^+ \cdot H_2O$ SO^+ O_3^+
32^+	$S^+, z<86km$ $O_2^+, z>86km$	$58^+, 60^+$	Ni^+	50^+	$O_2^+ \cdot H_2O$ SO^+
$37^+, 39^+$	$H_5O_2^+$				
55^+	$H_7O_3^+$				

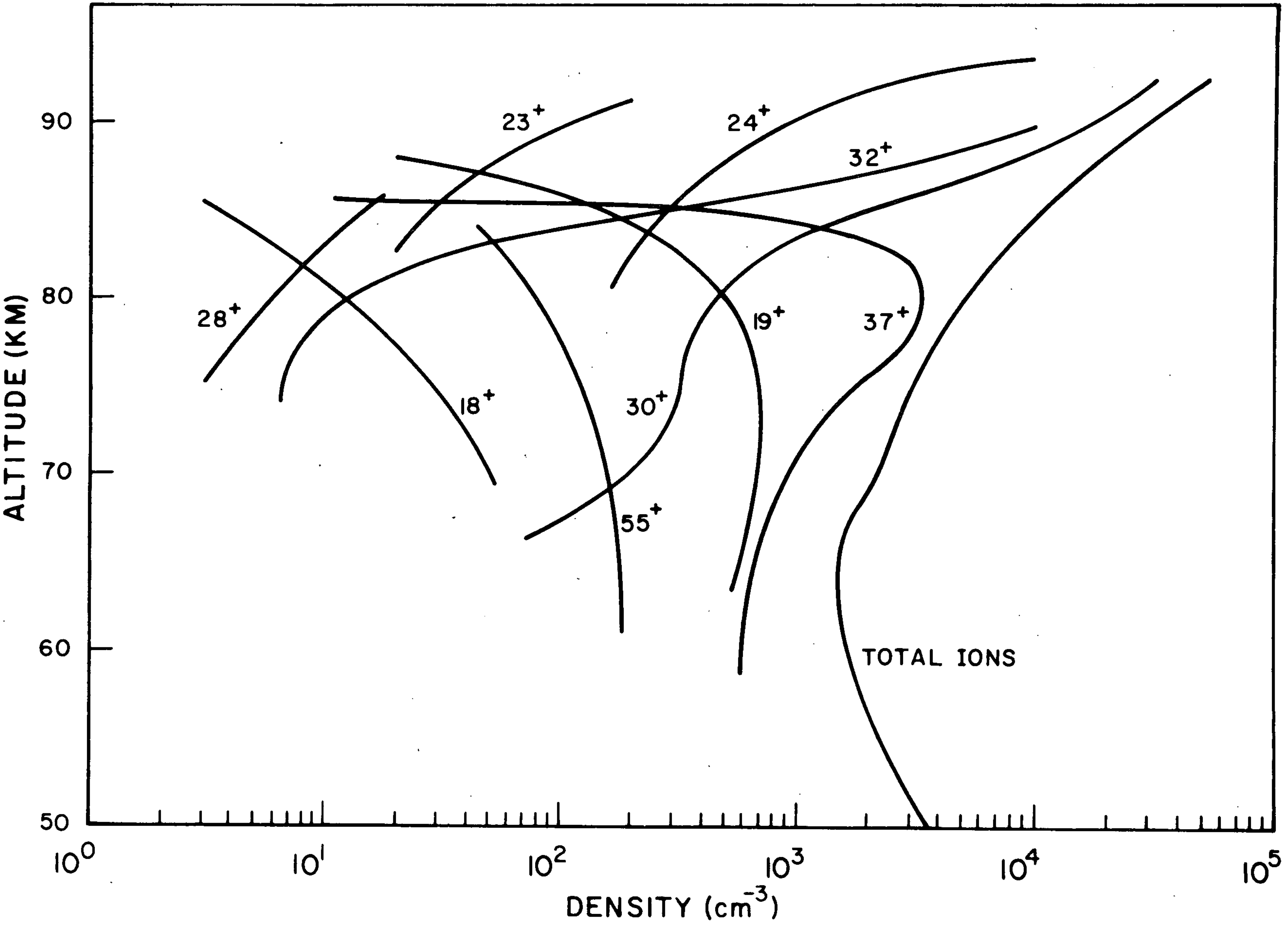

Figure 6.1 Daytime positive ion densities in the D region.

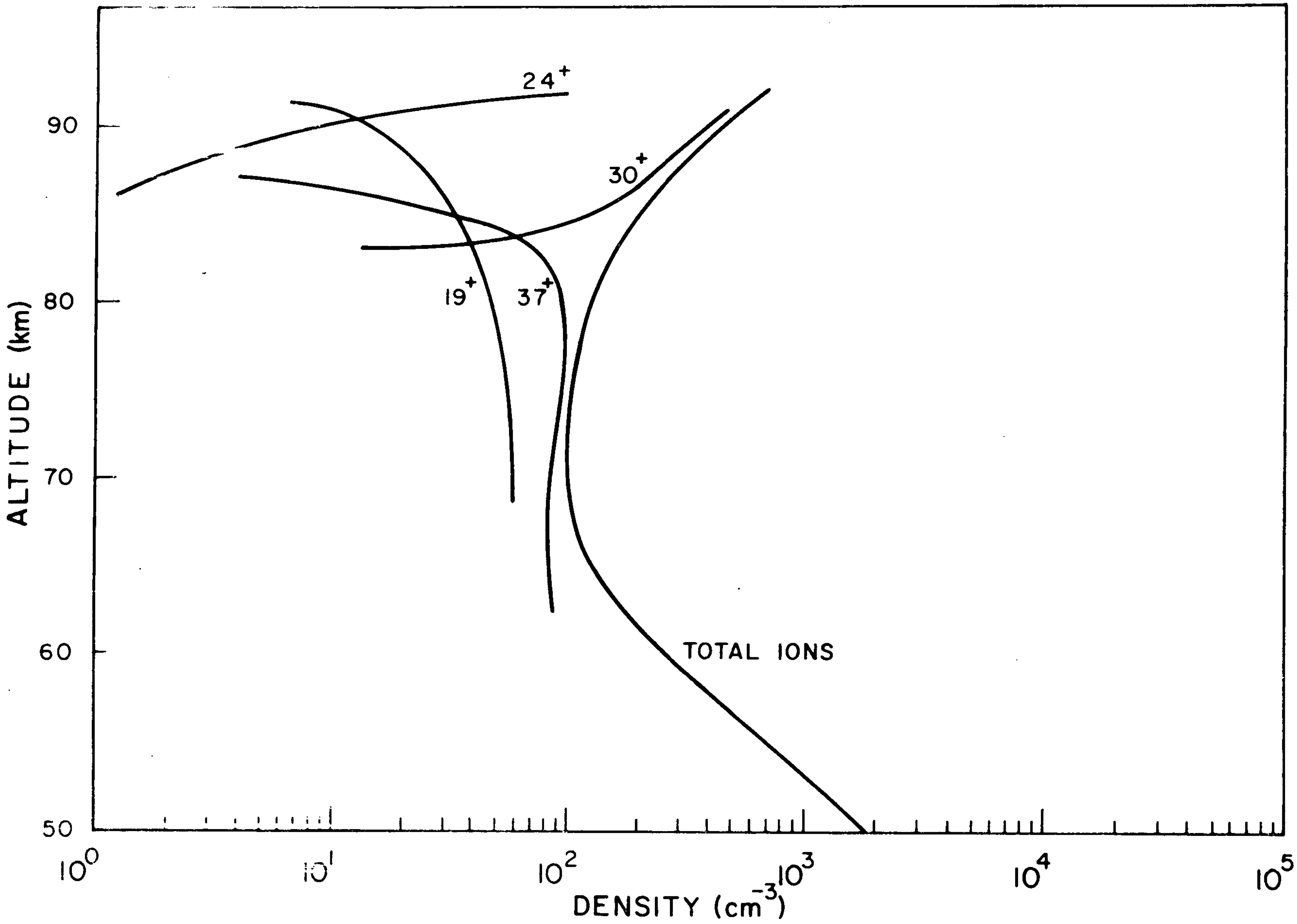

Figure 6.2 Nighttime positive ion densities in the D region.

At around 83 km the hydrated ions abruptly disappear. Reid (1970) has named this level the hydropause since it seems indicative of a rapid lapse in the water vapor density (Ferguson and Fehsenfeld, 1969); and because it does not correspond to the mesopause. As Reid pointed out, at the present time there is no suitable explanation for a lack of H_2O above this level. One possible explanation is that at around 83 km a process which can affect at least one link in the hydration chain becomes significant. This process must be present both day and night. Perhaps nearly thermalized precipitated electrons can effectively and rapidly neutralize the hydrates. More recently (Ferguson, 1970) it has been proposed that atomic oxygen will vigorously attack O_4^+ to short circuit the hydration chain above 80 km, so that a hydropause need not be postulated.

It is also probable that the water-derived ions that are observed using mass spectrometers are not the dominant water-derived ions in the D region, but that the heavier ions, $H_5O_2^+$, $H_7O_3^+$, etc., are more abundant. Such large aggregates could be easily fractionalized in a rocket's shock wave or during collisions while being accelerated in the spectrometer (Reid, 1970). Therefore, the results of mass spectrographic ion measurements in the D region are probabaly correct in indicating that hydrated ions are dominant below 83 km, but are very misleading as to which hydrates are actually present.

One can conclude from reviewing positive ion measurements that at the present state of the art these measurements, using both probe and mass spectrometers, are subject to error and ambiguity in the relatively dense atmosphere from 50-90 km. One aspect of the D-region positive ion structure which is fairly well established, however, is the rapid change of the dominant ions from water clusters below 83 km to molecules (NO^+, O_2^+) above 83 km. The importance of the clustered ions is that they may have large recombination coefficients, α, as large as $5\text{x}10^{-5}$ cm^3 sec^{-1} (Biondi, 1969; Sechrist, 1970; Reid, 1970). Very few measurements of their recombination coefficients are becoming available.

6.2 Positive Ion Reactions

Tables 6.2 and 6.3 contain many of the possible positive ion reactions which could be considered in the D region. Also listed are reaction rate constants which were selected by considering the available experimental values as well as aeronomic estimates. Some of these rates may be in error by 50% or more, some by an order of magnitude, but most are assumed to be accurate to about 10% or 20%. Table 6.2 is divided into four sections. The first group comprises the important reactions of molecular positive ions and is applicable to the upper D region (also to the lower D region when hydration channels are ignored). The second group contains additional, but unimportant, reactions of the same type. The third set consists of an atomic oxygen ion cycle, and can be ignored in the mesosphere. The last four reactions show the fate of other minor neutral constituents which are ionized by X-rays, precipitated electrons, and cosmic rays - i.e. mainly conversion into O_2^+.

Only the dissociative recombination of positive ions is considered in Table 6.2. The competing mechanisms of three-body recombination and radiative recombination have rates

$$\begin{aligned} &1.0\text{x}10^{-26}\left(\frac{T}{300}\right)^{-2.5} \\ &1.0\text{x}10^{-12}\left(\frac{T}{300}\right)^{-.7} \end{aligned} \qquad (5.15)$$

respectively (DASA,1967), and are totally negligible as loss mechanisms for ions and electrons in the D region.

Table 6.2 Positive ion reactions

REACTION	RATE CONSTANT	SOURCE
$N_2^+ + O_2 \rightarrow O_2^+ + N_2$	$\gamma_1 = 1.0\text{x}10^{-10}$	Ferguson *et al.* (1965)
$O_2^+ + NO \rightarrow NO^+ + O_2$	$\gamma_2 = 8.0\text{x}10^{-10}$	Ferguson *et al.* (1965)
$O_2^+ + e \rightarrow O + O$	$\alpha_1 = 2.2\text{x}10^{-7}(\frac{T}{300})^{-.7}$	DASA (1967)
$NO^+ + e \rightarrow N + O$	$\alpha_2 = 5.0\text{x}10^{-7}(\frac{T}{300})^{-1.2}$	DASA (1967)
$N_2^+ + O \rightarrow NO^+ + N$	$\gamma_3 = 2.5\text{x}10^{-10}$	Ferguson *et al.* (1965)
$N_2^+ + NO \rightarrow NO^+ + N_2$	$\gamma_4 = 4.8\text{x}10^{-10}$	Ferguson (1967)
$O_2^+ + N \rightarrow NO^+ + O$	$\gamma_5 = 1.8\text{x}10^{-10}$	DASA (1967)
$O_2^+ + NO_2 \rightarrow NO^+ + O_3$	$\gamma_6 = 1.0\text{x}10^{-11}$	DASA (1967)
$N_2^+ + e \rightarrow N + N$	$\alpha_3 = 2.8\text{x}10^{-7}(\frac{T}{300})^{1.2}$	DASA (1967)
$O_2^+ + N_2 \rightarrow NO^+ + NO$	$\gamma_7 = 1.0\text{x}10^{-17}$	DASA(1967)
$N_2^+ + O \rightarrow O^+ + N_2$	$\gamma_8 = 1.0\text{x}10^{-12}$	DASA (1967)
$O^+ + N_2 \rightarrow NO^+ + N$	$\gamma_9 = 1.5\text{x}10^{-12}$	Ferguson (1967)
$O^+ + O_2 \rightarrow O_2^+ + O$	$\gamma_{10} = 2.6\text{x}10^{-11}$	Ferguson (1967)
$O^+ + NO \rightarrow NO^+ + O$	$\gamma_{11} = 2.4\text{x}10^{-11}$	Ferguson *et al.* (1965)
$O^+ + CO_2 \rightarrow O_2^+ + CO$	$\gamma_{12} = 1.2\text{x}10^{-9}$	DASA (1967)
$O^+ + N_2O \rightarrow NO^+ + NO$	$\gamma_{13} = 1.3\text{x}10^{-9}$	DASA (1967)
$O^+ + H_2 \rightarrow OH^+ + H$	$\gamma_{14} = 2\text{x}10^{-9}$	DASA (1967)
$A_r^+ + N_2 \rightarrow N_2^+ + A_r$	$\gamma_{15} = 6.0\text{x}10^{-12}$	Ferguson *et al.* (1967)
$A_r^+ + O_2 \rightarrow O_2^+ + A_r$	$\gamma_{16} = 1.1\text{x}10^{-10}$	Ferguson *et al.* (1967)
$N_2^+ + CO_2 \rightarrow CO_2^+ + N_2$	$\gamma_{17} = 8.0\text{x}10^{-10}$	Ferguson *et al.* (1967)
$CO_2^+ + O_2 \rightarrow O_2^+ + CO_2$	$\gamma_{18} = 1.0\text{x}10^{-10}$	Ferguson *et al.* (1967)

Table 6.3 Positive ion reactions

REACTION	RATE CONSTANT	SOURCE
$O_2^+ + O_2 + M \rightarrow O_4^+ + M$	$\gamma_{19} = 1.0\mathrm{x}10^{-29}$	Ferguson & Fehsenfeld (1969)
$O_4^+ + H_2O \rightarrow O_2^+ \cdot H_2O + O$	$\gamma_{20a} = 1.5\mathrm{x}10^{-9}$	Ferguson & Fehsenfeld (1969)
$O_4^+ + O \rightarrow O_2^+ + O_3$	$\gamma_{20b} \sim 1.0\mathrm{x}10^{-10}$	Ferguson (1970)
$O_2^+ \cdot H_2O + H_2O \rightarrow H_3O^+ \cdot OH + O_2$	$\gamma_{21a} = 1.2\mathrm{x}10^{-9}$	Ferguson & Fehsenfeld (1969)
$\rightarrow H_3O^+ + OH + O_2$	$\gamma_{21b} = 1.2\mathrm{x}10^{-10}$	Ferguson & Fehsenfeld (1969)
$H_3O^+ \cdot OH + H_2O \rightarrow H_5O_2^+ + OH$	$\gamma_{22} = 1.2\mathrm{x}10^{-9}$	Ferguson & Fehsenfeld (1969)
$H_5O_2^+ + H_2O + M \rightarrow H_7O_3^+ + M$	$\gamma_{23} = 3.0\mathrm{x}10^{-27}$	Ferguson & Fehsenfeld (1969)
$H_7O_3^+ + H_2O + M \rightarrow H_9O_4^+ + M$	$\gamma_{24} = 2.0\mathrm{x}10^{-27}$	Ferguson & Fehsenfeld (1969)
$O_2^+ + H_2O + M \rightarrow O_2^+ \cdot H_2O + M$	$\gamma_{25} = 1.0\mathrm{x}10^{-27}$	Ferguson & Fehsenfeld (1969)
$H_2O^+ + H_2O \rightarrow H_3O^+ + OH$	$\gamma_{26} = 8.5\mathrm{x}10^{-10}$	Ferguson (1967)
$H_3O^+ + H_2O + M \rightarrow H_5O_2^+ + M$	$\gamma_{27} = 1.0\mathrm{x}10^{-27}$	Ferguson & Fehsenfeld (1969)
$H_2O^+ + O_2 \rightarrow O_2^+ + H_2O$	$\gamma_{28} = 2.0\mathrm{x}10^{-10}$	Ferguson (1967)
$\left.\begin{array}{l} O_4^+ + e \\ H_3O^+ + e \\ H_5O_2^+ + e \\ H_7O_3^+ + e \end{array}\right\}$ Neutrals	$\alpha_4 = 1.0\mathrm{x}10^{-6}$	Ferguson & Fehsenfeld (1969)
$NO^+ + H_2O + N_2 \rightarrow NO^+ \cdot H_2O + N_2$	$\gamma_{29a} = 2.3\mathrm{x}10^{-28}$	Ferguson (1970)
$NO^+ \cdot H_2O + H_2O + N_2 \rightarrow NO^+ \cdot (H_2O)_2 + N_2$	$\gamma_{29b} = 5.3\mathrm{x}10^{-28}$	Ferguson (1970)
$NO^+ \cdot (H_2O)_2 + H_2O + N_2 \rightarrow NO^+ \cdot (H_2O)_3 + N_2$	$\gamma_{29c} = 1.4\mathrm{x}10^{-27}$	Ferguson (1970)
$NO^+ \cdot (H_2O)_3 + H_2O \rightarrow H_7O_3^+ + HNO_2$	$\gamma_{29d} = 4.3\mathrm{x}10^{-10}$	Ferguson (1970)
$NO^+ + CO_2 + N_2 \rightarrow NO^+ \cdot CO_2 + N_2$	$\gamma_{29e} = 4.0\mathrm{x}10^{-29}$	Ferguson (1970)
$NO^+ \cdot CO_2 + H_2O \rightarrow NO^+ \cdot H_2O + CO_2$	γ_{29f} fast	Ferguson (1970)
$M_g^+ + O_3 \rightarrow M_gO^+ + O_2$	$\gamma_{30a} = 2.3\mathrm{x}10^{-10}$	Ferguson & Fehsenfeld (1968)
$M_gO^+ + O \rightarrow M_g^+ + O_2$	$\gamma_{30b} \sim 1.0\mathrm{x}10^{-10}$	Ferguson & Fehsenfeld (1968)
$M_gO^+ + e \rightarrow M_g + O$	$\alpha_5 \sim 1.0\mathrm{x}10^{-6}$	Ferguson & Fehsenfeld (1968)

Table 6.3 shows two groups of reactions. The first two reaction schemes lead to the production of the hydrated species H_3O^+, $H_5O_2^+$, etc. Included in the first scheme is a reaction channel starting with H_2O^+, but since according to Equation (5.7) the ionization threshold of H_2O is less than 1000Å (about 980Å) this is a negligible D-region channel (especially if there is a rapid lapse of water vapor above 80 km since the short wavelengths necessary to ionize H_2O cannot possibly penetrate below 80 km). The other source of aggregated ions begins with O_2^+, but this channel is probably not as important as was first assumed since the main source of O_2^+ in the upper D region, $O_2(^1\Delta)$ ionization, has been recently de-emphasized by Huffman, et al. (1970). Calculations by Ferguson and Fehsenfeld (1969) using this scheme show good qualitative agreement with Narcisi and Bailey's (1965) measurements. However, a lot of refinement in reactions and reaction rates is still needed before positive ion densities in the lower mesosphere can be confidently predicted. This is certainly true if even larger water clusters are actually the dominant positive ions below 80 km. Ferguson and Fehsenfeld (1969) suggest that Narcisi and Bailey's (1965) 37^+ measurements are much too large to be reconciled with other atmospheric data (Narcisi, 1970a). This might further indicate that dissociated heavier ions were actually being measured by Narcisi below 80 km.

The recombination coefficient $\alpha_4 = 10^{-6}$ cm^3 sec^{-1} is an estimate by Ferguson and Fehsenfeld (1969). They also use a 'high' value of α_4 for $H_5O_2^+$ of 10^{-5}. It has recently been suggested (Reid, 1970; Sechrist, 1970) that water-derived cluster ions may have recombination coefficients as high as 5×10^{-5}. Clusters, unlike simple molecules, have many internal degrees of freedom. An electron could be absorbed by an ionized cluster and subsequently neutralize its charge through a host of possible channels. Large ion clusters might act like surfaces for electron recombination, with nearly every collision resulting in a neutralization. Furthermore, large neutral water clusters could introduce surfaces on which electrons and ions would recombine very efficiently (Hunt, 1968). The fact that water molecules have a large permanent dipole moment greatly enhances their clustering tendencies, and this strong dipole moment may help to increase the capture rate of slow thermal electrons by water clusters (Turner, 1968).

The presence of large water clusters in the D region is limited not only by the water vapor content but by their destruction through photo and collisional dissociation. These processes could also lead directly to the hydrated ions discussed above. In addition, the buildup of hydrates of other positive ions is also possible, as is shown in the second reaction scheme of Table 6.3. These reactions also provide an effective loss process for NO^+ in the D region. The NO^+ hydrates are not believed to dominate the hydrated protons, $H^+ \cdot (H_2O)_n$, at mesospheric water pressures, however (Donahue, 1968). While it is obvious that a great deal of data about hydrates are still needed in order to evaluate their role in D-region chemistry, it remains plausible that clustered ions will have large recombination coefficients, and that they are dominant ions below 80 km in the D region.

Another set of positive ions found in the upper mesosphere are the metal ions, most of which are listed in Table 6.1. The metals are deposited in the atmosphere by the ablation of meteors. Typically, they have ionization thresholds $\lesssim$ 2000Å, and are found in dense, narrow ionized layers above 90 km. These metal layers have been used to explain sporadic-E ionization. The last group of reactions in Table 6.3 is a typical metal ion recombination sequence. These ions are unimportant to this analysis since they are very minor ions below 90 km.

In Figure 6.3 a simplified positive ion scheme for the D region is illustrated. A hydration channel for NO^+ is also included, but this by no means exhausts the possible hydration channels. Reactions are taken from Tables 6.2 and 6.3.

6.3 Positive Ions at Sunrise

It is clear that from night to day the total positive ion concentration changes by an order of magnitude over much of the D region. However, in trying to determine the electron density variation at sunrise the critical factor which must be considered is the positive ion composition, or more specifically, the dominant positive ions at each altitude and their recombination coefficients. The whole effect of the positive ions on sunrise can then be summarized by the changes in the 'average' recombination coefficients during sunrise. These average recombination coefficients are defined in Chapter 8 by Equations (8.4) and (8.9), and are to be distinguished from the 'effective' electron-ion recombination coefficient given by Equation (8.17) of Chapter 8.

In Figure 6.1 and 6.2 one sees that the dominant daytime ions at a particular altitude are the same dominant nighttime ions at that altitude. Narcisi et al. (1968) in discussing the sunrise and sunset positive ion transitions also indicate that below about 83 km the hydrated ions are dominant for both day and night. Above 83 km, NO^+ and O_2^+ are the dominant ions at all points in the diurnal cycle (only altitudes up to 90 km are being considered). In Figure 6.4 the average electron-ion recombination coefficient calculated by Reid (1970) is reproduced. Reid's calculations are based on the fact that the electron loss rate is controlled by recombination at high altitudes (barring an exceptionally fast attachment process).

He uses electron production rates similar to those in Chapter 5 and measured daytime electron densities to deduce the recombination rate. Reid's

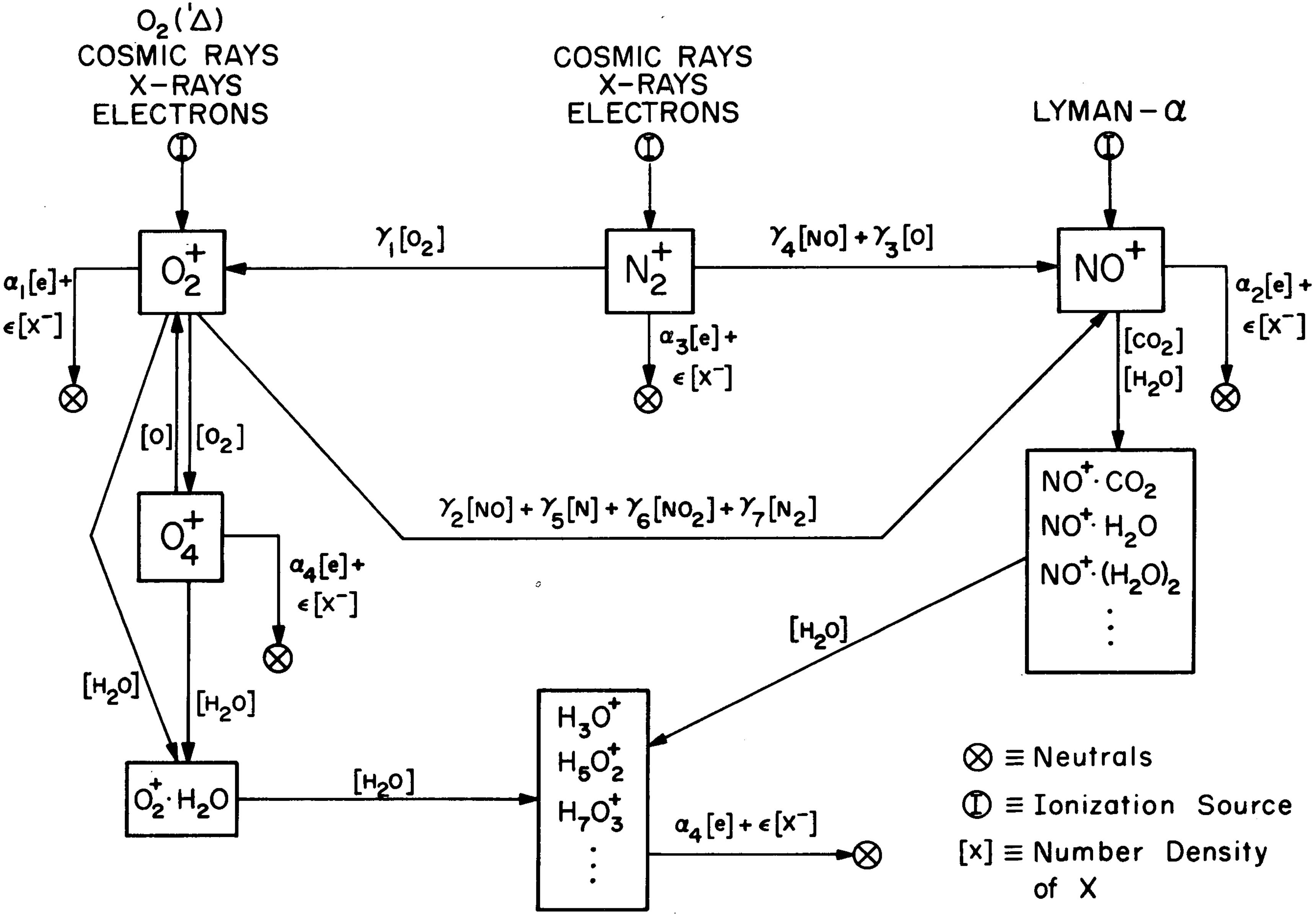

Figure 6.3 Positive ion reaction scheme.

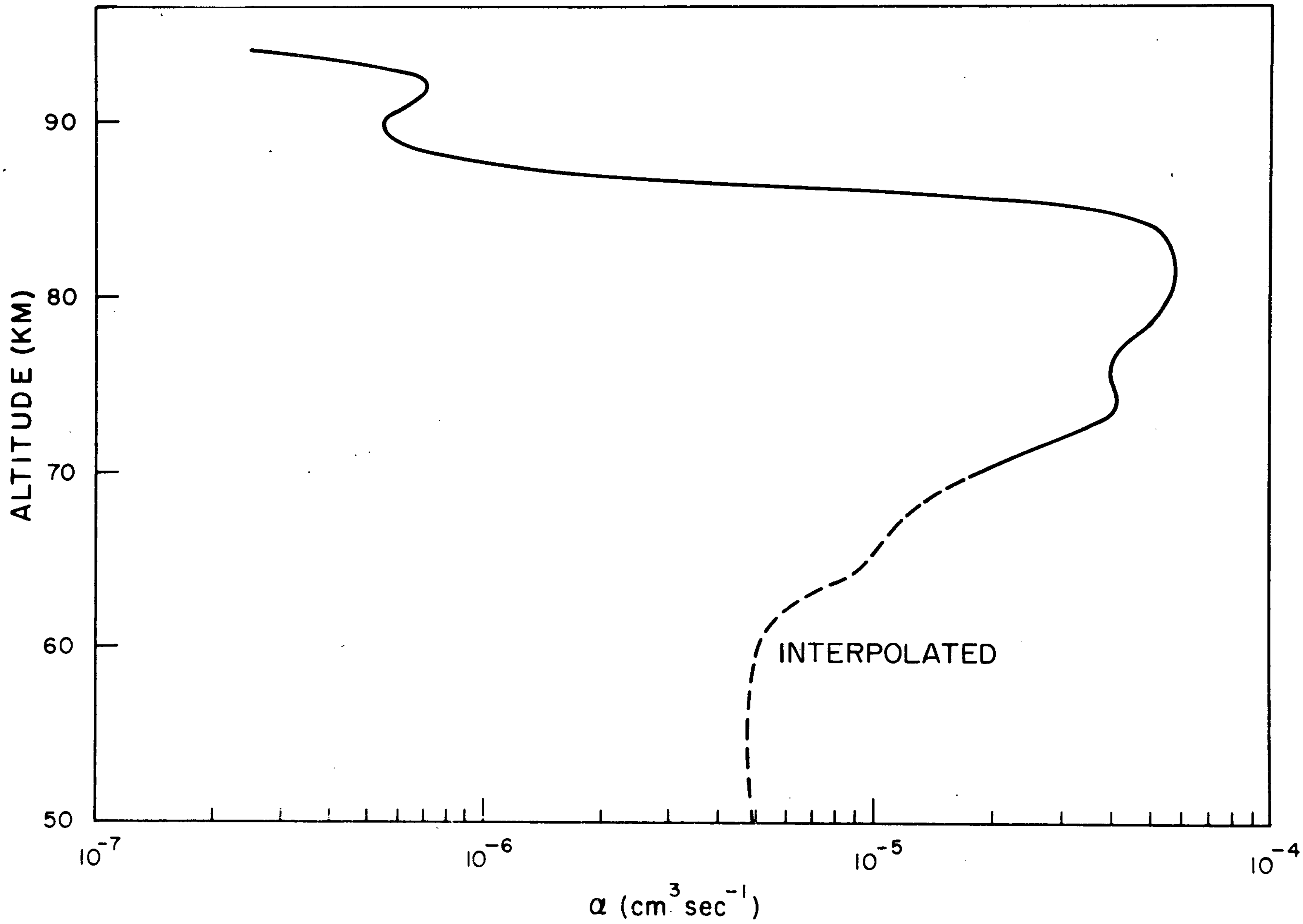

Figure 6.4 The average electron-ion recombination coefficient in the D region.

complete calculations indicate that below 75 km negative ions cannot be ignored, and below 70 km electron-ion recombination becomes insignificant as an electron loss process compared to attachment. Note that in Figure 6.4 there is a region with a high recombination coefficient (below about 80 kilometers) which can be explained by assuming that hydrates have a large recombination coefficient $\alpha \sim 5\text{x}10^{-5}$. Above 80 km the results indicate an average recombination coefficient of the same size as the dissociative recombination coefficients of NO^+ and O_2^+, which is consistent with the positive ion measurements.

Once the average electron-ion recombination coefficient is determined (such as in Figure 6.4) it becomes a fixed D-region parameter for the sunrise. Similar conclusions can be reached about the average ion-ion recombination coefficients, $\tilde{\varepsilon}_i$. One could then use the average $\tilde{\alpha}$ and $\tilde{\varepsilon}$'s and charge neutrality to eliminate the positive ions from the sunrise problem completely. This is a commonly used D-region simplification which can be invoked for the sunrise analysis. It would be especially useful in light of all the additional uncertainties in the positive ion chemistry which could be avoided. The continuity equations, utilizing average recombination coefficients, are developed in Chapter 8.

7. NEGATIVE ION CHEMISTRY

The solutions for the negative ion and electron densities in the D region require that a great bulk of data be available, and that it be sufficiently accurate so that valid conclusions can be deduced from the calculations. The problem is especially sensitive in the D region. Here the chemistry becomes very complex, and here too the ionizing fluxes are residual and are very sensitive to the other atmospheric parameters. There is also a large void in accurate experimental measurements of such quantities as positive and negative ion composition and minor neutral constituent densities and variations. Add to this the uncertainty in reaction rate constants and a variability in other quantities such as temperature and solar activity, and one will have trouble making predictions for more than a few special cases or conditions. Still, there is enough observed evidence to substantiate in part the theoretical models which are used in D-region work. In this case it is the goal of the researcher to vary the model parameters (within likely bounds) in step with the most recent knowledge until good agreement is attained between model and measurement.

The prediction of D-region electron densities is this type of a problem. In the next few sections, and with the data already developed in the previous chapters, the model which will be used to derive the sunrise electron densities will be completed.

7.1 Electrons in the D Region

Figures 7.1a-d depict the growth of the electron densities in the D region at sunrise. These profiles were measured using three different techniques. The data were taken from Mechtly and Smith (1968a) and Mechtly and

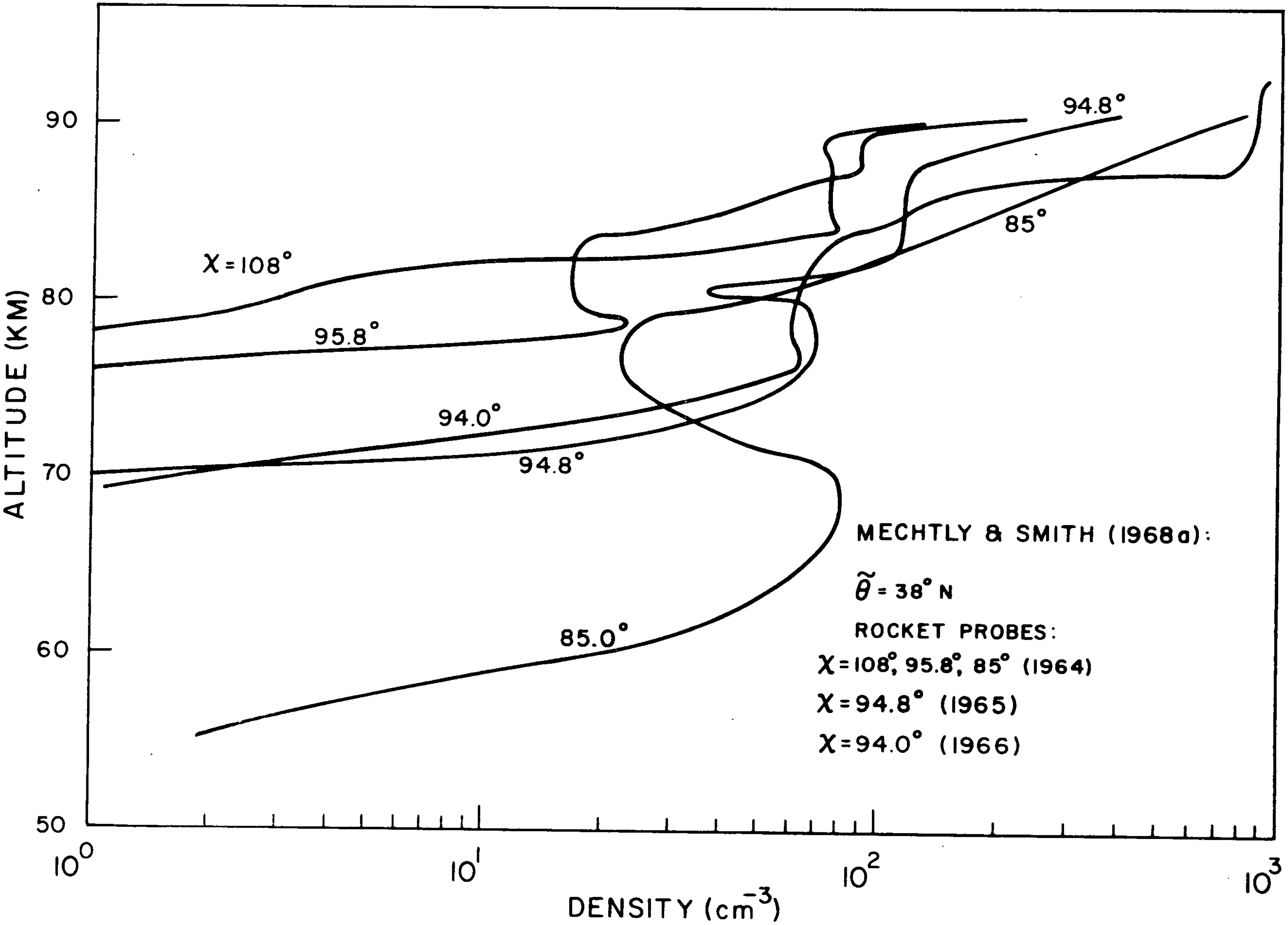

Figure 7.1a Experimental diurnal electron density variations in the D region.

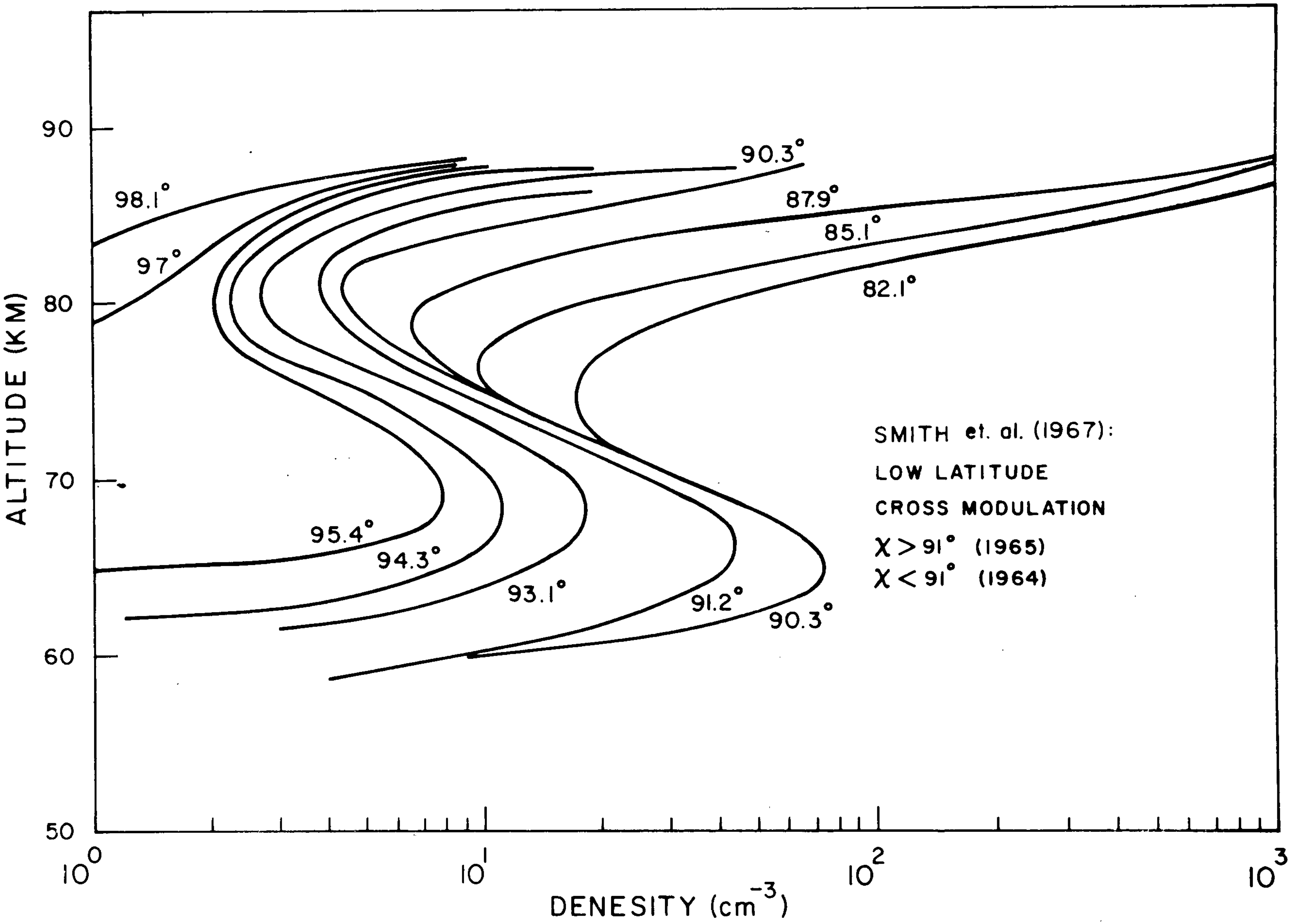

Figure 7.1b Experimental diurnal electron density variations in the D region.

FR

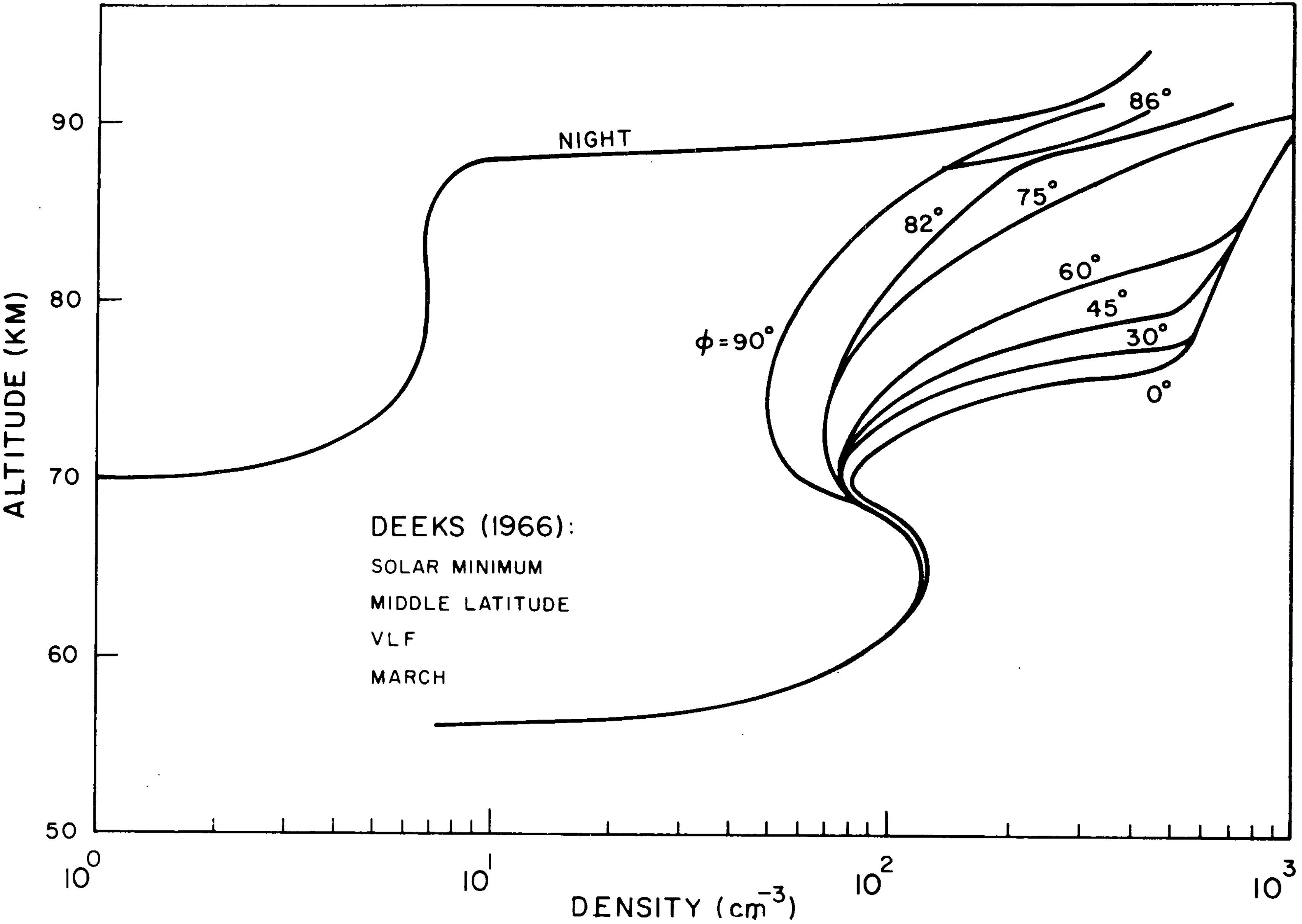

Figure 7.1c Experimental diurnal electron density variations in the D region.

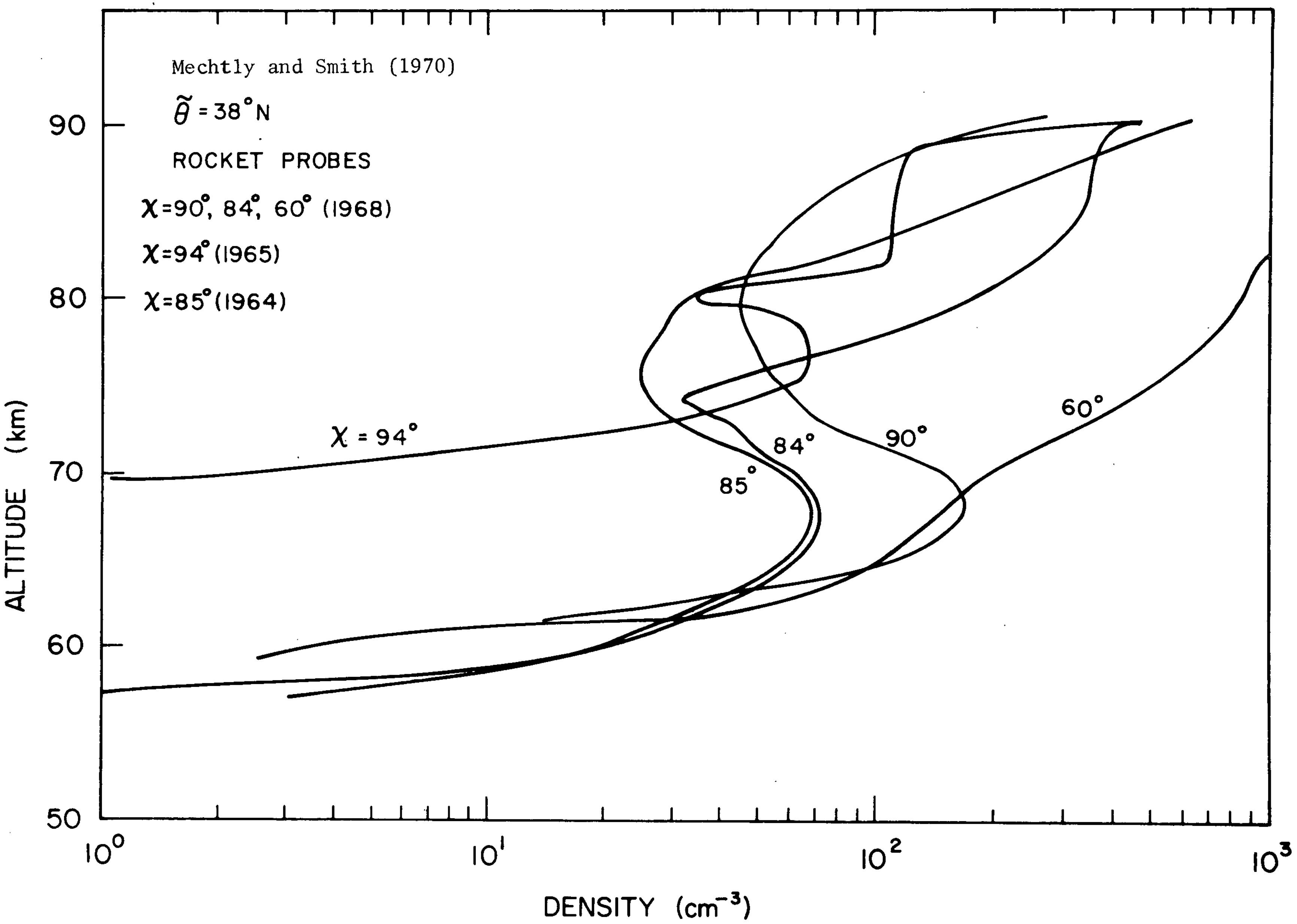

Figure 7.1d Experimental diurnal electron density variations in the D region.

Smith (1970) who utilized rocket probes, Smith *et al*. (1967) using cross modulation, and Deeks (1966) using VLF propagation. Deek's curves represent those solutions of the full wave equations which best fit the reflection data. Since VLF reflection is essentially from the first Fresnel zone the actual spatial resolution of this method is not good. Another technique, partial reflection, has also been implemented to measure D-region electron densities. The relative merits of each method, and the arguments for both ground-based and *in situ* measurements, are not relevant here. What is important are the several features of each measurement which seem to agree.

There is a prominent electron layer near 65 km with a peak value of about 100 electrons cm^{-3}. This is the C layer which appears before ground sunrise. The source of electrons for the C layer is primarily galactic cosmic ray ionization. Electron attachment is fast at these altitudes, and the negative ion to electron density ratio is large. The detachment of electrons from negative ions is responsible for the C-layer development at sunrise.

There is a nighttime ledge of electrons in the upper D region lying between 80 and 90 km. This ledge has a density on the order of 10^2-10^3 electrons cm^{-3}, but there is quite a variation from measurement to measurement. Mechtly and Smith's (1968a) data for 108° represent an average nighttime ledge. During sunrise this ledge deepens and builds up to a density of at least 1000 electrons cm^{-3}. After ground sunrise, the region between the D-region ledge and the C layer slowly fills with electrons. Generally, for $\chi < 60°$ the C layer can be obscured by the deepening D layer. The D layer is developed mainly by the ionization of nitric oxide and as the morning progresses the ionizing radiations can penetrate deeper into the D region. This effect is depicted in Figures 7.1-b, c, and d. Other measurements of the fully developed D region show the C layer to be more obscured by the D layer (Mechtly and Smith, 1968b). Deeks' (1966) results show that the lower layer is not fully hidden but in this case seasonal effects may be important since the measurements were made in March (i.e. near the end of winter).

The electron growth at sunrise is only one type of variation which might be considered in constructing and verifying a sunrise model. Besides the general sunrise behavior that has been observed by many independent researchers as discussed above, there are also diurnal, seasonal, latitudinal, and solar effects. The daytime electron density grows in the morning and decays in the afternoon. The variation is essentially symmetric about noon, although more and more examples of asymmetries are being measured (Reid, 1968). There is a seasonal variation in electron density at a fixed zenith angle, with winter densities being a factor between 0.1 and 1 smaller than the densities during the rest of the year. This decrease in electrons during the winter months is not yet fully understood. In addition there is the winter anomaly phenomena in which the electron densities between 65-85 km increase by a factor of about 10 over the normal winter densities on anomalous days. Since the anomalous winter densities are about the same as the normal densities that are found the rest of the year, there is speculation about which behavior is anomalous and which is normal on a winter day. In any case, there is at present no adequate explanation of the winter anomaly.

There haven't been any complete and consistent studies or measurements of the latitudinal electron density behavior as yet. The few profiles which have been obtained at different latitudes for comparison at a nearly constant zenith angle show no general pattern of behavior (Reid, 1968). The effect of solar activity on the D-region electron densities would be an issue for the chapter on ion-pair production rates. Since only quiet solar conditions are being considered in this work, the discussion of Chapter 5 is sufficient. One interesting effect is the decrease in cosmic ray ion-pair production at middle and low latitudes during high solar activity, and it is connected to the distortion of the earth's magnetic field by the enhanced flux of solar particles sweeping past the earth.

It can be concluded that many features of the global electron density distribution have yet to be sufficiently measured and explained. Enough consistency exists at present in the experimental measurements of sunrise variations, however, to justify a unified theoretical description of this phenomena, and subsequent conclusions based on this theory.

7.2 Negative Ions in the D Region

Negative ions are produced by the attachment of electrons to neutral species in any one of several processes, and the subsequent transfer of this charge in non-neutral interactions. Negative ions are lost by electron detachment, or by neutralization with positive ions. The electron affinities of the important D-region species (excepting hydrated ions and species which form unstable or short-lived negative ions) are listed in Table 7.1. The electron affinities of some important ions, notably NO_2^- and NO_3^-, can only be estimated while some affinities have not been measured at all, the electron affinities of O_2^- and O^- seem to be fairly well established.

Several methods are available for determining electron affinities. A calculation of the ionic binding energy usually leads to a good estimate of the electron affinity (e.g. $NO_2 \sim 1.6$ ev, $NO_3 \sim 3.9$ ev). One can also measure the photodetachment threshold, or vertical detachment energy, of a negative ion. If the threshold behavior, or the molecular potential functions, are known the electron affinity can be determined with good accuracy. Limits on the

Table 7.1 Electron affinities

Specie	Electron Affinity(ev)	Source
O_2	$.43\pm.02$	DASA (1967)
O_3	$1.9\pm.4$	DASA (1967)
	2.2	Beaty (private communication)
O	1.47	Branscomb (1964)
NO_2	2.75	DASA (1967)
	>1.8	Fehsenfeld, *et al*. (1969)
	3.8	DASA (1967)
NO_3	>3.3	Fehsenfeld, *et al*. (1969)
	$>EA(NO_2)$	Fehsenfeld, *et al*. (1969)
CO_3	?	
CO_4	$1.22\pm.07$	DASA (1967)
NO	$<.43$	DASA (1967)
O_4	~1.6	Hasted (1964)

electron affinity of a molecule can be determined by observing various reactions of its ion, and by noting whether the reaction is exothermic or endothermic (not always obvious) as well as knowing the formation energies of the neutral complexes involved. This has led to the limits on the electron affinities of the nitrogen-oxides in Table 7.1.

The rate of production of negative ions depends on the electron attachment cross sections of the neutral species at thermal energies, ∿.01 ev. Very few attachment cross sections are available, and those that are represent cross sections for radiative attachment. In the D region, three-body and dissociative attachment processes will dominate radiative attachment. However, the cross section for radiative attachment can be connected to the photodetachment cross section of a negative ion by the principle of detailed balancing. In this case one assumes an equilibrium system, that is, a Maxwellian electron velocity distribution and a black body radiation background both at the temperature of the gas. The equilibrium constant of the reaction can be calculated by applying statistical mechanics. In addition, one is presumed to know the electron affinity, E_a, in order to deduce the photodetachment cross section. The resulting relationship is

$$\sigma_\delta(\nu) = G\,\sigma_{att}(v)\left(\frac{mvc}{h\nu}\right)^2 \tag{7.1}$$

where G is a statistical weighting factor, and v and ν are related by the conservation of energy

$$h\nu = \frac{1}{2}mv^2 + E_a \quad . \tag{7.2}$$

Equations (7.1) and (7.2) can be invoked if the proper data are available, which is not yet the case for the negative ions of interest here for which photodetachment cross sections have not been measured.

In this work the negative ions NO_2^- and particularly NO_3^- will be used as effective terminating ions, or ions which do not undergo any further rapid ion-neutral reactions but which are slowly lost by photodetachment and neutralization with positive ions. Because of the presence of water vapor in the mesosphere it has been proposed that very stable clustered negative ions could be formed there, such as $(H_2O)_n \cdot X^-$, by three-body interactions (Pack and Phelps, 1966). The clusters O_4^- and CO_4^- have been quantitatively treated by Fehsenfeld, *et al*. (1969). But unfortunately there is no acceptable quantitative data on the formation and destruction of various hydrated negative ions, which could be the important terminating ions in the D region. For example, if the hydration of NO_3^- or any previous ion which leads to NO_3^- were faster than the conversion to NO_3^-, then the hydrate might qualify as the main terminating ion if it were very stable, or it could lead to a very stable terminal ion through further reaction. Since myriad possible reaction channels exist there is no way to predict accurately which reactions might be important or what their rates might be. For this reason the negative ion scheme usually used for D-region analysis, including the most recent cluster reaction measurements, is adopted here. Hydration channels can be added to the scheme as they become known (Narcisi, 1970b).

7.3 Negative Ion Reactions

Tables 7.2 and 7.3 list the known negative ion reactions of aeronomic significance along with rate constants which are either well established or have been chosen as the most likely values from among several measurements. The source from which each rate constant was obtained is also shown and, though generally it is not the original source for the rate, it does either represent the most recent measurement (or estimate) for the rate, or present

Table 7.2 Negative ion reactions

Reaction	Rate Constant	Source
$O_2 + O_2 + e \rightarrow O_2^- + O_2$	$\beta_{2a} = \begin{cases} 1.4x10^{-29}(\frac{300}{T})e^{-600/T} \\ 1.6x10^{-30} \end{cases}$	DASA (1967) Reid (1970)
$O_3 + e \rightarrow O^- + O_2$	$\beta_3 \leq 1.0x10^{-11}$	Fehsenfeld & Ferguson (1968)
$O_2^- + O \rightarrow O_3 + e$	$\delta_1 = 3.0x10^{-10}$	Ferguson, *et al*. (1967)
$O_2^- + O_2(^1\Delta) \rightarrow 2O_2 + e$	$\delta_{2a} = 2.0x10^{-10}$	Reid (1970)
$O_2^- + O_3 \rightarrow O_3^- + O_2$	$\gamma_{31} = 3.0x10^{-10}$	Fehsenfeld, *et al*. (1967)
$O_2^- + NO_2 \rightarrow NO_2^- + O_2$	$\gamma_{32} = 8.0x10^{-10}$	Fehsenfeld & Ferguson (1968)
$O^- + O \rightarrow O_2 + e$	$\delta_7 = 1.9x10^{-10}$	Fehsenfeld, *et al*. (1967)
$O^- + O_2(^1\Delta) \rightarrow O_3 + e$	$\delta_8 = 3.0x10^{-10}$	Fehsenfeld & Albritton (1969)
$O^- + O_3 \rightarrow O_3^- + O$	$\gamma_{33} = 7.0x10^{-10}$	Fehsenfeld, *et al*. (1967)
$O^- + NO_2 \rightarrow NO_2^- + O$	$\gamma_{34} = 1.2x10^{-9}$	LeLevier & Branscomb (1968)
$O^- + O_2 + O_2 \rightarrow O_3^- + O_2$	$\gamma_{35} = 2.0x10^{-30}$	LeLevier & Branscomb (1968)
$O_3^- + O \rightarrow O_2^- + O_2$	$\gamma_{36} = 1.4x10^{-10}$	Mitra (1968)
$O_3^- + CO_2 \rightarrow CO_3^- + O_2$	$\gamma_{37} = 4.0x10^{-10}$	Fehsenfeld, *et al*. (1967)
$O_3^- + NO \rightarrow NO_3^- + O$	$\gamma_{38} = 1.0x10^{-11}$	Fehsenfeld, *et al*. (1967)
$NO_2^- + O_3 \rightarrow NO_3^- + O_2$	$\gamma_{39} = 1.8x10^{-11}$	Fehsenfeld & Ferguson (1968)
$NO_2^- + NO_2 \rightarrow NO_3^- + NO$	$\gamma_{40} = 4.0x10^{-12}$	Ferguson & Fehsenfeld (1969)
$CO_3^- + O \rightarrow O_2^- + CO_2$	$\gamma_{41} = 8.0x10^{-11}$	Fehsenfeld, *et al*. (1967)
$CO_3^- + NO \rightarrow NO_2^- + CO_2$	$\gamma_{42} = 9.0x10^{-12}$	Fehsenfeld, *et al*. (1967)
$O_2^- + h\nu \rightarrow O_2 + e$	$\delta_3 = .33\ (\tau=0)$	DASA (1967)
$O^- + h\nu \rightarrow O + e$	$\delta_4 = 1.4\ (\tau=0)$	DASA (1967)
$O_3^- + h\nu \rightarrow O_3 + e$	$\delta_5 = .06\ (\tau=0)$	DASA (1967)
$NO_2^- + h\nu \rightarrow NO_2 + e$	$\delta_6 = .04\ (\tau=0)$	DASA (1967)

Table 7.3 Negative ion reactions

Reaction	Rate Constant	Source
$O_2^- + O_2 + M \rightarrow O_4^- + M$	$\gamma_{43} = 1.0\text{x}10^{-29}$	Fehsenfeld, et al. (1969)
$O_4^- + CO_2 \rightarrow CO_4^- + O_2$	$\gamma_{44} = 4.3\text{x}10^{-10}$	Fehsenfeld, et al. (1969)
$O_4^- + NO \rightarrow NO_3^- + O_2$	$\gamma_{45} = 2.5\text{x}10^{-10}$	Fehsenfeld, et al. (1969)
$O_4^- + O \rightarrow O_3^- + O_2$	$\gamma_{46} = 4.0\text{x}10^{-10}$	Fehsenfeld, et al. (1969)
$CO_4^- + NO \rightarrow NO_3^- + CO_2$	$\gamma_{47} = 4.8\text{x}10^{-11}$	Fehsenfeld, et al. (1969)
$CO_4^- + O \rightarrow CO_3^- + O_2$	$\gamma_{48} = 1.5\text{x}10^{-10}$	Fehsenfeld, et al. (1969)
$O_2 + e + N_2 \rightarrow O_2^- + N_2$	$\beta_{2b} = 1.0\text{x}10^{-31}$	DASA (1967)
$O_2 + e + H_2O \rightarrow O_2^- + H_2O$	$\beta_{2c} = 1.4\text{x}10^{-29}$	Phelps (1969)
$O_2^- + O_2 \rightarrow 2O_2 + e$	$\delta_{2b} = 2.7\text{x}10^{-10}\left(\frac{T}{300}\right)^{1/2} e^{-5600/T}$	DASA (1967)
$O_2^- + N_2 \rightarrow O_2 + N_2 + e$	$\delta_{2c} = 1.9\text{x}10^{-12}\left(\frac{T}{300}\right)^{3/2} e^{-5000/T}$	DASA (1967)
$O^- + NO \rightarrow NO_2 + e$	$\delta_9 = 1.6\text{x}10^{-10}$	Ferguson (1967)
$O^- + H_2 \rightarrow H_2O + e$	$\delta_{10} = 6.2\text{x}10^{-10}$	Ferguson (1967)
$O_2^- + N \rightarrow NO_2 + e$	$\delta_{11} = 3.0\text{x}10^{-10}$	Ferguson, et al. (1967)
$O^- + N \rightarrow NO + e$	$\delta_{12} = 1.6\text{x}10^{-10}$	Ferguson (1967)
$O_2 + e \rightarrow O_2^- + h\nu$	$\beta_4 = 2.0\text{x}10^{-19}$	DASA (1967)
$O + e \rightarrow O^- + h\nu$	$\beta_5 = 1.3\text{x}10^{-15}$	Branscomb (1964)
$O^- + N_2 \rightarrow N_2O + e$	$\delta_{13} = 2.0\text{x}10^{-19}$	DASA (1967)
	Secondary Channels	
$O_2^- + O \rightarrow O^- + O_2$	$\delta_1' = 1.0\text{x}10^{-11}$	DASA (1967)
$O_3^- + O \rightarrow O_2 + O_2 + e$		
$O_4^- + O \rightarrow O_2 + O_2 + O^-$		
$CO_4^- + O \rightarrow CO_2 + O_3^-$		
$O_2^- + N \rightarrow NO + O + e$; $NO + O^-$		
$NO_3^- + \{O,N,NO\} \rightarrow$ products	$\gamma_{49} < 10^{-11}$ $\sim 10^{-14}$	Fehsenfeld, et al. (1969) estimate

a summary of past measurements and arguments leading to the selection of the rate. Most of these arguments are aimed at experimental conditions (e.g. possible vibrational excitations, contamination, or alternative reaction channels) or temperature extrapolation and activation energy estimates. Table 7.4 lists ion-ion reactions, and it can be seen that there is a great dearth of data for these reactions.

Many of the reactions are of little importance to the analysis. For example, the radiative attachment reactions and the associative detachment of O^- and O_2^- by atomic nitrogen are obviously negligible in the D region. The secondary reaction channels in Table 7.3 are also completely ignorable. For the important clustering reaction sequence which begins with γ_{43}, a value of this rate as low as 7×10^{-31} was reported by E. C. Beaty (private communication). However, this measurement is only preliminary, and the experimental conditions may prove to be significant. A direct cluster electron attachment mechanism could also exist with a rate as high as 10^{-7}, but this possibility is only speculative. Recent measurements suggest that the ion-ion neutralization reactions occur with a rate $\sim 10^{-7}$ (Reid, 1970) although specific reactions appear to be slower by an order of magnitude (e.g. Biondi, 1969).

Figure 7.2 shows the negative ion ladder. Electrons that are produced by ionization are injected at the top, and except for the detachment of the initial oxygen allotrope ions, the electrons sift down the ladder where they are eventually neutralized (ignoring the slower detachment of the more stable negative ions). The rate for each path along the ladder can be calculated from Tables 7.2 and 7.3 and a knowledge of the neutral constituent densities. The negative ion scheme of Figure 7.2 (without all the ion-ion recombination channels shown) represents the most recent understanding of the D-region negative ion chemistry when hydration is not considered (Reid, 1970; Ferguson, 1970).

Table 7.4 Ion-ion reactions

Reaction	Rate Constant	Source
$O_2^+ + O_2^- \rightarrow O_2 + O_2$	$\varepsilon_1 = 4.0\times10^{-9}$	Mitra (1968)
$NO^+ + O_2^- \rightarrow NO + O_2$	$\varepsilon_2 = 2.0\times10^{-7}$	Mitra (1968)
$NO^+ + NO_2^- \rightarrow NO + NO_2$	$\varepsilon_3 = 2.0\times10^{-7}$	Nicolet (1965b)
$XY^+ + NO_2^- \rightarrow$ Neutrals	$\varepsilon_4 = 2.0\times10^{-8}$	Gunton (1969)
$XY^+ + NO_3^- \rightarrow$ Neutrals	$\varepsilon_5 = 4.4\times10^{-8}$	Biondi (1969)
$XY^+ + CO_3^- \rightarrow$ Neutrals	$\varepsilon_6 = 2.0\times10^{-8}$	Gunton (1969)
$X^+ + Y^- \rightarrow$ Neutrals	$\varepsilon = 1.0\times10^{-7}$	Reid (1970)
$X^+ + Y^- \rightarrow X + Y$	$\varepsilon \cong 4.0\times10^{-7}$	Dalgarno (1968)
	$\varepsilon = 2.0\times10^{-8}$	**LeLevier** & Branscomb (1968)
$X^+ + Y^- \rightarrow X + Y$	$\varepsilon = 2.0\times10^{-7}(\frac{300}{T})$	DASA (1967)
$X^+ + Y^- + M \rightarrow XY + M$	$\varepsilon = 2.0\times10^{-25}(\frac{300}{T})^{2.5}$	DASA (1967)

C 4

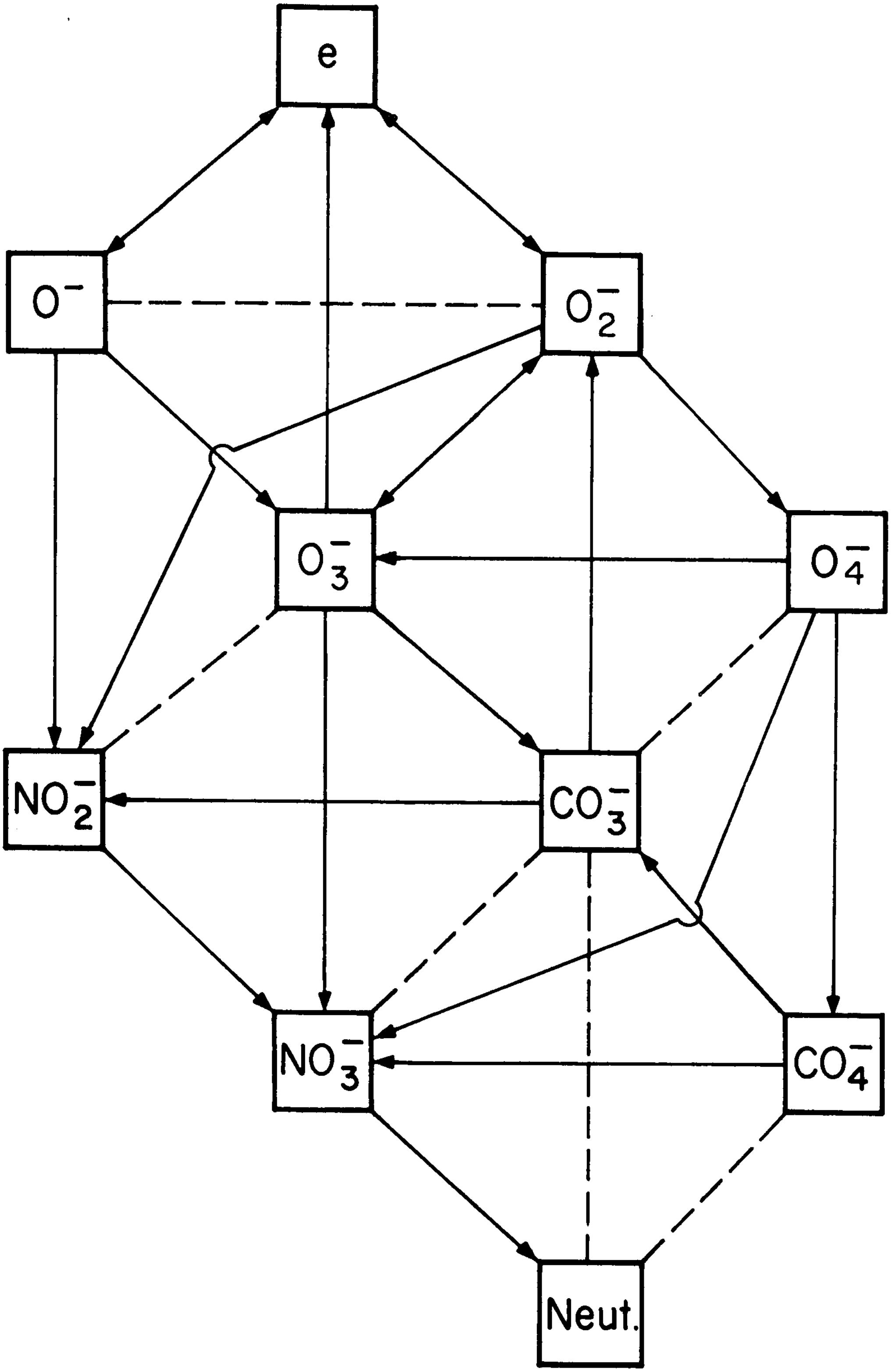

Figure 7.2 Negative ion ladder.

7.4 Photodetachment at Sunrise

The photodetachment of negative ions at sunrise is a potentially strong source of electrons in the D region since during the night large quantities of negative ions will be accumulated. In Figure 7.3 the photodetachment cross sections of O^-, O_2^-, and NO_2^- are illustrated (labelled solid curves). The data are incomplete in the ultraviolet and in the case of NO_2^- is very uncertain at all wavelengths (Branscomb, 1964; Branscomb, et al., 1958; Burch, et al., 1959). A theoretical photodetachment cross section for O_4^- is available in Hasted (1964) but is not reproduced here. Because most of the solar flux lies above 3000Å, even if the detachment cross sections rise by a couple of orders of magnitude in the uv most of the detachment still occurs for wavelengths > 3000Å. This can be seen from the zero optical depth differential detachment rates also plotted in Figure 7.3 (dashed curves). Table 7.2 gives the currently accepted zero optical depth photodetachment rates for O^-, O_2^-, O_3^-, and NO_2^-. The rates for O_4^-, CO_3^-, CO_4^-, and NO_3^- have not been measured, and the photodetachment cross sections for most negative ions are still not available. For the purposes of this work the following zero optical depth photodetachment rates will be initially utilized

$$\delta_{NO_3^-} = 2\text{x}10^{-3}\ \text{sec}^{-1} = \delta_{14} \tag{7.3}$$

$$\delta_{O_4^-} = \delta_{CO_3^-} = \delta_{CO_4^-} = \text{variable} < 10^{-2}\ \text{sec}^{-1} \ .$$

Since NO_3^- probably has a photodetachment threshold near $\lambda \lesssim 3500$Å it will be assumed that the sunrise increase in δ_{14} follows that of J_3, the ozone dissociation rate. Then

$$\delta_{14}(\chi) = J_3(\chi)\ \frac{\delta_{14}(0)}{J_3(0)} \tag{7.4}$$

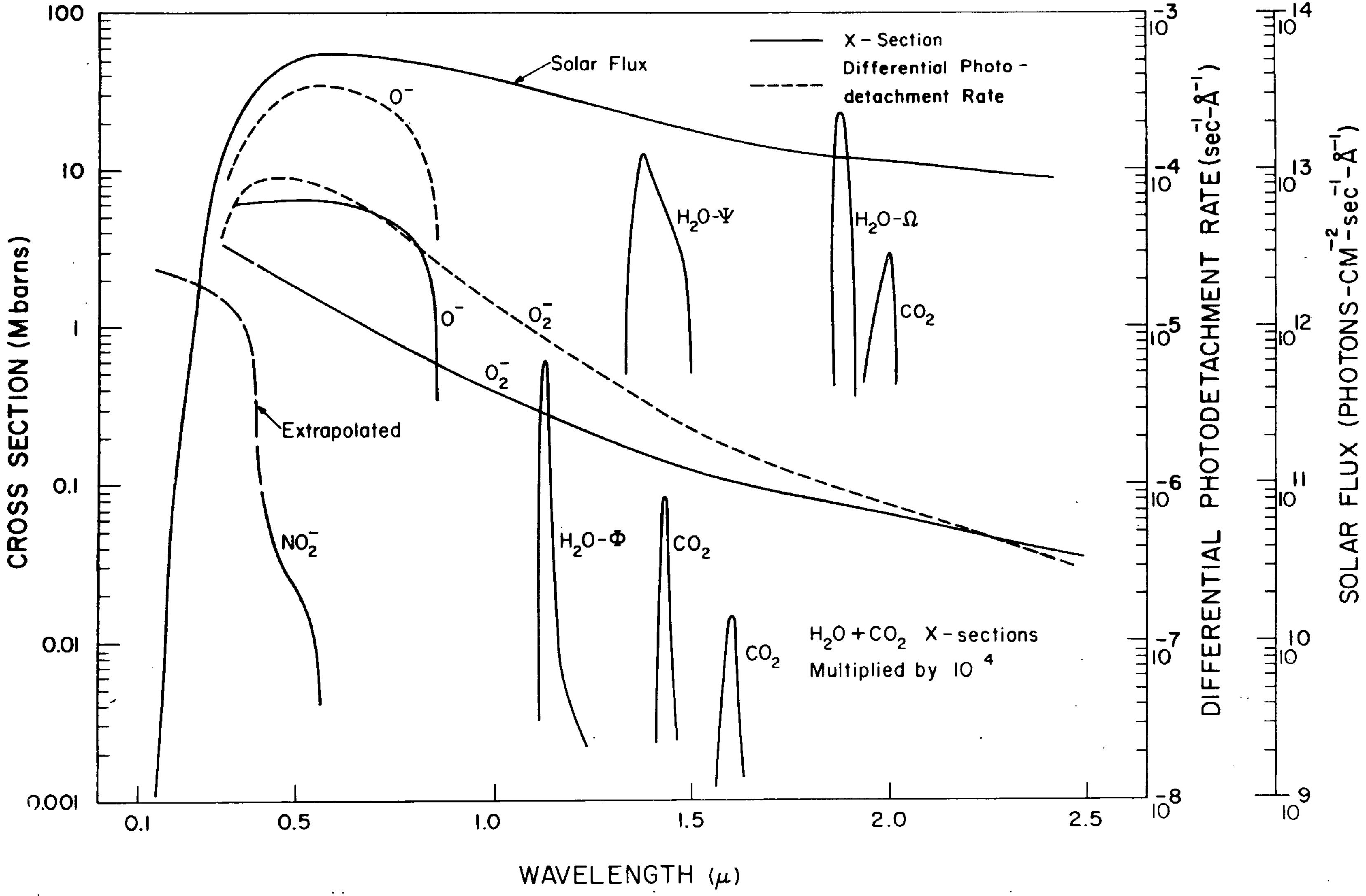

Figure 7.3 Photodetachment cross sections of negative ions and infrared absorption cross sections of H_2O and CO_2.

in renormalized form. If the process spectrums are assumed to be the same, the ratio of the rates for an overhead sun (or at any χ) will be the same as the ratio of the zero optical depth rates. Thus

$$\delta_{14}(\chi) = .2\ J_3(\chi) \quad . \tag{7.5}$$

The rates $\delta_{CO_3^-}$, $\delta_{CO_4^-}$, and $\delta_{O_4^-}$ will be specified later.

The ion O_3^- has a detachment threshold near 6000Å. Assuming that the O_3^- and O_2^- detachment spectrums are similar in the visible wavelength range one has

$$\delta_5(O_3^-) = .182\ \delta_3(O_2^-) \tag{7.6}$$

at all altitudes and for all χ.

The behavior of the NO_2^- photodetachment rate is harder to determine because its cross section is increasing rapidly (probably) where the solar flux is diminishing rapidly. The peak differential detachment rate will fall at about 3000Å. This wavelength will be used to determine $\delta_{NO_2^-}$ by the simple equation

$$\delta_6(\chi) = \delta_6 e^{-\tau(3000\text{Å},\chi)} \quad . \tag{7.7}$$

A calculation of the photodetachment rate of O_2^- at sunrise should include not only the ozone absorption and Rayleigh scattering of the solar radiation in the near infrared, but the molecular band absorption of CO_2 and H_2O as well. Table 7.5 gives the data which applies to the calculation of δ_3 and δ_4 for O_2^- and O^- respectively. The solar infrared spectrum corresponds closely to that of a black body radiator at 5900°K. Solar flux values were derived from Kondratyev (1969). The absorption bands of CO_2 and H_2O are illustrated in

Table 7.5 Infrared absorption data

λ, μ	$\Delta\lambda$, μ	Solar Flux cm^{-2}-sec^{-1}-$Å^{-1}$	σ_{O_3} cm^2	σ_R cm^2	σ_{H_2O} cm^2	σ_{CO_2} cm^2	$\sigma_{O_2^-}$ cm^2	σ_{O^-} cm^2	$\tilde{\sigma}_{O_2}$ cm^2
.300	---	9.2(12)	3.84(-19)	5.40(-26)	---	---	---	---	---
.375	.05	2.66(13)	---	2.20(-26)	---	---	---	6.2(-18)	---
.425	.05	4.14	---	1.28	---	---	2.4(-18)	6.3	---
.475	.05	5.01	4.80(-22)	8.29(-27)	---	---	2.0	6.4	---
.525	.05	5.15	2.06(-21)	5.55	---	---	1.7	6.3	---
.575	.05	5.51	3.98	3.86	---	---	1.4	6.2	---
.625	.05	5.40	3.66	2.77	---	---	1.2	6.0	---
.675	.05	5.20	1.53	2.04	---	---	1.0	5.6	---
.725	.05	4.95	5.23(-22)	1.53	---	---	8.6(-19)	5.0	---
.825	.15	4.35	---	9.10(-28)	---	---	7.5	1.9	---
.950	.10	3.90	---	5.48	1.35(-23)	---	4.6	---	6.7(-28)
1.05	.10	3.58	---	3.48	---	---	3.6	---	---
1.15	.10	3.20	---	2.43	1.1(-23)	---	2.8	---	5.5(-28)
1.275	.15	2.70	---	1.61	---	---	2.1	---	---
1.40	.10	2.24	---	1.10	3.5(-22)	1.68(-24)	1.5	---	2.0(-26)
1.50	.10	1.87	---	8.37(-29)	---	---	1.25	---	---
1.60	.10	1.60	---	---	---	7.4(-25)	1.1	---	1.1(-27)
1.70	.10	1.40	---	5.06	---	---	9.4(-20)	---	---
1.80	.10	1.30	---	4.02	---	---	8.0	---	---
1.90	.10	1.20	---	---	8.3(-22)	---	7.2	---	4.2(-26)
2.00	.10	1.13	---	---	---	2.6(-22)	6.4	---	3.9(-25)
2.10	.10	1.06	---	---	---	---	5.6	---	---
2.20	.10	1.00	---	---	---	---	5.0	---	---
2.30	.10	9.4(12)	---	---	---	---	4.4	---	---
2.40	.10	9.0	---	---	---	---	3.9	---	---
2.50	.10	8.6	---	---	---	---	3.5	---	---

Figure 7.3, except for the β-σ-τ bands of H_2O at about 0.95μ. Average absorption cross sections for the bands are listed in Table 7.5 and are based on integrated band strengths obtained from Goody (1964). These average cross sections for CO_2 and H_2O are suitable for this analysis (the average is over a 1000Å interval). Also given in Table 7.5 is an 'equivalent' O_2 absorption cross section which results from the formula

$$\tilde{\sigma}_{O_2} = \sigma_{O_2} + \frac{\gamma_{CO_2}\sigma_{CO_2} + \gamma_{H_2O}\sigma_{H_2O}}{\gamma_{O_2}} . \qquad (7.8)$$

where γ_i is the number density mixing ratio of the ith specie in the atmosphere. This approximation is especially applicable to the low grazing heights near sunrise, and allows the direct use of the same computer program which calculated J_2 and J_3 at sunrise for calculating δ_3 and δ_4.

Figures 7.4, 7.5, and 7.6 illustrate the photodetachment rates δ_3, δ_4, and δ_6 for O_2^-, O^-, and NO_2^- respectively. The O_2^- and O^- rates rise rapidly at sunrise, almost exponentially, and reach their full daytime values in about 2-4° after geometrical sunrise. A small amount of residual twilight photodetachment will exist for these ions. The NO_2^- rates, because of their dependence on shorter wavelengths, begin to rise later in the sunrise. By ignoring the details in their behavior, each set of photodetachment rates can be parameterized for a numerical analysis of the charged specie continuity equations at sunrise. This would include the photodetachment rates of NO_3^- and O_3^- as well as those of O_2^-, O^-, and NO_2^-. Reference can be made to Figures 3.7, 7.4, 7.5, and 7.6. In Chapter 8 suitable models will be developed where they are needed.

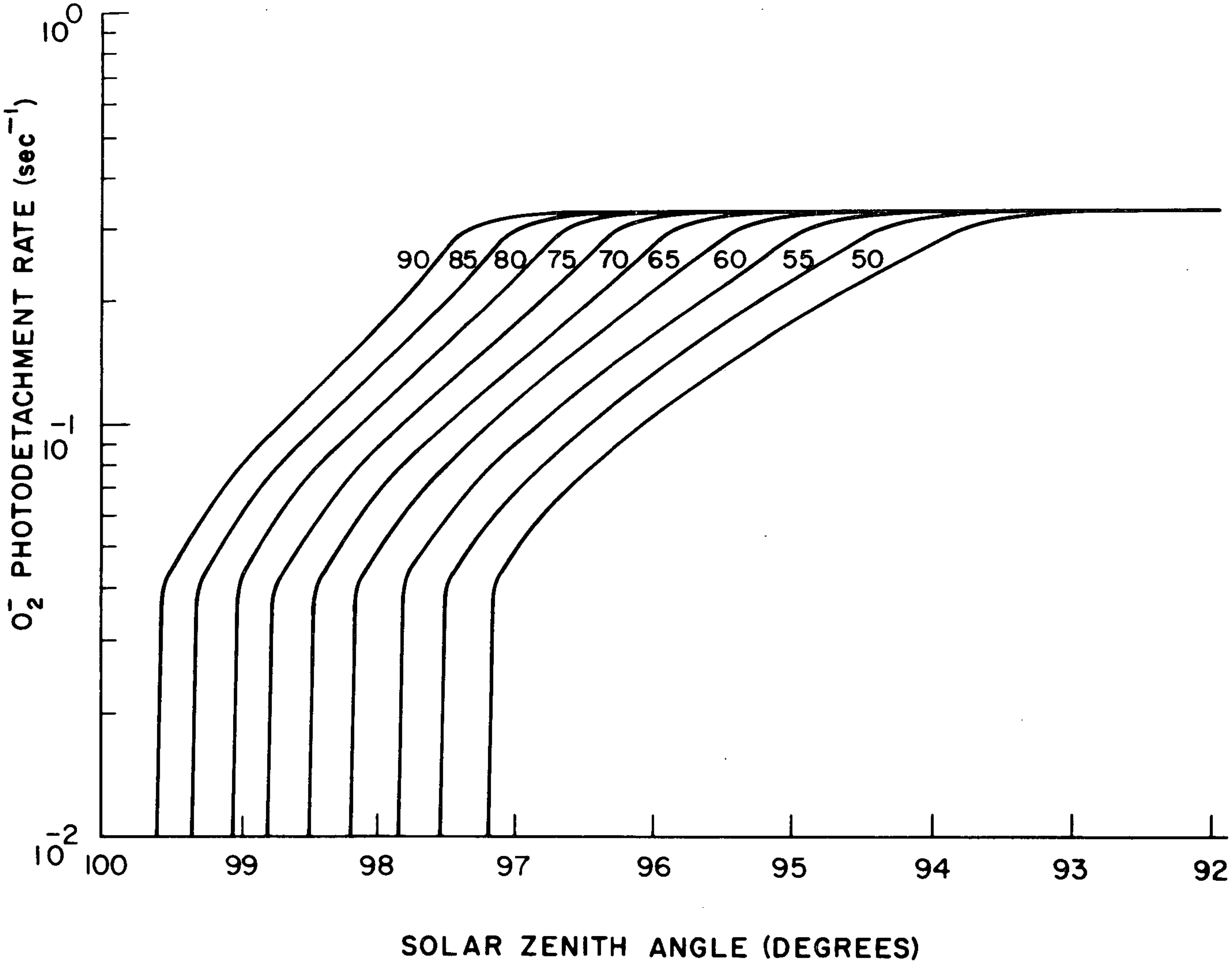

Figure 7.4 O_2^- photodetachment rates over sunrise.

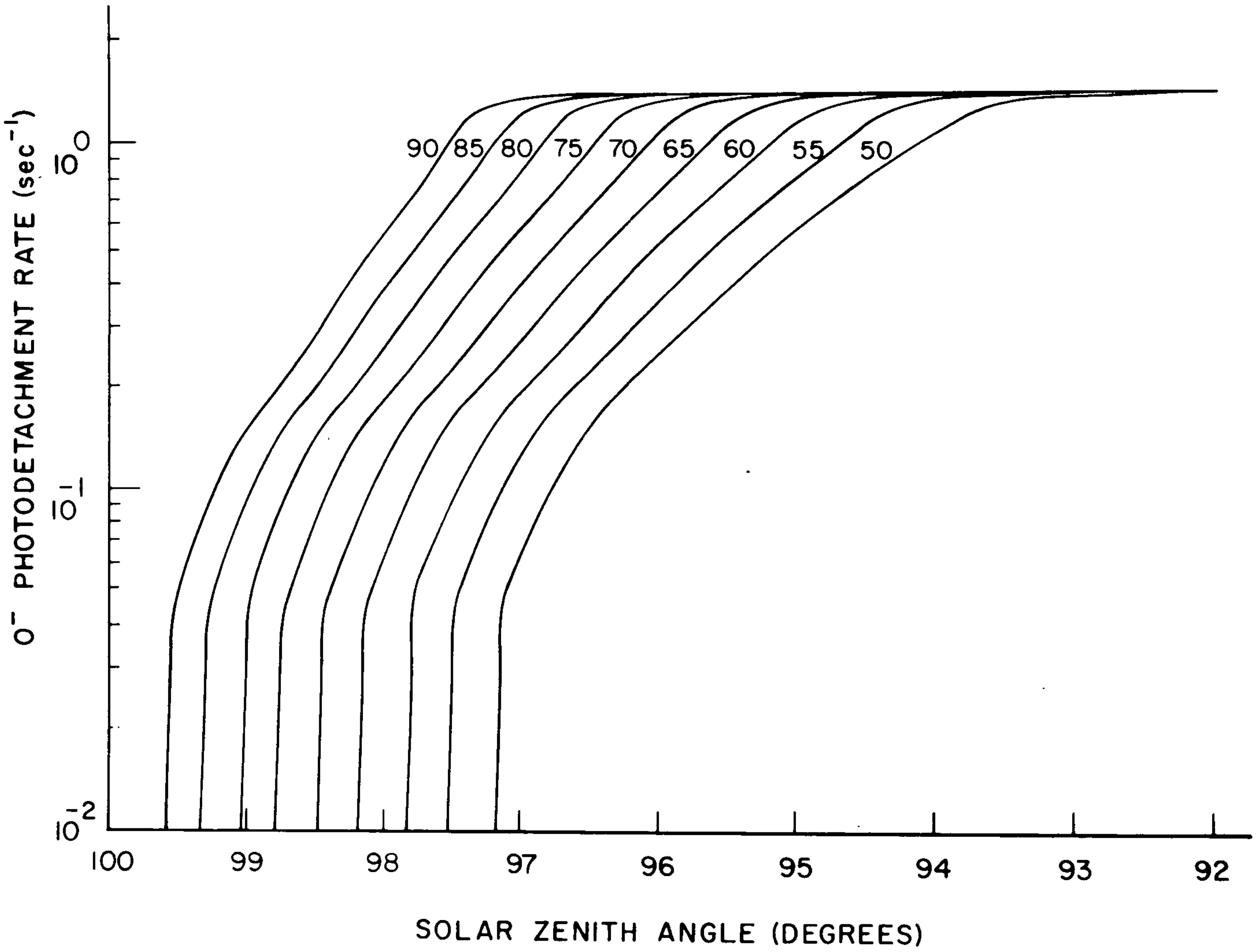

Figure 7.5 O^- photodetachment rates over sunrise.

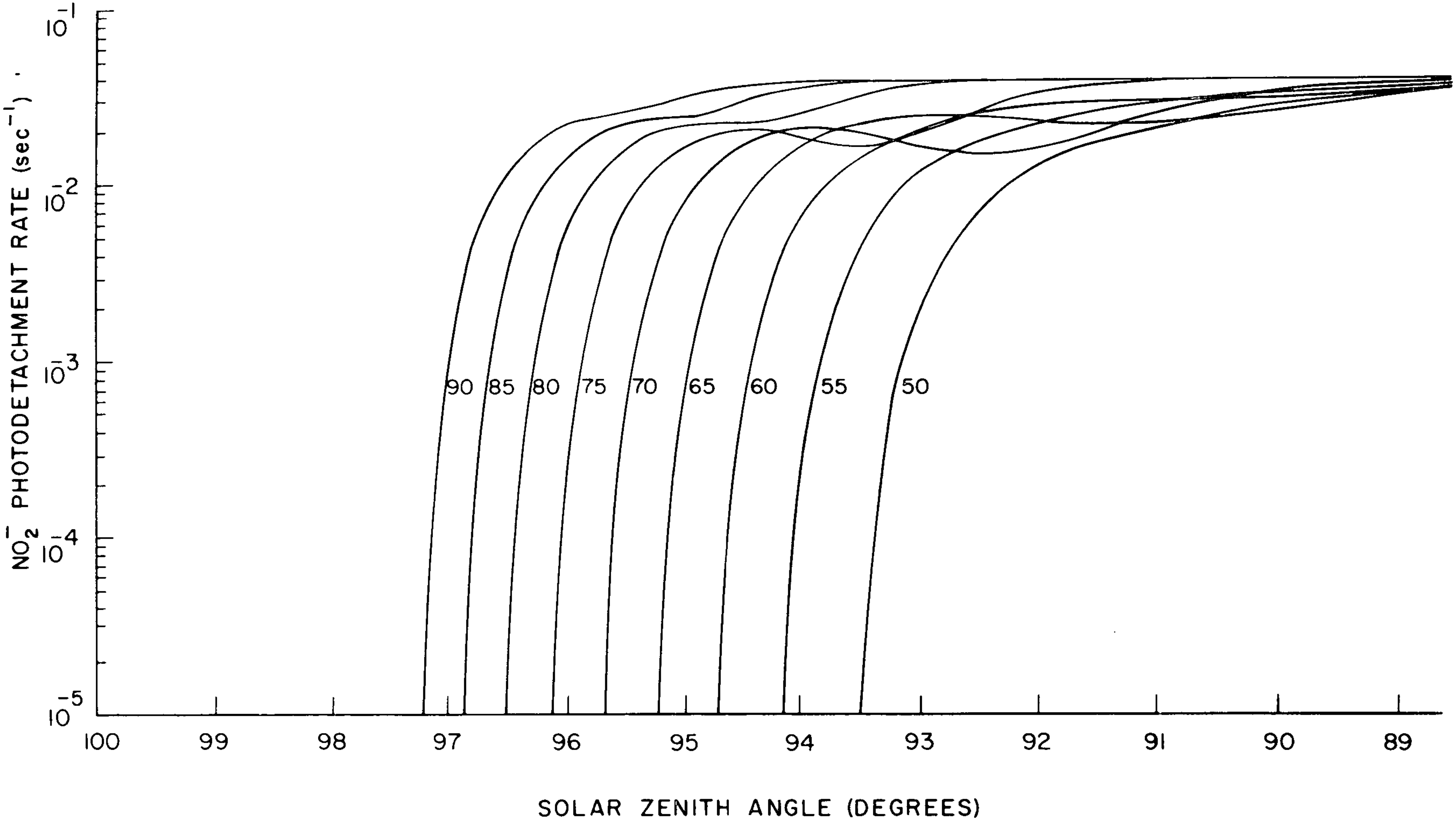

Figure 7.6 NO_2^- photodetachment rates over sunrise.

8. SOLUTION OF THE SUNRISE PROBLEM

Figure 8.1 is a block diagram of the basic processes which lead to the production and neutralization of charge in the D region (LeLevier and Branscomb, 1968). The various interactions between electrons and positive and negative ions are represented by the parameters α, β, ε, and δ for electron-ion recombination, attachment, ion-ion neutralization or recombination, and detachment, respectively. For ease in writing the chemical equations the following notation is used throughout

$$\left.\begin{array}{l} n_i \text{ - neutral specie density with the subscript assignments:} \\ \quad N_2\text{-}0,\ O\text{-}1,\ O_2\text{-}2,\ O_3\text{-}3,\ NO\text{-}4,\ NO_2\text{-}5,\ CO_2\text{-}6, \\ \quad H_2O\text{-}7,\ H_2\text{-}8,\ N\text{-}9,\ O_2({}^1\Delta)\text{ - }\Delta,\ \text{atmosphere - M} \end{array}\right\}$$

$$\left.\begin{array}{l} \bar{n}_i \text{ - negative ion density with the subscript assignments:} \\ \quad O^-\text{-}1,\ O_2^-\text{-}2,\ O_3^-\text{-}3,\ O_4^-\text{-}4,\ NO_2^-\text{-}5,\ NO_3^-\text{-}6,\ CO_3^-\text{-}7,\ CO_4^-\text{-}8 \end{array}\right\} \qquad (8.1)$$

$$\left.\begin{array}{l} n_i^+ \text{ - positive ion density} \\ n_e \text{ - electron density} \\ N^+ \text{ - total positive ion density} \\ N^- \text{ - total negative ion density} \end{array}\right\}$$

All densities are number densities in cm^{-3}.

8.1 The Continuity Equations

The electron continuity equation can be written

$$\dot{n}_e = q + \sum_i \delta_i \bar{n}_i - n_e \sum_{i,j} \beta_{ij} n_j - \tilde{\alpha} N^+ n_e \qquad (8.2)$$

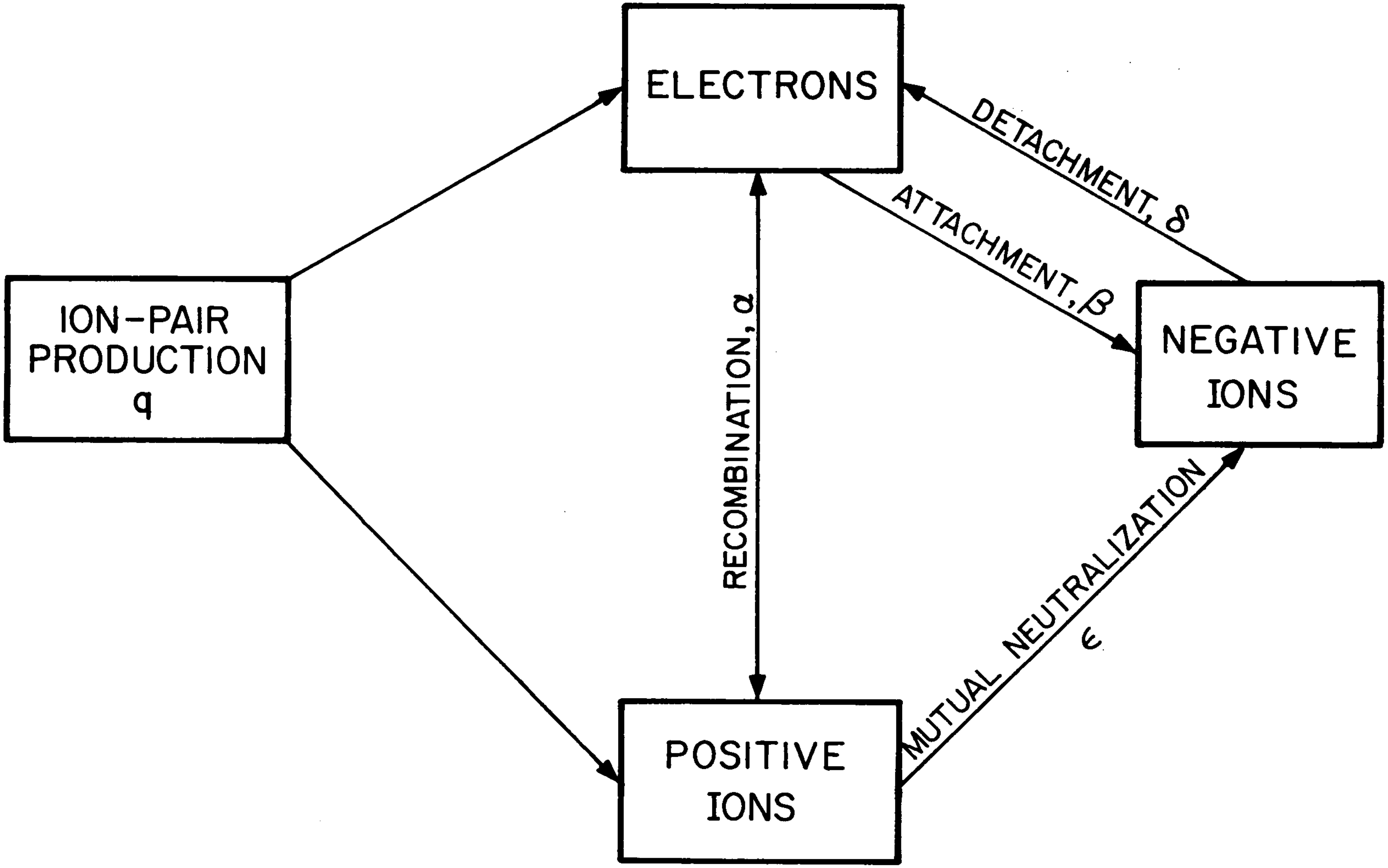

Figure 8.1 Ionization interaction scheme.

where,

$$q = q_{NO}(Ly\alpha) + q_{CR} + q_{\Delta}[O_2(^1\Delta)] + q_{el} \tag{8.3}$$

and the q's are specified in Chapter 5. The α's and β's are represented as equivalent two body rates (cm^3 sec^{-1}), and the δ's as one-body rates (sec^{-1}). $\tilde{\alpha}$, the average electron-ion recombination coefficient, can be defined for a given positive ion composition by

$$\begin{aligned} \tilde{\alpha} &= \sum_i \alpha_i n_i^+/N^+ \\ N^+ &= \sum_i n_i^+ \end{aligned} \tag{8.4}$$

where α_i is the electron-ion recombination coefficient for the ith positive ion. Also in (8.2), β_{ij} is the attachment rate of electrons to the jth neutral constituent to form the ith negative ion and, δ_i is the sum of all the detachment coefficients for the ith negative ion (photodetachment, associative detachment, etc.). Note: sums over i, j, etc. are over the range of the type of specie being considered, and the ranges of each type of specie are not necessarily the same.

Charge neutrality requires that

$$N^+ = n_e + \sum_i \bar{n}_i = n_e + N^- \quad . \tag{8.5}$$

One usually defines the ratio of a particular negative ion density to electron density by

$$\lambda_i = \bar{n}_i/n_e$$

and

$$\Lambda = \sum_i \lambda_i = N^-/n_e \tag{8.6}$$

so that charge neutrality is expressed as

$$N^+ = (1 + \Lambda)\, n_e = (1 + \frac{1}{\Lambda})N^- \quad . \tag{8.7}$$

The continuity equation for the total positive ions is

$$\dot{N}^+ = q - \tilde{\alpha}\, N^+\, n_e - \tilde{\varepsilon}\, N^+\, N^- \tag{8.8}$$

where $\tilde{\varepsilon}$ is formally defined by

$$\tilde{\varepsilon} = \sum_{i,j} \varepsilon_{ij}\, n_j^+\, \lambda_i / \Lambda N^+ \quad . \tag{8.9}$$

Here ε_{ij} is the ion-ion recombination coefficient for the ith negative ion and the jth positive ion. One can also define the average ion-ion recombination coefficient for the ith negative ion with all positive ions by

$$\tilde{\varepsilon}_i = \sum_j \varepsilon_{ij} n_j^+ / N^+$$

so that (8.10)

$$\tilde{\varepsilon} = \sum_i \tilde{\varepsilon}_i\, \lambda_i / \Lambda \quad .$$

Equation (8.8) is obtained by summing the individual continuity equations of each of the positive ions.

The typical negative ion continuity equation is

$$\dot{\overline{n}}_i = n_e \sum_j \beta_{ij} n_j - \delta_i \overline{n}_i - \tilde{\varepsilon}_i N^+\, \overline{n}_i + \sum_{jk} \gamma_{ijk} \overline{n}_j n_k - \overline{n}_i \sum_{jk} \gamma_{jik} n_k \tag{8.11}$$

where the two-body rate constant γ_{ijk} indicates the formation of the ith negative ion in an ion-neutral reaction between the neutral k and the negative ion j.

With the definitions

$$\beta_i = \sum_j \beta_{ij} n_j$$
$$\tilde{\beta} = \sum_i \beta_i \qquad (8.12)$$
$$\gamma_{ij} = \sum_{k(j)} \gamma_{ijk} n_k \quad .$$

Equations (8.2) and (8.11) become

$$\dot{n}_e = q + \sum_i \delta_i \overline{n}_i - \tilde{\beta} n_e - \tilde{\alpha} N^+ n_e$$
$$\dot{\overline{n}}_i = \beta_i n_e - \delta_i \overline{n}_i - \tilde{\varepsilon}_i N^+ \overline{n}_i + \sum_j [\gamma_{ij} \overline{n}_j - \gamma_{ji} \overline{n}_i] \quad . \qquad (8.13)$$

The various terms in the continuity Equations (8.13) are given in Table 8.1 based on the reactions and rate constants in Tables 7.2 and 7.3. The parameters $\tilde{\alpha}$ and $\tilde{\varepsilon}_i$ will have to be estimated at each altitude (such as in Figure 6.4). Quantities shown in Table 8.1 with an asterisk have a sunrise variation which is included in the calculations.

By summing all the negative ion continuity equations and defining the average detachment coefficient

$$\tilde{\delta} = \sum_i \delta_i \lambda_i / \Lambda \quad . \qquad (8.14)$$

Equations (8.13) become

$$\dot{n}_e = q + \tilde{\delta} N^- - \tilde{\beta} n_e - \tilde{\alpha} N^+ n_e$$
$$\dot{N}^- = \tilde{\beta} n_e - \tilde{\delta} N^- - \tilde{\varepsilon} N^+ N^- \quad . \qquad (8.15)$$

Table 8.1. Continuity Equation Parameters

Specie	β_i	δ_i	$\sum_j \delta_{ij}\bar{n}_j$	$\sum_j \gamma_{ji}$
$1{:}O^-$	$\beta_3 n_3^* + \beta_5 n_1^*$	$\delta_4^* + \delta_7 n_1^* + \delta_8 n_\Delta^* + \delta_9 n_4^*$ $+\delta_{10} n_8 + \delta_{12} n_9 + \delta_{13} n_o$	--------------------	$\gamma_{33} n_3^* + \gamma_{34} n_5^* + \gamma_{35} n_2^2$
$2{:}O_2^-$	$\beta_{2a} n_2^2 + \beta_{2b} n_2 n_o$ $+\beta_{2c} n_2 n_7 +$ $\beta_4 n_2$	$\delta_3^* + \delta_1 n_1^* + \delta_{2a} n_\Delta^*$ $+\delta_{2b} n_2 + \delta_{2c} n_o + \delta_{11} n_9$	$\gamma_{36} n_1^* \bar{n}_3 + \gamma_{41} n_1^* \bar{n}_7$	$\gamma_{31} n_3^* + \gamma_{32} n_5^* + \gamma_{43} n_M n_2$
$3{:}O_3^-$	--------	δ_5^*	$\gamma_{31} n_3^* \bar{n}_2 + \gamma_{33} n_3^* \bar{n}_1 + \gamma_{35} n_2^2 \bar{n}_1 + \gamma_{46} n_1^* \bar{n}_4$	$\gamma_{36} n_1^* + \gamma_{37} n_6 + \gamma_{38} n_4^*$
$4{:}O_4^-$	--------	--------------	$\gamma_{43} n_M n_2 \bar{n}_2$	$\gamma_{44} n_6 + \gamma_{45} n_4^* + \gamma_{46} n_1^*$
$5{:}NO_2^-$	--------	δ_6^*	$\gamma_{32} n_5^* \bar{n}_2 + \gamma_{34} n_5^* \bar{n}_1 + \gamma_{42} n_4^* \bar{n}_7$	$\gamma_{39} n_3^* + \gamma_{40} n_5^*$
$6{:}NO_3^-$	--------	δ_{14}^*	$\gamma_{38} n_4^* \bar{n}_3 + \gamma_{39} n_3^* \bar{n}_5 + \gamma_{40} n_5^* \bar{n}_5$ $+\gamma_{45} n_4^* \bar{n}_4 + \gamma_{47} n_4^* \bar{n}_8$	-------------------
$7{:}CO_3^-$	--------	-------------	$\gamma_{37} n_6 \bar{n}_3 + \gamma_{48} n_1^* \bar{n}_8$	$\gamma_{41} n_1^* + \gamma_{42} n_4^*$
$8{:}CO_4^-$	--------	------------	$\gamma_{44} n_6 \bar{n}_4$	$\gamma_{47} n_4^* + \gamma_{48} n_1^*$

Together with Equations (8.8) and (8.5), these four equations form a simplified set which can yield valuable information about the ionosphere (Hargreaves, 1962).

8.2 A Discussion of Some Solutions and the Behavior of the Continuity Equations

8.2.1 Equilibrium solutions

It follows immediately from Equation (8.8) that one implicit solution for the electron density under equilibrium conditions is

$$n_e = \sqrt{\frac{q}{\alpha_{eff}}} \tag{8.16}$$

where the effective electron recombination coefficient is

$$\alpha_{eff} = (1+\Lambda)\ (\tilde{\alpha} + \tilde{\varepsilon}\Lambda) \quad . \tag{8.17}$$

In a region where negative ions can be ignored

$$\alpha_{eff} = \tilde{\alpha} \quad ; \quad \Lambda << 1 \quad . \tag{8.18}$$

Note: The sign >> is to imply a factor of at least 10 in this study. Equation (8.16) with $\alpha_{eff} = \tilde{\alpha}$ is the explicit equilibrium solution for n_e. This follows since the positive ion density ratios are completely determined independently of n_e by the ionization sources, the positive ion chemistry, and the charge neutrality condition. In other regimes, where negative ions are important, the parameters $\tilde{\alpha}$, $\tilde{\varepsilon}$, and Λ will be chemically inter-related, however. One can make the assumption that $\tilde{\alpha}$ and $\tilde{\varepsilon}$ are fixed quantities, which would be strictly correct if the component α's and ε's of $\tilde{\alpha}$ and $\tilde{\varepsilon}$ were about the same size or if the ionic composition was not greatly affected with changing Λ, or if some proper combination of these possibilities were to exist. In any case it is an assumption which is used in this study.

Referring to Equations (8.7), (8.8), and (8.15) one can obtain some parametric equilibrium solutions for these equations which are useful under certain circumstances. When $\tilde{\delta} << \tilde{\varepsilon}N^+$, such as during the night below 80 km, one has

$$N^+N^- = \frac{q}{\tilde{\varepsilon}} \frac{1}{1 + \frac{\tilde{\alpha}}{\tilde{\varepsilon}} \frac{1}{\Lambda}}$$

$$N^+ = N^- \left(1 + \frac{1}{\Lambda}\right) \qquad (8.19)$$

$$n_e = \frac{q}{\tilde{\beta}} \frac{1}{1 + \frac{\tilde{\alpha}}{\tilde{\varepsilon}} \frac{1}{\Lambda}}$$

which simplify when $\Lambda >> 1$, or $\tilde{\varepsilon}\Lambda/\tilde{\alpha} >> 1$. If $\tilde{\delta} >> \tilde{\varepsilon}N^+$ one can write

$$N^+n_e = \frac{q}{\tilde{\alpha}} \frac{1}{1 + \frac{\tilde{\varepsilon}}{\tilde{\alpha}} \Lambda}$$

$$N^+ = n_e(1 + \Lambda) \qquad (8.20)$$

$$\Lambda = \tilde{\beta}/\tilde{\delta} \quad .$$

These equations will simplify when $\Lambda << 1$, or $\tilde{\varepsilon}\Lambda/\tilde{\alpha} << 1$ and can be used above 65 km during the day, and above 75 km at night also. Note that the first two equations of each set are the same equations written in different forms, and are equivalent to Equations (8.7), (8.16), and (8.17). If Λ is assumed to be a known quantity, the equilibrium densities can be determined exactly.

The use of Equations (8.19 and 20) depend on defining the regions where negative ion detachment is either dominant or absent. For example, at 60 km during the day detachment is important but Λ is also large, so that Equations (8.20) are not very useful (even though the first two equations of each set are exact equilibrium solutions, while only the third depends on the size of $\tilde{\delta}$).

There are also regimes where $\Lambda >> 1$, but $\tilde{\varepsilon}\Lambda/\tilde{\alpha} \sim 1$, especially when one assumes fast electron-ion recombination. Generally Equations (8.19 and 20) will give a very accurate estimate of the densities in the pre- and postsunrise regions; and in many cases discussed later, where the species are actually in quasi-equilibrium, the estimates are nearly exact.

The equilibrium continuity equations can yield information about the dependence of the electron density on the electron-ion recombination coefficient. One can show that

$$\frac{1}{n_e}\frac{dn_e}{d\tilde{\alpha}} = \begin{cases} -1/2\tilde{\alpha} & ; \quad \Lambda << 1 \\ -1/\tilde{\varepsilon}\Lambda & ; \quad \Lambda >> 1 \quad , \quad \tilde{\delta} << \tilde{\beta}/\Lambda, \text{ or } \tilde{\delta} << \tilde{\varepsilon}N^+ \end{cases} \quad . \tag{8.21}$$

The equations indicate that changes in $\tilde{\alpha}$ will have different effects on n_e at different altitudes. Basically, the lower one goes, the smaller is the effect. At the lowest altitudes (e.g. below 65 km during the day) a reduction in n_e is produced indirectly by a reduction in the positive and negative ion densities which is induced by electron-ion recombination. Since the electrons are controlled by attachment and detachment here, lower negative ion densities lead to smaller electron densities. At higher altitudes the electrons are directly controlled by electron-ion recombination.

One can continue this analysis and show that

$$\frac{1}{\Lambda}\frac{d\Lambda}{d\tilde{\alpha}} \doteq -\frac{1}{n_e}\frac{dn_e}{d\tilde{\alpha}}\left(\frac{\tilde{\varepsilon}N^+}{\tilde{\delta} + 2\tilde{\varepsilon}N^+}\right) \quad . \tag{8.22}$$

When $\tilde{\varepsilon}N^+ << \tilde{\delta}$, Λ (and the λ_i) is very insensitive to $\tilde{\alpha}$. This effect will be evident above 75 km at all times of the day. One could also arrive at this conclusion by considering the negative ion continuity equations. Each of these equations can be converted to an equation in λ

$$\dot{\lambda}_i + \lambda_i \frac{\dot{n}_e}{n_e} = \beta_i - \delta_i\lambda_i - \tilde{\varepsilon}_i N^+ \lambda_i + \sum_j [\gamma_{ij}\lambda_j - \lambda_{ji}\gamma_i] \quad . \tag{8.23}$$

For equilibrium conditions (i.e. $\dot{\lambda} \sim 0$), and when ion-ion recombination can be ignored compared to the other negative ion loss processes, the λ_i determined from Equations (8.23) will depend only on the β's, δ's, and γ's (N^+ will usually depend on $\tilde{\alpha}$). Thus, for the proper conditions, the λ's will be constants.

8.2.2 The time dependent continuity equations

Over sunrise the solutions of Equations (8.23) will remain independent of $\tilde{\alpha}$ at the higher altitudes. Here n_e is approximately in quasi-equilibrium, and is given by Equations (8.16) and (8.18). Then

$$\dot{n}_e/n_e = \dot{q}/2q = 1/\tau_q \tag{8.24}$$

and unless τ_q is of the same order as the other loss process rates for negative ions, the λ's will depend only on the behavior of the photodetachment rates and minor neutral constituent densities over sunrise (i.e. on the changes in the production and loss rates in the continuity equations). The condition for $\tilde{\alpha}$-independence expressed in Equation (8.22) is also applicable to the time dependent case. The properties predicted above were observed and verified in the sunrise computations.

One well-known approximation for the positive ion continuity equation, valid for the conditions that $N^+ \cong N^-$ and $\tilde{\alpha} n_e << \tilde{\varepsilon} N^-$ (e.g. below 75 km at night), is

$$\dot{N}^+ = q - \tilde{\varepsilon} N^{+2} \tag{8.25}$$

which has the solution

$$N^+(t) = N^+_{eq} \frac{1 - ae^{-t/\tau_+}}{1 + ae^{-t/\tau_+}}$$

$$N^+_{eq} = \sqrt{q/\tilde{\varepsilon}}$$

$$\tau_+ = 1/2N^+_{eq}\tilde{\varepsilon} = 1/2\sqrt{q\tilde{\varepsilon}} \tag{8.26}$$

$$a = (N^+_{eq} - N^+(0)/(N^+_{eq} + N^+(0)) \quad .$$

This solution is applied in Section 8.5 to the computation of initial conditions.

At sunrise the electron density (and the negative ion densities) undergo a rapid transitory period. Generally, these large transients are quickly damped out and the continuity equations then go into a state of quasi-equilibrium (or a quasi-steady state). In the presunrise region the species will be nearly in equilibrium, while in the postsunrise region a state of quasi-equilibrium will exist. Consider a particular specie $\bar{n}_i$ which has a very large loss term. It can assume its equilibrium value in a very short time. Thus if

$$\dot{\bar{n}}_i = P_i - L_i\bar{n}_i$$

$$\bar{n}_i \cong e^{-L_it} \int_0^t P_i e^{L_it'}dt' + \bar{n}_i(0)e^{-L_it}$$

$$\bar{n}_i \cong \frac{P_i}{L_i}(1-e^{-L_it}) + \bar{n}_i(0)e^{-L_it} \tag{8.27}$$

$$\bar{n}_i \cong \frac{P_i}{L_i} = \bar{n}_i(eq) \quad ; \quad t > \frac{1}{L_i}$$

where it was assumed that P_i and L_i will not vary much in a time $1/L_i$. $\bar{n}_i$ then adopts the time dependence of P_i and L_i. At sunrise, after a large adjustment in the P_i, L_i, and $\bar{n}_i$, these species quickly settle into a quasi-equilibrium state.

As an aid in interpreting the time dependent electron density behaviors which were calculated, and displayed in Section 8.6, one can differentiate the charge neutrality relation to obtain

$$\dot{n}_e = \dot{N}^+ - \dot{N}^-$$

or

$$\dot{\tau}_e = (1+\Lambda)\dot{\tau}^+ - \Lambda\dot{\tau}^- \tag{8.28}$$

$$\tau_i = \log n_i \quad .$$

At the same time the positive ion continuity equation can be arranged as

$$\dot{N}^+ = q - \tilde{\alpha} n_e N^+ (1 + \frac{\tilde{\varepsilon}}{\tilde{\alpha}}\Lambda)$$

or

$$\dot{N}^+ = q - \tilde{\alpha} n_e N^+ \tag{8.29}$$

when

$$\Lambda << \tilde{\alpha}/\tilde{\varepsilon} \quad .$$

For fast recombination this condition will occur early in the sunrise at some altitudes with the first large increase in electron density. The electron continuity equation for these conditions will be factored as

$$\dot{n}_e = (q - \tilde{\alpha} n_e N^+) - (\tilde{\beta} n_e - \tilde{\delta} N^-) = \dot{N}^+ - \dot{N}^- \quad . \tag{8.30}$$

Thus $\dot{N}^+$ is controlled by ion-pair production and electron recombination, and $\dot{N}^-$ by electron attachment and detachment. It then follows from Equations (8.28) that if $\dot{\tau}_e$, $\dot{\tau}^+$, and $\dot{\tau}^-$ have the same signs, the electrons are production-recombination controlled because $\dot{N}^+$ dominates. If $\dot{\tau}_e$ has the opposite sign of $\dot{\tau}^+$ and $\dot{\tau}^-$, the electrons are attachment-detachment controlled because $\dot{N}^-$ is dominant. If $\dot{\tau}^+$ and $\dot{\tau}^-$ have opposite signs the results are more ambiguous and either or both effects may be important. When $\dot{\tau}_e = 0$ a transition is occuring from one process set to the other (assuming $\ddot{\tau}_e \neq 0$).

More information about the electron density sunrise behavior can be obtained by developing the electron continuity equation further. Assume that the bulk of electrons produced by detachment are detached from O_2^-. Then

$$\dot{n}_e = q - \tilde{\alpha} n_e N^+ - \beta n_e + \delta_T \bar{n}_2$$
$$\delta_T = k_1 n_1 + \delta_2 + k_\Delta n_\Delta + k_c n_M \quad . \qquad (8.31)$$

The density notation (8.1) is being used here. The detachment rates, k_1, k_Δ, and k_c can be obtained from Tables 7.2 and 7.3. The total attachment rate $\tilde{\beta}$ is dominated by the three-body formation of O_2^- with the rate β. The continuity equation for O_2^- is

$$\dot{\bar{n}}_2 = \beta n_e - [k_1(n_1+n_3) + L_c + \delta_2 + k_\Delta n_\Delta + k_c n_M]\bar{n}_2$$
$$+ k_6 n_1 \bar{n}_2 + k_7 n_1 \bar{n}_7 \quad . \qquad (8.32)$$

Here L_c is the loss rate for clustering to form O_4^-, and the conversions of NO_3^- and CO_3^- into O_2^- by atomic oxygen are given the rates k_6 and k_7 respectively (The reaction of NO_3^- with atomic oxygen is discussed at length in Section 8.4. It is postulated as a possible source of O_2^- at sunrise). When these reactions are also the major loss process for these ions, one can write

$$\bar{n}_6 = \bar{n}_6^N e^{-k_6 N_1} + \bar{n}_6^D$$
$$\bar{n}_7 = \bar{n}_7^N e^{-k_7 N_1} + \bar{n}_7^D \qquad (8.33)$$
$$N_1 = \int^t (n_1 - n_1^N)\, dt'$$

where 'N' and 'D' indicate the pre- and postsunrise quasi-equilibrium densities, and it is assumed that $\bar{n}^N >> \bar{n}^D$. For the altitudes and integration intervals of interest in this analysis one can set $n_1^N = 0$. Equations (8.33) are only valid as long as the O_2^- and electrons which are produced do not quickly regenerate CO_3^- and NO_3^-. For example, since $k_6 << k_7$, and $\bar{n}_6^N > \bar{n}_7^N$, from 65-75 km the CO_3^- will be responsible for the early electron production, but will later be swamped by the NO_3^- process, which also produces CO_3^- by the reaction chains $O_2^- \rightarrow O_4^- \rightarrow CO_4^- \rightarrow CO_3^-$ and $O_2^- \rightarrow O_3^- \rightarrow CO_3^-$.

The O_2^- loss rates are very large over the sunrise, and so $\bar{n}_2$ at any time can be approximated by its equilibrium value (see Equation 8.27)

$$\bar{n}_2 = \frac{\beta n_e + k_6 n_1 \bar{n}_6 + k_7 n_1 \bar{n}_7}{k_1 n_3 + L_c + \delta_T} \quad . \tag{8.34}$$

By utilizing the following set of definitions and assumptions

$$\begin{aligned} & r \equiv O/O_3 \text{ ratio} = n_1/n_3 \\ & r_D \equiv n_1^D/n_3^D \\ & r^D \equiv n_1^D/n_3 \cong 1 + r \\ & \kappa_i \equiv k_i n_1^D \\ \text{and} \quad & \delta_T \cong k_1 n_1 \\ & k_1(n_1 + n_3) >> L_c \end{aligned} \tag{8.35}$$

Equation (8.31) becomes

$$\begin{aligned} \dot{n}_e &= q - \tilde{\alpha} n_e N^+ - \beta n_e \left(\frac{1}{1+r}\right) + \left[\frac{r^2}{(1+r) r^D}\right] (\kappa_6 \bar{n}_6 + \kappa_7 \bar{n}_7) \\ \bar{n}_i &= \bar{n}_i^N \exp\left\{- \kappa_i \int^t \frac{r}{r^D} dt'\right\} + \bar{n}_i^D \quad ; \; i = 6,7 \quad . \end{aligned} \tag{8.36}$$

If ion-ion recombination is negligible compared to other negative ion loss processes during the day one can put the electron continuity equation in the final form

$$\dot{n}_e = q - \tilde{\alpha} n_e N^+ - \beta_{eff}\, n_e + P_e(t)$$

$$P_e(t) \doteq \left(\frac{r}{1+r}\right)^2 \sum_i \kappa_i \overline{n}_i^N \exp\left\{-\kappa_i \int^t \left(\frac{r}{1+r}\right) dt'\right\} \qquad (8.37)$$

where $P_e(t)$ is a transient production function which disappears before and after sunrise at the altitudes of interest here, and β_{eff} is the 'effective' attachment rate defined by the relation

$$\beta_{eff} = \beta\left(\frac{1}{1+r}\right)\left[1 - \frac{r^2}{r^D r_D}\right] \quad . \qquad (8.38)$$

In the more general case, when clustering or other O_2^- charge transfer reactions as well as other O_2^- detachment processes are included in the calculations, one can show that β_{eff} and the prefactor in P_e become

$$\beta_{eff} = \beta\left(\frac{1+r_c}{1+r+r_c+r_\delta}\right)\left[1 - \frac{r(r+r_\delta)(1+r_c^D)}{r^D(r_D+r_\delta^D)(1+r_c)}\right]$$

$$P_e(t) \propto \left(\frac{r}{1+r}\right)\left(\frac{r+r_\delta}{1+r+r_c+r_\delta}\right) \qquad (8.39)$$

$$r_c \equiv L_c/k_1 n_3 \quad ; \quad r_\delta \equiv \delta/k_1 n_3$$

$$r_c^D = L_c/k_1 n_3^D \quad ; \quad r_\delta^D = \delta^D/k_1 n_3^D \quad .$$

The electron production function P_e will have peaks during sunrise because each component has the form xe^{-x}. For the case assumed above there will be two possible peaks - one for CO_3^- and one for NO_3^-. If one uses a model for $r/(1+r)$ in the form of a normalized Fermi distribution centered on χ_0 with a width 2Δ, one can show that the separation of the peaks will be given by

$$\chi_p(CO_3^-) - \chi_p(NO_3^-) = 8.7\Delta \quad . \tag{8.40}$$

The shape and width of the peaks will depend on the details of the O distribution. The production of O_2^- from one process can affect the other. This can be seen in the CO_3^- distributions for 65 and 70 km illustrated in Figures 8.7 and 8.8 of Section 8.6.2. The electron density at sunrise is proportional to some integral of P_e. Thus the electron density will grow most rapidly near a peak in P_e. As P_e decreases, the electron density will begin to decay toward an equilibrium value. These effects are discussed for specific cases in Section 8.6.

The effective attachment rate decreases during sunrise. Below 80 km before sunrise, $\beta_{eff} \doteq \beta$, and attachment will be the dominant electron loss process. Between 65 and 75 km after sunrise $\beta_{eff} \to 0$ as attachment and detachment begin to offset one another, and the electrons are then controlled by recombination. Note that $\beta_{eff} \to 0$ as the system equilibrates provided that ion-ion recombination is negligible. Below 65 km during the day Equations (8.37) are not valid because firstly, the behaviors of the CO_3^- and NO_3^- were not properly formulated for these heights; and secondly, the ion-ion recombination term, $\tilde{\epsilon}N^-N^+$, is significant here because $n_e << N^-$ even during the day. Ion-ion recombination provides a sink for those electrons which undergo attachment. Using the negative ion continuity equation one can see that as the system equilibrates

$$\beta n_e - \tilde{\delta} N^- \cong \tilde{\varepsilon} N^- N^+ .$$

or

$$\beta_{eff} n_e \cong \tilde{\varepsilon} N^- N^+ \qquad (8.41)$$

and so

$$\frac{\tilde{\alpha} n_e N^+}{\beta_{eff} n_e} \cong \frac{\tilde{\alpha}}{\tilde{\varepsilon}\Lambda} .$$

Thus attachment (followed by ion-ion recombination) will be the primary electron loss process when

$$\Lambda > \frac{\tilde{\alpha}}{\tilde{\varepsilon}} \qquad (8.42)$$

β_{eff} will still decrease in importance over the sunrise as Λ decreases, but it will not go to zero. The effects induced by transient electron production below 65 km as the system changes from one quasi-equilibrium state to another are not included in this analysis.

8.2.3 Some equilibrium properties of the continuity equations

As already discussed in Section 8.2.2, the continuity equations for some of the negative ions are dominated by only one or two fast loss reactions, and their densities are essentially in equilibrium with some other specie densities. Considering altitudes below 80 km (not a necessary condition) several close couplings can be found and verified by studying the calculated density variations over sunrise which are illustrated in Section 8.6. O_4^- is formed by clustering from O_2^-, and is rapidly lost by reacting with CO_2. One can show that

$$\bar{n}_4 = 3.25 \times 10^{-17} \, n_M \bar{n}_2 \quad . \qquad (8.43a)$$

Once atomic oxygen appears at sunrise, and as long as O > NO, the CO_3^- and CO_4^- densities are closely coupled by the relation

$$\bar{n}_7 = 1.88\ \bar{n}_8 \tag{8.43b}$$

O_3^- is produced by charge transfer from O_2^- to O_3, and is quickly lost by reacting with CO_2. This leads to the relation

$$\bar{n}_3 = 2.5 \times 10^3 \frac{n_3}{n_M} \bar{n}_2 \quad . \tag{8.43c}$$

A complete discussion of the equilibrium continuity equations would be very lengthy. Specific processes are discussed later where they are relevant. The terms in the continuity equations can be obtained from Table 8.1, using the rate constants in Tables 7.2 and 7.3.

The electron density scale height, H_e, can be estimated for the topside and bottomside of the C layer by utilizing the continuity equations and some of the results already obtained. The layer is formed by galactic cosmic rays and lies below 75 km with its peak near 65 km. Above 65 km just after sunrise one has

$$n_e^2 \propto q_{CR} \propto n_M \propto e^{-z/H_M}$$

or (8.44)

$$H_e = 2H_M \quad ; \quad z > 65\ \text{km} \quad .$$

Below 65 km the situation is more complex, but assuming that electrons are produced mainly by O_2^- associative detachment and are lost by three-body attachment to form O_2^- (Reid, 1968a), then

$$n_e \propto \frac{n_1}{n_M^2}\,\overline{n}_2 \qquad (8.45a)$$

$\overline{n}_2$ at low altitudes is controlled by the clustering reaction sequence, which leads to

$$\overline{n}_2 \propto \frac{n_1}{n_M^2}\,\overline{n}_7 \quad . \qquad (8.45b)$$

It can also be shown that

$$\overline{n}_7 \overset{\propto}{\sim} \frac{N^-}{n_4}$$

and

$$N^+ \sim N^- \propto q_{CR}^{1/2} \propto n_M^{1/2} \quad . \qquad (8.45c)$$

If one allows that $n_4 \propto n_M$ Equations (8.45a to c) yield

$$n_e \propto \frac{n_1^2 N^-}{n_M^5} \propto e^{2z/H_O}\, e^{9z/2H_M}$$

$$H_e = -\left(\frac{2}{H_O} + \frac{9}{2H_M}\right)^{-1} \quad ; \; z < 65 \text{ km} \quad . \qquad (8.46)$$

H_O, the atomic oxygen scale height is given as a negative scale height for these altitudes. One can roughly determine $H_O \sim 7$ km from Table 8.3, and with $H_M \sim 8$ km one has

$$H_e = 16 \text{ km} \; ; \; z > 65 \text{ km}$$

$$H_e = -1.2 \text{ km} \; ; \; z < 65 \text{ km} \quad . \qquad (8.47)$$

This indicates that the C layer will have a very flat bottom and a slowly decreasing topside. There will only be a short period during sunrise when the topside C layer can be observed--after the initial electron density increase but before the Lyman α radiation can penetrate below 80 km.

8.3 Models of the Sunrise Variables

Many of the time variable quantities of Table 8.1 can be modeled using combinations of the following simple forms (see Appendix V)

$$
\begin{aligned}
&\text{(a)} \quad f(\chi) = f_o + \Delta f/[1 + e^{(\chi-\chi_o)/\delta}] \\
&\text{(b)} \quad f(\chi) = f_o + \Delta f[1 - e^{(\chi-\chi_o)/\delta}] \qquad (8.48) \\
&\text{(b)} \quad f(\chi) = f_o + \Delta f(\chi-\chi_o)^{\delta} \quad .
\end{aligned}
$$

In Table 8.2 the parameters f_o, Δf, χ_o, and δ are given at each altitude for the variables listed. The type of model (a, b, or c) is also listed, and where two types are given the total model is a sum of the two models with the top parameters for each altitude going with the first model, etc. Angles, χ_o, with an asterisk represent minimum angles for the $\delta_{O_2^-}$ and δ_{O^-} models. For $\chi < \chi_o^*$ these photodetachment rates are constant at their full daytime values. In these cases the χ_o listed applies to both the component models. For some of the other models certain size limitations must be placed on the exponentials when performing a numerical analysis.

The ionization rates of NO due to direct and scattered Ly α were calculated over sunrise and are illustrated in Figures 8.2 and 8.3. The I_{NO} direct rates are negligible below 75 km for this anslysis. In Table 8.2 these small values are not indicated by f_o, and must be accounted for in the computations by either setting f_o to a large negative value, or $I_{NO} = 0$ (similarly for I_{NO} - scattered and I_Δ).

Table 8.2 Sunrise parameter models

Alt. km		f_o	Δf	χ_o	δ		f_o	Δf	χ_o	δ		f_o	Δf	χ_o	δ		f_o	Δf	χ_o	δ
50		.5	.0	87.0	1.0		--	0	90.	1.0		0	0	90.	1		-1.34 0	.37 -.316	97.20 93.77*	.47 1
55		.257	-.075	88.0	1.0		--	0	90.	1.0		0	0	90.	1		-1.34 0	.32 -.359	97.52 94.37*	.36 1
60		.200	-.111	87.96	1.08	Log_{10}	--	0	90.	1.0		0	0	90.	1	Log_{10}	-1.34 0	.32 -.380	97.82 94.86*	.31 1
65	$n(O_3)$	.467	-.414	88.48	1.44	I_{NO}	--	0	90.	1.0	$q_{el.}$	0	0	90.	1	δ_{O^-}	-1.34 0	.27 -.416	98.15 95.34*	.28 1
70	$\times 10^{-11}$	.603	-.583	90.90	1.10	Direct Flux	--	0	90.	1.0		1.03(-4)	-2.15(-6)	90.	1	(b,c)	-1.34 0	.24 -.460	98.47 95.82*	.24 1
75	(a)	.0603	-.0563	92.64	1.06		-10.00	2.25	81.97	5.52		6.08(-4)	-1.03(-5)	90.	1		-1.34 0	.24 -.470	98.77 96.18*	.23 1
80		.001	-4.25(-4)	93.20	.45	(b)	-10.00	3.00	87.22	3.75	(c)	1.68(-3)	-2.83(-5)	90.	1		-1.34 0	.24 -.510	99.03 96.62*	.22 1
85		6.45(-4)	-2.19(-4)	93.88	.41		- 8.52	1.92	88.65	2.60		3.65(-3)	-5.85(-5)	90.	1		-1.34 0	.24 -.522	99.30 96.97*	.21 1
90		5.0(-4)	-1.38(-4)	94.46	.25		- 7.50	1.08	89.50	2.20		7.83(-3)	-1.08(-4)	90.	1		-1.34 0	.21 -.554	99.57 97.30*	.20 1
50		0	9.04	85.25	1.0		--	0	100.	1		0	1.46(-3)	84.95	1.0		-2.50	.97	92.80	.62
55		0	8.90	86.85	1.0		--	0	100.	1		0	1.64(-3)	86.41	.95		-2.56	1.03	93.59	.56
60	Log_{10}	5.30	3.40	88.12	1.08	Log_{10}	--	0	100.	1	$\delta_{NO_3^-}$	0	1.78(-3)	86.73	.90	Log_{10}	-2.61	1.08	94.26	.51
65	$n(NO)$	7.93	.52	89.85	1.44	I_{NO}	-10.59	-.01	100.	1		0	1.88(-3)	87.05	.85		-2.63	1.10	94.79	.44
70		8.08	.07	91.42	1.10	Scattered	- 9.32	-.01	100.	1		0	1.96(-3)	88.45	.77	$\delta_{NO_2^-}$	-2.69	1.16	95.30	.39
75	(a)	7.85	0	92.60	1.06		- 8.65	-.01	100.	1	(a)	0	2.00(-3)	91.25	.45	(b)	-2.69	1.21	95.76	.41
80		7.54	0	93.37	.45	(c)	- 8.34	-.01	100.	1		0	2.00(-3)	92.90	.29		-2.79	1.38	96.18	.40
85		7.26	0	94.05	.41		- 8.20	-.01	100.	1		0	2.00(-3)	93.75	.27		-2.93	1.52	96.60	.35
90		7.00	0	90.	.25		- 8.15	-.01	100.	1		0	2.00(-3)	94.49	.26		-2.87	1.46	96.97	.36
50		8.68	-2.03	85.25	1.0		--	0	90.	1.0		-1.41 0	.22 -.208	97.20 93.70*	.57 1		3.1(-2)	----	----	---
55		8.76	-2.53	86.85	1.0		--	0	90.	1.0		-1.41 0	.20 -.226	97.50 94.23*	.42 1		1.8(-2)	----	----	---
60	Log_{10}	8.48	-2.85	88.12	1.08	Log_{10}	--	0	90.	1.0	Log_{10}	-1.41 0	.16 -.260	97.85 94.80*	.27 1		8.8(-3)	----	----	---
65	$n(NO_2)$	7.90	-3.00	89.85	1.44	I_Δ	--	0	90.	1.0	$\delta_{O_2^-}$	-1.41 0	.14 -.274	98.20 95.27*	.30 1		3.9(-3)	----	----	---
70		6.81	-2.51	91.42	1.10		--	0	90.	1.0		-1.41 0	.14 -.289	98.50 95.73*	.37 1	q_{CR}	1.7(-3)	----	----	---
75	(a)	5.78	-1.81	92.60	1.06	(b)	-11.72	2.25	78.97	5.52	(b,c)	-1.41 0	.14 -.297	98.80 96.10*	.30 1		7.5(-4)	----	----	---
80		4.85	-1.15	93.37	.45		-12.06	3.00	84.22	3.75		-1.41 0	.12 -.325	99.05 96.55*	.25 1		3.3(-4)	----	----	---
85		3.98	- .68	94.05	.41		-10.67	1.92	85.65	2.60		-1.41 0	.11 -.339	99.30 96.92*	.19 1		1.2(-4)	----	----	---
90		0	0	90.	.25		- 9.53	1.08	86.50	2.20		-1.41 0	.10 -.371	99.55 97.30*	.15 1		0	----	----	---

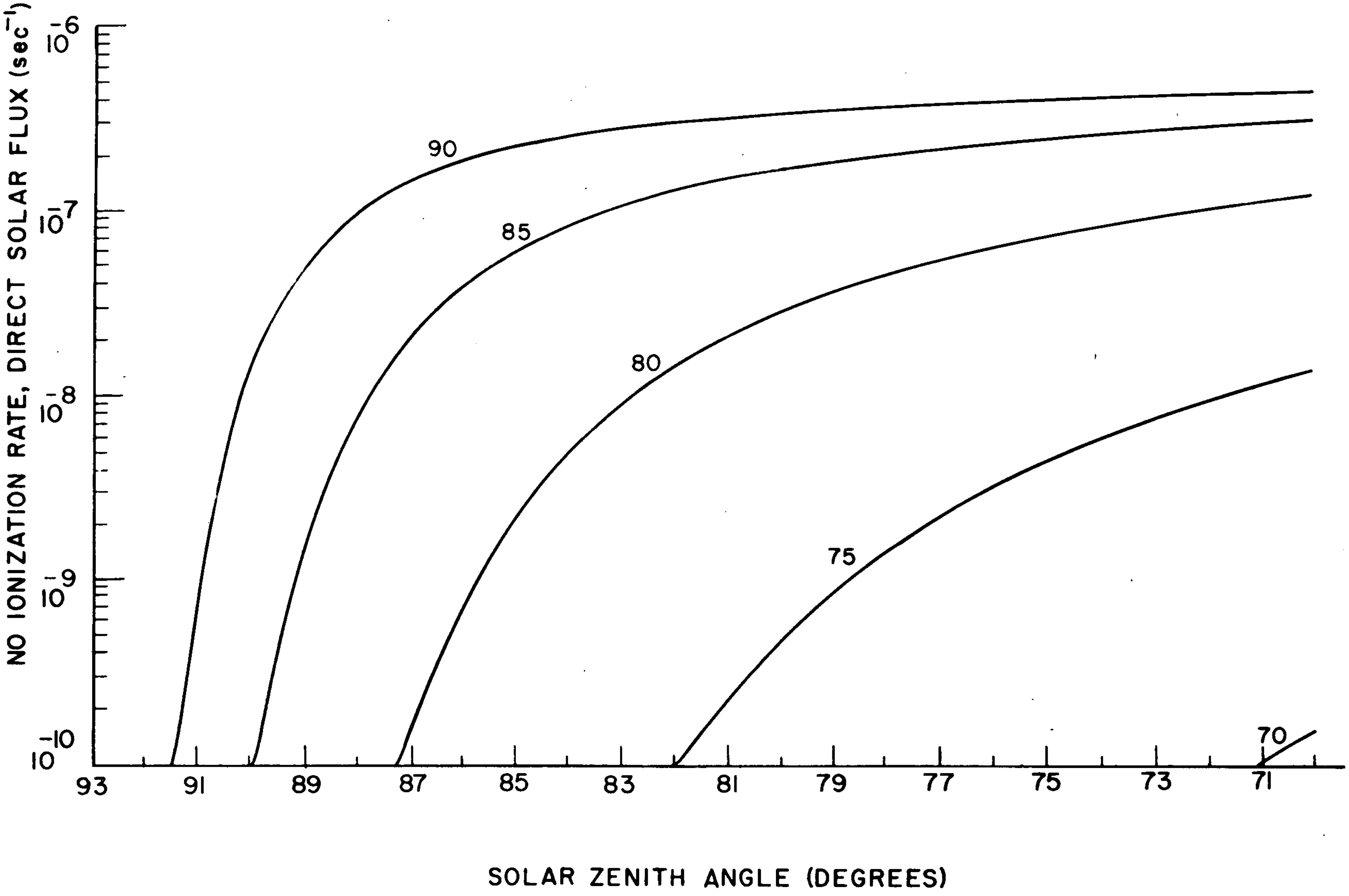

Figure 8.2 Nitric oxide ionization rates by direct solar radiation over sunrise.

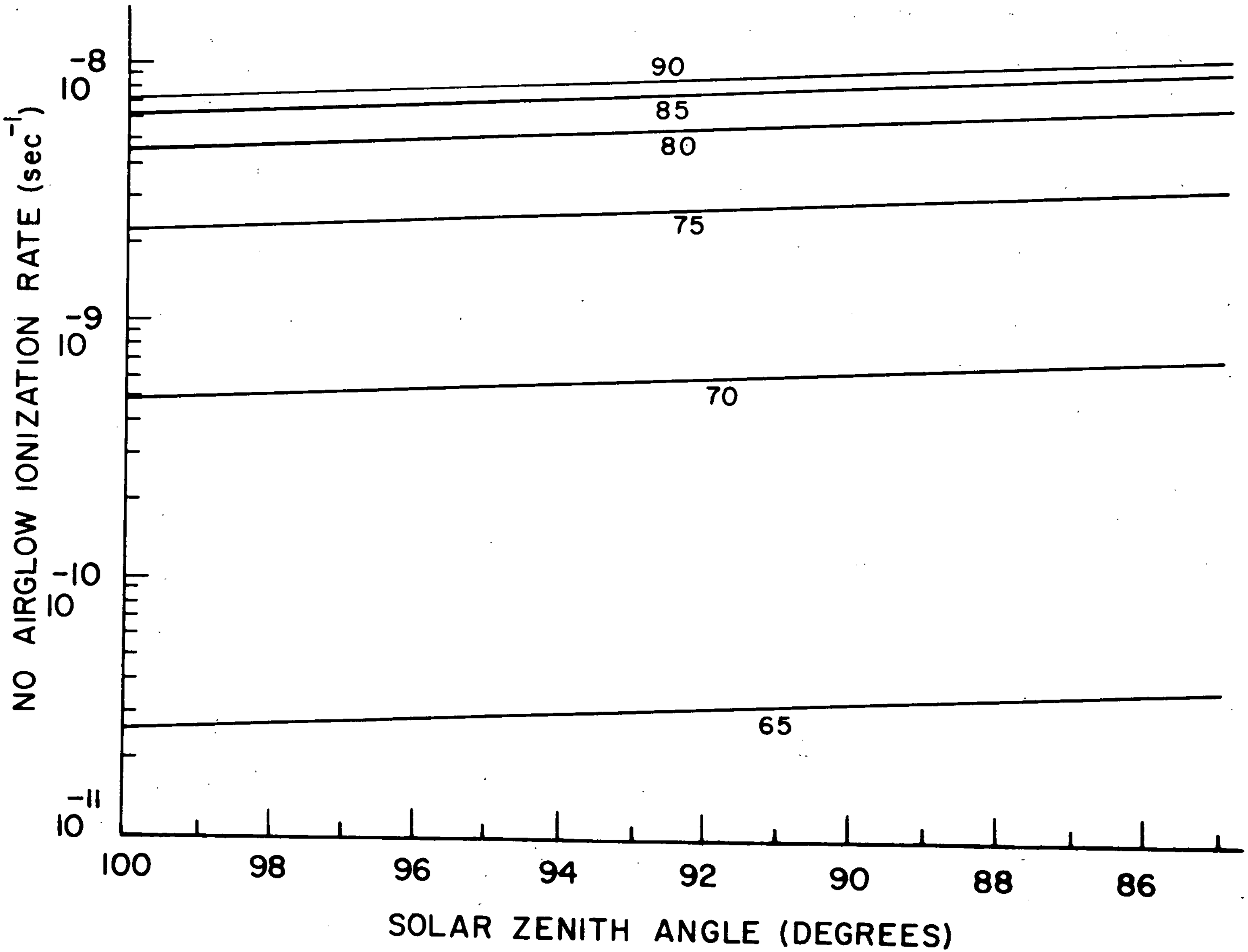

Figure 8.3 Nitric oxide ionization rates by scattered Lyman alpha radiation over sunrise.

The NO and NO_2 density models are given a χ_o corresponding to that of the uniform ozone photodissociation rates as well as the same angular widths as the ozone distribution models. Wherever their density goes to zero, a value of 1 is specified. It should be noted that the NO and NO_2 daytime and nighttime densities are taken from Tables 4.4 and 4.5 and are not necessarily consistent with a simple photochemical $NO_2 \rightarrow NO$ conversion at sunrise. Perhaps a better model for NO and NO_2 would result by using the uniform ozone density distribution parameters. But this change would not significantly alter the results or analyses which will follow. The NO_3^- photodetachment rate is modelled after the nonuniform ozone photodissociation rates since the ozone Hartley band threshold probably corresponds approximately to the NO_3^- photodetachment threshold.

The ion-pair production rates q_{CR} and q_{el} are tabulated for 0° magnetic latitude, and q_{el} is reduced by a factor of 1/20 from the values in Figure 5.1. The q_{el} variation has been linearized over the sunrise. The $O_2(^1\Delta)$ ionization rates were given the same parameters as the NO direct flux ionization rate except that the curves were shifted away from the sunrise by 3° because of the shorter wavelength threshold. The daytime I_Δ values are calculated from Hunten and McElroy's (1968) q_Δ and Evans' et al. (1968) $O_2(^1\Delta)$ densities. Since I_Δ is a negligible parameter in this study, the fact that Huffman, et al. (1970) lowered the Hunten and McElroy (1968) $O_2(^1\Delta)$ ionization rates is not critical here. The I_Δ values in Table 8.2 could be proportionately reduced without affecting the results of this work.

The ozone distributions of Table 8.2 were determined from Figures 3.2 and 3.7. The atomic oxygen and $O_2(^1\Delta)$ densities were modelled from Figures 3.9 and 4.5, respectively, using piecewise linear representations, and those data are not reproduced here.

8.4 Specification of the Variable Parameters in the Computations

Two parameters in the sunrise calculations which were considered as variable were the atomic oxygen and nitric oxide densities. Several model daytime distributions were constructed and tested. In particular, two daytime values of O and NO were selected at each height. These values are listed in Table 8.3. Combinations of these models, such as a high-O-low-NO model, were utilized in performing the calculations. Both of the NO models of Table 8.3 were lower than the model of Table 4.5. The larger of the NO models was taken to correspond to the behavior suggested by Meira (1970). The electron-ion recombination coefficient, $\tilde{\alpha}$, was kept within upper and lower limits at each height: Reid's (1970) predictions (see Figure 6.4); and 8×10^{-7} cm^3 sec^{-1}. Reid's $\tilde{\alpha}$ values were derived using NO densities which are larger than those of the models used here. Since $\tilde{\alpha}$ is determined by

$$\tilde{\alpha} = q/n_e^2 \qquad (8.49a)$$

and

$$q \doteq q_{NO} \propto n(NO)$$

(where $\Lambda << 1$), then an equivalent $\tilde{\alpha}$ can be defined for a particular daytime NO model by

$$\tilde{\alpha}_{eq} = \tilde{\alpha}_R \frac{n(NO)}{n(NO)_R} \qquad (8.49b)$$

where the subscript 'R' indicates Reid's values. The $\tilde{\alpha}_{eq}$ would approximately reproduce the high altitude electron densities (> 70 km) assumed by Reid (1970) for daytime conditions. In this study the ratio $n(NO)/n(NO)_R$ was always less than one. The value of $\tilde{\alpha} = 8 \times 10^{-7}$ cm^3 sec^{-1} is typical of the dissociative recombination of electrons with simple molecular positive ions such as NO^+ at D-region temperatures (Gunton, 1969; Reid, 1970).

Table 8.3. Atomic oxygen and nitric oxide daytime distributions

Alt. km	High O cm^{-3}	Low O cm^{-3}	High NO cm^{-3}	Low NO cm^{-3}
50	1.0(10)	5.0(9)	1.1(9)	5.5(8)
55	1.4(10)	7.0(9)	8.0(8)	3.2(8)
60	4.0(10)	1.0(10)	5.0(8)	1.5(8)
65	6.3(10)	2.0(10)	1.9(8)	5.6(7)
70	1.0(11)	1.0(10)	7.0(7)	2.8(7)
75	7.8(10)	7.0(9)	2.8(7)	1.4(7)
80	6.0(10)	1.0(10)	1.3(7)	7.0(6)
85	1.0(11)	8.0(10)	8.3(6)	4.6(6)
90	7.4(11)	2.0(11)	1.0(7)	2.0(6)

In addition, the reaction

$$NO_3^- + O \xrightarrow{\gamma_{49}} O_2^- + NO_2 \qquad (8.50)$$

was included with a variable rate. Reaction (8.50) represents only one possible channel for the reaction of NO_3^- and O. The most energetic channel for the reaction produces NO_2^-, which is quickly reconverted into NO_3^- by the action of ozone. The NO_2^- channel will be exothermic unless the electron affinity of NO_3 exceeds that of NO_2 by about 2.9 eV or more. Two other channels for the reaction of NO_3^- with O are less energetic than the two channels described above and are most probably endothermic. Fehsenfeld et al. (1969) have placed an upper limit on the rate constant for the sum of all the channels for the reaction of NO_3^- with O of 1×10^{-11} cm^3 sec^{-1}. Reaction (8.50) will be exothermic only if the electron affinity of NO_3 is less than 3.3 eV. Since the electron affinities of NO_2 and NO_3 are unknown, it is possible that reaction (8.50) may be exothermic, and may have a rate constant of the order of 1×10^{-14} cm^3 sec^{-1}. Further, assuming that this channel and the NO_2^- channel have comparable rates ($\sim 10^{-14}$ cm^3 sec^{-1}) one can show that the NO_2^- channel can be ignored as an NO_3^- loss process compared to Reaction (8.50) as long as the O/O_3 ratio is less than about 100. This condition will be met in the sunrise D region below 80 km (see Figure 3.10).

Reaction (8.50) is important even with a small rate constant because NO_3^- is the dominant sunrise negative ion between 60 and 80 kilometers in this model, and the reaction leads to the production of electrons at sunrise. The critical implication of Reaction (8.50) which will be discussed later is that at sunrise the dominant negative ion will either have its electron detached, (Sechrist, 1968), or be converted into another negative ion which is subsequently detached. The detachment or conversion process can have its onset with the sudden increase in a minor neutral constituent [e.g. O or $O_2(^1\Delta)$] or in the intensity of the penetrating radiation. For the model used in this study the photodetachment of NO_3^- occurs too late at sunrise (because the electron affinity of NO_3 is assumed to be about 3 eV) to reproduce the electron density behavior. Reaction (8.50) is then postulated as one source of O_2^-, and then electrons, over part of the D region at sunrise. The much faster conversion of CO_3^- to O_2^- by O at sunrise will also be important, but primarily very early in the sunrise. CO_3^- conversion alone will not account for the electron density sunrise behavior in this model.

Instead of varying the parameters at each separate height until the desired results were obtained, the parameters were varied in a consistent manner over the entire altitude range simultaneously, and the predicted electron layer behaviors (C and D layers) were used to check the model. In this way the O and NO distributions did not become disjointed in an effort to achieve some particular output values for the electron density, while a certain amount of detailed agreement between predictions and measurements was thereby sacrificed.

The photodetachment rates of O_4^-, CO_3^-, and CO_4^- were set equal to zero in the calculations. These rates have very little effect on the electron density behavior at sunrise relative to the photodetachment of NO_3^- if all their rates are of the same size. Since none of the rates have been measured this procedure is only an approximation. Actually, it will be seen that the photodetachment of any negative ion is not a critical sunrise mechanism. The inclusion of O_4^-, CO_3^-, and CO_4^- photodetachment with reasonable sunrise behaviors would only slightly enhance the sunrise electron densities.

8.5 Computational Method

The numerical code which is used to solve the charged species' Equations (8.8) and (8.13) was developed by Gear (1967, 1968a and b) at the University of Illinois to solve systems of ordinary differential equations. The code has been slightly altered by adding a subroutine to calculate the time dependent coefficients, and by including a plotting routine. Because of its length the code is not reproduced here, but it may be obtained from Dr. Gear at the University of Illinois Digital Computer Laboratory. The code is especially designed for stiff systems of equations, i.e., those having several time constants that are widely different. The numerical integration technique is thoroughly explained in Gear's (1967, 1968a and b) papers. In identical calculations using Gear's code, Keneshea's (1967) code, and a fourth order Runge-Kutta method on a large scale ion-neutral atmospheric model D. McIntyre (private communication) found the Gear results to be more accurate than the Keneshea results with a higher operating efficiency (some of the Keneshea results were off by an order of magnitude). The Runge-Kutta output for a very small step interval provided the check on the calculations.

In applying the code all integrations were begun at 100° zenith angle and continued for two hours. The approximate Wallops Island values of latitude and geomagnetic latitude of 38° N and 50° N, respectively, were used. The earth's declination angle, δ, was set equal to zero. Where necessary the sunrise parameter values were corrected to the proper latitude.

The initial conditions for the charged species at each altitude were determined by performing an integration with the time dependent coefficients fixed at their $\chi = 100°$ values. The initial conditions for these preliminary runs were estimated (Radicella, 1968; Gunton, 1969). It was found that a large time step could be used in calculating the initial conditions, and that equilibrium was not achieved at some altitudes for many hours. This suggests that the charged constituents may actually be in nonequilibrium throughout the night. One is referred to Equations (8.26), which accurately describe the nighttime N^+ behavior below 80 km.

N^+_{eq} is the nighttime equilibrium value of N^+. τ_+ may be as long as a day or more depending on the values of q and $\tilde{\varepsilon}$. It is then possible that if a significant disparity exists between the presunset and nighttime positive ion densities at some altitude, the presunrise N^+ density may be significantly different than N^+_{eq}, and will be either larger or smaller than N^+_{eq} depending on whether N^+ before sunset was larger or smaller than N^+_{eq}. One altitude range where this effect could be important is between 60 and 75 km where the daytime electron and positive ion densities are lower than N^+_{eq} because of recombination, so that the presunrise positive ion densities will also be lower. Since the daytime positive ion densities are nearly in equilibrium (electron-ion recombination is fast relative to ion-ion recombination) almost independently of the presunrise conditions, one could estimate the departure in the pre-sunrise positive ion density from equilibrium by using Equations (8.26). It was less than 10% at all altitudes for this study. The nonequilibrium effect may not be ignorable under other circumstances, however.

The charge neutrality condition, Equation (8.7), was not used to eliminate the positive ion density as a variable. Instead it was used as a check on the integration accuracy by applying it to the initial and final charged specie densities. Excellent agreement always resulted.

8.6 The Negatively Charged Species at Sunrise in the D Region

The charged specie densities calculated for nine altitudes from 50 to 90 km in 5 km steps are illustrated in the following pages. Each figure is labelled with its altitude, and the species depicted there are indicated by their symbols. The O^-, O_3^-, and O_4^- densities are increased by a scale factor of 100, the O_2^- densities by a factor of 10. Three altitude ranges will first be discussed separately; 50-60 km, 65-75 km, and 80-90 km; and then the development of the electron distributions over the entire mesosphere at sunrise will be investigated.

8.6.1 Sunrise from 50-60 kilometers

This altitude range comprises a negative ion layer where the dominant negatively charged species are ions for all zenith angles, i.e. $\Lambda > 1$. The ion-pair production source is almost exclusively galactic cosmic rays with the total rate, q, ranging between 0.31 cm^{-3} sec^{-1} at 50 km to 0.088 cm^{-3} sec^{-1} at 60 km.

Figures 8.4-8.6 show the charged species over sunrise. There is very little diurnal variation in the total ion density at these altitudes, and essentially all that happens at sunrise is a reshuffling of the negative ion composition. In each figure the dominant sunrise ion is CO_4^- which indicates that three body clustering processes will dominate the negative ion chemistry in this region (i.e. for processes with equivalently fast rates). NO_3^- is a major ion, but not the dominant one.

An effect which occurs early in the sunrise and is clearly depicted in each figure is the conversion of CO_4^- to CO_3^- by the action of atomic oxygen. As sunrise progresses the CO_3^- to CO_4^- density ratio quickly approaches the fixed value of 1.88 (i.e. the ratio of the rate constants γ_{48}/γ_{41} of Tables 7.2 and 7.3. These are the rate constants for the primary, O-driven loss reactions of CO_3^- and CO_4^- (see Equation 8.43b). The conversion is accompanied by an atomic oxygen induced increase in O_2^- and O_4^-. Electrons are not produced

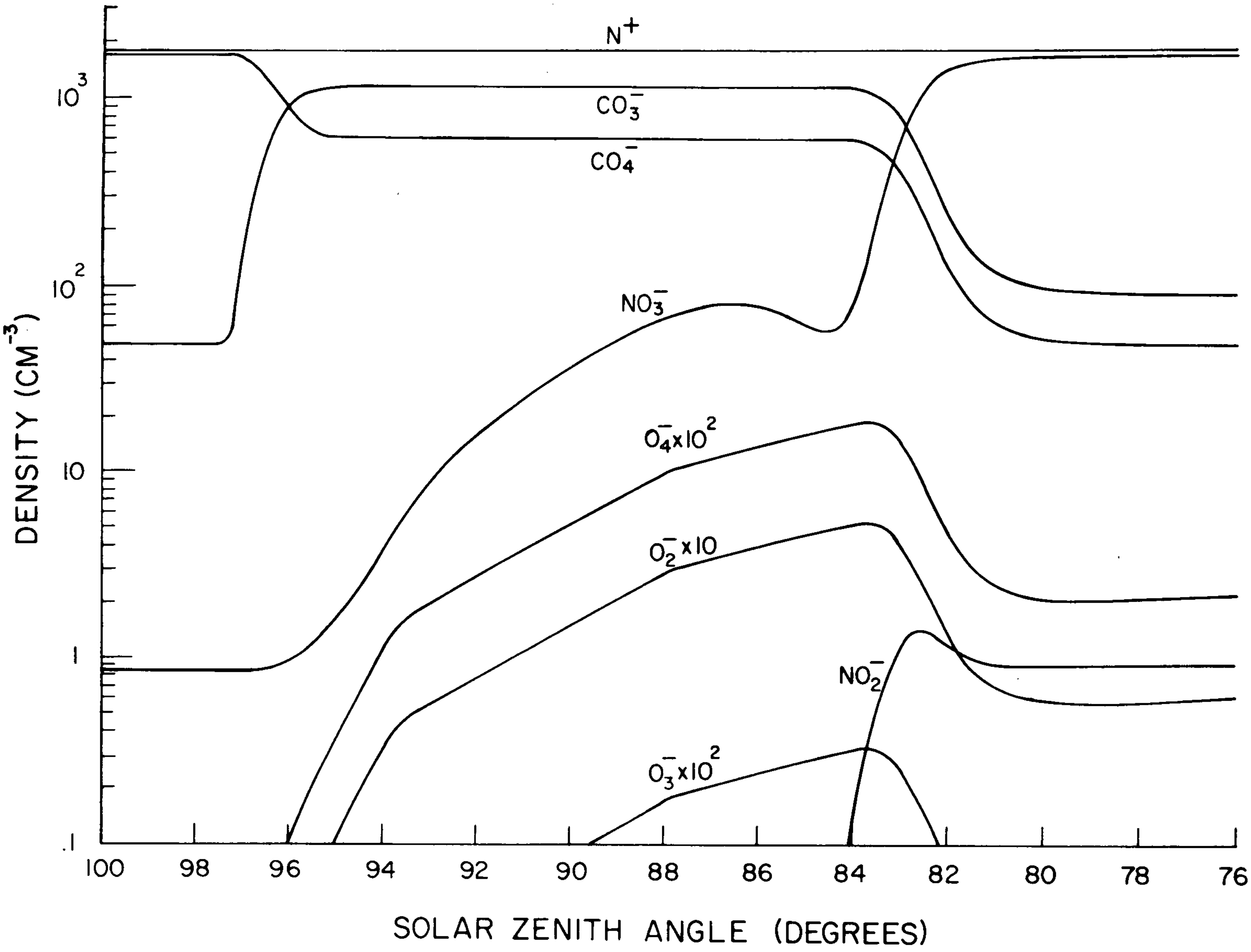

Figure 8.4 The charged species at 50 kilometers during sunrise.

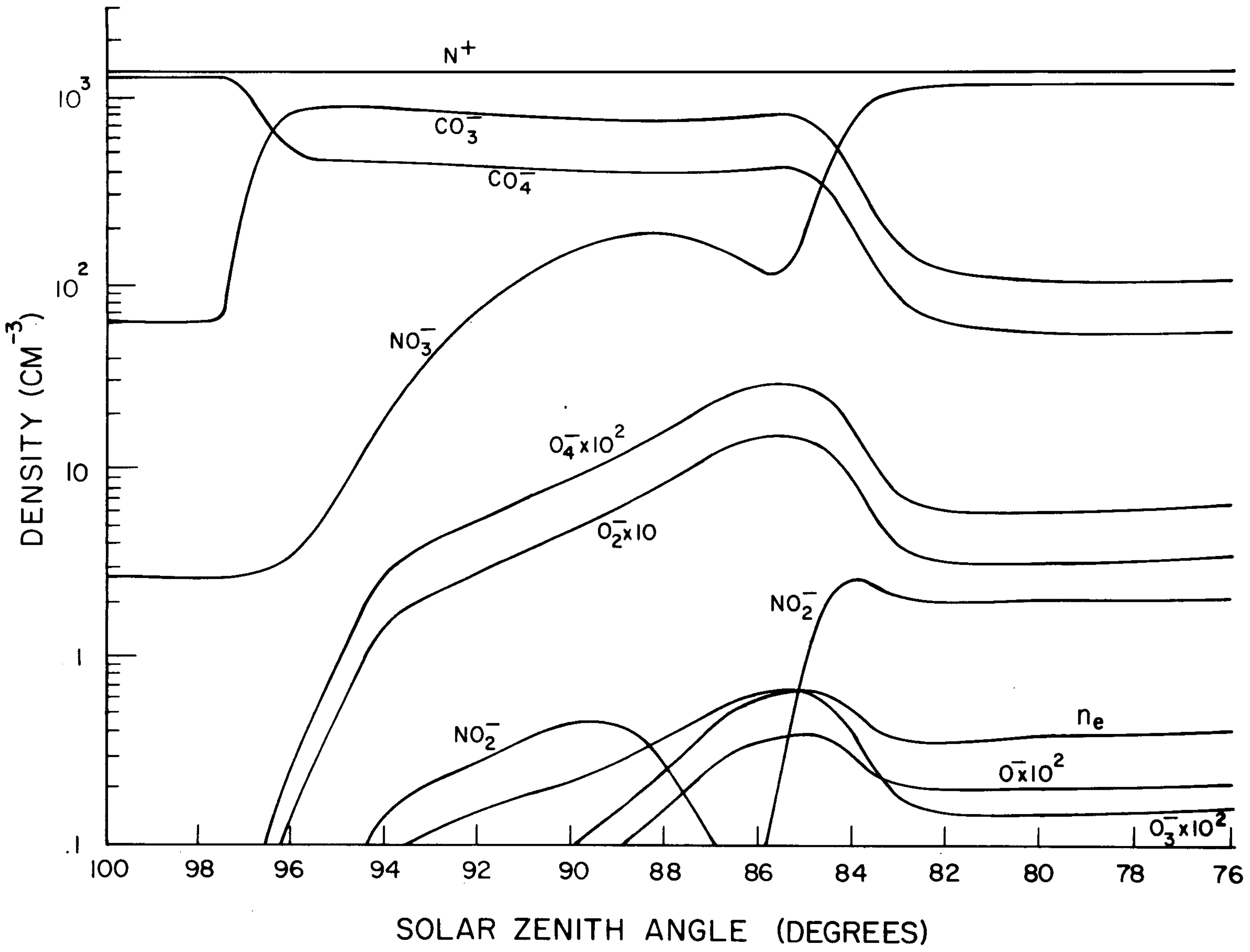

Figure 8.5 The charged species at 55 kilometers during sunrise.

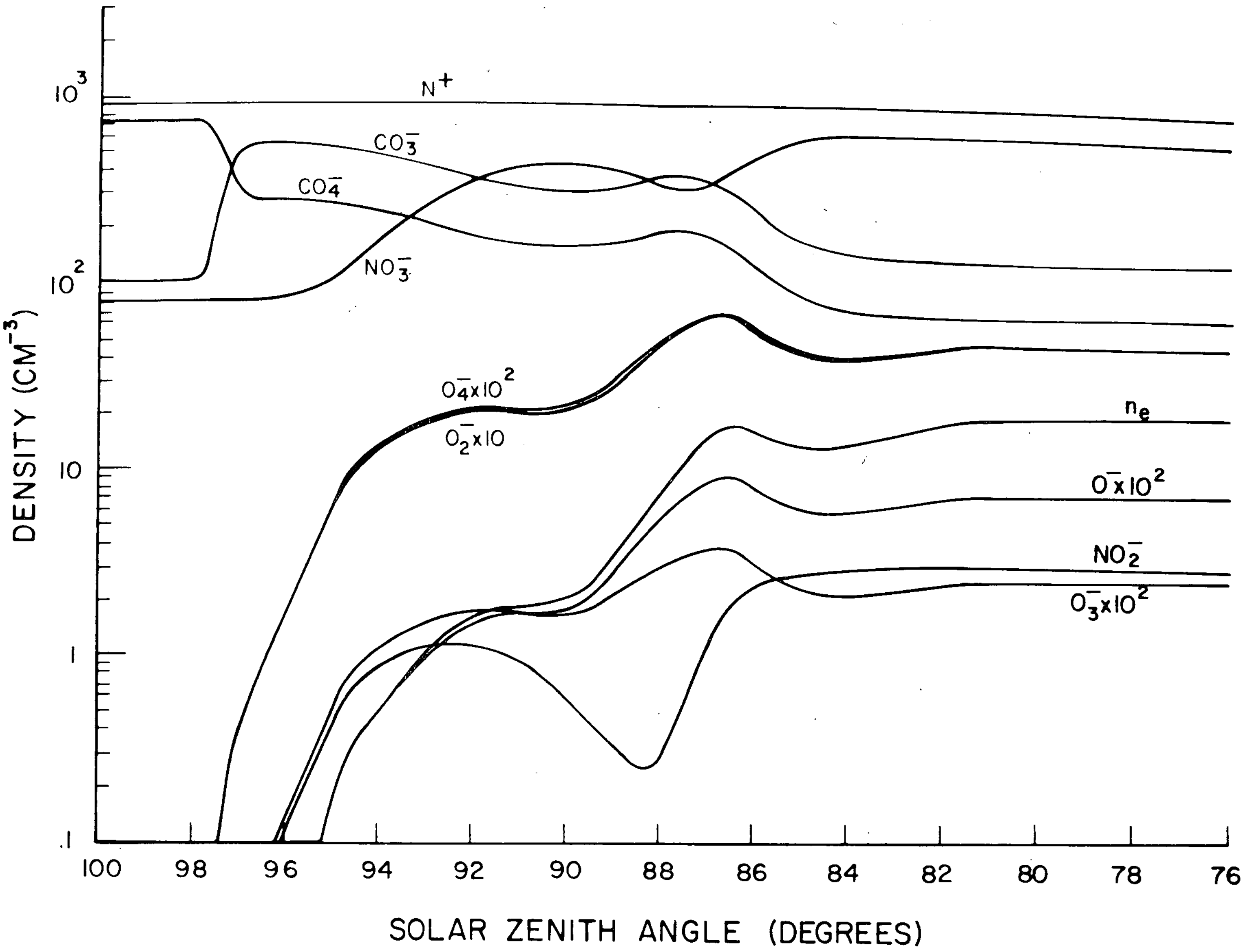

Figure 8.6 The charged species at 60 kilometers during sunrise.

in large numbers as a result of this chain of reactions because the O_2^- densities are limited by both the rapid loss to clustering to form O_4^-, and the relatively low O concentrations at these altitudes early in the sunrise.

The NO_3^- density increases slowly after the CO_4^- to CO_3^- conversion until photodetachment begins to destroy it. A depression in the NO_3^- density near $\chi = 86°$ at each of the altitudes indicates the onset of photodetachment. The photodetachment of CO_3^- and CO_4^- are not included in these calculations. They are unmeasured parameters which will be unimportant in this region because, as with NO_3^-, photodetachment is not a decisive process here. The rapid NO_3^- increase soon after the onset of photodetachment is due to the sunrise increase in NO. If the NO increase is attributed to the photodissociation of NO_2 then it will probably commence at larger zenith angles than those given by the NO sunrise model (i.e. with a χ_0 corresponding to the half-rise in the uniform ozone photodissociation rates) and the NO_3^- photodetachment may even occur later (i.e. after the nonuniform ozone photodissociation rate increase as used in the model). Then an NO_3^- depression would not occur. Since the CO_3^- and CO_4^- will probably not undergo photodetachment any earlier than NO_3^-, and by this time their densities will have been greatly reduced by the action of O and NO, the photodetachment of these negative ions can be ignored. The net effect of photodetachment on the NO_3^- is to decrease its photoequilibrium density somewhat. NO_3^- still remains the dominant daytime negative ion.

The dip in the NO_2^- distributions near 86° at each height is also due to a combination of the onset of photodetachment followed by an increase in the NO density.

The electron density is less than 1.0 cm^{-3} at 55 km and below for all sunrise zenith angles. Electrons are produced in the 50-60 km region at sunrise principally by the action of atomic oxygen in driving the reaction chain: $CO_3^- \rightarrow O_2^- \rightarrow e$. As already mentioned, O_2^- is quickly lost through clustering to form O_4^- with a time constant less than one second, while associative detachment by O (as well as other loss processes) is slower by at least an order of magnitude. Most of the O_2^- is produced from CO_3^-, the rest by electron attachment to O_2.

The electrons at these altitudes are lost by attachment (see Equation 8.41 and the discussion in Section 8.2.2). For example, at 60 km at the end of one set of calculations the loss rates of electrons by attachment to O_2, dissociative attachment to O_3, and positive ion recombination were 66.3, 1.68, and 0.071 cm^{-3} sec^{-1}, respectively; while electrons were produced by O_2^- detachment (mainly associative detachment by O), NO_3^- photodetachment, and q at the rates of 66.2, 0.96, and 0.088 cm^{-3} sec^{-1}, respectively. The attachment and detachment rates do not exactly offset one another. It is clear that small changes in the O_2^- density will drive the electron density; i.e. if the O_2^- increases so does the electron density by detachment, and if the O_2^- decreases the electrons are rapidly lost by attachment. Equation (8.45a) describes the $n(O_2^-)$-n_e dependence adequately. The negative ion chemistry determines the O_2^- density, which determines n_e.

One observes that $n(O_4^-) \propto n(O_2^-)$ for all zenith angles as in Equation (8.43a). This is a consequence of the fact that O_4^- is produced by O_2^- clustering with O_2 and lost by reacting with CO_2, and both neutral species are assumed to have no sunrise variation. It can also be seen that $n(O_4^-) \propto n_M^{-1}$ as predicted in Equation (8.43a).

It was found that the effect of increasing the electron-ion recombination coefficient was to slightly decrease the electron density (see Equation 8.21).

The size of the reduction substantiates the analysis of Section 8.2.2, where it was also found that the loss of electrons is due indirectly to electron-ion recombination, which induces a reduction in the densities of ions available for detachment, and so, a reduction in electron production. For the altitudes considered here this effect will be noticeable only where the electron density is still large enough to affect the N^+ density, i.e. only at 60 km for $\chi \lesssim 88°$.

Increasing the NO daytime density decreases the electron density at each height for zenith angles after the NO sunrise. With more NO present the conversion of negative ions into NO_3^- is more efficient. The NO_3^- density increases at the expense of the CO_3^- density (and CO_4^-, which is also a source of CO_3^-). This reduces the O_2^- density, and so the electron density.

By increasing the atomic oxygen density, n_e is increased because both the production and associative detachment of O_2^- are accelerated. The atomic oxygen and nitric oxide densities which were used in the calculations of Figures 8.4-8.6 are for the high-O-high-NO model used in this study (see Table 8.3). The high values of $\tilde{\alpha}$ were also used, but this parameter had only a small effect on the computations. Reaction (8.50) was included with a rate of 5×10^{-14} cm^3 sec^{-1}, and it also had very little effect on the computations.

8.6.2 Sunrise from 65-75 kilometers

This is a transition region where the dominant negative specie changes during the sunrise from negative ions at night to electrons during the day. The important early reactions at these heights will involve the production of O_2^-, and its subsequent detachment to produce electrons. The reaction of atomic oxygen with NO_3^- discussed in Section 8.4 is an important source of O_2^- at sunrise. The effect of O_2^- production on the electron density behavior at sunrise has been discussed in Section 8.2.2 and the equations derived there can be used to help analyze the computational results. The negatively charged species over sunrise are illustrated in Figures 8.7-8.9 for 65, 70, and 75 kilometers, respectively.

The ion-pair production rates at these altitudes are composed, to varying degrees, of cosmic ray ionization, precipitated electron ionization, and nitric oxide Lyman α ionization. At 65 km the pre- and postsunrise rates are 0.040 and 0.047 cm^{-3} sec^{-1}. The corresponding rates for 70 and 75 km are 0.046 and 0.076, and 0.072 and 0.25 cm^{-3} sec^{-1}, respectively. The electron density at each height is less than 1.0 cm^{-3} in the presunrise region. The dominant nighttime negative ions are NO_3^-, CO_3^-, and CO_4^- in that order.

The first effect that can be seen at sunrise is the conversion by atomic oxygen of CO_3^- into O_2^-, O_4^-, and CO_4^- which occurs at each altitude. One can see in Figures 8.7-8.9 the close CO_3^--CO_4^-, O_2^--O_4^-, and O_2^--O_3^- couplings which were discussed in Section 8.2.3 (see Equations 8.43, noting that ozone is decreasing over sunrise). O^- and n_e are also closely coupled by ozone attachment and atomic oxygen associative detachment.

The electron density reaches a value of 1.0 cm^{-3} at about 97.3° zenith angle at 75 km, 96.2° at 70 km, and 95.1° at 65 km. The electron density then rises rapidly over the next few degrees. At 75 km there is a distinct change in the electron density as early as 98.5°. Although this effect is very small, it is expected that between 75 and 80 km there will be a larger electron density enhancement near 98° due to the early rise in atomic oxygen. This early growth of the lower D layer between 75 and 80 km could explain the 98° VLF effect. The possibility is discussed further in Section 8.7. Because the height resolution in this work is only 5 km, the behavior of the region between 75 and 80 km must be extrapolated. The most likely altitude

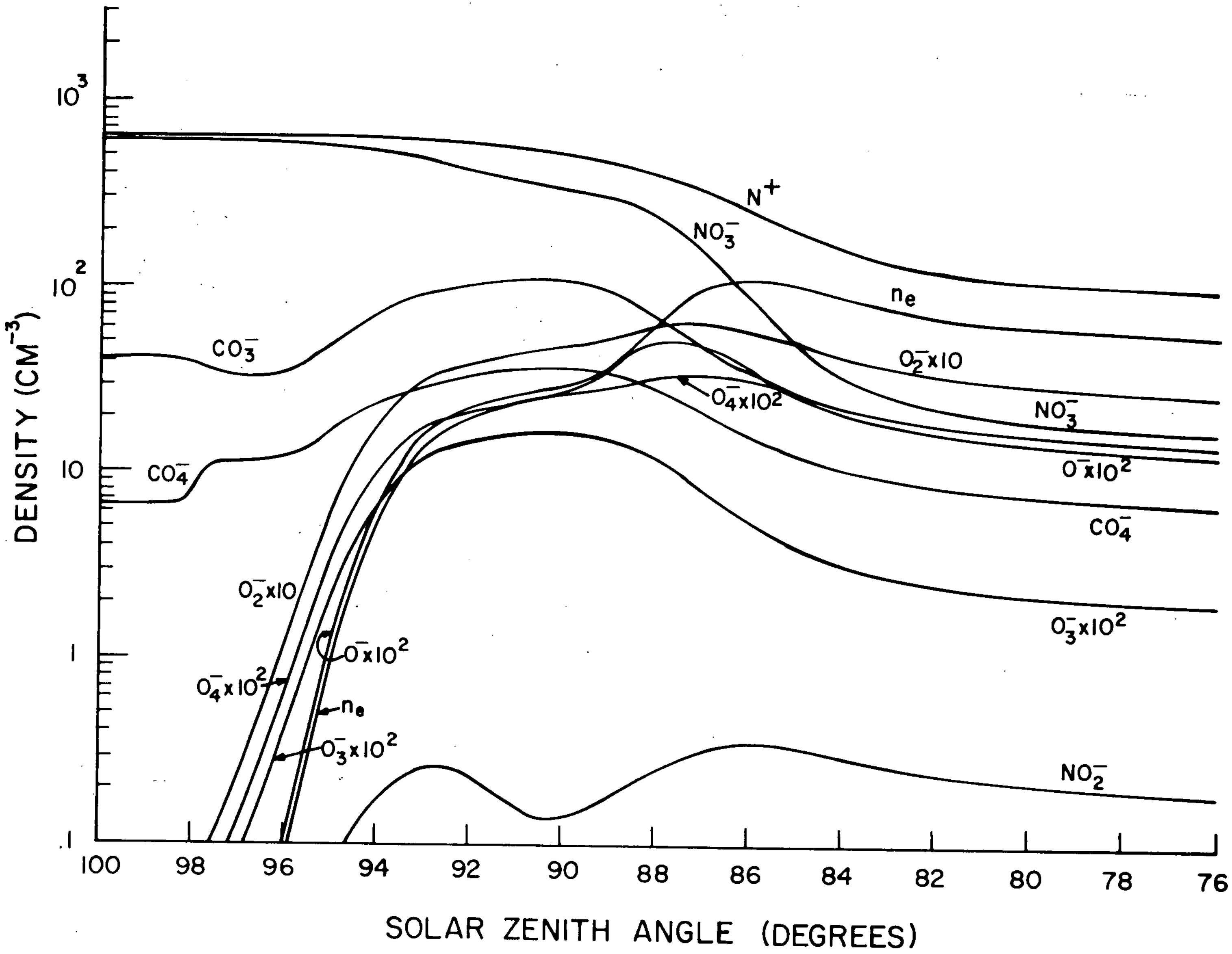

Figure 8.7 The charged species at 65 kilometers during sunrise.

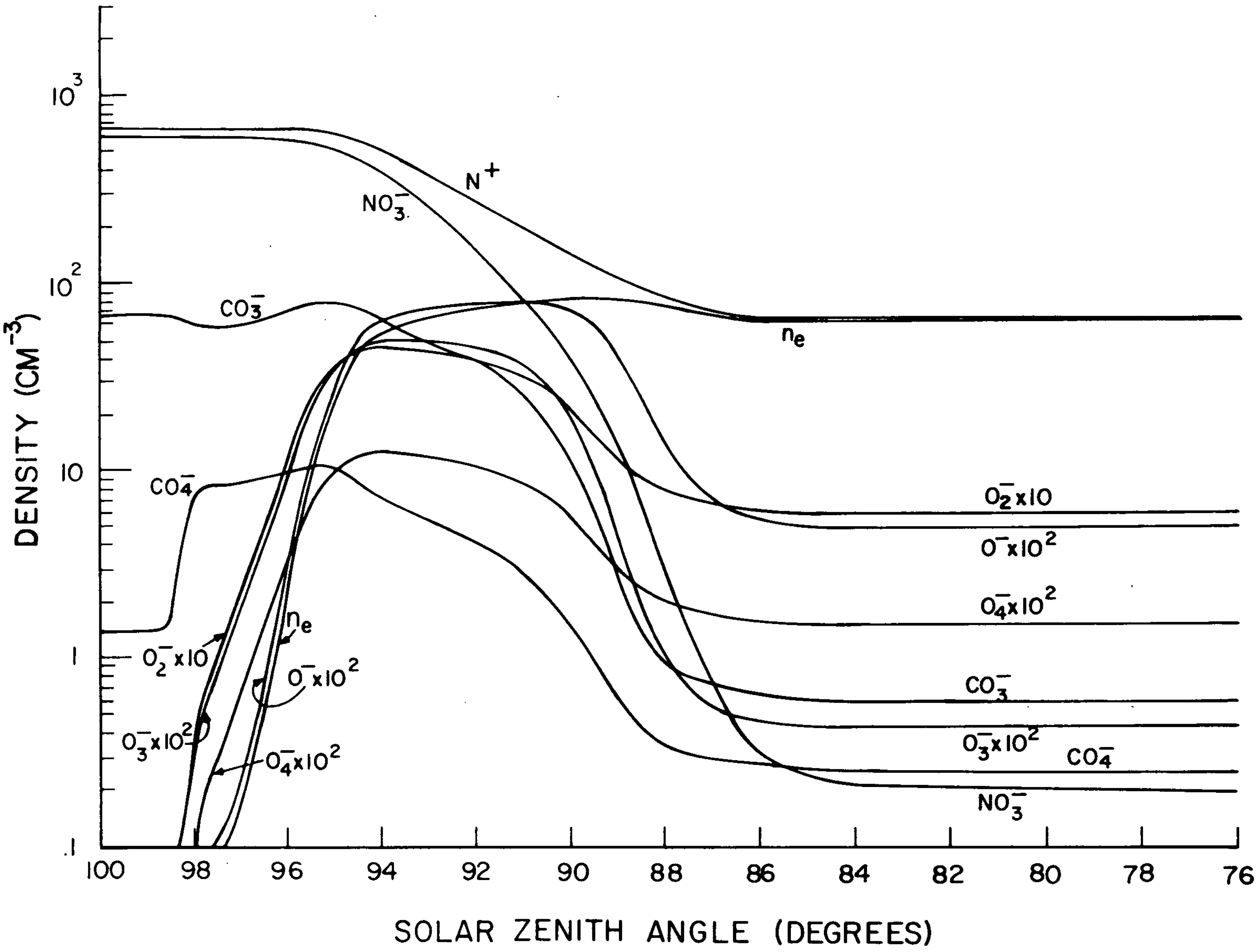

Figure 8.8 The charged species at 70 kilometers during sunrise.

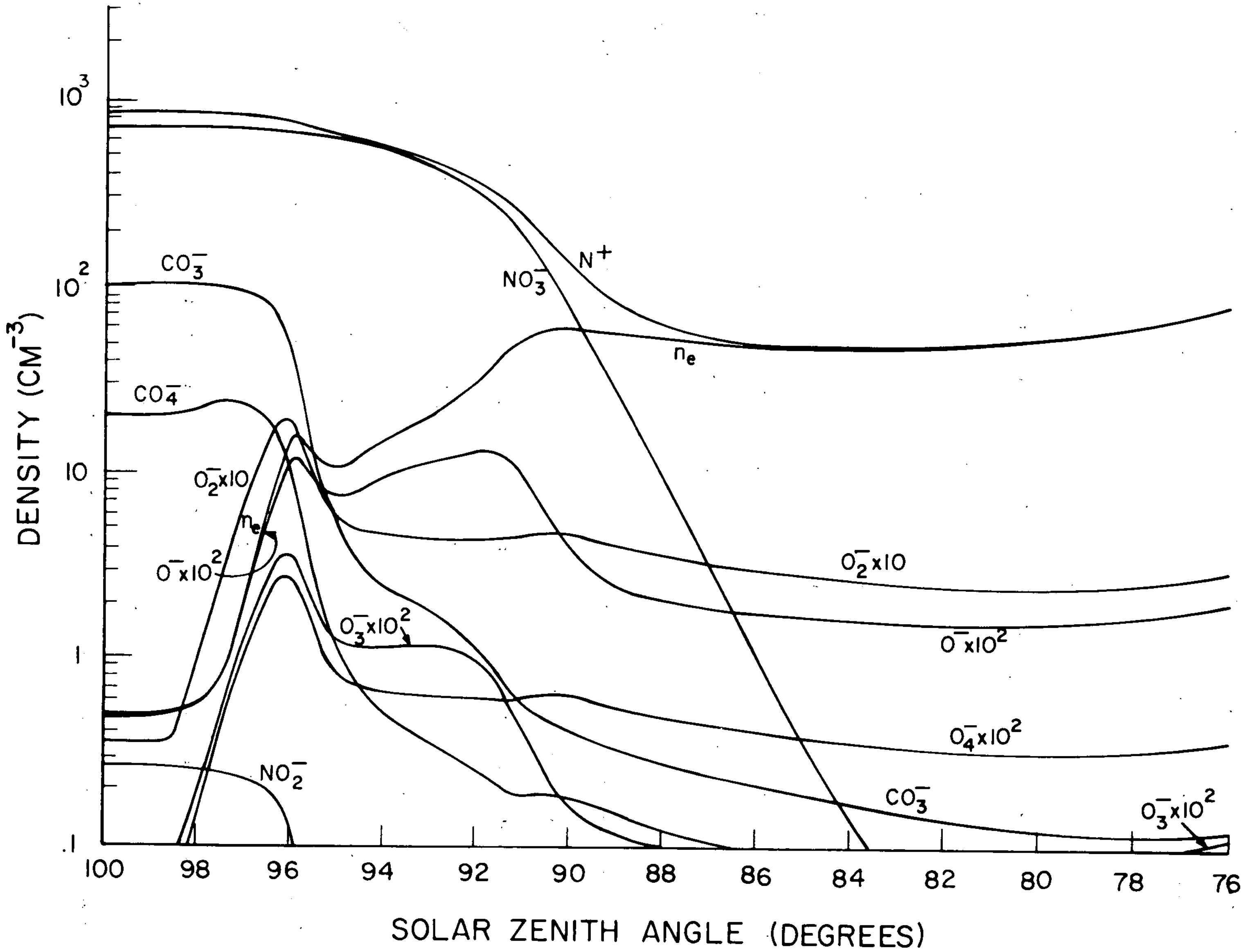

Figure 8.9 The charged species at 75 kilometers during sunrise.

for an early enhancement is just above 75 km where there are still large quantities of O_2^- and CO_3^- available for conversion and detachment. The most likely effect would be an increase in the slope of the electron distribution at these heights. From 98° to 96° there is a steady electron buildup between 70 and 75 km which is also consistent with VLF data.

The electron density at 75 km has a peak near 96° in the sunrise (see Figure 8.9). It is due to the combination of electron production by the sequence $CO_3^- \rightarrow O_2^- \rightarrow e$ followed by electron-ion recombination. After a small decrease, the electron density again begins to increase due to the slower conversion of NO_3^- into electrons. As the zenith angle continues to decrease the sequence $NO_3^- \rightarrow O_2^- \rightarrow e$ must compete with the direct photodetachment of NO_3^- to produce electrons. At most heights for the model used here photodetachment commences after most of the NO_3^- has already been lost. Photodetachment of NO_3^- then becomes a secondary process in this study. At 75 km, however, photodetachment is producing about 30% of the electrons between 92° and 90°.

Using the analysis developed in Section 8.2.2 one can deduce that the electrons at 75 km are lost after the CO_3^- and NO_3^- production peaks by recombination rather than by attachment. This is because $\beta_{eff} < \tilde{\alpha}N^+$ in both cases. An inspection of the N^+, NO_3^-, and n_e slopes also confirms that conclusion. Below 75 km the NO_3^- process swamps the CO_3^- process very early, and begins to regenerate CO_3^- through the reaction sequences $NO_3^- \rightarrow O_2^- \rightarrow O_3^- \rightarrow CO_3^-$ and $O_2^- \rightarrow O_4^- \rightarrow CO_4^- \rightarrow CO_3^-$ (see Figures 8.7 and 8.8). The charge stored in the regenerated CO_3^- is eventually released when the O density becomes large enough. The CO_3^- process is still responsible for the early electron rise, for which $n_e < 1.0$ cm^{-3}.

At the lower altitudes the NO_3^- process has a broad production peak, and the electron density does not have a sharp peak in its distribution. The spread in the NO_3^- process is due to a great extent to the slower atomic oxygen increase at sunrise which was calculated in Chapter 3. The slowness of the O increase also reduces the effectiveness of the CO_3^- conversion process at sunrise by reducing both the production and detachment of O_2^-. If the NO_3^- conversion process were turned off at each altitude, a distinct peak resulting from CO_3^- conversion would occur in n_e. After a substantial delay the photodetachment of NO_3^- would produce large quantities of electrons, with $\delta(NO_3^-) \sim 0.002\ sec^{-1}$. If the NO_3^- photodetachment were also turned off the electron densities would decay after the CO_3^- process toward their equilibrium values for those heights, values that are too low (for any of the sunrise models adopted here) to be reconciled with measurements. It was therefore necessary in this study to postulate a mechanism by which the dominant presunrise negative ions could be converted into electrons. Whether this mechanism is photodetachment or the production of an easily detached intermediary ion, the effect must occur as early as 98° at the higher altitudes. The CO_3^- and NO_3^- to O_2^- conversion processes have proven to be adequate mechanisms.

The calculations illustrated in Figures 8.7-8.9 are for the high-O-high-NO model, as in the previous section. The high $\tilde{\alpha}$ values were used, and Reaction (8.50) was given a rate of $5 \times 10^{-14}\ cm^3\ sec^{-1}$ as before.

Variations in $\tilde{\alpha}$ have a large effect on the positive ion and electron densities at these heights (see Equation 8.21). In fact, n_e and N^+ are proportional to $\tilde{\alpha}^{-1/2}$ after sunrise. Before sunrise the effect of changes in $\tilde{\alpha}$ are negligible. Increasing the NO densities has several effects on the computations. In the presunrise regions an increase in NO increases q because there is a production component due to scattered Lyman α radiation. The presunrise positive ion densities are therefore larger (especially at 70 and 75 km). The increased NO also increases the NO_3^- density at the expense of the CO_3^- density. The decrease in $n(CO_3^-)$ is not just a percentage decrease, but an absolute decrease. A reduction in CO_3^- means fewer early electrons at sunrise. With the low-O densities the electron densities are too small at the large zenith angles ($\chi > 90°$) for all other conditions in this study. For the most favorable conditions with low-O the best results were at 75 km where n_e was still much too small for zenith angles greater than 94°, and then was too large for $\chi < 90°$. At lower altitudes no similarity between calculations and measurements could be achieved.

The points where $\Lambda = 1$ during sunrise in Figures 8.7-8.9 are about 90° at 75 km, 91° at 70 km, and 86.5° at 65 km. Note that at 65 km the negative ions persist for a longer time. After sunrise $\Lambda \sim 0.7$, and negative ions are important in the daytime charged specie photochemistry at 65 km. The equilibrium Equation (8.20) can be applied to the postsunrise region by using $\Lambda = 0.7$ at 65 km. O_2^- is a major daytime ion at all altitudes (particularly above 65 km), being produced by three-body electron attachment to O_2. O_2^- becomes more important with increasing altitude (although its density decreases) because the rates of formation of more stable negative ions from O_2^- is rapidly decreasing as a result of the lapse in the ozone and atmospheric densities.

During sunrise n_e depends on O_2^- as its production source, but after sunrise O_2^- (and O_4^-, CO_4^-, CO_3^-, O^-, etc.) is determined by the electron density through fast attachment and detachment processes (and fast loss processes control the other ions). Above 65 km $\Lambda \lesssim 10^{-2}$ in the postsunrise region, and negative ions can be ignored.

8.6.3 Sunrise from 80-90 kilometers

At these altitudes the negative ions are nearly absent at all zenith angles for all conditions in this study. Under the most favorable conditions (i.e. low O densities) $\Lambda \sim 0.01$ at 80 km, but it was generally much lower than this at higher altitudes and for other conditions. There was a direct correlation between increasing atomic oxygen densities and decreasing Λ, indicating that the associative detachment of O_2^- by atomic oxygen is responsible to a great extent for the absence of negative ions in this region. Other factors such as the lapse of the O_2 and CO_2 densities also contribute to the lack of formation of negative ions here. Unless another fast attachment process which bypasses O_2^- is discovered, negative ions will probably never be important in this region. The attachment of electrons to water clusters or hydrated molecules followed by internal excitation or dissociation could be such a process if water vapor is present above 80 km.

It was found that changes in $\tilde{\alpha}$ have practically no effect on the negative ion to electron density ratios, λ, at any given height in the presunrise region. It was shown in Sections 8.2.1 and 8.2.2 that this could be expected when detachment was much faster than ion-ion recombination, as it is in this altitude range. It was also observed that the λ's during sunrise were likewise independent of $\tilde{\alpha}$, and that they were slightly smaller than the presunrise equilibrium λ values. The decrease is due primarily to photodetachment after sunrise. The $\tilde{\alpha}$-independence of the time dependent continuity equations is discussed in Section 8.2.2, and applies to these altitudes.

The ion-pair production sources in the presunrise region from 80-90 km are NO ionization by scattered Lyman α radiation and ionization by precipitated electrons. For the high-NO model the values of the total rate, q, are 0.085, 0.059, and 0.070 cm^{-3} sec^{-1} at 90, 85, and 80 km, respectively. The corresponding low-NO model values are 0.028, 0.030, and 0.022 cm^{-3} sec^{-1}. The postsunrise q values, near $\chi = 76°$ where the penetration of direct solar Ly-α radiation controls the ionization, are 8.4, 5.4, and 2.0 and 5.2, 4.3, and 1.2 cm^{-3} sec^{-1} at 90, 85, and 80 km, respectively, for the high- and low-NO models. Comparisons showed that the electron densities were nearly in equilibrium at the ends of the calculations, and that Equations (8.16) and (8.18) for the electron density were correct with an error of less than 5% at this point.

Figures 8.10-8.12 illustrate the charged specie distributions over sunrise from 80-90 km. Obviously $N^+ \doteq n_e$ here. The electrons are strictly recombination controlled. The major negative ions are O_2^- and O^- with O_2^- being dominant at 80 and 85 km, and O^- at 90 km consistent with measurements (Narcisi, 1970b). The O_2^- densities have only a small sunrise variation due to photodetachment near 98°. The O^- first undergoes photodetachment near 98°, and then decreases again because of a reduction in its primary production source, the dissociative attachment of electrons to ozone, as the ozone density decreases over sunrise. The associative detachment of O^- by O dominates the O^- loss rate. $O_2(^1\Delta)$ associative detachment of O^- represents less than 10% of the postsunrise O^- loss rate.

The negative ion densities closely follow the electron density variations in the postsunrise region. The O_2^- and O^- are formed by electron attachment to O_2 and O_3 respectively, and are both rapidly lost by dissociative attachment with O. Their densities should then be in quasi-equilibrium, and are related to n_e by

$$\begin{aligned} n(O_2^-) &= \bar{n}_2 \propto \frac{n_M^2}{n_1} n_e \\ n(O^-) &= \bar{n}_1 \propto \frac{n_3}{n_1} n_e \quad . \end{aligned} \tag{8.51}$$

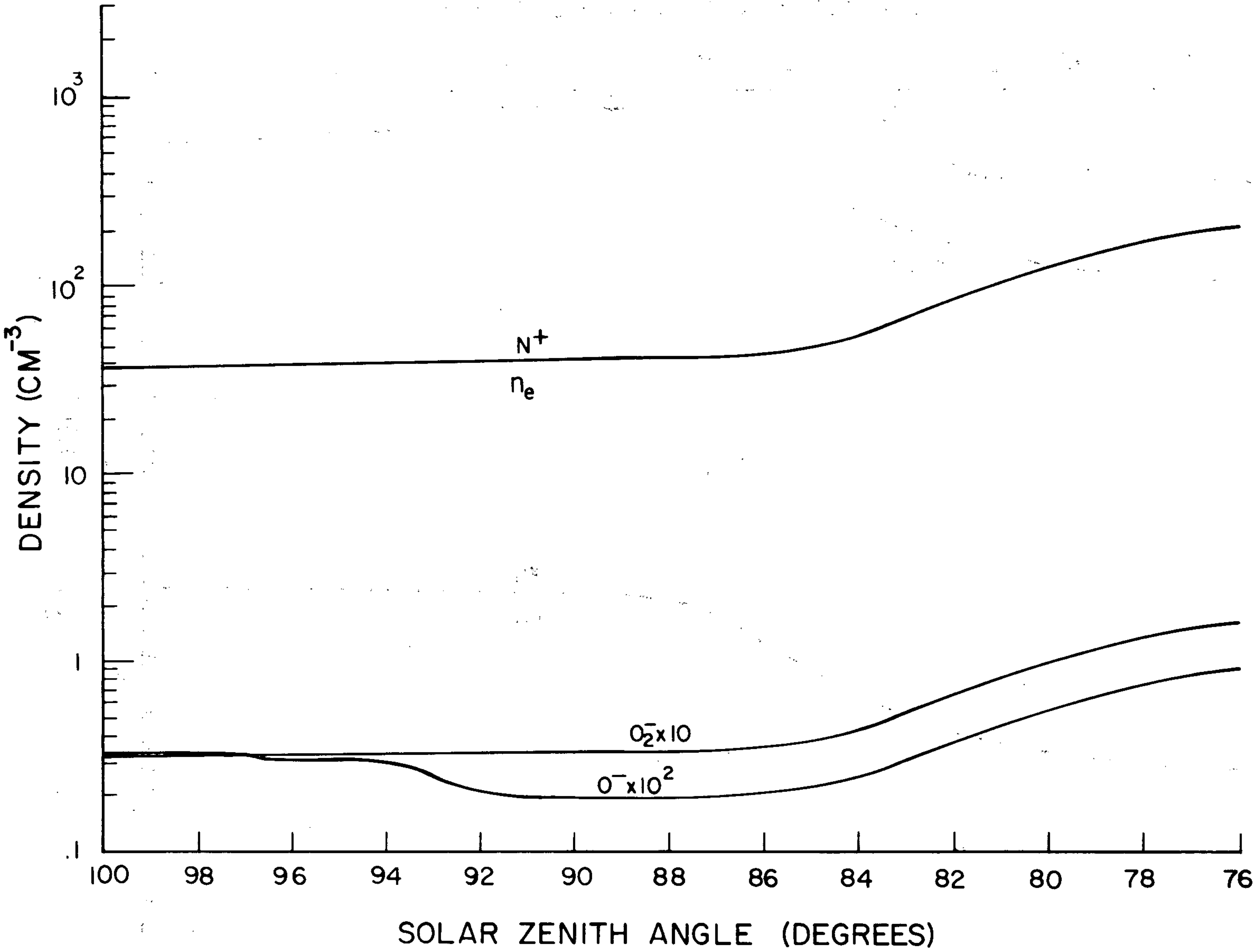

Figure 8.10 The charged species at 80 kilometers during sunrise.

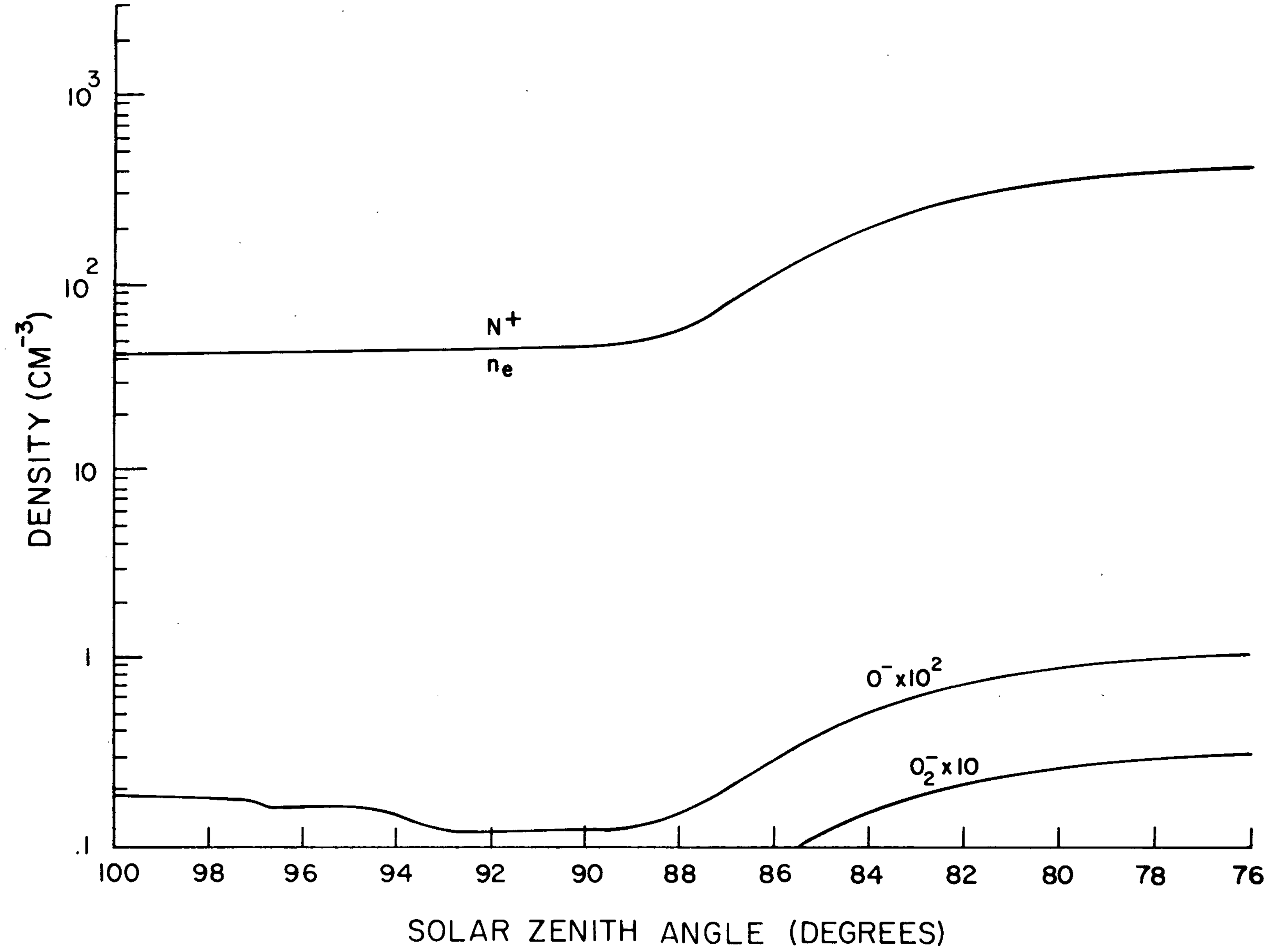

Figure 8.11 The charged species at 85 kilometers during sunrise.

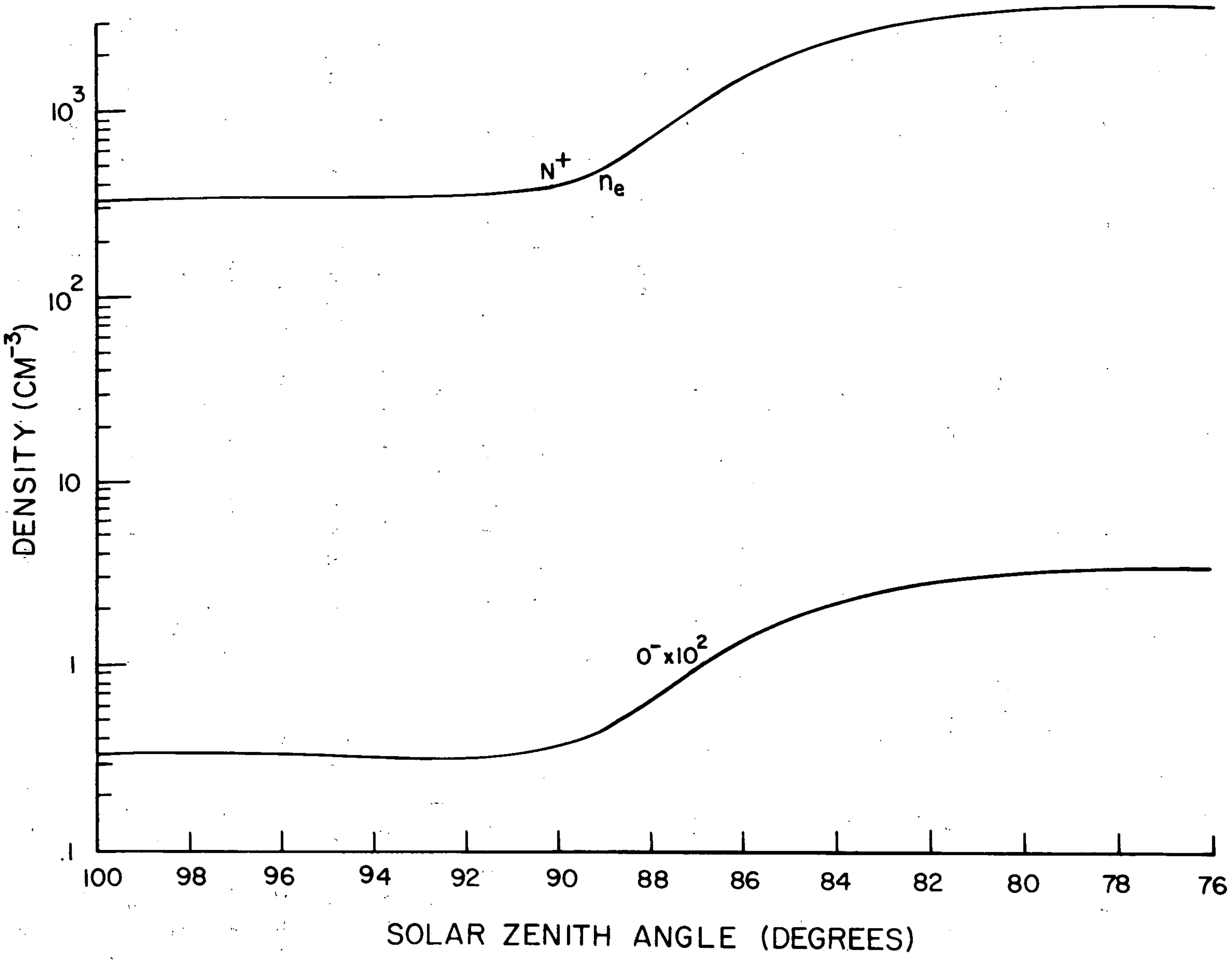

Figure 8.12 The charged species at 90 kilometers during sunrise.

The relevant reaction rate constants can be obtained from Table 7.2 . The increase in the electron and positive ion densities due to the increasing ion-pair production rate during sunrise can be seen at the smaller zenith angles at each height. The entire chemical system appears to be in quasi-equilibrium after sunrise with the λ's showing little variation.

Unlike the negative ion to electron density ratios, the electron density is strongly dependent on $\tilde{\alpha}$ and the NO density. In fact, the direct dependences; $n_e \propto n(NO)^{1/2}$, $n_e \propto \tilde{\alpha}^{-\frac{1}{2}}$; were observed in the calculations. With $\tilde{\alpha}$ fixed the electron density (and N^+) varies approximately as the square root of the ion-pair production rate, q, if n_e and N^+ are almost in equilibrium. Figures 8.10-8.12 clearly illustrate this behavior. Since q is approximately proportional to n(NO), increasing the NO density will increase the electron density at all points over the sunrise (see Equations 8.49). Another smaller effect of increasing the NO is to increase the NO_2^- and NO_3^- densities (their λ's also), but they still remain negligible ions for both the NO models used in this study.

Changes in the atomic oxygen density will have no influence on the electron density as long as there is enough O present to suppress (via the associative detachment of O_2^-) the formation of large numbers of negative ions. O densities less than 1×10^8 cm^{-3} at 80 km would result in the production of large quantities of negative ions. For the low-O model, $n(O) = 1 \times 10^{10}$ cm^{-3} at 80 km, which resulted in $\Lambda \sim 0.01$ for one set of calculations. At higher altitudes electron attachment is even slower ($\tau > 400$ sec compared to 66 sec at 80 km) and so even less O could be tolerated here. Continuing to decrease the O density below a certain level would not be meaningful, however, because other O_2^- loss processes [such as $O_2(^1\Delta)$ detachment and clustering] will impose a lower limit on the loss rate. Since it seems unlikely that such low values

C.5.

for the O density could exist from 80 to 90 kilometers (i.e. less than 10^{10} cm^{-3}), the electron density behavior will be independent of the atomic oxygen density at these altitudes (barring, say, a strong O-NO photochemical coupling; and noting also that the direct attachment of electrons to O is very slow at these heights). As with the other altitude ranges, Figures 8.10-8.12 are from the high-O-high-NO model. The high values of $\tilde{\alpha}$ were also utilized in the calculations. Again, Reaction (8.50) was included with a rate of 5×10^{-14} $cm^3\ sec^{-1}$, but it had no effect on the computations because there is practically no NO_3^- present at these altitudes. As a result of the high O densities very few negative ions are present anywhere in this region.

8.6.4 The charged specie distributions in the mesosphere

The negative ion -to-electron density ratios are illustrated in Figures 8.13 and 8.14 for presunrise and postsunrise conditions respectively. Figure 8.15 shows the presunrise and postsunrise electron and positive ion densities. Also shown in Figure 8.15 are the limiting theoretical distributions for n_e ($\Lambda \ll 1$) and N^+ ($\Lambda \gg 1$) (see Equations 8.19 and 8.20). All the data were obtained from the computations illustrated in Figures 8.4-8.12.

There is a sharp negative ion cutoff between 75 and 80 km at night. This cutoff is due primarily to the increase in atomic oxygen in this region; but contributing factors include decreases in the attachment rates and lapses in the densities of neutral species which react to form the terminal negative ions. Using the equilibrium negative ion continuity Equation (8.15) one can show (also see Equations 8.19 and 8.20)

$$\begin{aligned} \Lambda &= \tilde{\beta}/\tilde{\delta} \quad ; \quad \tilde{\delta} > \tilde{\varepsilon}N^+ \quad , \quad z > 75 \text{ km} \\ \Lambda &= \tilde{\beta}/\tilde{\varepsilon}N^+ \propto \tilde{\beta}q^{-1/2} \quad ; \quad \tilde{\delta} < \tilde{\varepsilon}N^+ \quad , \quad z < 75 \text{ km} \quad . \end{aligned} \tag{8.52}$$

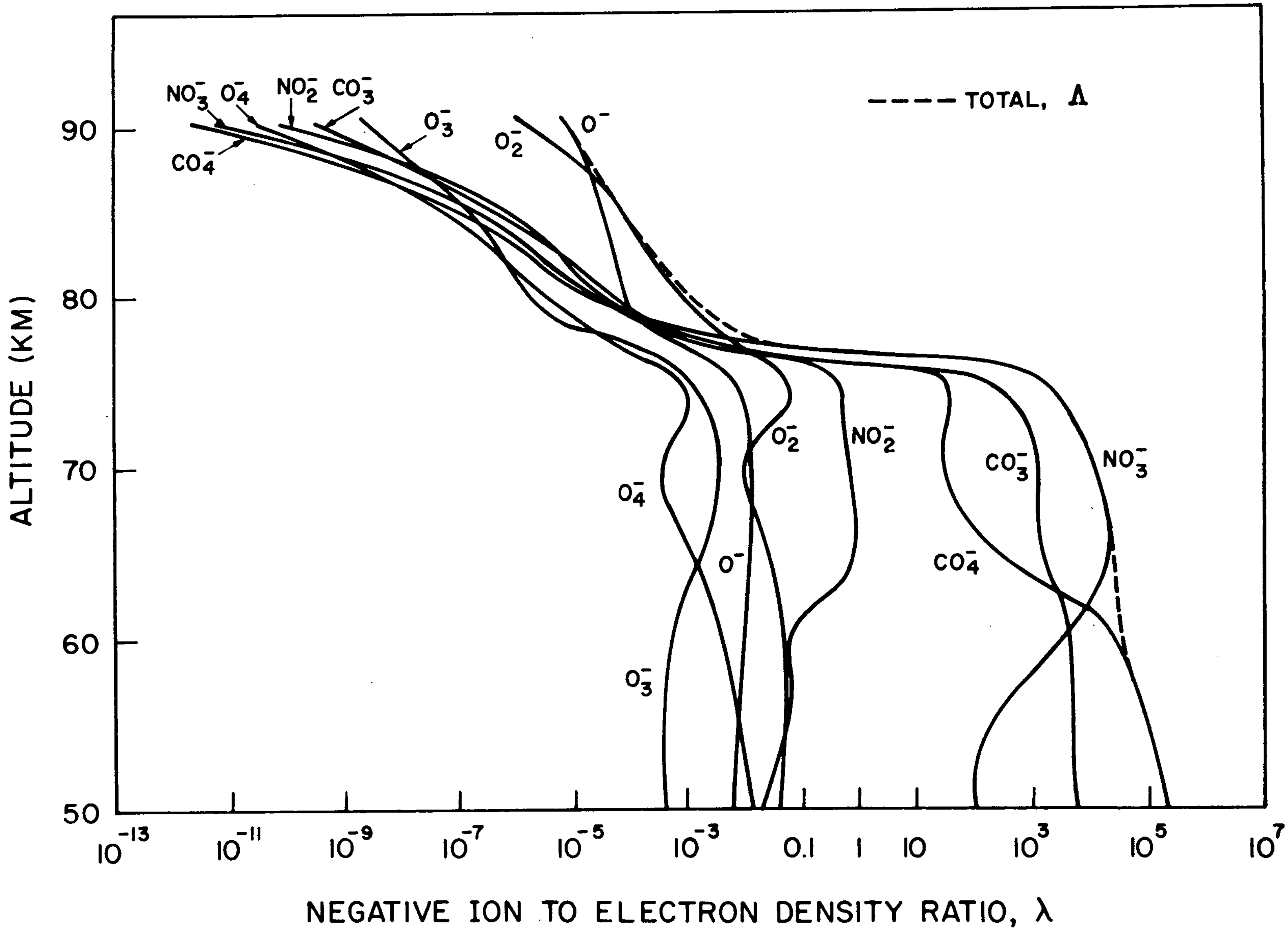

Figure 8.13 Negative ion-to-electron density ratios in the presunrise D region.

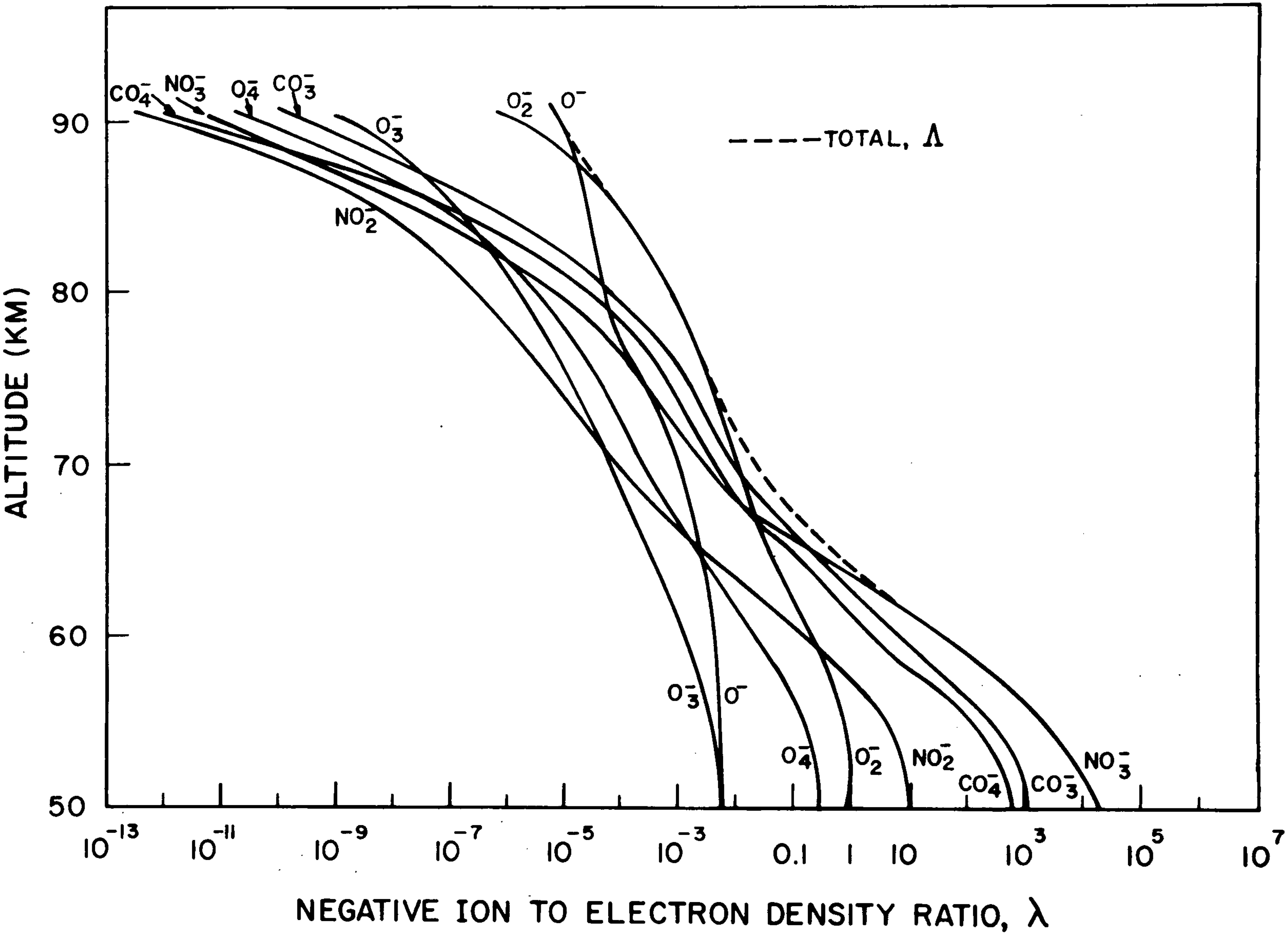

Figure 8.14 Negative ion-to-electron density ratios in the postsunrise D region.

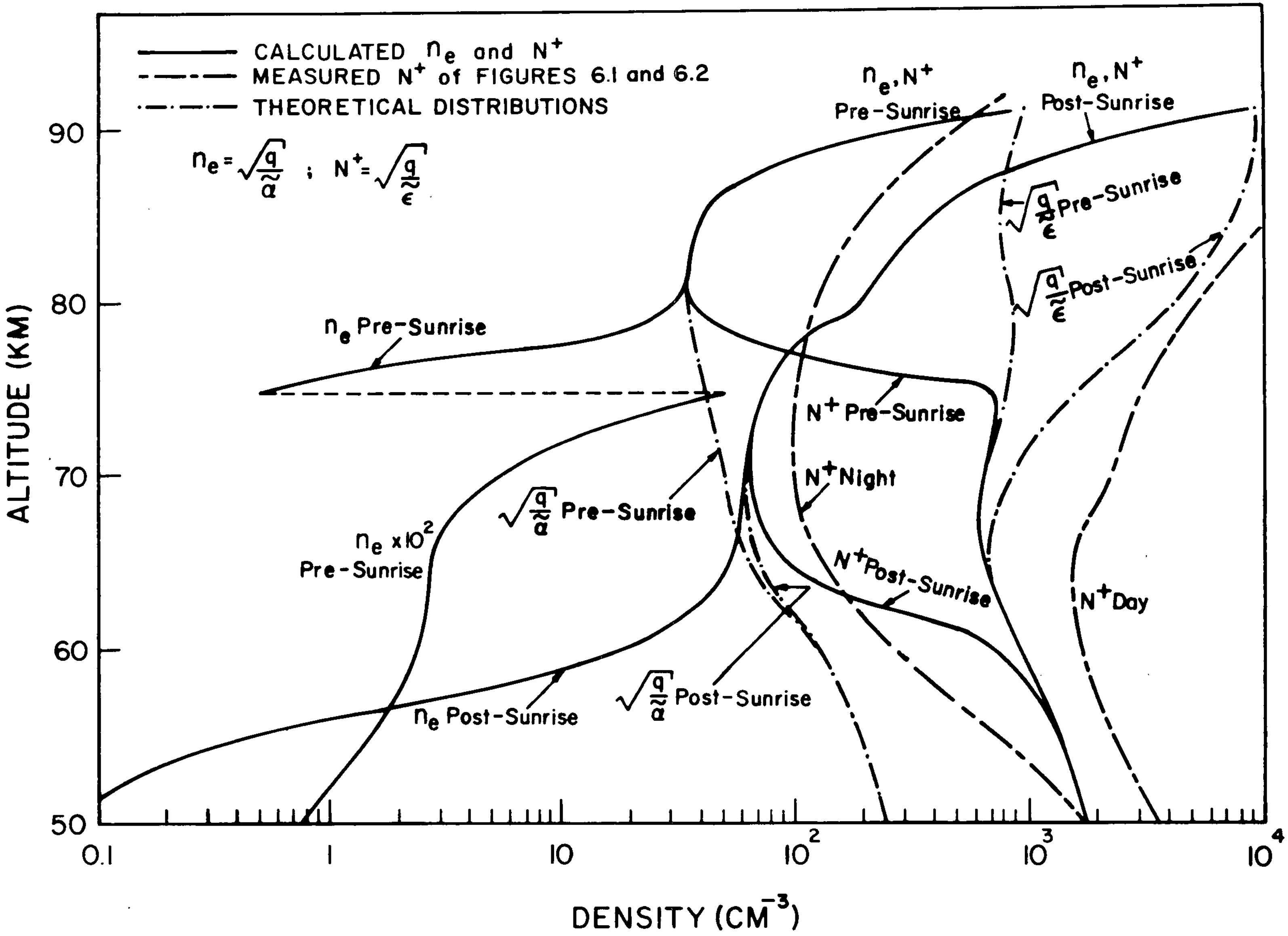

Figure 8.15 Presunrise and postsunrise electron and positive ion densities.

The negative ions are in a region where they are ion-ion recombination controlled at low altitudes, while detachment is dominant above 75 km. Note also that increases in the ion-pair production rate will decrease Λ, because at low altitudes $n_e \propto q$ while $N^- \propto q^{1/2}$. If $\tilde{\delta}$ were negligible at all altitudes Λ would have approximately the lapse rate of $\tilde{\beta}$, or $\Lambda \propto n_M^2$. Clearly this is not the case, and between 75 and 80 km detachment becomes dominant and produces a steep gradient in Λ.

Between 60 and 65 km at night there is a shift in the major negative ion from CO_4^- below to NO_3^- above this level. This is also the demarcation between the lower negative ion layer and the transition layer. Attachment and clustering from 50 to 60 km are so fast that negative ions are always important. Figure 8.14 shows that $\Lambda >> 1$ during the day at these altitudes also, and that NO_3^- has replaced CO_4^- as the dominant negative ion.

Although $\Lambda < 1$ from 65 to 75 km during the day (see Figure 8.14) negative ions still affect the equilibrium chemistry somewhat, especially around 65 km where $\Lambda \sim 1$. Above 75 km Λ is not significantly different than during the night. The reduction in Λ below 80 km during the day can be partially explained by the downward spread of the important detachment processes over sunrise. The most significant of these is the associative detachment of O_2^- by atomic oxygen, but photodetachment and $O_2(^1\Delta)$ detachment also play a role. Simultaneously, the alterations in the neutral chemistry at sunrise induce a shift in the negative ion composition toward the more easily detached ions, particularly O_2^-. Both of these effects must occur during sunrise if the electron densities are to display the proper behavior in this model.

It is interesting to compare the pre- and postsunrise positive ion distributions of Figure 8.15 with the nighttime and daytime distributions of Figures

6.1 and 6.2 (which have been reproduced in Figure 8.15). The daytime curves compare qualitatively but not quantitatively. One must consider that, firstly, the distributions displayed in Figures 6.1 and 6.2 are themselves only qualitative in nature, and secondly, that Figure 6.1 represents the positive ion densities during the day while in Figure 8.15 the values are for $\chi = 76°$. It would be expected that as the Lyman α radiation penetrated deeper into the D region, N^+ above 65 km would increase thereby bringing the two curves into a closer agreement. The smaller calculated positive ion densities are due in part to the larger values of the electron-ion recombination coefficient used in this study. Decreasing $\tilde{\alpha}$ would increase N^+ above 60 km in the postsunrise region.

The nighttime positive ion densities in Figures 6.2 and 8.15 agree quite well at the highest and lowest altitudes, but the calculated N^+ shows a marked depression near 85 km and large values below 75 km which are not seen in the measurements of Figure 6.2. Again, Figure 6.2 is only qualitative. In Figure 8.15 the valley near 85 km is due to the facts that electron-ion recombination is faster than ion-ion recombination, and a fast detachment mechanism exists above 75 km at night. One should find that the nighttime positive ion density will exceed the daytime density for altitudes between 60 and 80 km as long as

$$\tilde{\varepsilon} q_{Day} < \tilde{\alpha} q_{Night} \quad . \tag{8.53}$$

One can see that this condition is met for the calculated pre- and postsunrise N^+ in Figure 8.15.

The computed n_e and N^+ can be compared to the simple theoretical equilibrium values plotted in Figure 8.15. It can be seen that the theoretical n_e (for $\Lambda << 1$) are correct at 80 km and above during the night and above 65 km during the day. The theoretical N^+ (for $\Lambda >> 1$) are correct below 75 km at night and below 60 km during the day. When one considers that the post-sunrise values were extracted from a time dependent calculation, it is surprising that the agreement is so good. Other limiting expressions for n_e and N^+ could be obtained from Equations (8.19 and 8.20) and plotted for comparison in Figure 8.15. One would find that the high altitude N^+ and low altitude n_e were also very close to their equilibrium values both at night and during the day. All these correlations were observed in the computations and discussed in previous sections.

8.7 The Development of the C and D Layers at Sunrise

The measured electron densities which were illustrated in Figures 7.14a-d in Chapter 7 are reproduced here for convenience in Figures 8.16a-d. Calculated electron distributions over sunrise are illustrated for six different cases in Figures 8.17-8.22. One should note that in each of these figures the topside and bottomside C-layer electron distribution scale heights calculated in Section 8.2.3 can be seen only after the electron density has gone into quasi-equilibrium, but before the deepening D layer starts to obscure the C layer. The observation must therefore be confined approximately to zenith angles between 80° and 90°. The general shape of the C layer is reproduced quite consistently and accurately in each of the calculated distributions, as a comparison of Figures 8.16 and 8.17-8.21 shows. The C layer has a very sharp lower cutoff, and a topside scale height which is theoretically proportional to twice the atmospheric scale height.

All of the calculated distributions show the distinctive nighttime D-layer ledge at about 80 km (i.e. the pre-sunrise or $\chi = 98°$ distributions here). The ledge has a magnitude between 10-100 electrons-cm^{-3} and above 90 km it quickly grows into the nighttime E layer (Thomas and Harrison, 1970). In Figure 8.22 where the low-NO and slow recombination model was used the nighttime ledge is significantly larger than the measurements would suggest.

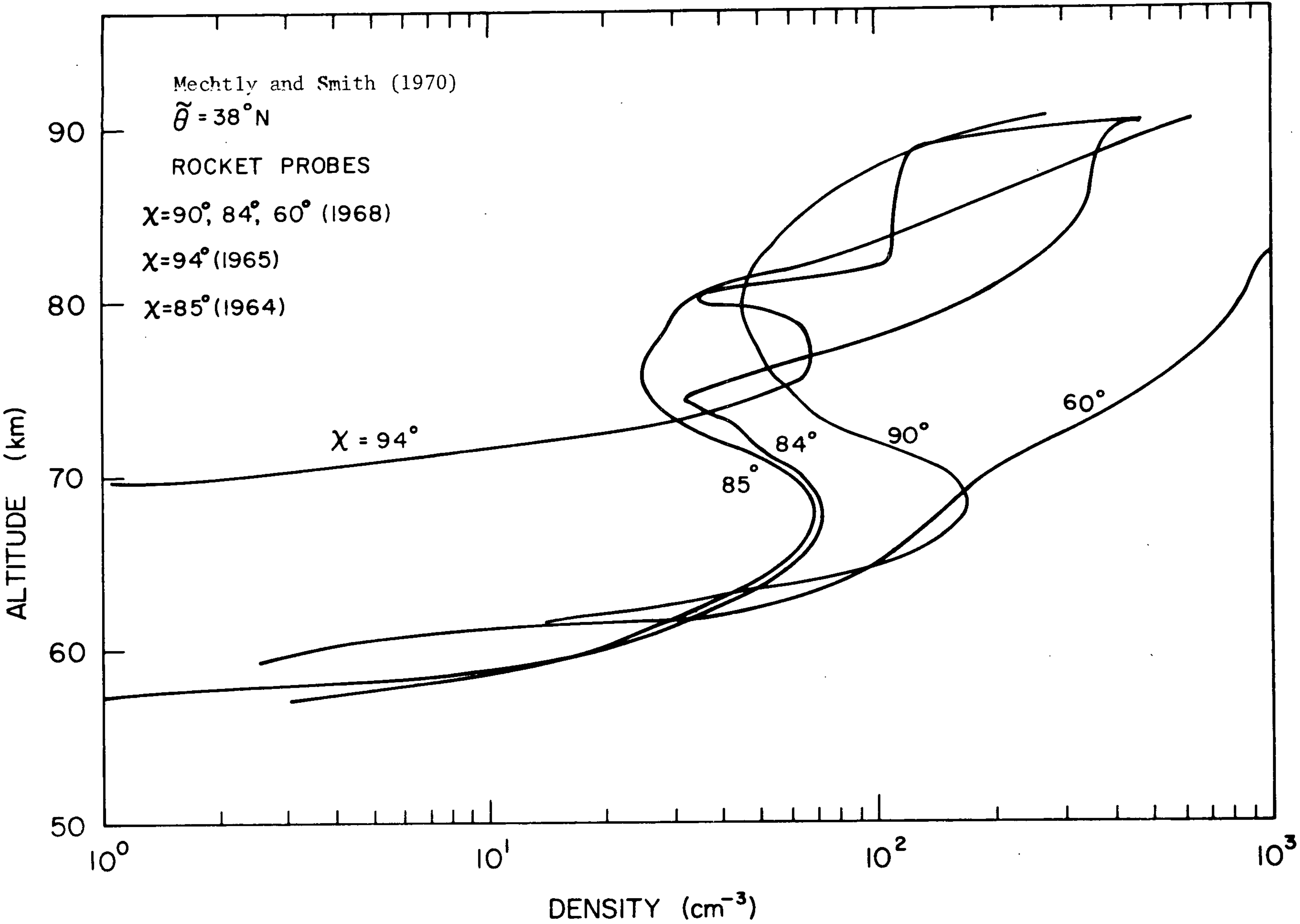

Figure 8.16a Experimental diurnal electron density variations in the D region

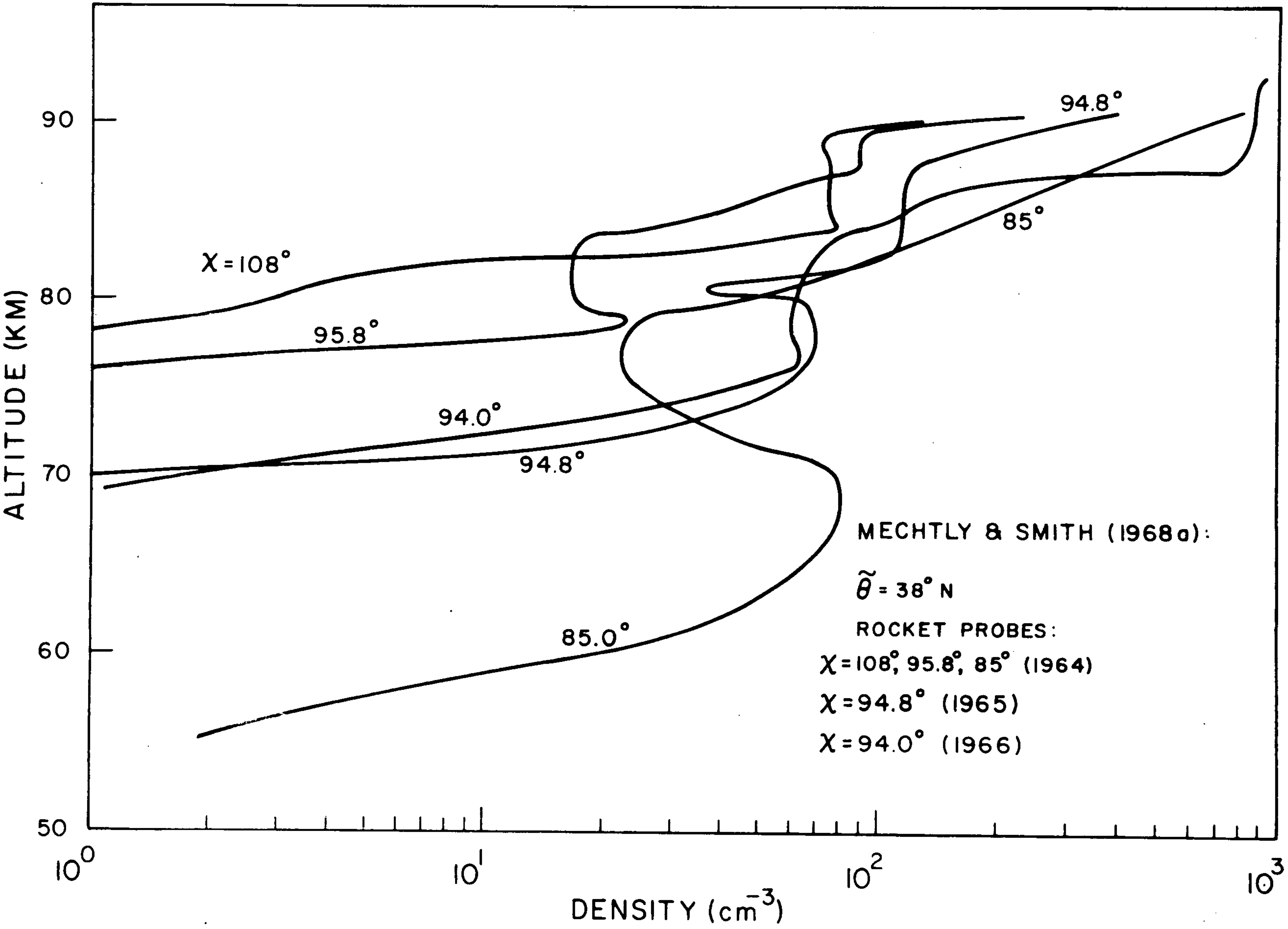

Figure 8.16b Experimental diurnal electron density variations in the D region.

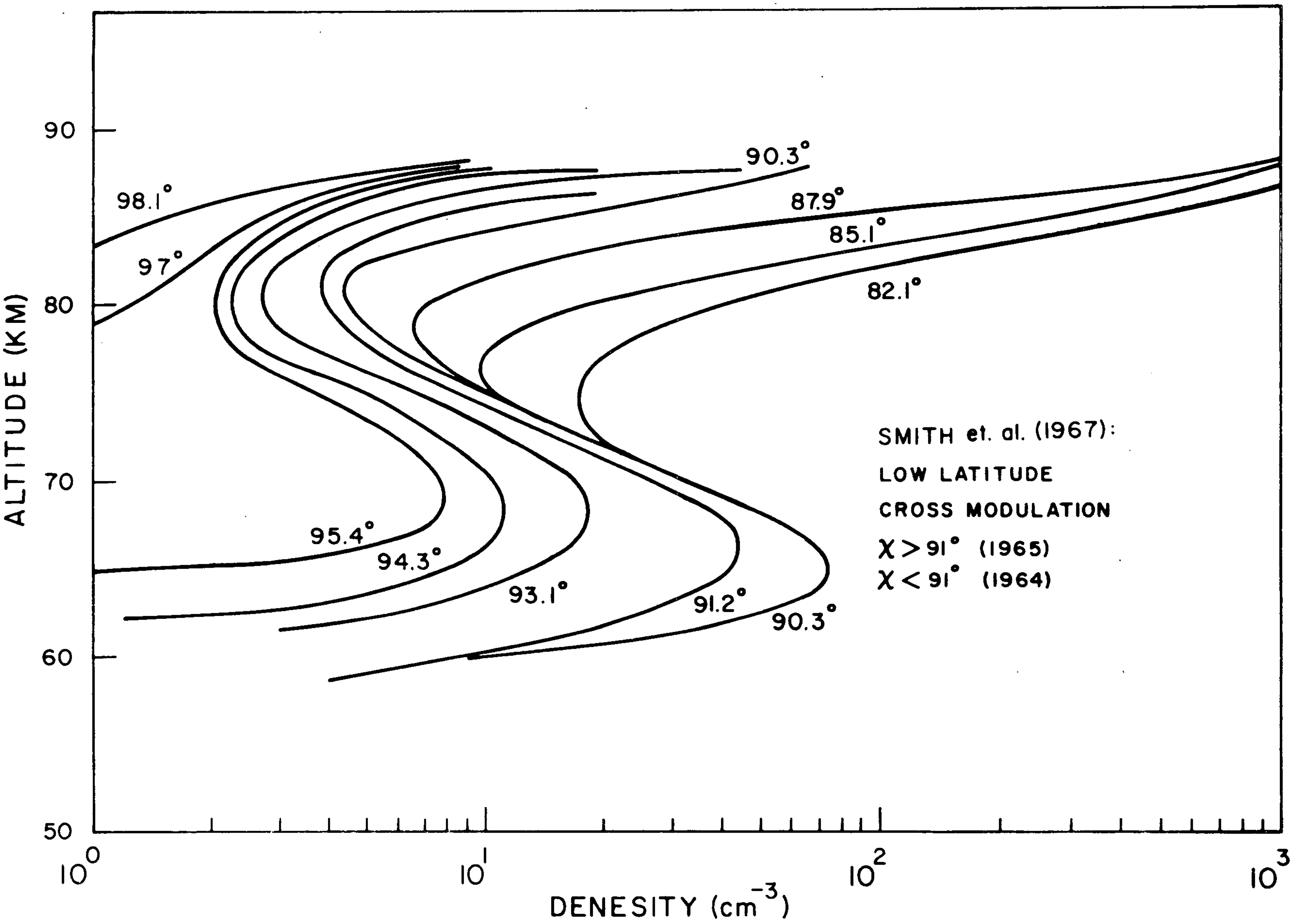

Figure 8.16c Experimental diurnal electron density variations in the D region.

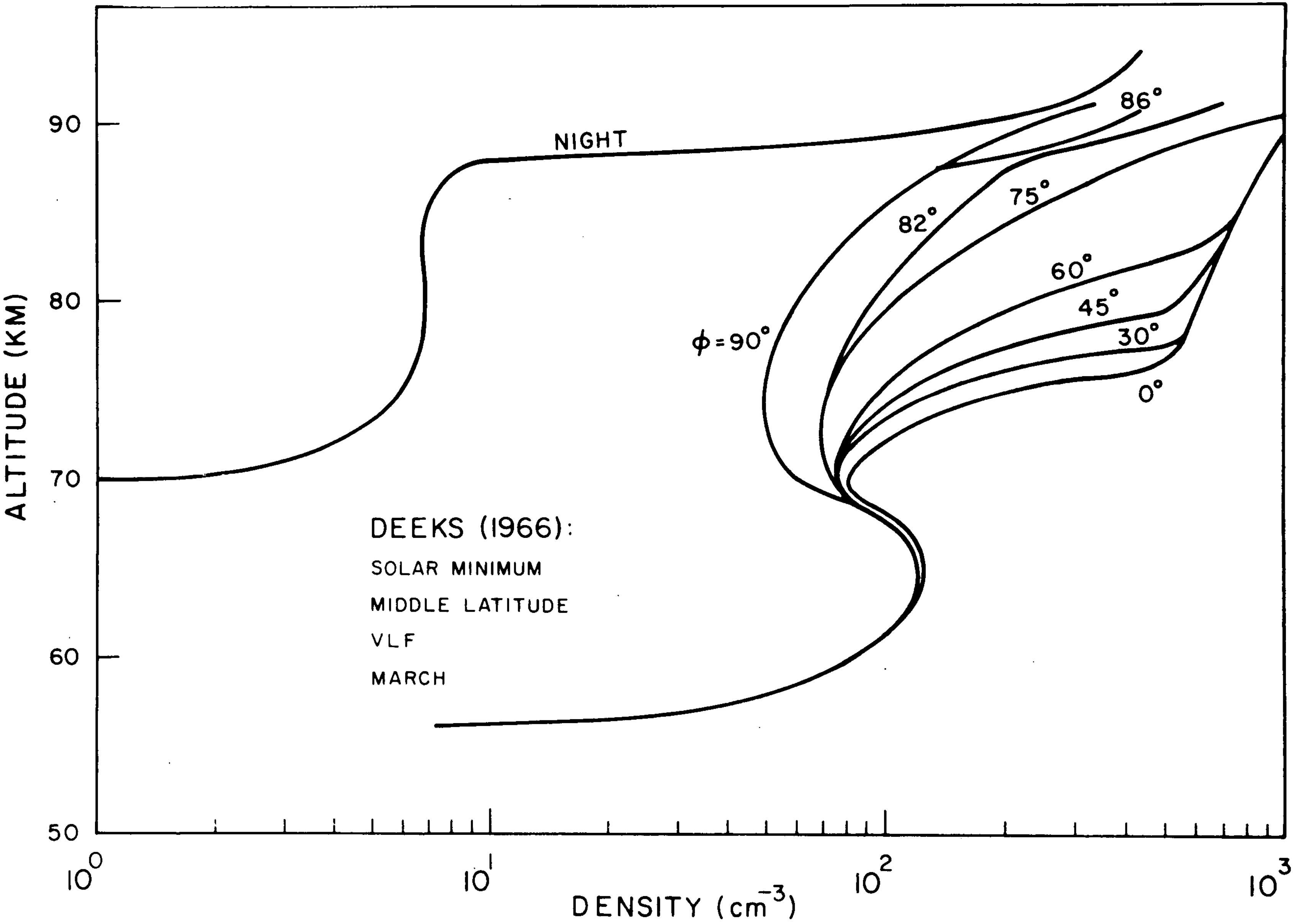

Figure 8.16d Experimental diurnal electron density variations in the D region.

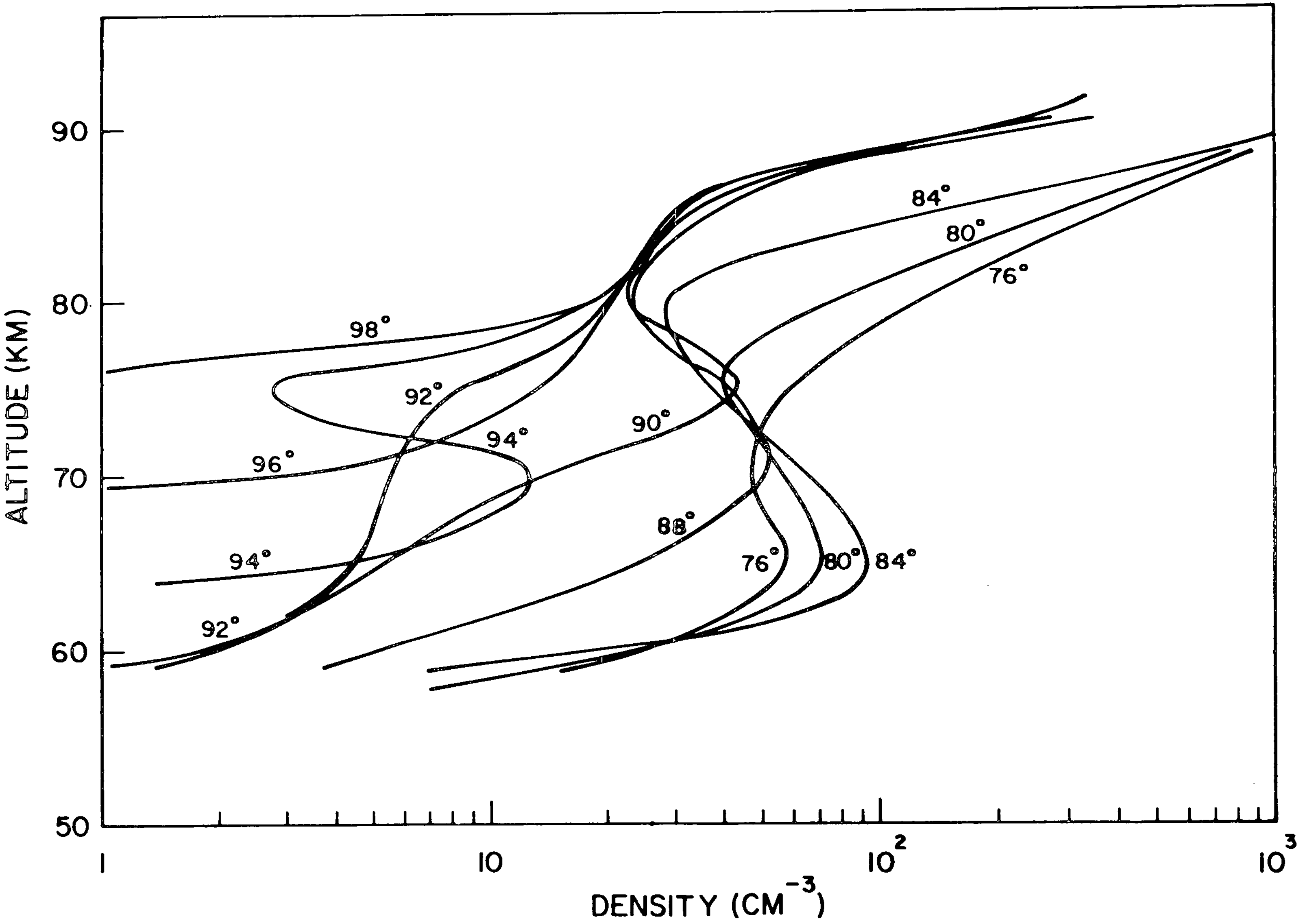

Figure 8.17 Calculated diurnal electron density variations in the D region: Case I. High-O-Low-NO model, fast electron-ion recombination, NO_3^- reaction rate with O, $k(NO_3^-) = 0$.

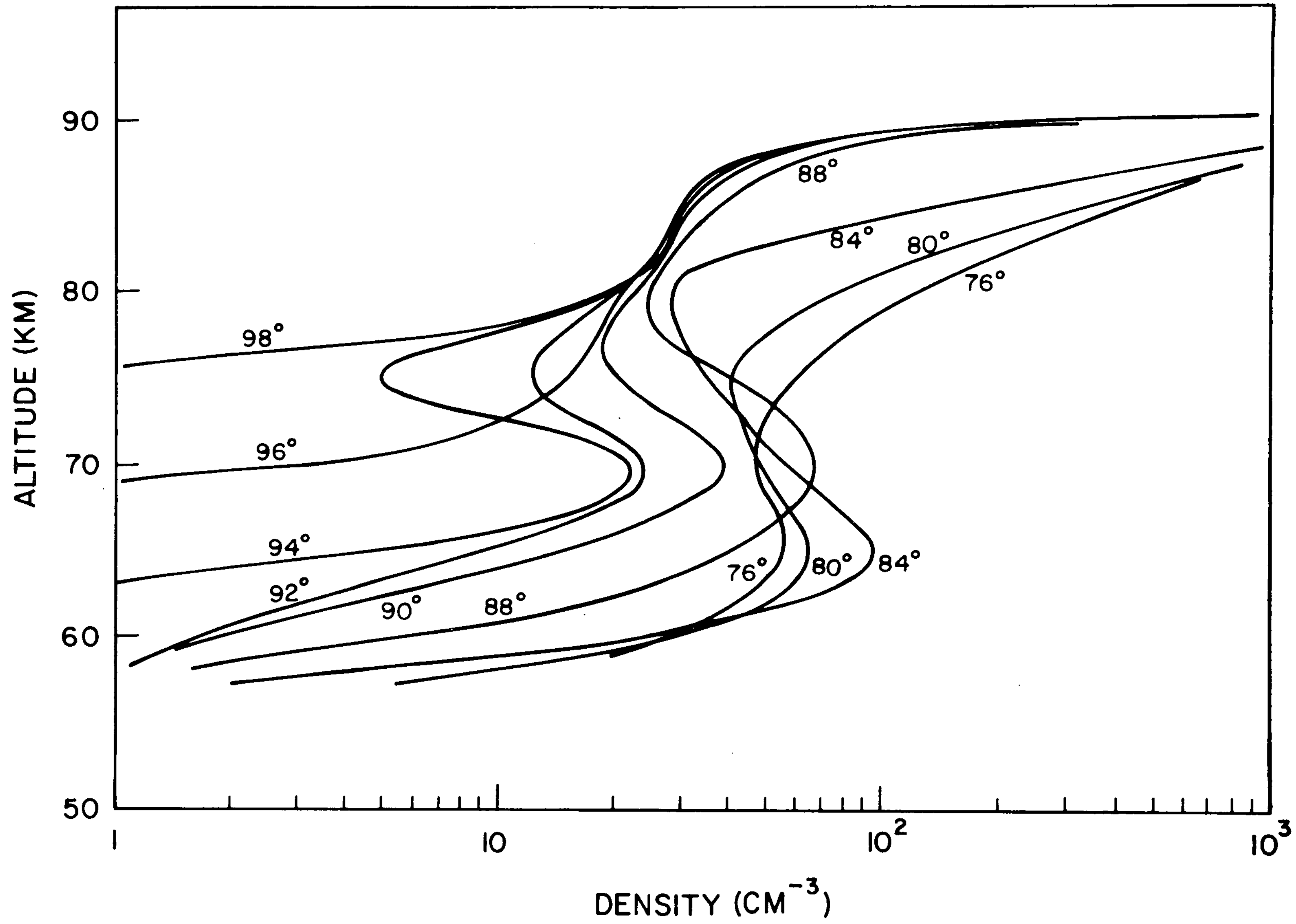

Figure 8.18 Calculated diurnal electron density variations in the D region: Case II. High-O-Low-NO model, fast recombination, $k(NO_3^-) = 10^{-14}$ cm^3 sec^{-1}.

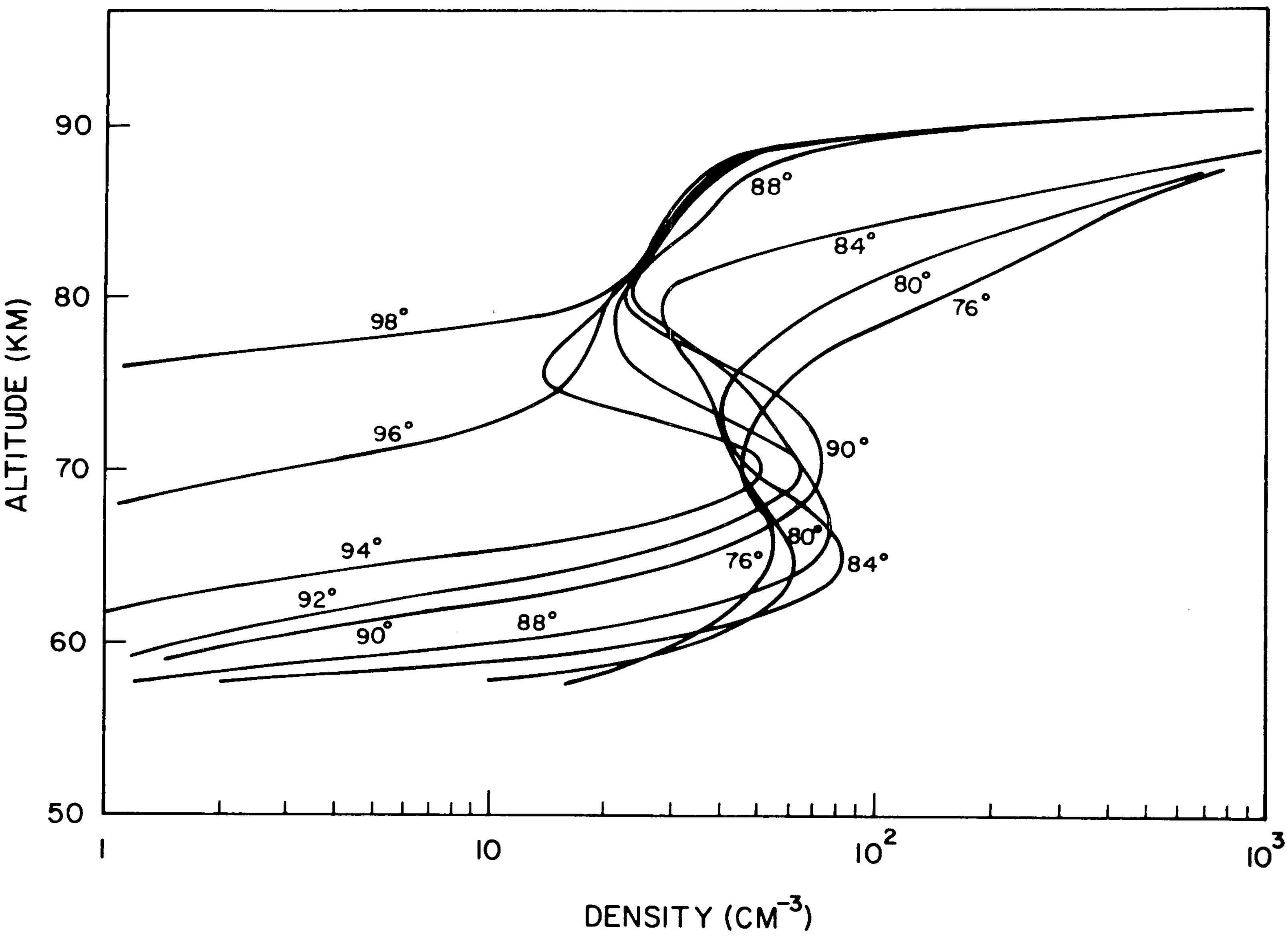

Figure 8.19 Calculated diurnal electron density variations in the D region: Case III. High-O-Low-NO model, fast recombination, $k(NO_3^-) = 5 \times 10^{-14}$ cm^3 sec^{-1}.

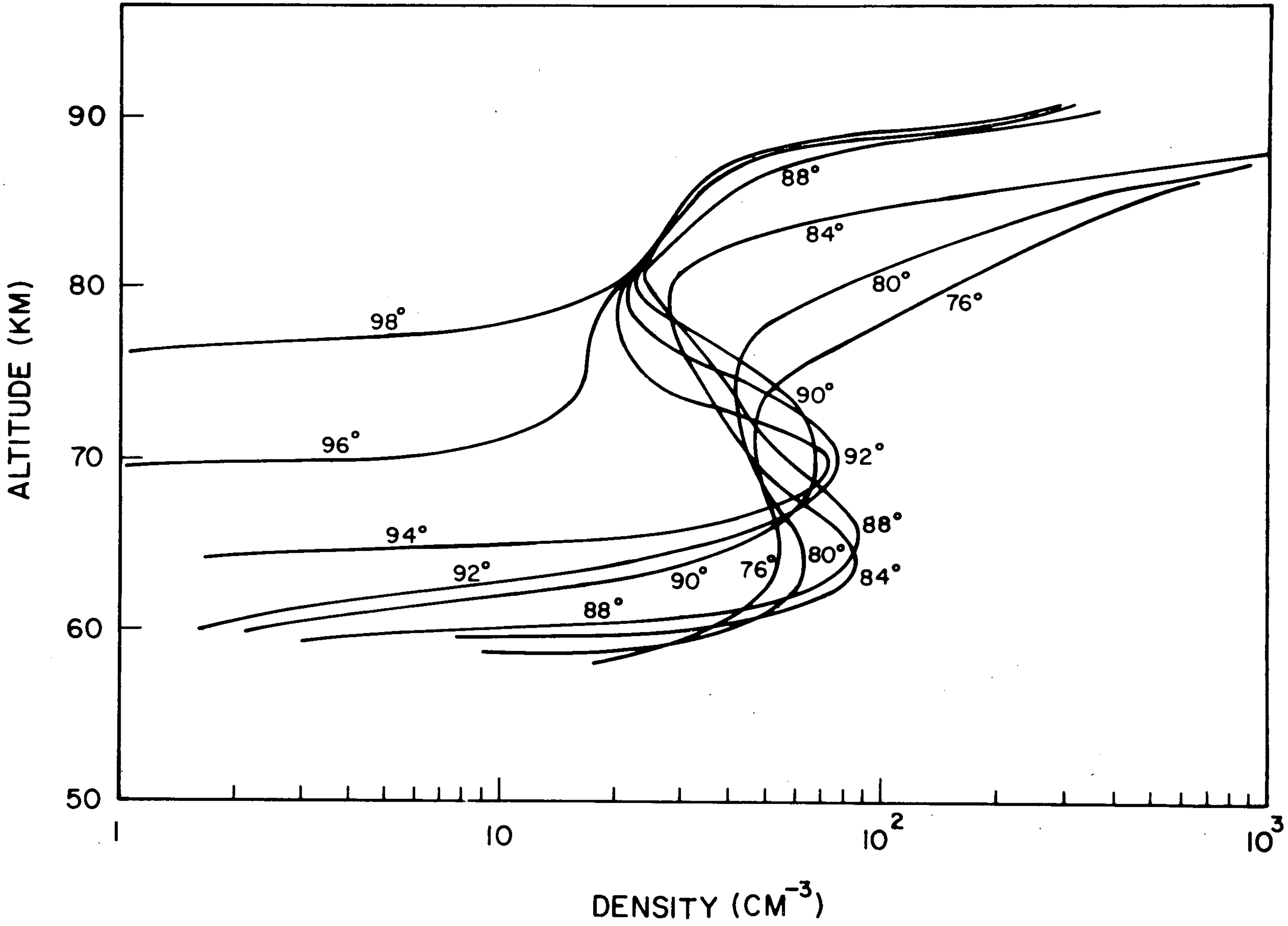

Figure 8.20 Calculated diurnal electron density variations in the D region: Case IV. High-O-Low-NO model, fast recombination, $k(NO_3^-) = 10^{-13}$ cm^3 sec^{-1}.

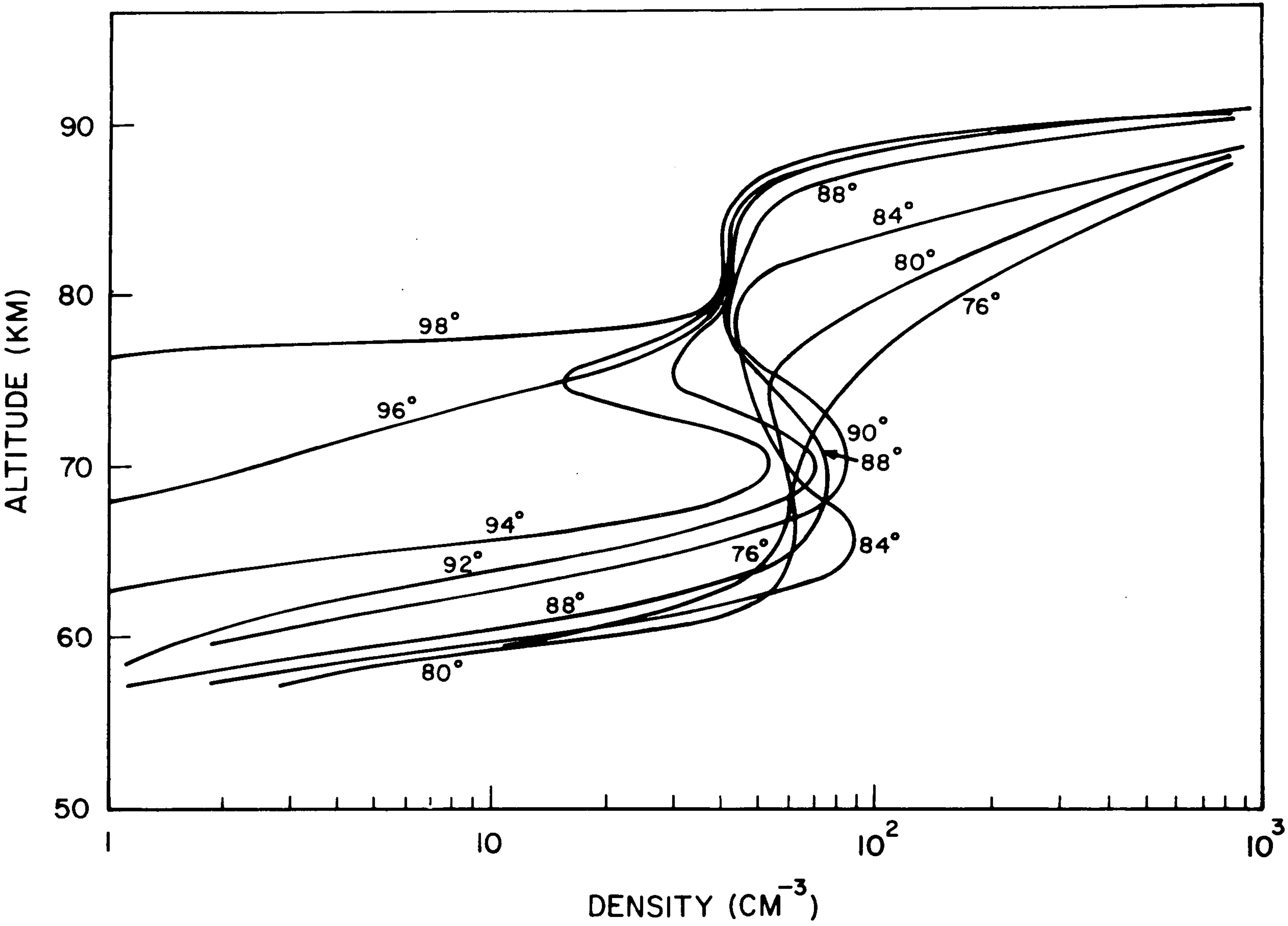

Figure 8.21 Calculated diurnal electron density variations in the D region: Case V. High-O-High-NO model, fast recombination, $k(NO_3^-) = 5 \times 10^{-14}$ cm^3 sec^{-1}.

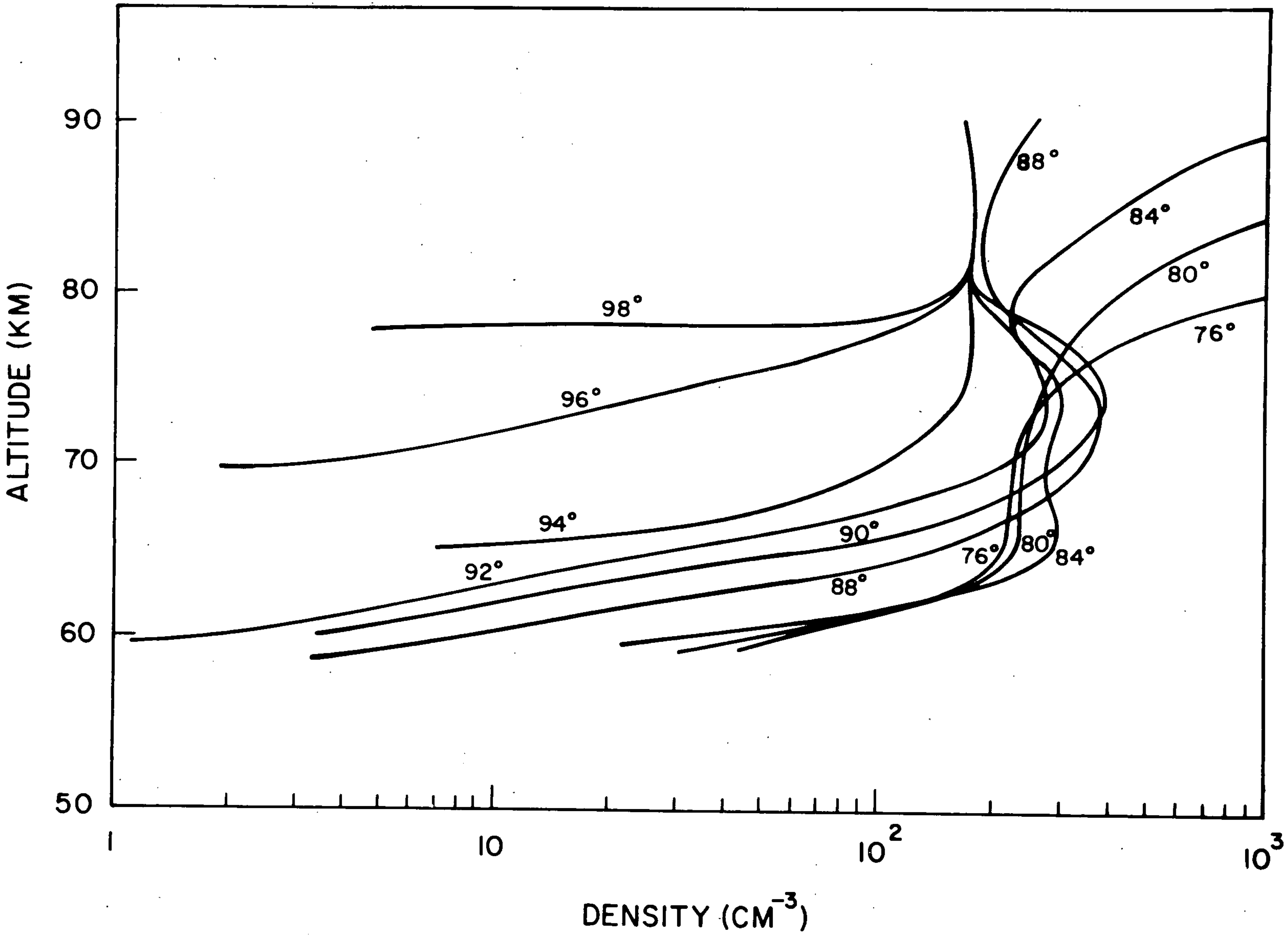

Figure 8.22 Calculated diurnal electron density variations in the D region: Case VI. High-O-Low-NO model, slow recombination, k(NO_3^-) = 5 x 10^{-14} cm^3 sec^{-1}.

Figure 8.17 shows the results for the high-O-low-NO model with fast recombination, but with the $NO_3^- \rightarrow O_2^-$ conversion process absent. There are essentially two layer growths during the sunrise. The first is created by the CO_3^- to O_2^- conversion process at sunrise. It begins near 98° and has grown significantly by 96°. At 94° the peak has moved lower and is beginning to be damped out; by 92° the peak has disappeared through electron-ion recombination. The second peak, produced by the photodetachment of NO_3^-, begins to develop near 90°. As sunrise progresses the peak increases, broadens, and moves lower in the mesosphere producing a distinct C layer. By 84° the peak is fully developed. One can note a slight overshoot effect which occurs after 84°. The timing of the second, major peak depends on the behavior of the NO_3^- photodetachment rate at sunrise. This is an unknown quantity and has only been estimated here.

The early electron behavior ($\chi > 90°$) for this model does not agree with measured electron distributions. The comparison is especially bad near 92° where the model n_e values are very low. The large overshoot decay could be partially compensated by an earlier photodetachment commencement.

Figures 8.18-8.20 were calculated for the same conditions as in Figure 8.17 except that the NO_3^- to O_2^- conversion process was included with rate constants of 1×10^{-14}, 5×10^{-14}, and 1×10^{-13} cm^3 sec^{-1}, respectively. Above 80 km no effect is present. But in the sequence of figures one can see that the early electron densities (i.e. $\chi > 90°$) are progressively increased as the rate is increased. The altitude of the C-layer peak remains constant at about 70 km during the early sunrise and then drops down to about 65 km for $\chi \lesssim 90°$. In Figure 8.17, on the other hand, the early peak moves down as sunrise progresses because the very fast CO_3^- conversion process begins with the first atomic oxygen increase at sunrise and then quickly disappears, while the NO_3^- conversion process is a long term process and depends more on the time development of the O density rather than just on its point of initial increase. Thus the CO_3^- process will move downward at sunrise as the ozone dissociating radiation penetrates to lower and lower altitudes, while the NO_3^- process will be most effective at the altitude where the O-NO_3^- density product is the largest (i.e. at 70 km for $\chi > 90°$ in these calculations. By comparison, a layer which is formed by photodetachment would also move steadily downward as sunrise progressed and more radiation could penetrate to the lower altitudes. This is illustrated by the C-layer development in Figure 8.17, which is essentially a photodetachment layer.

The smallest value of the rate constant, $k(NO_3^-) = 1 \times 10^{-14}$ cm^3 sec^{-1} produces a smooth C-layer increase over the sunrise which is very similar to Smith's (1967) curves in Figure 8.16c. Increasing the rate has its largest effect near 94° where n_e is sharply increased. For $\chi < 90°$ there is only a small variation in n_e with changes in the rate constant.

Several significant differences exist between the rocket data in Figures 8.16a and b and the calculated data in Figures 8.18-8.20. First, the 96° layer cuts off about 5 km higher for the rocket measurements, and the 94° peak is closer to 75 km than to 70 km as it is for the calculations. There is also a substantial overshoot in n_e at 90° in Figure 8.16a which is not evident in Figures 8.18-8.20, and the layer at 90° is lower in altitude too by several kilometers.

The electron ledges at 98°, 96°, and 94° are determined principally by the atomic oxygen densities early in the sunrise. A delay in the O density increase between 65 and 75 km at sunrise would bring the measured and calculated electron densities into closer juxtaposition. A delay in atomic oxygen could also increase the overshoot effect on 90°; and, depending on the detailed time behavior of the O, in conjunction with the NO_3^- process a delay could resolve the discrepancy in the altitude of the 90° peak. In Chapter 3, however, where the sunrise variations in the O densities were calculated it was seen that even a substantial delay in the ozone sunrise will not affect the early atomic oxygen increase very much. It would seem to be very difficult to delay the atomic oxygen increase significantly at sunrise although it can be slowed down. This is not meant to imply that the postsunrise O densities must therefore be lower such that the O densities over the entire sunrise will be proportionately decreased.

Figure 8.21 gives the electron distributions for the high-O-high-NO model with fast recombination and $k(NO_3^-) = 5 \times 10^{-14}$ cm^3 sec^{-1}. These are the same calculations which are illustrated in Section 8.6, Figures 8.4-8.12. Of all the calculations which were done, the electron densities in Figure 8.21 compare the best qualitatively and quantitatively with the rocket and VLF data.

By contrast, in Figure 8.22 where a high-O-low-NO, slow recombination, $k(NO_3^-) = 5 \times 10^{-14}$ cm^3 sec^{-1} model is utilized one can see that there are practically no points of comparison with the measurements. The distributions show one large peak near 75 km, with a lower altitude peak appearing at about 84°. These general characteristics were found to hold for all the calculations using slow recombination.

The D-layer development after sunrise ($\chi < 90°$) is practically the same for all the calculations, and compares well with the measured D-layer growth. There are no significant changes in the D layer until Lyman α radiation begins to penetrate below 90 km and ionize nitric oxide. This occurs near 90°, and the layer grows steadily in the postsunrise region. The C layer also continues to decay somewhat below 70 km because of electron-ion recombination while the D layer is filling in the electron distribution above 65 km. Calculations were only performed to a zenith angle of 76° but one can already see (in Figure 8.21) the similarity in behavior to the 60° curve of Figure 8.16a.

The well-known VLF effects near 98° and 94° can be explained qualitatively from the calculated electron distributions in Figure 8.21. It was found in Section 8.6.2 that the electron density begins to grow just before 98° at 75 km. This implies that there is a change in the slope of the electron density between 75 and 80 km near 98°, although this change is not shown in the calculations because a height resolution of only 5 km has been used. The 96° curve in Figure 8.21 also suggests a change in the electron density slope propagating from around 98° at sunrise. Near 94° a well defined layer with a sharp peak has developed, and this feature then continues to grow in size for several degrees. By this time the D layer has begun to develop above 80 km. No calculations of the resulting VLF absorption were done, but the comparison to observed VLF absorption data roughly confirms the calculated electron distributions.

The 98° effect depends on the earliest electron development between 75 and 80 km, which in turn depends a great deal on the atomic oxygen development there. Variations in the amount of radiation reaching large zenith angles, or in the presunrise ozone densities could then enhance or eliminate the 98° effect on different days. If more atomic oxygen were transported below 80 km on certain nights the 98° effect could be masked at sunrise. One might also postulate that changes in the nitric oxide densities bewteen 75 and 80 km could alter the CO_3^- densities sufficiently to alter the 98° effect.

In all, the calculated electron distributions of Figure 8.21 (and Figures 8.4-8.12) seem to represent a good description of the sunrise D region. The model on which these calculations are based would therefore seem to be an accurate model of the sunrise D region.

9. SUMMARY AND CONCLUSIONS

This study of the D region of the ionosphere has attempted to explain some of the features in the electron density variations over sunrise. In particular, the development of the C and D layers in the mesosphere were investigated. There have been several measurements of these electron layers for various conditions. Generally, measuring techniques which rely on radio wave propagation can only suggest a large number of possible electron distributions because the spatial resolution with low electron densities is very poor. On the other hand, techniques such as rocket probes measure the electron densities for perhaps a unique set of conditions which may vary from day to day, and enough consistent measurements of this type have not yet been made to be able to deduce a long-term average electron density behavior. The parameters which were utilized in this study and the electron densities which were predicted are to be considered as average values for these quantities. They are the results of a particular model of the D-region ion and neutral chemistry. Certainly, any one ionospheric measurement would not agree in all details with such a set of calculations because every possible variation in the model which might reflect a real occurrence in the terrestrial atmosphere was not considered. The measured electron distributions shown in Figures 7.1a-d are then to be taken as typical measures of the electron densities in the mesosphere for various times of the day.

The electron densities which were computed here showed a limited range of values for reasonably large changes in some of the model parameters. This suggests a certain amount of ambiguity in the results since several different models could reproduce any given set of sunrise features. By varying the model parameters consistently over the entire altitude range of the calculations simultaneously, and observing the electron density behavior at several altitudes over the entire sunrise (as in Figures 8.17-8.22) a great deal of the ambiguity can be removed. Even so, the range of electron densities which could be predicted by the various models was large enough to encompass most of the measured electron density distributions.

Several parameters which were discussed in the text are worthy of mention here. The average electron-ion recombination coefficient $\tilde{\alpha}$ was assumed to have values as large as those deduced by Reid (1970). An $\tilde{\alpha}$ of the order of 10^{-5} cm^3 sec^{-1} may be consistent with the presence of hydrated positive ions. Whether hydrated positive ions are dominant over parts of the D region, and whether their recombination coefficients can be this large are still matters of conjecture. The calculations performed in this study lead to the conclusion that $\tilde{\alpha}$ must be greater than 8×10^{-7} cm^3 sec^{-1} although it can be less than the values of Reid (1970). An $\tilde{\alpha}$ of 5×10^{-6} to 1×10^{-5} cm^3 sec^{-1} would seem reasonable (Biondi, 1969). One could then resolve the measured daytime electron densities above 65 km with theoretical predictions by assuming lower NO densities (such as Meira, 1970) than those suggested by earlier measurements (Barth, 1966a and b; Pearce, 1969).

The reaction of atomic oxygen with NO_3^- was also included in the charged specie reaction scheme with a rate constant of 5×10^{-14} cm^3 sec^{-1}. This was necessitated by the need for a process which could produce electrons (or lead to the production of electrons) early in the sunrise, or just after 94° in the transition region from 65-75 km for the model used here. The process had to involve the dominant negative ion, NO_3^-. Possible candidates for the process were photodetachment or an ion-neutral reaction which would lead to the eventual release of electrons. Photodetachment of NO_3^- would probably occur too late to explain the sunrise electron behavior. The atomic oxygen reaction was a reasonable choice and it is discussed in Chapter 8 of the text. An important point to consider is the possibility that NO_3^- may not be the dominant presunrise negative ion. Recent studies have shown that hydrated negative ions will be present in the D region. If these ions are dominant ones in a relatively stable nighttime environment they will be the most numerous sunrise ions. It is reasonable to assume that hydrated negative ions may be easily photodetached, or may undergo a series of reactions with O or $O_2(^1\Delta)$ which could ultimately produce electrons early in the sunrise (possibly replacing even the earliest CO_3^- source of electrons). Since the photochemistry of hydrated negative ions is not known at this time the series of assumptions made above cannot be quantitatively tested. The model used in this study has been tested, however, and it can reproduce many general features in the development of the electron densities over the sunrise. Until further knowledge of the more complex charged hydrated species in the D region is accumulated, models similar to the one proposed here will have to be studied. Such models which ignore the negative hydrates may ultimately prove to be substantially correct anyway.

The mesospheric O and NO densities are important parameters in the D-region negative ion photochemistry. It was found that the O density controls most of the important sunrise processes such as the associative detachment of O_2^- and the conversion of CO_3^- and NO_3^- into O_2^-. Substantial quantities of O are necessary to drive these processes. In the absence of O, other processes such as $O_2(^1\Delta)$ detachment would not produce enough electrons at sunrise in the model assumed here to explain observed electron densities. Postsunrise

O densities on the order of those reported by researchers such as Hunt (1966), Hesstvedt (1968), and Shimazaki and Laird (1970) are sufficiently large. The mesospheric NO distribution is still a questionable quantity; and so reasonable values between the high values of Barth (1966a and b) and Pearce (1969) and the lower values of Nicolet (1965a and b) and Meira (1970) were adopted.

The computed electron distributions in the mesosphere agree quite well quantitatively with the measured electron distributions. The general time development of the C and D layers also corresponds closely to the measured time development. Detailed comparisons are discussed in Section 8.7. The following conclusions have been reached concerning the computations done here. Besides the relatively high $\tilde{\alpha}$ values which seem necessary, the reaction of NO_3^- with atomic oxygen is also needed to bring the calculated and measured electron densities into agreement. Although a small rate of 5×10^{-14} cm^3 sec^{-1} was assumed, this reaction is still uncertain. The resulting electron distributions are capable of explaining the observed VLF effects near 98° and 94°. The first can be attributed to a change in the slope of the electron density distribution between 75 and 80 km. The 94° effect corresponds to the formation and growth of a distinct peak in the electron density, the C layer. It is felt that the model proposed here is a good one for describing the mesosphere at sunrise.

Some suggestions can be made concerning future work in the sunrise D region. Until more is known about hydrate chemistry and the photodetachment of negative ions, critical hindrances to theoretical calculations will remain. But one could expand the negative ion chemistry, consider the details of the positive ion chemistry, or attempt to solve the entire charged and neutral specie photochemistry simultaneously over the sunrise, including transport effects; and could extend the analysis over many diurnal cycles to establish the consistency of the daytime and nighttime photochemical predictions. The work done here would hopefully provide some guidelines. Variations from the normal D-region behavior could also be studied, as well as seasonal and solar cycle effects.

Coordinated measurements of the sunrise D region are also needed. A series of rocket probes might measure the electron and negative ion densities in the pre- and postsunrise regions, as well as the electron densities at zenith angles of 96°, 94°, 92°, and 90° in order to observe systematically the early development of the D region on one particular (quiet, non-winter, low or mid-latitude) day. Probes at 85° and 80° (the latter could be the postsunrise probe) would make a complete set of sunrise electron distributions. If only a limited number of probes were available they could be used near 95° and 90° along with either a presunrise or postsunrise probe. Unfortunately the important minor neutral constituents are not easily measurable. VLF or partial reflection measurements might be carried out in conjunction with the rocket probes so that one could establish more clearly the relationships between the electron densities being measured by each technique.

APPENDIX I. RAYLEIGH SCATTERING CROSS SECTIONS

The total cross sections for Rayleigh (dipole) scattering of natural (unpolarized) light is given by Goody (1964) as

$$\sigma_R = \frac{32\pi^3}{3} \frac{(\mu-1)^2}{N^2\lambda^4} \tag{I.1}$$

where μ is the index of refraction, and N is the gas density. Goody has tabulated values of $(\mu-1)/N$ for air as well as a correction factor to Equation (I.1) which is necessary because the polarizabilities of the air constituents are not scalar. Using Equation (I.1) and Goody's corrections and data one can calculate σ_R from 2000 Å through optical wavelengths.

For the purposes of this Appendix, it is assumed that the scattering is isotropic, so that the differential scattering cross section is given by

$$\frac{d\sigma}{d\Omega} \equiv \tilde{\sigma} = \frac{1}{4\pi} \sigma_R \quad . \tag{I.2}$$

To obtain the effect of Rayleigh scattering on impinging solar radiation consider the model proposed in the text, i.e., an infinite medium with a plane wave of energy incident. Consider the scattering into three segments, forward scatter into a cone defined by the angle, θ_ℓ, backscatter into a similar cone of θ_ℓ, and 'lossy' scatter into all other angles. The scattering into the cones represents energy transmitted and reflected along the beam, while the lossy scattering represents the absorption or loss of energy from the beam. One calculates the total cross sections for forward and reverse scattering, and lossy scattering as

$$\begin{aligned} \sigma_{\text{for.}} &= \sigma_{\text{back.}} = \sigma = \frac{1}{2}\sigma_R(1-\cos\theta_\ell) \\ \sigma_{\text{loss}} &= \sigma_\ell = \sigma_R \cos\theta_\ell \quad . \end{aligned} \tag{I.3}$$

Suppose one now looks at a thin slab of gas of density, n, and thickness, δx, at x, and defines the following steady state intensities:

$I(x)$ = incoming flux incident from the right of the slab

$R(x)$ = total flux reflected back toward the right from the slab

$I(x+\delta x)$ = outgoing flux from the left of the slab

$R(x+\delta x)$ = total reflected flux incident from the left of the slab.

Using superposition one arrives at the following equations

$$I(x+\delta x) = I(x)[1-n(x)(\sigma+\sigma_\ell)\delta x] + R(x+\delta x)n(x)\sigma\delta x$$

$$R(x) = I(x)n(x)\sigma\delta x + R(x+\delta x)[1-n(x)(\sigma+\sigma_\ell)\delta x] \quad .$$

Passing to the limit, $\delta x \to 0$, these equations become

$$\begin{aligned} I'(x) &= -n(x)(\sigma+\sigma_\ell)I(x) + n(x)\sigma R(x) \\ R'(x) &= -n(x)\sigma\, I(x) + n(x)(\sigma+\sigma_\ell)R(x) \quad . \end{aligned} \tag{I.4}$$

The solution of Equations (I.4) is

$$\begin{pmatrix} I \\ R \end{pmatrix} = \exp\left\{ \int_0^x n(x')dx' \, A_\sigma \right\} \begin{pmatrix} I_0 \\ R_0 \end{pmatrix} \tag{I.5}$$

where

$$A_\sigma = \begin{pmatrix} -\sigma_p & \sigma \\ -\sigma & \sigma_p \end{pmatrix} \; ; \quad \sigma_p = \sigma + \sigma_\ell \quad .$$

The solution is readily expanded yielding

$$\begin{pmatrix} I \\ R \end{pmatrix} = \left\{ \cosh(\bar{n}\sigma_0) \mathcal{I} + \frac{\sinh(\bar{n}\sigma_0)}{\sigma_0} A_\sigma \right\} \begin{pmatrix} I_0 \\ R_0 \end{pmatrix} \tag{I.6}$$

where

$$\bar{n} = \int_0^x n(x')dx' \quad ; \quad \sigma_0{}^2 = \sigma_p{}^2 - \sigma^2 = \sigma_R \sigma_\ell$$

and $\mathcal{I}$ is the identity matrix.

Applying the boundary condition; $I, R \to 0$, $x \to \infty$, one gets the simple result

$$I(x) = I(0) \exp\left\{ -\sigma_0 \int_0^x n(x')dx' \right\} \quad . \tag{I.7}$$

This leads directly to the definition of an effective Rayleigh scattering cross section

$$\sigma_{Re} = \sigma_R \sqrt{\cos\theta_\ell} \quad . \tag{I.8}$$

The use of Equation (I.8) entails a specification of $\theta_\ell < \frac{\pi}{2}$, and for $\theta_\ell \lesssim \frac{\pi}{4}$, $\sigma_{Re} \sim \sigma_R$. Although the model includes the effects of multiple scattering, it does so in a very simple way. The specification of θ_ℓ should be based on the shape and distribution of the atmosphere, but is otherwise arbitrary. Noting that the atmosphere is quite 'thin' vertically, a very small θ_ℓ is expected, so that $\sigma_{Re} = \sigma_R$ is a good approximation in this case. However, since $\tilde{\sigma}_R$ is in reality anisotropic, with large relative forward and backward scattering amplitudes, the lossy scattering will be less than for the model just analyzed. Thus the effective cross section would be smaller than σ_{Re}. Still, the approximation $\sigma_{Re} = \sigma_R$ is possible.

To calculate the optical depth due to Rayleigh scattering the data for the standard neutral atmosphere are used, i.e., $n(M)$, H_M or n_0, H_0 of the text.

APPENDIX II. A TWO-EXPONENTIAL ATOMIC OXYGEN MODEL

A two-exponent model for atomic oxygen may be written

$$n_1(w') = n_{11}e^{-w'/H_1} - n_{12}e^{-w'/H_2} \tag{II.1}$$

where the subscript '1' is for atomic oxygen, and the parameters n_{11}, n_{12}, H_1, and H_2 could be specified by considering the peak density, the high altitude behavior, and the total vertical column content. For the distribution of (II.1) the optical depth can be written

$$\tau_1/\sigma_1 = n_{11}(w)\ H_1 \left\{F_1 - e^{-(w+w_p-2w_o)\left(\frac{1}{H_2} - \frac{1}{H_1}\right)} F_2\right\} \tag{II.2}$$

where F_1 and F_2 are the optical depth factors for each distribution separately, w_p is the altitude of the peak density, and w_o is the altitude where $n_1 = 0$.

As a particular case of Equation (II.1), consider the altitude as measured from the height where $n_1 = 0$. Then the following equations will hold

$$\begin{aligned} n_1(w') &= n_1\left(e^{-w'/H_1} - e^{-w'/H_2}\right) \\ n_1 &= \frac{N_1}{H_1-H_2} \\ \frac{n_{1p}}{N_1} &= \frac{1}{H_1}\, e^{-w_p/H_1} = \frac{1}{H_2}\, e^{-w_p/H_2} \end{aligned} \tag{II.3}$$

where N_1 is the total vertical daytime column content of atomic oxygen, and n_{1p} is the peak density occurring at $w' = w_p$. The model values of H_1 and H_2 are then the solutions of the last equation of (II.3) with $H_1 > H_2$.

APPENDIX III. A MODEL OF THE ABSORPTION OF THE LOW ALTITUDE OZONE PEAK

A parabolic ozone layer can be written as:

$$n(w') = n_p \left[1 - \gamma \left(\frac{w'-w_p}{\delta} \right)^2 \right] \quad ; \quad n \geq 0 \tag{III.1}$$

where subscripts indicating ozone are not written, n_p and w_p are values at the ozone distribution peak, and γ and δ are defined by

$$\begin{aligned} \gamma &= 1 - \frac{n_0}{n_p} \quad ; \quad n_0 = n(w_1) \;,\; n(w_2) \\ \delta &= w_p - w_1 \;,\; w_2 - w_p \end{aligned} \tag{III.2}$$

that is, δ is the halfwidth of the peak at $n = n_0$. The absorption equation is

$$\tau_p/\sigma = \int_{s_0}^{\infty} ds \; n(w') \tag{III.3}$$

where τ_p is the absorption due to the peak and σ is the absorption cross section. Since all the s_0 are in the altitude range 50-90 km, and w_p lies well below 50 km, the ray passes symmetrically through the peak. If the distribution is truncated at $w' = w_p \pm \delta$ one has

$$\frac{\tau_p}{\sigma} = 2 \int_{\bar{w}}^{w_p+\delta} \frac{dw'}{\sqrt{\frac{2(w'-h)}{a}}} \; n(w') \tag{III.4}$$

where Equation (2.96) for ds' has been used, and is certainly very accurate at these low altitudes, and where $\overline{w}$ is defined by

$$\overline{w} = \begin{cases} w_p + \delta & ; \quad h \geq w_p + \delta \\ h & ; \quad w_p - \delta < h < w_p + \delta \\ w_p - \delta & ; \quad h \leq w_p - \delta \end{cases} \tag{III.5}$$

where h is the minimum ray height. Equation (III.4) can be transformed into

$$\frac{\tau_p}{\sigma} = \sqrt{2a\delta}\; n_p \int_{\alpha_0}^{1} dx \, \frac{(1-\gamma x^2)}{\sqrt{x + \alpha}}$$

$$\alpha = \frac{w_p - h}{\delta} \quad ; \quad \alpha_0 = \frac{\overline{w} - w_p}{\delta} \tag{III.6}$$

which has the solution

$$\frac{\tau_p}{\sigma} = 2\sqrt{2a\delta}\; n_p \left\{ \sqrt{X+\alpha} \left[1 - \frac{1}{5}\gamma X^2 + \frac{4}{15}\gamma\alpha X - \frac{8}{15}\gamma\alpha^2 \right] \right\}_{\alpha_0}^{1} . \tag{III.7}$$

The solutions corresponding to (III.5) are

$$\frac{\tau_p}{\sigma} = 2\sqrt{2a\delta(1+\alpha)}\; n_p \begin{cases} 0 & ; \quad h \geq w_p + \delta \\ [1 - \frac{1}{5}\gamma + \frac{4}{15}\gamma\alpha - \frac{8}{15}\gamma\alpha^2] & ; \quad w_p - \delta < h < w_p + \delta \\ [1 - \frac{1}{5}\gamma + \frac{4}{15}\gamma\alpha - \frac{8}{15}\gamma\alpha^2] - \sqrt{\frac{\alpha-1}{\alpha+1}} & \\ [1 - \frac{1}{5}\gamma - \frac{4}{15}\gamma\alpha - \frac{8}{15}\gamma\alpha^2] & ; \quad h \leq w_p - \delta \end{cases} . \tag{III.8}$$

The absorption above the level $(w_p+\delta)$ must also be included in the calculation. Assume that the portion of the ray path above $w_p+\delta$ for $\chi<\pi/2$ is in the daytime ozone region. Then the absorption due to this segment is given by

$$\frac{\tau_{p1}}{\sigma} = n_T\, H_T\, F_0(\chi_T, X_T) \quad ; \quad \chi_T < \frac{\pi}{2}$$

$$X_T = \frac{a+w_p+\delta}{H_T} \quad ; \quad \sin\chi_T = \frac{a+h}{a+w_p+\delta} \qquad \text{(III.9)}$$

where n_T and H_T are the local daytime ozone density and scale height at the altitude $w_p+\delta$ (formally, $n_T = n_0$).

To evaluate the ray segment for $\chi > \pi/2$ above $w_p+\delta$ one can use Equation (2.102) with $\overline{g} = 1$, $\overline{g}^* = 0$ to calculate ΔF_T. Then the absorption will be given approximately by

$$\frac{\tau_{p2}}{\sigma} = n_T H_T [F_0(\chi_T, X_T) + \Delta F_T] - nHF_0(\pi-\chi, X) \qquad \text{(III.10)}$$

where n and H are evaluated at the end of the ray path, and X is normalized to H. The total absorption for ray paths with minimum ray heights, h, less than $w_p+\delta$ can then be written

$$\frac{\tau}{\sigma} = \frac{\tau_p}{\sigma} + n_T H_T \left[2F_0(\chi_T, X_T) - \frac{nH}{n_T H_T} F_0(\pi-\chi, X) + \Delta F_T\right] \quad . \qquad \text{(III.11)}$$

Equation (III.11) will be used in calculations for the ozone peak. The absorption above the peak must be included in the computation so that the transition from one solution to another will be consistent.

APPENDIX IV. COMPUTER PROGRAM USED TO OBTAIN THE SUNRISE SOLUTIONS

Presented below is the main body of the Fortran IV program used to solve for the ozone and atomic oxygen dissociation rates at sunrise. The solutions of the continuity equation for an all oxygen atmosphere were performed using a standard Runge-Kutta method and that program is not included here. The symbolism of the program is very nearly that of the text.

```
      DIMENSION S2(89),S3(89),SR(89),DL(89),FX(89),C20(37),H20(37),
     1 O30(37),H30(37),DGO(9),CGO(9),DXJ20(9,240),DXJ30(9,240),
     2 TD(9,240)
      COMMON/HEX/DXJ20,DXJ30,PO
      COMMON/HEX1/TD,W,DW,DT,DM,B,C
      GB(UA,UB)=DG/(UA-UB)*ALOG((1.+ALG*EXP(UA/DG))/(1.+ALG*EXP(UB/DG)))
      DF30(Y,G1,G2)=FP/H3H*SQRT(2.*A)*EXP(-(W3-Y-D3**2/(4.*H3H))/H3H)*
     1   (G1*DI1*SQRT(W-Y)+G2*DI2*SQRT(90.-Y))
      FT1(X,WX,EX,CI)=-X*CI+SQRT(1.+2.*X-WX)*(EX+.886*(1.-ERF(EX))*EXP(
     1        WX))
      FT2(X,WX,EX,CI)=-X*CI+SQRT(1.+2.*X-WX)*(EX+(.5/EX)*(1.-.5/WX
     1        +.75/(WX**2)-1.875/(WX**3)))
      READ 91, S2,S3,SR,DL,FX
91    FORMAT ( 11(8F10.6/),F10.6)
      READ 92,C20,H20,O30,H30
92    FORMAT(4(8F10.6/),5F10.6)
      READ 93,DGO,CGO
93    FORMAT(8F10.6/F10.6)
      READ(5,94)YO,A,ALP,FB,W3,D3,O3P,WP,DP,H3T,O3T
94    FORMAT(8F10.6/3F10.6)
      IPRINT=1
1     DO 1000 N=1,9
      T=0.0
      K1=2*N+19
      C2=C20(K1)
      H2=H20(K1)
      C3=C30(K1)
      H3=H30(K1)
      DG=DGO(N)*.01745
      CG=CGO(N)*.01745
      GAM=1.-O3T/O3P
      XT=(A+WP+DP)/H3T
      ALG=EXP(-(CG-1.5708)/DG)
      POR=ARSIN((SIN((PO-90.)*.01745)+SIN(B)*SIN(C))/(COS(B)*COS(C)))
2     DO 999 L=1,240
      TD(N,L)=90.+ARSIN(SIN(POR-DM*T*.01745)*COS(B)*COS(C)-
     1  SIN(B)*SIN(C))/.017453
      CI=-SIN((TD(N,L)-90.)*.017453)
```

```
      SI=SQRT(1.0-CI**2)
      Y=A*((1.0+W/A)*SI-1.0)
      CC1=(W-Y)/D3
      CC2=(50.-Y)/D3
       UA=2.0
      UB=1.0
      GB1=0.0
      GB2=0.0
      IF(Y-W3-D3+.05)3,7,7
 3    UA=ARCOS((A+Y)/(A+W3+D3))
 4    IF(Y-W3+D3)5,6,6
 5     UB=ARCOS((A+Y)/(A+W3-D3))
      GO TO 7
 6    UB=0.0
 7    IF(-CI)10,10,8
 8    IF(Y-YC)99,81,81
 81   G=(Y-YC)/DW*2.
      IY=1+INT(G)
      YI=1.0+AINT(G)
     C2H=C20(IY)+(C20(IY+1)-C20(IY))*(G-YI+1.)
     H2H=H20(IY)+(H20(IY+1)-H20(IY))*(G-YI+1.)
     IF(Y-WP-DP)83,83,82
 82   C3H=C30(IY)+(C30(IY+1)-C30(IY))*(G-YI+1.)
     H3H=H30(IY)+(H30(IY+1)-H30(IY))*(G-YI+1.)
     GO TO 11
 83  C3H=C3T
     H3H=H3T
     ALC=(WP-Y)/DP
     SIT=(A+Y)/(A+WP+DP)
     CT=SQRT(1.-SIT**2)
     XN=(A+W)/H3
     WXN=XN*(1.-SI)
     EXN=SQRT(WXN)
     WXT=XT*(1.-SIT)
     EXT=SQRT(WXT)
     GO TO 11
 10   C2H=C2
     H2H=H2
     C3H=C3
     H3H=H3
 11  X2=(A+W)/H2H
     X3=(A+W)/H3H
     CCO=-(W3-Y-D3**2/(2.*H3H))/D3
 12  DI1=0.0
     DI2=0.0
     ZZ=0.0
     DO 14 J=1,20
     ZZ1=(CC1*ZZ**2+CCO)**2
     ZZ2=(CC2*ZZ**2+CCO)**2
     IF(ZZ1-50.)121,122,122
 121 EZZ1=EXP(-ZZ1)
     GO TO 123
 122 EZZ1=0.0
 123 IF(ZZ2-50.)124,125,125
```

```
124     EZZ2=EXP(-ZZ2)
        GO TO 126
125     EZZ2=0.0
126     DI1=DI1+.05*EZZ1
        DI2=DI2+.05*EZZ2
14      ZZ=ZZ+.05
25      IF(-CI)40,40,26
26      IF(Y-Y0)99,27,27
27      E2=-SQRT(X2*SI/2.)*CI/SI
        ER2=ERF(E2)
        F2=(1.+ER2)*SQRT(X2*SI*1.5708)
        IF(Y-WP-DP)28,30,30
 28     IF(WXN-9.5)281,282,282
 281    FP1=FT1(XN,WXN,EXN,-CI)
        GO TO 283
 282    FP1=FT2(XN,WXN,EXN,-CI)
 283    IF(WXT-9.5)284,285,285
 284    FP2=FT1(XT,WXT,EXT,CT)
        GO TO 286
 285    FP2=FT2(XT,WXT,EXT,CT)
 286    IF(Y-WP+DP)287,287,288
287     FP=D3P/(D3H*H3H)*SQRT(8.*A*DP*(1.+ALO))*((1.-.2*GAM+.267*GAM*ALO
       1   -.533*GAM*ALO**2)-SQRT((ALO-1.)/(ALO+1.))*(1.-.2*GAM-.267*GAM*
       2   ALO-.533*GAM*ALO**2))
        GO TO 289
288     FP=D3P/(D3H*H3H)*SQRT(8.*A*DP*(1.+ALO))*(1.-.2*GAM+.267*GAM*ALO
       1   -.533*GAM*ALO**2)
289     GB1=GB(LA,LP)
        DF3=DF30(Y,GB1,0.0)
        F3=(FP+2.*FP2-EXP(-(W-WP-DP)/H3H)*FP1)
        GO TO 90
30      E3=-SQRT(X3*SI/2.)*CI/SI
        ER3=ERF(E3)
        F3=(1.0+ER3)*SQRT(X3*SI*1.5708)
        IF(Y-W3-D3+.05)31,32,32
31      GB1=GB(LA,LP)
        GB2=GB(-UB,-LA)
        GO TO 33
32      GB1=ALG/(1.+ALG)
        GB2=GB1
33       DF3=DF30(Y,GB1,GB2)
        GO TO 90
40      C2=1.+.125*ALP**2*X2
        C3=1.+.125*ALP**2*X3
        WX2=X2*(1.0-SI)
        WX3=X3*(1.0-SI)
        EX2=SQRT(WX2)
        EX3=SQRT(WX3)
        IF(WX2-9.5)41,42,42
41      F21=FT1(X2,WX2,EX2,CI)
        GO TO 43
42      F21=FT2(X2,WX2,EX2,CI)
```

```
43     IF(WX3-9.5)44,45,45
44     F31=FT1(X3,WX3,EX3,CI)
       GO TO 46
45     F31=FT2(X3,WX3,EX3,CI)
46     F2=F21*C2
       F3=F31*C3
       IF(Y-W3-D3+.05)48,47,47
47     GB2=ALG/(1.+ALG)
       GO TO 49
48     GB2=GB(-UB,-UA)
49     DF3=DF30(Y,-GB2,GB2)
90     XJ2N=0.0
       XJ3N=0.0
       DXJ2N=0.0
       DXJ3N=0.0
       DO 98 K=1,89
       TAU2=(SR(K)+.2090*S2(K))*O2H*H2H*F2
       TAU3=S3(K)*O3H*H3H*F3
       IF(-CI)900,900,899
899    C2=1.+.125*ALP**2*X2*(SI+X2*CI**2*(1.-TAU2))
       C3=1.+.125*ALP**2*X3*(SI+X3*CI**2*(1.-TAU3))
       TAU2=TAU2*C2
       TAU3=TAU3*C3
       F2=F2*C2
       F3=F3*C3
900    TAU=TAU2+TAU3
       TAU=(SR(K)+.2090*S2(K))*O2H*H2H*F2+S3(K)*O3H*H3H*F3
       DTAU=(SR(K)+.2090*S2(K))*O2H*H2H*F2+S3(K)*O3H*H3H*(F3+DF3)
       IF(TAU-50.)902,902,901
901    ETAU=0.0
       GO TO 903
902    ETAU=EXP(-TAU)
903    IF(DTAU-50.)905,905,904
904    EDTAU=0.0
       GO TO 906
905    EDTAU=EXP(-DTAU)
906    XJ2N=XJ2N+DL(K)*S2(K)*FX(K)*ETAU
       XJ3N=XJ3N+DL(K)*S3(K)*FX(K)*ETAU
       DXJ2N=DXJ2N+DL(K)*S2(K)*FX(K)*EDTAU
98     DXJ3N=DXJ3N+DL(K)*S3(K)*FX(K)*EDTAU
       GO TO 100
99     XJ2N=0.0
       XJ3N=0.0
       DXJ2N=0.0
       DXJ3N=0.0
100    M=L
       IF(IGO.GT.0)GO TO 50
       DXJ20(N,M)=XJ2N
       DXJ30(N,M)=XJ3N
       GO TO 51
50     DXJ20(N,M)=DXJ2N
       DXJ30(N,M)=DXJ3N
```

```
51      IF(IPRINT.GT.0)GO TO 52
        ATD=TC(N,M)
        WRITE(6,96)T,ATD,XJ2N,XJ3N,DXJ2N,DXJ3N
96      FORMAT(2F20.2,4E20.4)
52      T=T+DT
999     CONTINUE
        W=W+DW
1000    CONTINUE
        RETURN
        END
```

The following data were used in the analysis. A=a=6375km, B=δ=0, C=$\tilde{\theta}$=38°, FB=35, W3=70, D3=7, 03P=75, WP=25, DP=12.5, H3T=3.10, 03T=6.0. The altitude range was from 50-90 km in 5km steps. The time interval used was 30 seconds. Other data, related to the angular behavior of the ozone, was obtained from the initial runs. Arbitrary scaling was also performed.

APPENDIX V. EMPIRICAL MODELS FOR OZONE AT SUNRISE

Referring to Equations (2.66) and (2.87) of the text one has for ozone

$$\log n_3 = \log n_3^D + \log\left[\frac{1+f_B e^{(\chi-\chi_o)\delta}}{1+e^{(\chi-\chi_o)/\delta}}\right] \tag{V.1}$$

where n_3^D is the uniform 'daytime' ozone density, and χ is used as the angular variable. By defining

$$\begin{aligned} \Delta &= \log n_3 - \log n_3^D \\ \Delta_M &= \log f_B \end{aligned} \tag{V.2}$$

one can calculate the quantities

$$\begin{aligned} \Delta_o &= \Delta_M - \log\left(\frac{1+f_B}{2}\right) \quad ; \quad \chi = \chi_o \\ \Delta_+ &= \Delta_M - \log\left(\frac{1+ef_B}{1+e}\right) \quad ; \quad \chi - \chi_o = \delta^+ \\ \Delta_- &= \Delta_M - \log\left(\frac{e+f_B}{1+e}\right) \quad ; \quad \chi - \chi_o = -\delta^- \quad . \end{aligned} \tag{V.3}$$

These equations were used to calculate the ozone parameters χ_o and δ for each iteration of the ozone sunrise solutions in Chapter 3, and to arrive at the set of parameters for an ozone model based on the final results of Chapter 3 which can be utilized in Chapter 8 (see Table 8.2). It was generally found that the smaller of the two angular widths of (V.3) gave the best model fit to the ozone distributions.

An alternative to the model which leads to Equation (V.1) can be found by defining

$$n_3(\chi) = \exp[\tau_3(\chi)] \qquad (V.4)$$

and writing

$$\tau_3 = \tau_{30} + \frac{\Delta\tau_3}{1+e^{-(\chi-\chi_o)/\delta}} \qquad (V.5)$$

where τ_{30} and $\Delta\tau_3$ are determined from the daytime (or presunrise) equilibrium densities of ozone. In this case χ_o and δ represent, respectively, the point on a log-density plot where the night-to-day ozone transition reaches half its value and approximately, the half width of its 25% points. This model can be applied to the sunrise distributions of other minor constituents such as NO, NO_2, and O in certain cases, and it is utilized in Chapter 8.

APPENDIX VI. OPTICAL DEPTH CORRECTION FOR THE FINITE SIZE OF THE SUN

A correction to the optical depth due to the finite size of the sun can be obtained by averaging the absorption over the solar disc. Consider the averages

$$<e^{-\tau(\alpha)}>_\lambda = \int_{-\alpha_o}^{\alpha_o} d\alpha \ \phi_\lambda(\alpha) e^{-\tau(\alpha)} \Big/ \int_{-\alpha_o}^{\alpha_o} d\alpha \ \phi_\lambda(\alpha)$$

$$<\tau(\alpha)>_\lambda = \int_{-\alpha_o}^{\alpha_o} d\alpha \ \phi_\lambda(\alpha) \ \tau(\alpha) \ \Big/ \int_{-\alpha_o}^{\alpha_o} d\alpha \ \phi_\lambda(\alpha) \qquad \text{(VI.1)}$$

$$I_{TOT}(\lambda) = \int_{-\alpha_o}^{\alpha_o} d\alpha \ \phi_\lambda(\alpha)$$

$I_{TOT}(\lambda)$ is the total solar flux at wavelength λ, $\phi_\lambda(\alpha)$ is a weighting function which depends on the distribution of the radiation intensity at wavelength λ over the solar disc, and α_o is half the angle subtended by the sun at the earth. The solar disc is divided into infinitesimal horizontal slits, and α measures the angle between the horizontal planes along the central ray and the ray intersecting the slit of interest. $\phi_\lambda(\alpha)$ is then the solar intensity distribution at a wavelength λ integrated across the slit. In effect, very small lateral changes in the origin of the ray (with fixed α) are assumed to have no effect on $\tau(\alpha)$. For this analysis a uniform intensity distribution is assumed and ϕ is then the geometrical factor

$$\phi(\alpha) = \sqrt{1 - \alpha^2/\alpha_o^2} \ . \qquad \text{(VI.2)}$$

Expanding e^{τ} and τ to third order in α yields

$$<e^{-\tau(\alpha)}> = e^{-\tau_o} [1 - \frac{1}{2} <\alpha^2>(\tau''(0) - \tau'(0)^2)]$$

$$<\tau(\alpha)> = \tau_o [1 + \frac{1}{2} <\alpha^2> \frac{\tau''(0)}{\tau_o}] \qquad \text{(VI.3)}$$

$$\tau_c = \tau_o[1 + \frac{1}{2} <\alpha^2> (\frac{\tau''(0)}{\tau_o} - \frac{\tau'(0)^2}{\tau_o})]$$

with

$$<e^{-\tau(\alpha)}> \underset{\sim}{\Delta} e^{-\tau_c} \quad ; \quad \frac{1}{2} <\alpha^2> = \frac{1}{8} \alpha_o^2 \quad .$$

Here τ_o is the optical depth for the central ray, and τ_c as defined above is valid for small corrections to τ_o. Using the relations

$$\tau(\alpha) = \tau[h(\alpha), \chi(\alpha)]$$

$$h = (a+\omega) \sin(\chi_o-\alpha) - a$$

$$\chi = \chi_o - \alpha$$

$$\frac{dh}{d\alpha} = - HX \cos \chi \qquad \text{(VI.4)}$$

$$\frac{d^2h}{d\alpha^2} = - HX \sin \chi$$

$$\frac{d\chi}{d\alpha} = - 1 \quad ; \quad \frac{d^2\chi}{d\alpha^2} = 0$$

$$X_o = X \sin \chi_o$$

one can evaluate $d\tau/d\alpha$ and $d^2\tau/d\alpha^2$, and so evaluate Equations (VI.3) for different forms of τ. Consider the following cases.

Case A. $\tau = \sigma n_o H F_o e^{-h/H}$; n_o, H, F_o constant. It can be shown that

$$
\begin{aligned}
<\tau(\alpha)> &= \tau_o \left\{1 + \frac{1}{8}\alpha_o^2 [X_o + (X^2 - X_o^2)]\right\} \\
\tau_c &= \tau_o \left\{1 + \frac{1}{8}\alpha_o^2 [X_o + (X^2 - X_o^2)(1-\tau_o)]\right\} \quad .
\end{aligned}
\tag{VI.5}
$$

Case B. $\tau = \sigma H n_o \sec\chi\, e^{-h/H}$; H, n_o constant. This case can be applied for smaller zenith angles, $\chi \lesssim 75°$, and yields (with $\chi \equiv \chi_o$ here)

$$
\begin{aligned}
<\tau(\alpha)> &= \tau_o \left\{1 + \frac{1}{8}\alpha_o^2 [X_o + \sec^2\chi + (X\cos\chi - \tan\chi)^2]\right\} \\
\tau_c &= \tau_o \left\{1 + \frac{1}{8}\alpha_o^2 [X_o + \sec^2\chi + (X\cos\chi - \tan\chi)^2(1-\tau_o)]\right\} \quad .
\end{aligned}
\tag{VI.6}
$$

Case C. Generally F will depend on h and χ. Referring to Equation (2.52) of the text which is an approximation to the optical depth factor for the sunrise region, one can calculate the optical depths as above and get

$$
\begin{aligned}
<\tau(\alpha)> &\doteq \tau_o \left\{1 + \frac{1}{8}\alpha_o^2 [X_o(1+C_1) + (X\cos\chi - C_2)^2]\right\} \\
\tau_c &\doteq \tau_o \left\{1 + \frac{1}{8}\alpha_o^2 [X_o(1+C_1) + (X\cos\chi - C_2)^2(1-\tau_o)]\right\} \\
C_1 &= \sqrt{\frac{X_o}{2}}\,\mathrm{ctn}\,\chi\, e^{-C_o} - \frac{1}{2} e^{-2C_o} \\
C_2 &= \sqrt{\frac{X_o}{2}}\, e^{-C_o}
\end{aligned}
\tag{VI.7}
$$

$$C_o = \frac{1}{2} X_o \operatorname{ctn}^2 \chi \quad .$$

Higher order correction terms, of the order of $1/X_o$ and greater, are ignored in (VI.7). These results can be applied at sunrise, or Equations (VI.5) could be substituted since they are a good approximation for $\chi \sim \pi/2$. Note that in all cases $<\tau(\alpha)>$ and τ_c will be different when $\tau_o \gtrsim 1$, a sunrise region condition. So taking a simple average of τ over the solar disc will not suffice for a sunrise analysis.

APPENDIX VII. AN ILLUSTRATION OF TIME CONSTANT EFFECTS ON ATOMIC OXYGEN AT SUNRISE

A simplified set of continuity equations for ozone and atomic oxygen may be written

$$\dot{n}_1 = J_2 n_2 + J_3 n_3 - n_1/\tau_1$$

$$\dot{n}_3 = - J_3 n_3 + n_1/\tau_R \qquad \text{(VII.1)}$$

$$1/\tau_1 = 1/\tau_R + 1/\tau_H \quad .$$

τ_R is the time constant for O-O_2 three-body recombination and τ_H is the time constant for the total hydrogen-oxygen loss rate. Assume that τ_H, J_2, and J_3 are constant, and that $n_1 = 0$ at $t = 0$ (or that the J's are turned on at $t = 0^-$). One can then derive

$$\ddot{n}_1 + \frac{1}{\hat{\tau}_1}\dot{n}_1 + \frac{n_1}{\tau_3\tau_H} = \frac{n_1^H}{\tau_3\tau_H} \qquad \text{(VII.2)}$$

with

$$\tau_3 = 1/J_3$$
$$\hat{\tau}_1 = \tau_1\tau_3/(\tau_1+\tau_3)$$
$$n_1^H = \tau_H J_2 n_2$$
$$n_1^S = \hat{\tau}_1(J_2 n_2 + J_3 n_3(0)) \qquad \text{(VII.3)}$$

and

$$\dot{n}_1(0) = J_2 n_2 + J_3 n_3(0) = n_1^S/\hat{\tau}_1 \quad .$$

The solution of Equation (VII.2) when $\hat{\tau}_1 << \tau_H$ is given by

$$n_1(t) = n_1^S[1-e^{-(1-\alpha)t/\hat{\tau}_1}]e^{-\alpha t/\hat{\tau}_1} + n_1^H[1-e^{-\alpha t/\hat{\tau}_1} - \alpha(1-e^{-t/\hat{\tau}_1})] \qquad \text{(VII.4)}$$

with

$$\alpha = \hat{\tau}_1^2/\tau_3\tau_H \quad .$$

When $\alpha << 1$,

$$n_1(t) \doteq n_1^S(1-e^{-t/\hat{\tau}_1})e^{-\alpha t/\hat{\tau}_1} + n_1^H(1-e^{-\alpha t/\hat{\tau}_1}) \ . \tag{VII.5}$$

Now for times, $t < \hat{\tau}_1/\alpha$, one has

$$n_1(t) \doteq n_1^S(1-e^{-t/\hat{\tau}_1}) \tag{VII.6}$$

provided $n_1^S \sim n_1^H$. If $t > \hat{\tau}_1/\alpha$

$$n_1(t) \doteq n_1^H(1-e^{-\alpha t/\hat{\tau}_1}) + n_1^S e^{-\alpha t/\hat{\tau}_1} \quad . \tag{VII.7}$$

A measure of the sizes of n_1^H and n_1^S is given by

$$\frac{n_1^S}{n_1^H} = \frac{\hat{\tau}_1}{\tau_H}\left[1 + \frac{J_3}{J_2}\ \frac{n_3(0)}{n_2}\right] \quad . \tag{VII.8}$$

At sunrise the atomic oxygen density growth is dominated by the oxygen reactions, i.e., by $\tau_1 \doteq \tau_R$, $\hat{\tau}_1$, and n_1^S. After a time on the order of $\tau_3\tau_H/\hat{\tau}_1 = \hat{\tau}_1/\alpha$ the atomic oxygen growth has shifted to the longer time constant hydrogen distribution. In fact, for the chemical model adopted here the final equilibrium O density is determined solely by the hydrogen loss rate. The shift from the oxygen distribution occurs when the atomic oxygen production and loss with ozone has approached sufficiently close to equilibrium.

For the data quoted in Chapter 4 the following order of magnitude calculations, valid for altitudes below 80 km, were compiled

$$\begin{aligned} &\hat{\tau}_1 \lesssim 100 \text{ sec} \\ &\alpha \sim .01 \\ &\hat{\tau}_1/\alpha \gtrsim 10^4 \text{ sec} \\ &n_1^S/n_1^H \sim 1 \quad , \end{aligned} \tag{VII.9}$$

These numbers imply that the hydrogen chemistry will not affect the atomic oxygen for several hours after sunrise. In calculating τ_H the smallest value between the day and night values was used at each height, which represents an extreme case.

APPENDIX VIII. IONIC REACTIONS

Below is a partial list of the different types of ionic reactions. In each reaction M is a neutral third body, and X, Y, and Z are atoms or molecules.

Dissociative Recombination: $XY^+ + e \xrightarrow{\alpha} X + Y$
Three Body Recombination: $X^+ + e + M \xrightarrow{\alpha} X + M$
Radiative Recombination: $X^+ + e \xrightarrow{\alpha} X + h\nu$
Mutual Neutralization: $X^+ + Y^- \xrightarrow{\varepsilon} X + Y$
Three Body Ion-Ion Recombination: $X^+ + Y^- + M \xrightarrow{\varepsilon} XY + M$
Ion-Ion Neutralization: $X^+ + Y^- \xrightarrow{\varepsilon} Z_1 + Z_2 + \ldots$
Photoionization: $X + h\nu \xrightarrow{I} X^+ + e$
Photodetachment: $X^- + h\nu \xrightarrow{\delta} X + e$
Collisional Detachment: $X^- + M \xrightarrow{\delta} X + e + M$
Associative Detachment: $X^- + Y \xrightarrow{\delta} XY + e$
Dissociative Attachment: $XY + e \xrightarrow{\beta} X^- + Y$
Three Body Attachment: $X + e + M \xrightarrow{\beta} X^- + M$
Radiative Attachment: $X + e \xrightarrow{\beta} X^- + h\nu$
Charge Transfer: $X^\pm + Y \xrightarrow{\gamma} X + Y^\pm$
Ion-Atom Interchange: $XY^\pm + Z \xrightarrow{\gamma} X + YZ^\pm$
$X^\pm + YZ \xrightarrow{\gamma} XY^\pm + Z$
Ion-Neutral Association: $X^\pm + Y + M \xrightarrow{\gamma} XY^\pm + M$
Hydration: $X^\pm \cdot (H_2O)_n + H_2O \xrightarrow{\gamma} X^\pm \cdot (H_2O)_{n+1}$

Cluster reactions also occur where the reactants are all molecules or aggregates.

REFERENCES

Archer, D. (1964), The influence of albedo radiation on the photodetachment rate for O_2^- in the D-region, J. Geophys. Res. 69, 991-1000.

Barth, C. A. (1966a), Rocket measurements of nitric oxide in the upper atmosphere, Planet. Space Sci. 14, 623-630.

Barth, C. A. (1966b), Nitric oxide in the upper atmosphere, Annales de Geophys. 22, 198-207.

Biondi, M. A. (1969), Atmospheric electron-ion and ion-ion recombination processes, Can. J. Chem. 47, 1711-1722.

Blake, A. J., J. H. Carver, and G. N. Haddad (1965), Molecular oxygen photo-absorption cross sections between 1050 Å and 2350 Å, University of Adelaide, Department of Physics, Australia.

Bourdeau, R. E., A. C. Aikin, and J. L. Donley (1966), Lower ionosphere at solar minimum, J. Geophys. Res. 71, 727-740.

Branscomb, L. M. (1964), A review of photodetachment and related negative ion processes relevant to aeronomy, Annales de Geophys. 20, 88-105.

Branscomb, L. M., D. S. Burch, S. J. Smith, and S. Geltman (1958), Photodetachment cross sections and the electron affinity of atomic oxygen, Phys. Rev. 111, 504-513.

Burch, D. S., S. J. Smith, and L. M. Branscomb (1959), Photodetachment of O_2^-, Phys. Rev. 112, 171-175 and Errata (1959), Phys. Rev. 114, 1652.

Carver, J. H., B. H. Horton, and F. G. Burger (1966), Rocket determination of the night ozone distribution and the lunar ultra-violet flux, Aus. Weapons Res. Est.

Chapman, S. (1931), The absorption and dissociative or ionizing effect of monochromatic radiation in the atmosphere on a rotating earth, Proc. Phys. Soc. 43, 483-501.

Dalgarno, A. (1969), Metastable mesospheric species, Aeronomy Report No. 32, Aeronomy Laboratory, University of Illinois, Urbana, 235-239.

DASA Reaction Rate Handbook (1967), GE Tempo, Santa Barbara, California.

Deeks, D. G. (1966), D-region electron distributions in middle latitudes deduced from the reflexion of long radio waves, Radio and Space Research Station, Ditton Park, Slough, England, 413-437.

Donahue, T. M. (1966), The problem of atomic hydrogen, Annales de Geophys. 22, 175-188.

Donahue, T. M. (1968), Positive ion chemistry of the D-region including highlights of the Toronto IAGA Conference, Aeronomy Report No. 32, Aeronomy Laboratory, University of Illinois, Urbana, 286-294.

Evans, W. F. J., D. M. Hunten, E. J. Llewellyn, and A. Vallance-Jones (1968), Altitude profile of the infrared atmospheric system of oxygen in the dayglow, J. Geophys. Res. 73, 2885-2896.

Fehsenfeld, F. C. and D. L. Albritton (1969), Associative detachment reaction of O^- and O_2^- by $O_2(^1\Delta_g)$, Can. J. Chem. 47, 1793-1795.

Fehsenfeld, F. C. and E. E. Ferguson (1968), Further laboratory measurements of negative reactions of atmospheric interest, Planet. Space Sci. 16, 701-702.

Fehsenfeld, F. C., E. E. Ferguson, and D. K. Bohme (1969), Additional flowing afterglow measurements of negative ion reactions of D-region interest, Planet. Space Sci. 17, 1759-1762.

Fehsenfeld, F. C., A. L. Schmeltekopf, H. I. Schiff, and E. E. Ferguson (1967), Laboratory measurements of negative ion reactions of atmospheric interest, Planet. Space Sci. 15, 373-379.

Ferguson, E. E. (1967), Ionospheric ion-molecule reaction rates, Rev. Geophys. 5, 305-327.

Ferguson, E. E. (1970), Laboratory measurements of D-region ion-molecule reactions, ESSA Laboratories, Boulder, Colorado.

Ferguson, E. E. and F. C. Fehsenfeld (1968), Some aspects of the metal ion chemistry of the earth's atmosphere, J. Geophys. Res. 73, 6215-6223.

Ferguson, E. E. and F. C. Fehsenfeld (1969), Water vapor ion cluster concentrations in the D-region, J. Geophys. Res. 74, 5743-5751.

Ferguson, E. E., F. C. Fehsenfeld, P. D. Goldan, and A. L. Schmeltekopf (1965), Positive ion-neutral reactions in the ionosphere, J. Geophys. Res. 70, 4323-4329.

Ferguson, E. E., F. C. Fehsenfeld, and A. L. Schmeltekopf (1967), Laboratory measurements of ionospheric ion-molecule reactions, Space Research VII, 1, ed. R. L. Smith-Rose, North-Holland Pub. Co., Amsterdam, 135-139.

Gattinger, R. L. (1968), Observation and interpretation of the $O_2(^1\Delta_g - ^3\Sigma_g^-)$ airglow emissions, Can. J. Phys. 46, 1613-1626.

Gear, C. W. (1967), Numerical integration of stiff ordinary differential equations, Department of Computer Science, Rept. No. 221, University of Illinois, Urbana.

Gear, C. W. (1968a), The control of parameters in the automatic integration of ordinary differential equations, Department of Computer Science, File No. 757, University of Illinois.

Gear, C. W. (1968b), The automatic integration of stiff ordinary differential equations, Proc. IFIPS, A81-A85.

Goody, R. M. (1964), Atmospheric Radiation, Vol. I, Oxford Press.

Gunton, R. C. (1969), Electrons in the D-region at sunrise, Lockheed Palo Alto Labs., California.

Handbook of Geophysics (1961), Macmillan Co.

Hargreaves, J. K. (1962), The behavior of the lower ionosphere near sunrise, J. Atmosph. Terr. Phys. 24, 1-7.

Hasted, J. B. (1964), Physics of Atomic Collisions, Butterworths.

Hesstvedt, E. (1968), On the effect of vertical eddy transport on atmospheric composition in the mesosphere and lower thermosphere, Geofys. Publ. 27, 1-35.

Hesstvedt, E. (1969), A simplified time dependent oxygen-hydrogen atmosphere model with vertical eddy diffusion, European Research Office, University of Oslo, Oslo, Norway.

Hesstvedt, E. and U. B. Jansson (1969), On the effect of vertical eddy transport on the distribution of neutral nitrogen components in the D-region, Institute of Geophysics, University of Oslo, Oslo, Norway.

Hudson, R. D., V. L. Carter, and E. L. Breig (1969), Predissociation in the Schumann-Runge band system of O_2: Laboratory measurements and atmospheric effects, J. Geophys. Res. 74, 4079-4086.

Huffman, R. E. (1970), Photoionization of $O_2(^1\Delta_g)$ in the ionosphere, Spring 1970 AGU, Washington, D. C.

Huffman, R. E., D. E. Paulsen, J. C. Larrabee, and R. B. Cairns (1970), Photoionization of $O_2(^1\Delta_g)$ in the ionosphere, J. Geophys. Res. (in the press).

Hunt, B. G. (1965a), Influence of metastable oxygen molecules on atmospheric ozone, J. Geophys. Res. 70, 4990-4991.

Hunt, B. G. (1965b), A nonequilibrium investigation into the diurnal photochemical atomic oxygen and ozone variations in the mesosphere, J. Atmosph. Terr. Phys. 27, 133-144.

Hunt, B. G. (1966), Photochemistry of ozone in a moist atmosphere, J. Geophys. Res. 71, 1385-1398.

Hunt, W. W., Jr. (1968), Water conglomerates in the D-region, Aeronomy Report No. 32, Aeronomy Laboratory, University of Illinois, Urbana, 311-318.

Hunten, D. M. and M. B. McElroy (1968), Metastable $O_2(^1\Delta)$ as a major source of ions in the D-region, J. Geophys. Res. 73, 2421-2428.

Hunten, D. M. and M. B. McElroy (1969), Reply to V. I. Krassovsky, J. Geophys. Res. 74, 3067.

Inn, E. C. Y. and Y. Tanaka (1959), Ozone absorption coefficients in the visible and ultraviolet regions, Adv. Chem. Ser. 21, 263-268.

Inn, E. C. Y., K. Watanabe, and M. Zelikoff (1953), Absorption coefficients of gases in the vacuum ultraviolet. Part 3. CO_2, J. Chem. Phys. 21, 1648-1650.

Ivanov-Kholodny, G. S. (1965), Maintainence of the night ionosphere and corpuscular fluxes in the upper atmosphere, Space Res. V, ed. D. G. King-Hele, P. Muller, and G. Righini, North-Holland Pub. Co., Amsterdam, 19-42.

Keneshea, T. J. (1967), A technique for solving the general reaction rate equations in the atmosphere, AFCRL Environ. Res. Paper 263.

Kondratyev, K. Ya. (1969), Radiation in the Atmosphere, Academic Press.

Krassovsky, V. I. (1969), Discussion of Paper by D. M. Hunten and M. B. McElroy, J. Geophys. Res. 74, 3064-3066.

LeLevier, R. E. and L. M. Branscomb (1968), Ion chemistry governing mesospheric electron concentrations, J. Geophys. Res. 73, 27-41.

Lloyd, K. H. (1968), Calculation of the effective height of the earth's shadow, Planet. Space Sci. 16, 1071-1073.

Manson, A. H. and M. W. J. Merry (1970), Particle influx and the "winter anomaly" in the mid-latitude lower ionosphere, J. Atmosph. Terr. Phys. (in the press).

Mechtly, E. A. and L. G. Smith (1968a), Growth of the D-region at sunrise, J. Atmosph. Terr. Phys. 30, 363-369.

Mechtly, E. A. and L. G. Smith (1968b), Seasonal variation of the lower ionosphere at Wallops Island during the IQSY, J. Atmosph. Terr. Phys. 30, 1555-1561.

Mechtly, E. A. and L. G. Smith (1970), Changes of lower ionosphere electron densities with solar zenith angle, Radio Sci. 5,

Meira, L. G. (1970), Rocket measurements of upper atmospheric nitric oxide and their consequences to the lower ionosphere, Ph.D. Thesis, Department of Astro-Geophysics, University of Colorado.

Mitra, A. P. (1968), A review of D-region processes in non-polar latitudes, J. Atmosph. Terr. Phys. 30, 1065-1114.

Moler, W. F. (1960), VLF propagation effects of a D-region layer produced by cosmic rays, J. Geophys. Res. 65, 1459-1468.

Nakayama, T., M. Y. Kitamura, and K. Watanabe (1959), Ionization potential and absorption coefficients of nitrogen dioxide, J. Chem. Phys. 30, 1180-1186.

Narcisi, R. S. (1970a), Shock wave and electric field effects in D-region water cluster ion measurements, Spring 1970 AGU, Washington, D. C.

Narcisi, R. S. (1970b), Composition studies of the lower ionosphere, AFCRL, L. G. Hanscom Field, Bedford, Massachusetts.

Narcisi, R. S. and A. D. Bailey (1965), Mass spectrometric measurements of positive ions at altitudes from 64-112 kilometers, J. Geophys. Res. 70, 3687-3700.

Narcisi, R. S., C. R. Philbrick, A. D. Bailey, and L. Della Lucca (1968), Review of daytime, sunrise and sunset ion composition of the D-region, Aeronomy Report No. 32, Aeronomy Laboratory, University of Illinois, Urbana, 355-363.

Nawrocki, P. J. and R. Papa (editors) (1963), *Atmospheric Processes*, Prentice Hall.

Nicolet, M. (1945), A study of the structure of the ionosphere, Inst. Roy. Met. Belg. Mem. 19, 74.

Nicolet, M. (1965a), Nitrogen oxides in the chemosphere, J. Geophys. Res. 70, 679-689.

Nicolet, M. (1965b), Ionospheric processes and nitric oxide, J. Geophys. Res. 70, 691-701.

Nicolet, M. and A. C. Aikin (1960), The formation of the D-region of the ionosphere, J. Geophys. Res. 65, 1469-1483.

Pack, J. L. and A. V. Phelps (1966), Electron attachment and detachment II. Mixtures of O_2 and CO_2 and of O_2 and H_2O, J. Chem. Phys. 45, 4316-4329.

Pearce, J. B. (1969), Rocket measurement of nitric oxide between 60 and 96 kilometers, J. Geophys. Res. 74, 853-861.

Phelps, A. V. (1969), Laboratory studies of electron attachment and detachment of aeronomic interest, Can. J. Chem. 47, 1783-1793.

Radicella, S. M. (1968a), Theoretical models of electron and ion density in the nighttime D-region, J. Atmosph. Terr. Phys. 30, 1745-1760.

Radicella, S. M. (1968b), On the NO concentration and the negative ion chemistry in the D-region, Aeronomy Report No. 32, Aeronomy Laboratory, University of Illinois, Urbana, 391-394.

Radicella, S. M. and D. Stowe (1970), D-region ion chemistry, Aeronomy Report No. 38, Aeronomy Laboratory, University of Illinois, Urbana.

Rees, M. H. (1968), Bremsstrahlung X-rays as a midlatitude ion pair source, Aeronomy Report No. 32, Aeronomy Laboratory, University of Illinois, Urbana, 379-381.

Reid, G. C. (1968a), Electron loss in the mid-latitude D-region, Aeronomy Report No. 32, Aeronomy Laboratory, University of Illinois, Urbana, 295-297.

Reid, G. C. (1968b), Review of daytime electron density profiles, Aeronomy Report No. 32, Aeronomy Laboratory, University of Illinois, Urbana, 324-331.

Reid, G. C. (1970), Production and loss of electrons in the quiet daytime D-region of the ionosphere, J. Geophys. Res. 75, 2551-2562.

Sechrist, C. F., Jr. (1968), Interpretation of pre-sunrise electron densities and negative ions in the D-region, J. Atmosph. Terr. Phys. 30, 371-389.

Sechrist, C. F., Jr. (1970), Interpretation of D-region electron densities, submitted to Radio Sci.

Shimazaki, T. and A. R. Laird (1969), Dynamic effects on vertical distributions of minor neutral constituents in the region 40 to 150 km, ESSA Research Lab., Boulder, Colorado.

Shimazaki, T. and A. R. Laird (1970), A model calculation of the diurnal variation in minor neutral constituents in the mesosphere and lower thermosphere including transport effects, J. Geophys. Res. 75, 3221-3235.

Smith, L. G. (1969), Rocket observations of ozone above 50 km, presented at COSPAR, Prague.

Smith, R. A., T. N. R. Coyne, R. G. Loch, and I. A. Bourne (1967), Small perturbation wave interaction in the lower ionosphere - Part III. Measurements of electron densities, Proc. Ground Based Radio Wave Propagation Studies Conf., 335.

Strobel, D. F., D. M. Hunten, and M. B. McElroy (1970), Production and diffusion of nitric oxide, J. Geophys. Res. 75, 4307-4321.

Snelling, D. and J. Hampson (1968), Water vapour concentration and neutral reactions in the mesosphere and stratosphere, Aeronomy Report No. 32, Aeronomy Laboratory, University of Illinois, Urbana, 223-224.

Swider, W. (1964), The determination of the optical depth at large solar zenith distances, Planet. Space Sci. 12, 761-782.

Swider, W. and M. E. Gardner (1967), On the accuracy of certain approximations for the Chapman function, USAF, Rept. No. 272.

Thomas, L. and M. R. Bowman (1969), Atmospheric penetration of solar radiation during twilight periods, J. Atmosph. Terr. Phys. 31, 1311-1322.

Thomas, L. and M. D. Harrison (1970), The electron density distribution in the D-region during the night and pre-sunrise period, J. Atmosph. Terr. Phys. 32, 1-14.

Tulinov, V. F. (1967), On the role of corpuscular radiation in the formation of the lower ionosphere (below 100 km), Space Research VII, 1, ed. R. L. Smith-Rose, North-Holland Pub. Co., Amsterdam, 386-390.

Turner, B. R. (1968), Formation and destruction of water vapor ions, Aeronomy Report No. 32, Aeronomy Laboratory, University of Illinois, Urbana, 305-310.

U. S. Standard Atmosphere (1962).

Wallace, L. and D. M. Hunten (1968), Dayglow of the oxygen A band, J. Geophys. Res. 73, 4813-4834.

Watanabe, K. (1958), Ultraviolet absorption processes in the upper atmosphere, Advances in Geophysics 5, ed. H. E. Landsberg and J. Van Mieghen, Academic Press.

Watanabe, K. and H. E. Hinteregger (1962), Photoionization rates in the E and F regions, J. Geophys. Res. 67, 999-1006.

Webber, W. (1962), The production of free electrons in the ionospheric D layer by solar and galactic cosmic rays and the resultant absorption of radio waves, J. Geophys. Res. 67, 5091-6000.

Weeks, L. H. and L. G. Smith (1968), A rocket measurement of ozone near sunrise, Planet. Space Sci. 16, 1189-1195.

Zipf, E. C. (1969), The collisional deactivation of metastable atoms and molecules in the upper atmosphere, Can. J. Chem. 47, 1863-1870.

Zmuda, A. J. (1966), Ionization enhancement from Van Allen electrons in the south Atlantic magnetic anomaly, J. Geophys. Res. 71, 1911-1917.